APPLIED COMPUTATIONAL ELECTROMAGNETICS SOCIETY JOURNAL

November 2018
Vol. 33 No. 11
ISSN 1054-4887

The ACES Journal is abstracted in INSPEC, in Engineering Index, DTIC, Science Citation Index Expanded, the Research Alert, and to Current Contents/Engineering, Computing & Technology.

The illustrations on the front cover have been obtained from the research groups at the Department of Electrical Engineering, The University of Mississippi.

EMERITUS ASSOCIATE EDITORS-IN-CHIEF

EMERITUS EDITORIAL ASSISTANTS

NOVEMBER 2018 REVIEWERS: REGULAR PAPERS

Manikandan A.
Danial Abdorahimi
Wazie Abdulkawi
Kiran Ajetrao
Marco Arjona
John Daniel
Qiuzhao Dong
Atef Elsherbeni
José-Manuel Fernandez
Sulmer Fernandez Gutierrez
Robert Foster
Guang Fu
Jiahui Fu
Si-Ping Gao
Zhengwei Hao
Shian Hwu
Fan Jiang
Li Jun Jiang
Rajesh Kumar
Maokun Li
Antonino Musolino
Payam Nayeri
Branislav Notaros
Anthony Pendurthy
Andrew Peterson
Umair Rafique
Hassan Ragheb
Rama Rao T.
Jagdishkumar Rathod
C.J. Reddy
Rocco Rizzo
Pavel Roy Paladhi
Kamalesh Sainath
Rashid Saleem
Theodoros Samaras
Christopher Trueman
Mauro Tucci
Gaobiao Xiao
Salah Yahya
Peng Yang
Xiaohua Yi
Tara Yousefi

THE APPLIED COMPUTATIONAL ELECTROMAGNETICS SOCIETY JOURNAL

Vol. 33 No. 11 November 2018

TABLE OF CONTENTS – REGULAR PAPERS

Mutual Coupling Compensation in Transmitting Arrays of Thin Wire Antennas

Sana Khan, Hassan Sajjad, Mehmet K. Ozdemir, and Ercument Arvas

Department of Electrical and Electronics Engineering
Istanbul Medipol University, Kavacik, Beykoz 34810, Turkey
skhan@st.medipol.edu.tr

Abstract — This paper presents a numerical technique for the compensation of mutual coupling in transmitting arrays of thin wire antennas. The Method of Moments is used to compute the scattering parameters of the array. Using these parameters and the original excitations, a set of new excitation values are computed. The new excitation values compensate the effect of the mutual coupling. Computed results are given for linear, circular, and 3-Dimensional arrays. Uniform and binomial excitations are studied. Results obtained are compared with other available data and very good agreement is observed.

Index Terms — 3-Dimensional arrays, circular arrays, dipole antenna arrays, linear arrays, Method of Moments, mutual coupling compensation, planar arrays, transmitting arrays.

I. INTRODUCTION

In a simplistic array design approach the classical pattern multiplication method is used. In this method the radiation pattern of an array of identical antenna elements is the product of an element pattern and an array factor. The element pattern is the pattern of an isolated element with its center at the origin. This element is assumed to be excited by a unit voltage. The array factor is a sum of fields from isotropic point sources located at the center of each array element and is found from the elements excitation (amplitude and phase) and their locations [1]. Therefore, in the classical array theory, it is assumed that all the elements of the array have equal radiation pattern, in other words, the coupling between individual elements is ignored. For a practical array, this is not true since mutual coupling causes each element to see a different environment and consequently has a different radiation pattern from its neighboring elements.

Mutual coupling between the antenna elements in an antenna array is a classical problem, which is responsible for the degradation of array performance [2–4]. The purpose of this work is to include the effect of mutual coupling and still produce the same pattern as the array factor method.

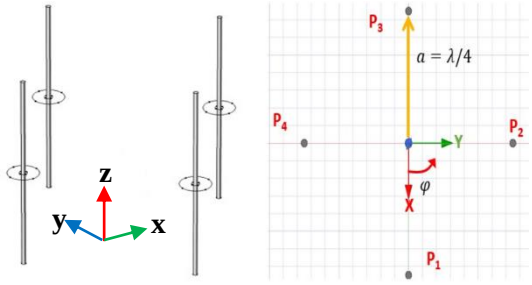

(a) (b)

Fig. 1. (a) Circular array of four thin wire antennas with length λ/2. (b) Top view of the system.

However, this requires replacing the original excitations of the array with a new set of excitations. These new excitation values can be found if the scattering matrix of the array is measured or computed.

Here, the Method of Moments [5] is used to compute the scattering parameters of the array. For example, consider the circular array of four thin halfwave dipoles as shown in Fig. 1 (a). The radius of the circle is λ/4 and the radii of the dipoles are λ/200. Assume that the antennas are excited with the same magnitude and with phase progression of 30°. We call these excitations as the original excitations. The resulting pattern computed using these original excitations and classical array theory is shown in Fig. 2. We will call this result as the desired pattern. It is incorrect because the mutual coupling effects are not included in the classical approach. When mutual coupling effects are included, the pattern shown in Fig. 3 is obtained. We call this pattern the practical pattern and it is quite different than the desired pattern given in Fig. 2.

Using the method described in Section II, a set of new excitations for the array is computed. The true practical pattern of the array computed using these new excitations and by including mutual coupling effects is shown in Fig. 4. It is quite similar to the desired pattern

Submitted On: February 22,2018
Accepted On: August 11, 2018

of Fig. 2. In the next section, we will summarize a numerical method for computing the new excitations.

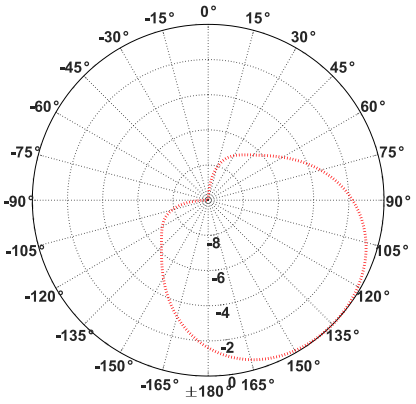

Fig. 2. The *desired pattern* (theoretical pattern using array factor) of circular array of four halfwave dipole antennas excited with uniform phase progression.

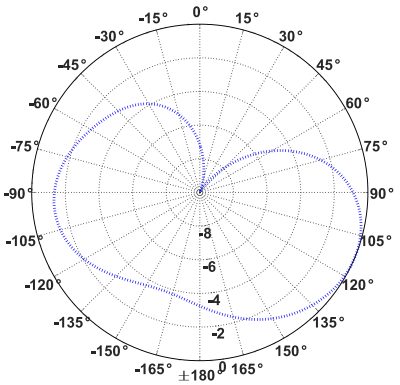

Fig. 3. The *practical pattern* of circular array of four halfwave dipole antennas excited with uniform phase progression.

Several techniques to reduce mutual coupling and improve the isolation between antennas have been investigated [6–11]. Some of these include decoupling networks (DN) which use lumped elements and hybrid couplers to reduce mutual coupling. Another common technique uses the defected ground plane structure (DGS) in which the ground plane is modified by introducing slits of different shapes.

Inductance and capacitance are introduced using electromagnetic band gap (EBG) structures to create forbidden band of frequencies which helps in isolation of the antennas. Metamaterials are also used due to existence of band gaps in their frequency responses. Neutralization lines are also used to feed reverse current to lessen the amount of coupled current. All the techniques mentioned above increase complexity of the network in one way or another. Physical modification of the structure is required, e.g., introduction of lumped elements, parasitic elements, and sometimes special materials may be required to reduce the mutual coupling.

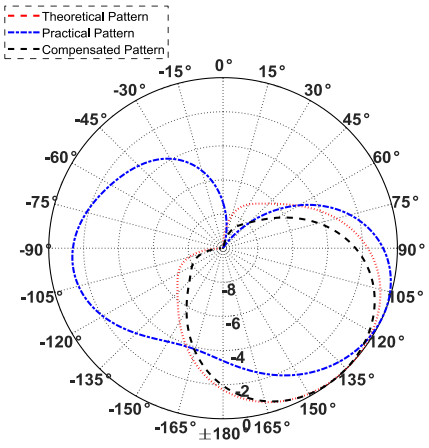

Fig. 4. Theoretical pattern obtained using the classical pattern multiplication method and the original sources (*solid*), the true practical pattern obtained using the original sources (*dashed-dotted*), and the compensated pattern obtained using the compensated voltages (*dashed*).

This paper uses a non-invasive method in which the physical structure or design of the antenna is not changed. Only the excitation voltages of the antennas are changed and these new excitation voltages which are called *compensated voltages* produce a radiation pattern which is similar to the pattern obtained from pattern multiplication method with the original voltages. The pattern multiplication method uses the original excitations and assumes no mutual coupling between the elements. The resulting *theoretical desired pattern* is usually much different than the actual practical pattern as shown in the above example. On the other hand, the new pattern, obtained by using the compensated voltages and by assuming the existence of the mutual coupling does agree with the *theoretical desired pattern*. Only thin wire dipole antennas of lengths less than or equal to λ/2 are considered. Such antennas are usually called as single mode antennas. The individual elements in the array may or may not be identical in dimensions (length, wire radius). A number of similar methods have been suggested for the compensation of mutual coupling [12–14]. This paper is an extension of the work published in [15]. Here, in addition to simple linear arrays we consider circular and 3-Dimensional arrays. We also consider linear arrays with non-uniform excitations.

II. COMPUTATION OF COMPENSATED VOLTAGES

Consider a transmitting array of N identical elements. Each element is assumed to be driven by a voltage source, V_{gk}, for $k = 1,2,...,N$. All sources are assumed to have an

identical internal impedance of Z_o. When mutual coupling is ignored, the input impedance, Z_{in}, of all antennas are the same. Then, the current entering the k^{th} element is simply,

$$I_k = \frac{V_{g_k}}{Z_o + Z_{in}}. \quad (1)$$

The pattern of the k^{th} element is basically fixed by this I_k. The array multiplication method assumes this pattern for the k^{th} element. This is the ideal desired pattern.

In a practical array, because of the existence of mutual coupling, the actual input impedance of the k^{th} element, $Z'_{k_{in}}$, is not anymore equal to Z_{in}. Hence, the actual current entering the k^{th} element is now given by,

$$I'_k = \frac{V_{g_k}}{Z_o + Z'_{k_{in}}}. \quad (2)$$

Since this current is different than I_k, the pattern of this antenna will be different. However, if instead of V_{gk} we use a new voltage,

$$V'_{g_k} = \frac{V_{g_k}(Z_o + Z'_{k_{in}})}{Z_o + Z_{in}}, \quad (3)$$

then, the current entering the k^{th} element will be equal to I_k and hence the pattern of the k^{th} element will be the same as the desired pattern. It is not easy to measure $Z'_{k_{in}}$ directly. However, the scattering matrix of the array can be computed or measured easily. As shown in Appendix, the new compensated voltages can be obtained in terms of the original voltages and the S-matrix as follows,

$$[V'_g] = \frac{2Z_0}{Z_o + Z_{in}}\{U - S\}^{-1}[V_g]. \quad (4)$$

Where U represents an $N \times N$ unit matrix, S is the $N \times N$ matrix of the scattering parameters of the array, $[V_g]$ and are $[V'_g]$ column vectors showing the original and compensated voltages, respectively.

In this work the scattering matrix of the array is computed using the Method of Moments. The feeds are modeled by magnetic frill currents. The unknown currents are approximated by piece-wise sinusoidal functions and Galerkin's method is used for matching [16]. Using the moment matrix and its inverse, one can compute the open circuit parameter matrix, short circuit parameter matrix and hence the scattering parameter matrix of the array. The details are available in [17–19].

III. NUMERICAL RESULTS

Results are given for three different arrays: (i) Circular array of four wire antennas, (ii) Linear array of five wire antennas, and (iii) 3-Dimensional array of seven wire antennas. For each case three different patterns are computed. The *theoretical pattern* is computed using pattern multiplication method which uses the original voltages and assumes no mutual coupling. The *practical pattern* is computed using the original voltages but including the effect of mutual coupling. Finally, the *compensated pattern* is computed using the newly computed voltages and assuming the presence of mutual coupling. Note that all patterns computed in this work are normalized. The results are verified using COMSOL Multiphysics® [20].

A. Circular array of four antennas

In this section, four halfwave dipole antennas have been arranged in a circular array of radius $a = \lambda/4$. The elements are identical with radius $\lambda/200$. The number of expansion functions used for all the MoM simulations are 63 per antenna. In order to find the array factor for the circular array of four dipole antennas, the antennas are replaced by four isotropic sources at their centers, as shown in Fig. 1 (b). The radiation pattern of such an array can be found easily using pattern multiplication method. The element pattern of a halfwave dipole antenna in the H-plane is a unit circle. Since the total pattern is the product of the element pattern and array factor, then the total pattern, in this case, is equal to the array factor. The array factor is given by,

$$AF = \sum_{n=1}^{4} V_n e^{j\beta(x_n \sin\theta\cos\varphi + y_n \sin\theta\sin\varphi)}, \quad (5)$$

where β is the wave number and V_n is the complex input voltage at n^{th} antenna.

A.1. Uniform excitation of circular array

In the first case we excite the array uniformly with $V = 1$ V. The compensated voltages were computed to be equal to $V' = 1.75\angle 45^o$ for each antenna element. Figure 5 shows, the three computed patterns in the H-plane. At first sight, it might be surprising to see that the theoretical and the practical patterns are identical, as if there was no mutual coupling between the elements. Of course there is mutual coupling as indicated by the compensated voltage being different than the original one, however, due to the symmetry of the structure and uniform excitations the effect of mutual coupling is automatically compensated. This can be seen by examining the current distributions on the antennas as shown in Fig. 6. Note that although the magnitude of the currents is different, their distribution and hence their radiation patterns are identical.

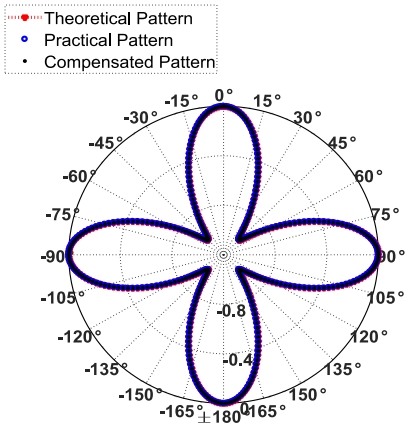

Fig. 5. Radiation pattern (H-plane) for four element circular array of halfwave dipole antennas with uniform excitation.

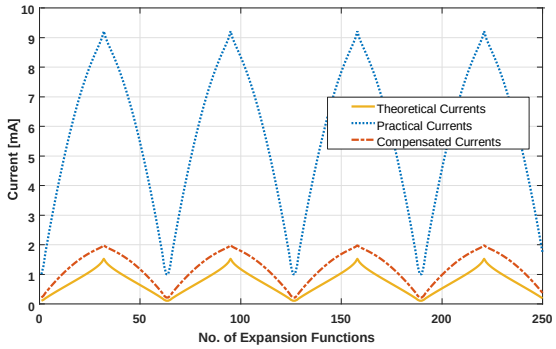

Fig. 6. Current distribution for uniformly excited four halfwave dipole antennas arranged in a circular array.

A.2. Non-uniform excitation

In this case the elements (P_1, P_2, P_3, and P_4) in Fig. 1 (b) are assumed to be excited with voltages $V_1 = 1\angle 0^o$, $V_2 = 1\angle 30^o$, $V_3 = 1\angle 60^o$, and $V_4 = 16\angle 90^o$, respectively. The computed compensated voltage values are $V_1' = 3.06\angle 78^o$, $V_2' = 2.29\angle 82^o$, $V_3' = 1.32\angle 134^o$, and $V_4' = 0.29\angle -92^o$. The three computed patterns are shown in Fig. 4. The current distribution on the antennas are shown in Fig. 7. It can be seen that the currents are not symmetric which explains the significant difference in the patterns of Fig. 4. Figure 8 compares our computed practical patterns with those of COMSOL and excellent agreement is observed. Figure 9 compares three patterns computed by (i) using (5), (ii) using MoM with compensated voltages, and (iii) using COMSOL with compensated voltages.

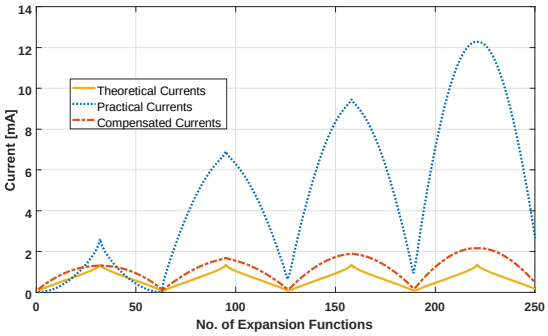

Fig. 7. Current distribution of circular array of four halfwave dipole antennas with a progressive phase excitation.

IV. LINEAR ARRAY OF FIVE ANTENNAS

Here we consider a linear array of five identical halfwave dipoles as shown in Fig. 10 with inter-element spacing of 0.1λ. A binomial excitation of the linear array with $V_1 = 0.25\angle 180^o$, $V_2 = 1\angle 90^o$, $V_3 = 1.5\angle 0^o$, $V_4 = 1\angle 90^o$, and $V_5 = 0.25\angle 180^o$ was used. Figure 11 compares the theoretical and the practical patterns for this array.

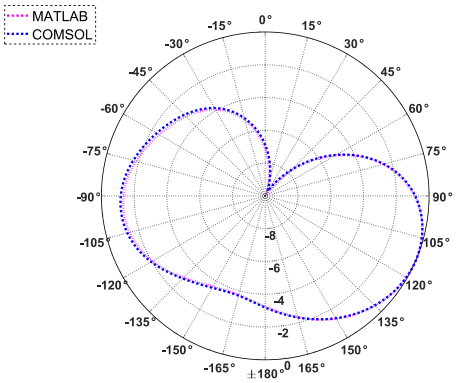

Fig. 8. Comparison of practical pattern for circular array in H-plane.

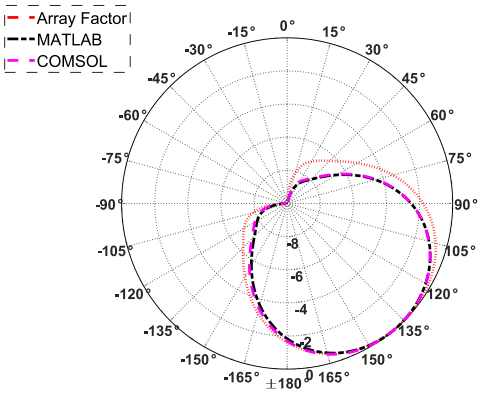

Fig. 9. Comparison of compensated pattern for four element circular array of halfwave dipole antennas (H-plane).

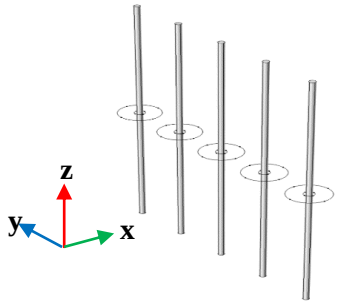

Fig. 10. Linear array of five halfwave dipole antennas uniformly spaced with a separation of 0.1λ.

It is seen that because of mutual coupling the practical pattern is much different than theoretical pattern although both methods use the same original excitations. The computed compensated voltage values are $V_1' = 2.05\angle 84^o$, $V_2' = 2.47\angle 126^o$, $V_3' = 3.86\angle 135^o$, $V_4' = 2.47\angle 126^o$, and $V_5' = 2.05\angle 84^o$. Figure 12 compares the compensated pattern, computed using these new voltage values, with the theoretical pattern computed using array factor method with original voltages. It is observed that the use of the new voltages has

compensated the effect of mutual coupling to a considerable extent.

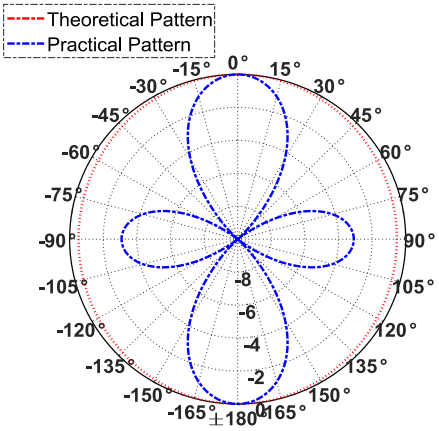

Fig. 11. Comparison of theoretical pattern and practical pattern for the five element linear dipole array using binomial excitation (H-plane).

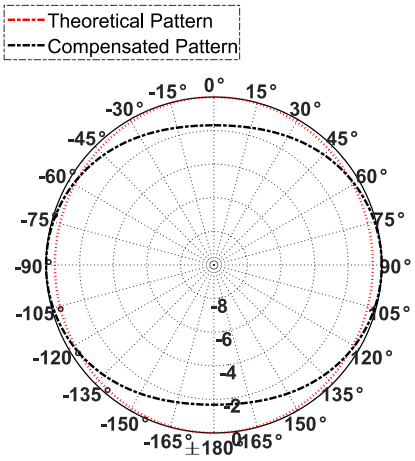

Fig. 12. Comparison of theoretical pattern and compensated pattern for the five element linear dipole array (Fig. 10) using binomial excitation (H-plane).

V. COMPENSATION OF 3-DIMENSIONAL ARRAYS

In this section, a 3-Dimensional array is studied. As shown in Fig. 13 (a), seven dipoles are arranged in two circles.

Four dipoles are placed along a circle in the lower ring and three dipoles in the upper circular ring which is displaced along z-axis. The dipoles are identical, having length L=λ/2 and radius a=λ/200. The centers of the dipoles in the lower ring are at z=0 plane whereas the centers of the upper dipoles are at z=λ/4 plane. When the elements of the array shown in Fig. 13 (b) are excited by $V_1 = 1\angle 0^o$, $V_2 = 0.5\angle 180^o$, $V_3 = 1.5\angle 0^o$, $V_4 = 0.75\angle 180^o$, $V_5 = 1\angle 0^o$, $V_6 = 0.5\angle 0^o$, and $V_7 = 0.75\angle 0^o$, then the computed compensated voltages are given by $V_1' = 4.9\angle 89.6^o$, $V_2' = 5.8\angle -94^o$, $V_3' = 6.3\angle 87.8^o$, $V_4' = 5.12\angle -130^o$, $V_5' = 3.7\angle 82.5^o$, $V_6' = 4.56\angle -128.6^o$, and $V_7' = 2.48\angle 100.4^o$. The patterns in the three principle planes can be seen in Figs. 14, 15, and 16. It is seen that the newly computed voltages compensate the effect of mutual coupling to a large extent.

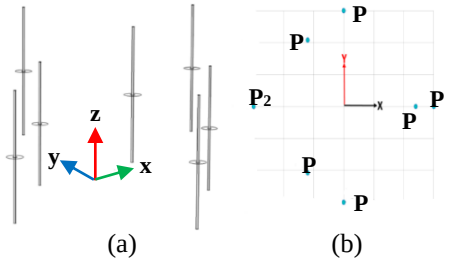

(a) (b)

Fig. 13. (a) Three-dimensional dipole array with seven elements. Four dipoles are placed along a circle of radius 0.5λ and three dipoles along a radius of 0.4λ which are moved in the z-direction by λ/4. (b) Top view of the system.

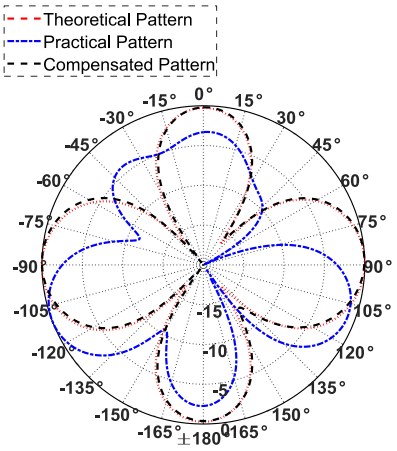

Fig. 14. XY-plane pattern for 3-dimensional array.

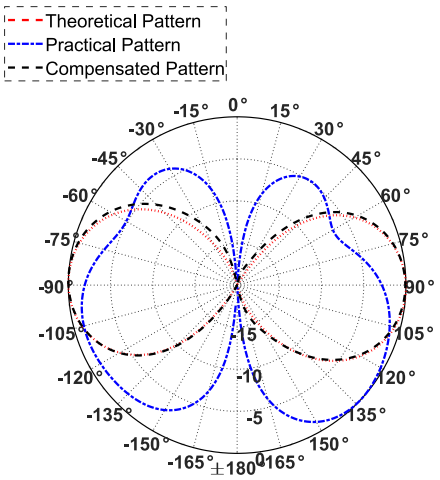

Fig. 15. YZ-plane pattern for 3-dimensional array.

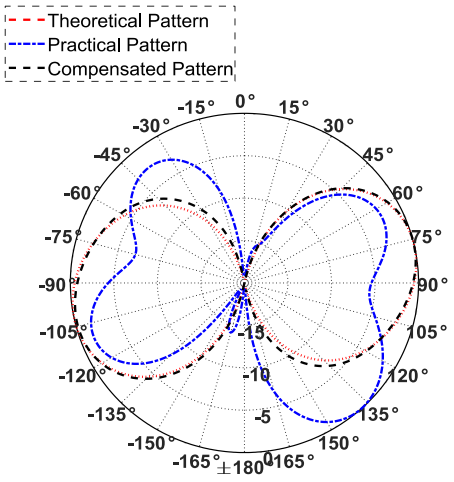

Fig. 16. XZ-plane pattern for 3-dimensional array.

VI. CONCLUSION

In this work the effect of mutual coupling in transmitting arrays of thin wire antennas has been effectively compensated. This is established without changing the antenna structure but only modifying the excitation voltages. These modified excitation voltages were computed using the scattering matrix of the array which was computed using a simple moment method technique. Three different arrays and different methods of excitations were considered. In some cases, the effect of mutual coupling was drastic compared to others. The effect of mutual coupling was successfully reduced in all cases. The patterns computed were verified with COMSOL. The limitation of this method is that it only applies to transmitting arrays. The extension of this simple method to receiving antenna array is not straight forward. In the transmitting case the excited ports are actual physical ports, whereas in the receiving case the excitation source is far away shown by the $(N+1)^{th}$ port which brings some complications. We are in the process of developing a simple method for the receiving antenna array.

ACKNOWLEDGMENT

This work was partially supported by TUBITAK (TURKEY) under the project number 215E316.

A. APPENDIX

Using transmission line theory, we know that the current entering the k^{th} antenna can be expressed as,

$$I_k = \frac{V_k^+ - V_k^-}{Z_0}, \tag{A.1}$$

where V_k^+ is the forward (incident) voltage entering the k^{th} antenna of the N-port network defined by,

$$V_k^+ = \frac{V'_{gk}}{2}, \tag{A.2}$$

and V_k^- is the reflected voltage from the k^{th} antenna It can be written as,

$$\begin{aligned} V_k^- &= S_{k1}V_1^+ + S_{k2}V_2^+ + \cdots S_{kN}V_N^+, \\ &= (S_{k1}V'_{g1} + S_{k2}V'_{g2} + \cdots S_{kN}V'_{gN})/2. \end{aligned} \tag{A.3}$$

Where, S_{ij} is the element of the scattering matrix for the system. Substituting the values of (2) and (3) in (1) we get,

$$\begin{aligned} I_1 &= (V_1^+ - V_1^-)/Z_0, \\ &= \frac{V'_{g1}}{(2Z_0)} - (1/Z_0)\{S_{11}V_1^+ + S_{12}V_2^+ \ldots S_{1N}V_N^+\}, \\ &= \frac{1}{(2Z_0)}\{V'_{g1} - S_{11}V'_{g1} - S_{12}V'_{g2} \ldots S_{1N}V'_{gN}\}, \end{aligned} \tag{A.4}$$

$$I_2 = \frac{1}{(2Z_0)}\{V'_{g2} - S_{21}V'_{g1} - S_{22}V'_{g2} \ldots S_{2N}V'_{gN}\}, \tag{A.5}$$

$$I_N = \frac{1}{(2Z_0)}\{V'_{gN} - S_{N1}V'_{g1} - S_{N2}V'_{g2} \ldots S_{NN}V'_{gN}\}. \tag{A.6}$$

The above equations can be written in matrix form as,

$$\begin{bmatrix} I_1 \\ I_2 \\ \vdots \\ I_N \end{bmatrix} = \frac{1}{2Z_0}\begin{bmatrix} V'_{g1} \\ V'_{g2} \\ \vdots \\ V'_{gN} \end{bmatrix} - \frac{1}{2Z_0}\begin{bmatrix} S_{11} & S_{12} & \ldots & S_{1N} \\ S_{21} & S_{22} & \ldots & S_{2N} \\ \vdots & \vdots & \vdots & \vdots \\ S_{N1} & S_{N2} & \ldots & S_{NN} \end{bmatrix}\begin{bmatrix} V'_{g1} \\ V'_{g2} \\ \vdots \\ V'_{gN} \end{bmatrix},$$

or in short hand notation as,

$$[I] = \frac{1}{2Z_0}\{U - S\}[V'_g]. \tag{A.7}$$

Here, $[I]$ is the N×1 column vector of the desired input currents. U is N×N unit matrix and $[V'_g]$ is the N×1 column vector of the desired compensated source voltages feeding the antennas. Then, the desired compensated source voltages (in the presence of mutual coupling) are given by,

$$[V'_g] = (2Z_0)\{U - S\}^{-1}[I], \tag{A.8}$$

or

$$[V'_g] = (2Z_0)\{U - S\}^{-1}\begin{bmatrix} \frac{V_{g1}}{Z_0+Z_1} \\ \\ \frac{V_{g2}}{Z_0+Z_2} \\ \vdots \\ \frac{V_{gN}}{Z_0+Z_N} \end{bmatrix}.$$

Where, Z_i, is the input impedance of the i^{th} element. When the elements are identical (A.8) reduces to (4).

REFERENCES

[1] W. L. Stutzman and G. A. Thiele, *Antenna Theory and Design*. 3rd Ed., John Wiley & Sons Inc., 2013.

[2] H. T. Hui, M. E. Bialkowski, and H. S. Lui, "Mutual coupling in antenna arrays," *International Journal of Antennas and Propagation*, vol. 2010, pp. 1-7, 2010.

[3] C. Craeye and D. Gonzlez-Ovejero, "A review on array mutual coupling analysis," *Radio Science*, vol. 46, no. 2, 2011.

[4] M. K. Ozdemir, E. Arvas, and H. Arslan, "Dynamics of spatial correlation and implications on MIMO systems," *IEEE Communications Magazine*, vol. 42. no. 6, pp. S14-S19, June 2004.

[5] R. F. Harrington, *Field Computation by Moment*

Methods. Wiley-IEEE Press, 1993.

[6] A. C. J. Malathi and D. Thiripurasundari, "Review on isolation techniques in MIMO antenna systems," *Indian Journal of Science and Technology*, vol. 9, no. 35, 2015.

[7] H. T. Hui, "Decoupling methods for the mutual coupling effect in antenna arrays: A review," *Recent Patents on Engineering*, vol. 1, no. 2, pp. 187-193, Jan. 2007.

[8] C. H. Niow, Y. T. Yu, and H. T. Hui, "Compensate for the coupled radiation patterns of compact transmitting antenna arrays," *IET Microwaves, Antennas Propagation*, vol. 5, no. 6, pp. 699-704, Apr. 2011.

[9] M. Zamlynski and P. Slobodzian, "Comment on 'compensate for the coupled radiation patterns of compact transmitting antenna arrays'," *IET Microwaves, Antennas Propagation*, vol. 8, no. 10, pp. 719-723, July 2014.

[10] A. G Demeryd, "Compensation of mutual coupling effects in array antennas," *IEEE Antennas and Propagation Society International Symposium. 1996 Digest*, vol. 2, pp. 1122-1125, July 1996.

[11] H. Sajjad, S. Khan, and E. Arvas, "Mutual coupling reduction in array elements using EBG structures," *2017 International Applied Computational Electromagnetics Society Symposium Italy (ACES)*, pp. 1-2, Mar. 2017.

[12] S. Henault and Y. M. M. Antar, "Comparison of various mutual coupling compensation methods in receiving antenna arrays," *IEEE Antennas and Propagation Society International Symposium*, pp. 1-4, June 2009.

[13] H. S. Lui, H. T. Hui, and M. S. Leong, "A note on the mutual-coupling problems in transmitting and receiving antenna arrays," *IEEE Antennas Propag. Mag.*, vol. 51, no. 5, pp. 171-176, 2009.

[14] H. Steyskal and J. S. Herd, "Mutual coupling compensation in small array antennas," *IEEE Trans. Antennas Propag.*, vol. 38, no. 12, pp. 1971-1975, 1990.

[15] S. Khan and E. Arvas, "Compensation for the mutual coupling in transmitting antenna arrays," *2016 IEEE Asia-Pacific Conference on Applied Electromagnetics (APACE)*, pp. 84-88, Dec. 2016.

[16] W. L. Stutzman and G. A. Thiele, *Antenna Theory and Design*. 1st Ed., John Wiley & Sons Inc., 1981.

[17] G. V. Eleftheriades and J. R. Mosig, "On the network characterization of planar passive circuits using the method of moments," *IEEE Transactions on Microwave Theory and Techniques*, vol. 44, no. 3, pp. 438-445, Mar. 1996.

[18] B. Hamdi, T. Aguili, N. Raveu, and H. Baudrand, "Calculation of the mutual coupling parameters and their effects in 1-D planar almost periodic structures," *Progress in Electromagnetics Research*, vol. 59, pp. 269-289, 2014.

[19] S. Khan, "Compensation of Mutual Coupling in Transmitting Arrays of Thin Wire Antennas," *Master's Thesis*, Istanbul Medipol University, Turkey, 2017.

[20] COMSOL Multiphysics, V5.2a, Stockholm, Sweden, 2016.

Sana Khan received her B.S. degree in Engineering Sciences from Ghulam Ishaq Khan Institute (GIKI) of Engineering Sciences and Technology, Topi, KPK, Pakistan in 2013 and M.S. degree from Istanbul Medipol University, Istanbul, Turkey in August 2017. Currently, she is pursuing her Ph.D. degree in Electrical Engineering at the same university. Her research interests include computational electromagnetics, antennas, and optical communication.

Hassan Sajjad received his B.S. degree in Telecommunication Engineering from FAST-NUCES Peshawar, Pakistan in 2009 and M.S. degree in Electrical Engineering from Linnaeus University, Vaxjo, Sweden in 2012. Since 2015, he is pursuing his Ph.D. degree in Electrical Engineering at Istanbul Medipol University, Istanbul, Turkey. His research interests include numerical electromagnetics, RF/Microwave devices, and antennas.

Kemal Ozdemir received the B.S. and M.S. degrees in Electrical Engineering from Middle East Technical University, Ankara, Turkey in 1996 and 1998, respectively, and the Ph.D. degree in Electrical Engineering from Syracuse University, Syracuse, NY in 2005. Currently, he is with the Electrical and Electronics Engineering Department of Istanbul Medipol University, Istanbul, Turkey. His research interests include channel modelling, PHY layer design, parameter estimation, and 5G massive MIMO systems.

Ercument Arvas was born in 1953, in Van, Turkey. He received his B.Sc. and M.Sc. degrees in electrical engineering from the Middle East Technical University, Ankara, Turkey, in 1976 and 1979, respectively, and his Ph.D. degree in electrical engineering from Syracuse University, Syracuse, NY, USA, in 1983. From 1983 to 1984, he was with the Department of Electrical Engineering, Yildiz Technical University, Istanbul, Turkey. Between 1984 and 1987, he was with Rochester Institute of Technology, Rochester, NY, USA, and from 1987 to 2014, he was with Syracuse University. He is now teaching at the Electrical and Electronics Engineering Department, Istanbul Medipol University, Istanbul, Turkey. His research interests include electromagnetics scattering and microwave devices. Dr. Arvas is a Fellow of the Electromagnetics Academy.

Series-fed Dipole Array for Near-field RFID Application

Yi Wang [3], Laiwei Shen [4], Cheng Huang [4], Jianping Zhu [4], and Wanchun Tang [1,2]

[1] Jiangsu Province Engineering Laboratory of Audio Technology, School of Physics and Technology
Nanjing Normal University, Nanjing, China

[2] Jiangsu Center for Collaborative Innovation in Geographical Information Resource Development and Application
Nanjing, China
eewctang@njnu.edu.cn

[3] College of Electronic and Information Engineering
Nanjing University of Aeronautics and Astronautics, Nanjing, China
jflsjfls@nuaa.edu.cn

[4] School of Electronic and Optical Engineering, Nanjing University of Science and Technology, Nanjing, China
shenlaiwei@yeah.net, hc_win8er@126.com, 169148076@qq.com.

Abstract ─ In this paper, the series-fed dipole array is proposed and studied for near-field radio frequency identification (RFID) applications. The dipole array is composed of several dipoles with a series feed line. Closed form expressions for current distribution and near-field distribution are presented in this paper. To verify the feasibility of this kind of antenna as a reader antenna in near-field ultra-high frequency (UHF) RFID, a prototype that contains three dipoles is designed, fabricated and tested. The theoretic analysis, simulations and experiments agree well and it is shown that the series-fed dipole array is capable of generating strong magnetic field over a rectangular area, which is very useful in near-field UHF RFID applications.

Index Terms ─ Near-field, radio frequency identification, series-fed.

I. INTRODUCTION

Near-field ultra-high frequency (UHF) radio frequency identification (RFID) has become more and more popular for identification and tracking in item level. One of the most common used techniques in near-field UHF RFID is inductive coupling technique for its capability of operating in close proximity to metals and liquids [1, 2].

In general, tags employed in near-field UHF RFID consist of an IC and a loop antenna. To identify such a tag, the magnetic field component that normal to the loop antenna surface should be strong enough [1]. Besides, in some scenarios such as supermarket or library, the goods or books with RFID tags may be distributed at any area of the shelf; hence, the reader antenna is expected to generate a uniform and strong magnetic field over the large rectangular area of the shelf to ensure that every tag can be identified.

There are several strategies to achieve such kind of magnetic field distribution [3-13]. One method is based on zero-phase-shifted (ZPS) line, which is also called segmented line when first proposed in [3]. In this method, capacitors, either lumped [3] or distributed [4, 5], are added to the wire loop to compensate the current phase shift, hence transforming the electrically large antenna to an electrically small antenna and finally enhancing the magnetic field within the antenna area. However, if the antenna is requested to cover a larger area, the design of this kind of antenna will be complicated [6, 7].

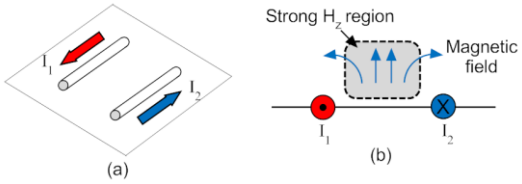

Fig. 1. Schematic of ODCs: (a) perspective view and (b) side view.

Another method is based on the concept of oppositely directed currents (ODCs) [8] shown in Fig. 1, to generate strong magnetic field (referred as strong H_z region here in after) in the area between the two closely spaced currents. To cover a bigger area, a folded dipole antenna is proposed in [9] based on the concept of ODCs, where a 4λ-long loop antenna is folded every half wave length

Submitted On: April 25, 2017
Accepted On: October 19, 2018

to form two "arms" to construct the ODCs. Thanks to its periodic property, this antenna can be extended along the length direction [10, 11] to cover an even longer area.

As can be seen, loop antennas are studied in most of the published literatures for generating strong and uniform magnetic field over a larger area. Less research is reported on the dipole antenna for near-field UHF RFID applications. Inspired by the work of [9], the series-fed dipole array is proposed in this paper, which is composed of several dipoles and a feed line. The dipoles are used to form more than one pair of ODCs, so as to produce strong magnetic field over a larger area for near-field UHF RFID applications. Closed form expressions for the current distributions on the dipoles and near-field magnetic field distributions are presented in this paper. To verify the feasibility of this kind of antenna as a reader antenna in near-field UHF RFID, a prototype that contains three dipoles with series feed line is designed, fabricated and tested. The performance of the prototype is tested by a commercial RFID reader with 30dBm output power and several impinj J41 near-field tags. The prototype occupies an area of 229mm × 126mm, while the measured 100% tag detecting area is bigger than 300mm × 144mm when the observing height is 10mm. The simulations and experiments agree well and it is shown that the series-fed dipole is capable of generating strong magnetic field over a rectangular area, which is very useful in near-field UHF RFID applications.

II. THEORETIC ANALYSIS

Assuming the series-fed dipole array is composed of N dipoles connected in series by a feed line, as shown in Fig. 2. All the N dipoles are made of metal line with radius a, while the lengths l_i (i= 1 to N) of the dipoles and the distances between the adjacent dipoles d_i (i= 1 to N-1) are different and should be optimized. The characteristic admittance of the feed line is denoted as Y_0 with the propagation constant $\beta_0=2\pi/\lambda_g$, where λ_g is the guided wave length of the feed line.

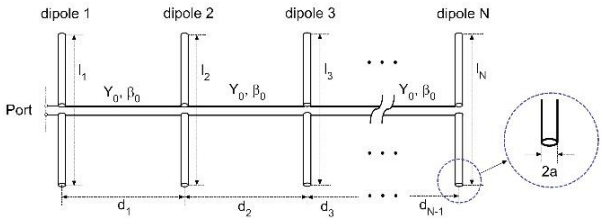

Fig. 2. Configuration of series-fed dipole array.

Before the analysis of this series-fed dipole array, the corresponding equivalent circuit model should be established and shown in Fig. 3, in particular: element circuit model (Fig. 3 (a)) for the N dipoles, feed line circuit model (Fig. 3 (b)), and total equivalent circuit model (Fig. 3 (c)). The analysis of this series-fed dipole will include the currents distribution on the N dipoles and the field distribution of H_z over the antenna area. One should note that the currents on adjacent dipoles should be in opposite direction (or in 180 degree phase difference) in order to form the ODCs. The analysis method is similar to that of log-periodic dipole antenna in [12].

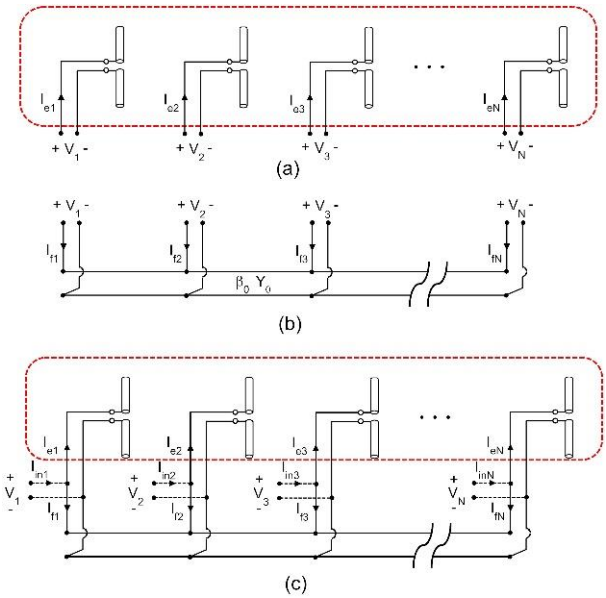

Fig. 3. Equivalent circuit of the series-fed dipole array: (a) element circuit, (b) feed line circuit, and (c) complete circuit.

A. Currents distribution calculation

Considering the element circuit in Fig. 3 (a), the N driving currents of the N dipoles can be represented by $[I_e]$ with the response voltages $[V]$. Let $[Y_e]$ be the admittance matrix of the element circuit, then,

$$[I_e]=[Y_e][V]=[Z_e]^{-1}[V]. \quad (1)$$

The matrix $[Z_e]$ in the above equation is composed of the self- and mutual-impedance of the dipole antenna array, which can be roughly calculated by the formulas in [13, 14] using the induced EMF Method. The formulas are not given here for clarity.

As for the feed line circuit in Fig. 3 (b), similarly, the N driving currents of the N driving ports are represented by $[I_f]$. Since the two circuits (Figs. 3 (a) and (b)) share the same driving ports, the response voltages of the feed line circuit are the same with those of the element circuit, i.e., $[V]$. Let $[Y_f]$ be the admittance matrix of the feed line circuit, we have,

$$[I_f]=[Y_f][V]. \quad (2)$$

$$\left[Y_f\right]=\begin{bmatrix} -jY_0cot\left(\beta_0 d_1\right) & jY_0csc\left(\beta_0 d_1\right) & 0 & & 0 \\ jY_0csc\left(\beta_0 d_1\right) & -jY_0\begin{bmatrix} cot\left(\beta_0 d_1\right) \\ +cot\left(\beta_0 d_2\right)\end{bmatrix} & jY_0csc\left(\beta_0 d_2\right) & \cdots & 0 \\ 0 & jY_0csc\left(\beta_0 d_2\right) & -jY_0\begin{bmatrix} cot\left(\beta_0 d_2\right) \\ +cot\left(\beta_0 d_3\right)\end{bmatrix} & & 0 \\ & \vdots & & \ddots & \vdots \\ 0 & 0 & 0 & \cdots & -jY_0cot\left(\beta_0 d_{N-1}\right) \end{bmatrix}. \quad (3)$$

Table 1: Calculated current phase and magnitude of driving currents of the three dipoles

	$\lvert\angle I_2 - \angle I_1\rvert$	$\lvert\angle I_3 - \angle I_2\rvert$	$\lvert I_1\rvert$	$\lvert I_2\rvert$	$\lvert I_3\rvert$
$d_1 = d_2 = 0.4\ \lambda_g$	142.7	261.7	0.76	0.21	0.18
$d_1 = d_2 = 0.5\ \lambda_g$	166.9	166.9	0.34	0.33	0.34
$d_1 = d_2 = 0.6\ \lambda_g$	94.3	205.9	0.92	0.35	0.07

$*\lambda_g$ is assumed to be equal to λ in the calculation, but actually smaller than λ due to the existence of substrates

From the transmission line theory and with the parameters of the feed line (Y_0, β_0 and d_i (i = 1 to N-1)),the matrix $[Y_f]$ can be expressed as equation (3), By connecting the two circuits in Figs. 3 (a) and (b), the input currents at the driving ports shown in Fig. 3 (c) can be obtained by,

$$\left[I_{in}\right]=\left[I_e\right]+\left[I_f\right]=\left(\left[Y_e\right]+\left[Y_f\right]\right)\left[V\right]. \quad (4)$$

Where

$$\left[I_{in}\right]=\left[1 \quad 0 \quad \cdots \quad 0\right]^{-1}. \quad (5)$$

For simplicity, the input current is set equal to 1A.

Substituting equation (1) into equation (4), we have:

$$\left[I_{in}\right]=\left(\left[Y_e\right]+\left[Y_f\right]\right)\left[Z_e\right]\left[I_e\right]. \quad (6)$$

That is,

$$\left[I_{in}\right]=\left(\left[U\right]+\left[Y_f\right]\left[Z_e\right]\right)\left[I_e\right]. \quad (7)$$

where $[U]$ is the unit matrix.

From equation (7), the current distribution $[I_e]$ on the series-fed N dipoles can then be calculated by:

$$\left[I_e\right]=\left[T\right]^{-1}\left[I_{in}\right]. \quad (8)$$

With

$$\left[T\right]=\left[U\right]+\left[Y_f\right]\left[Z_e\right]. \quad (9)$$

As an example, a three-element series-fed dipole array is analyzed. According to the standard UHF RFID in China, 0.92 GHz is selected as the operating frequency, and the lengths of the dipoles are a little shorter than half wavelength (e.g., 0.46λ in this paper) to make the dipole resonant. As to the feed line, typical parameters are used: Y_0 = 1/200 S, $\beta_0 = 2\pi/\lambda_g$ = 19.3 rad/m (λ_g is assumed to be equal to λ).

Using equations (1) – (8), the driving currents of the individual dipole with different d_i (the distance between two adjacent dipoles) are calculated and listed in Table 1. As can be seen, when $d_1 = d_2 = 0.5\lambda_g$, the magnitude of driving currents on the three dipoles are almost the same, and the phase difference of the currents on adjacent dipoles ($|\angle I_2 - \angle I_1|$and $|\angle I_3 - \angle I_2|$) are both equal to 166.9°, near to 180°. As a result, two pairs of ODCs can be formed by the adjacent two dipoles. On the other hand, when $d_1 = d_2 = 0.4\lambda_g$ and $d_1 = d_2 = 0.6\lambda_g$, the current phase difference between the adjacent dipoles do not satisfy the constraints of ODCs, and the current magnitude on the dipole 1 is much bigger than those on other two dipoles. Hence, the distances between two adjacent dipoles are chosen as $d_1 = d_2 = 0.5\lambda_g$.

B. The magnetic field distribution

Once the driving current of each dipole is obtained, the near-field H_z of the array can be roughly calculated by the following equations,

$$H_z\left(x,y,z\right)=\sum_{i=1}^{N}H_{zi}\left(x,y,z\right). \quad (10)$$

Where

$$\mathrm{H}_{zi}\left(x,y,z\right)=-\frac{I_{id}\left(y-y_{0i}\right)}{4\pi r_i^2 j}\begin{bmatrix} e^{-jkR_{1i}}+e^{-jkR_{2i}} \\ -2cos\left(\frac{kl}{2}\right)e^{-jkr_i}\end{bmatrix}. \quad (11)$$

And

$$r_i=\sqrt{((y-y_0i)^2+(z-z_0i)^2)}, \quad (12)$$

$$\mathrm{R}_{1i}=\sqrt{\left(x-x_{0i}+l_i/2\right)^2+\mathrm{r}_i^2}, \quad (13)$$

$$R_{2i}=\sqrt{((x-x_0i-l_i/2)^2+r_i^2)}. \quad (14)$$

where $k=\omega\sqrt{\mu\varepsilon}$. The location of field point is denoted as (x, y, z), while the location at the center of each dipole is represented by (x_{0i}, y_{0i}, z_{0i}) (i = 1 to N). I_{id} (i = 1 to N) is the driving point currents, which can be obtained by equation (8). Here, in this paper, the dipole is assumed very thin and the current distribution along the center-

fed dipole has sinusoidal form [14].

The $|H_z|$ distribution of the three-element series-fed dipole array at different height is then calculated using equation (9) - (10), and the results are plotted in Fig. 4. The three dipoles are all placed on *xoy* plane, and the center point coordinates of the three dipoles are, respectively, (0 mm, 0 mm, 0 mm), (0 mm, 163 mm, 0 mm) and (0 mm, 326 mm, 0 mm).

As can be seen from the Fig. 4, H_z is strong in the area between adjacent dipoles and weak right above the dipoles, just the same as that of the ODCs. When the observing height is 10mm, the $|H_z|$ is relatively strong within the antenna area (0 mm < y < 326 mm) while declines very quickly outside this antenna area. When the observing height h increases, the fluctuation of H_z becomes small and the average $|H_z|$ will decrease. In the region right above the three dipoles, the $|H_z|$ is very small because the magnetic field is in horizontal direction. Such a "weak H_z regions" can be compensated by the same technique in [11].

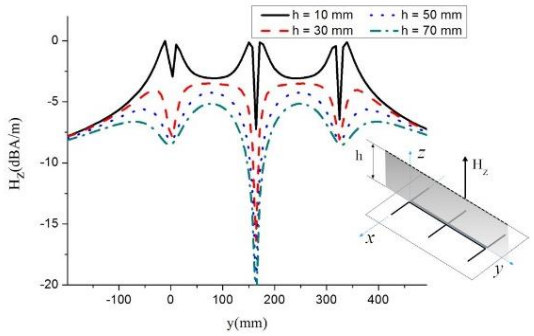

Fig. 4. Calculated $|H_z|$ distribution of the three-element series-fed dipole array f = 0.92 GHz.

III. REALIZATION AND EXPERIMENTS

To verify the performance of the proposed series-fed dipole array, a prototype antenna is design and fabricated. As shown in Fig. 5, the prototype antenna consists of three identical dipoles fed in series by a coplanar stripline (CPS). The antenna is printed on a FR-4 board of 4.4 in dielectric constant and 1.6 mm in thickness. To better match the antenna impedance at the feeding port to 50 Ω, a lumped capacitor is added to the antenna port and taken as 5 pF. Because the prototype antenna is fabricated using standard PCB process, the dimensions of the prototype will be adjusted according to the initial values in section II. Final dimensions of the antenna are: L = 300 mm, W = 144 mm, t = 1.6 mm, L_d = 126 mm, d = 110 mm, w_1 = 3 mm, and w_2 = 2 mm. The current distribution of the antenna at the operating frequency f = 0.92 GHz is obtained by HFSS [15] and shown in Fig. 6. As can be seen, the surface currents I_1 and I_2 are opposite in direction, and the same for I_2 and I_3. This indicates that two pairs of ODCs are formed over the three dipoles.

Figure 7 gives the simulated $|H_z|$ distribution along y-axis of the antenna at observing height of 10mm, 30mm, 50mm and 70mm, respectively. One can see that the simulated magnetic field distribution is similar to that in Fig 4. The "weak H_z regions" occur right above the three dipoles. When the observing height increases ($h \geqslant$ 30 mm), the $|H_z|$ in these three regions decreases quickly and may be smaller than -20dBA/m, the threshold value of $|H_z|$ to identify the tags [8, 13]. Compensation techniques will be employed in the future work to increase the $|H_z|$ above the three dipoles.

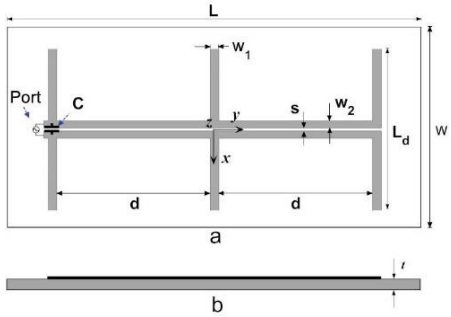

Fig. 5. Geometry of the prototype antenna that contains three elements: (a) top view, and (b) side view.

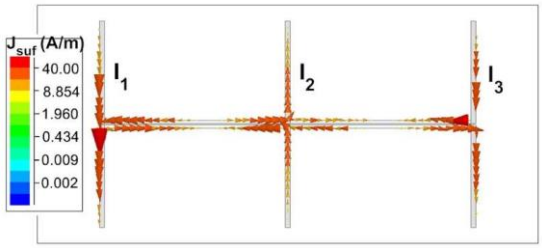

Fig. 6. Simulated current distribution of the prototype antenna.

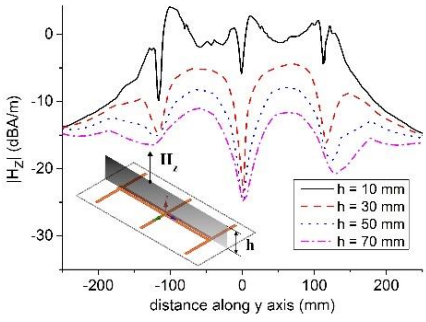

Fig. 7. Simulated $|H_z|$ distribution of the prototype antenna with different observing height (h) at the operating frequency f = 0.92 GHz.

The measured reflection coefficient of the proposed array is given in Fig. 8, together with the simulated results for comparison. One can see that the measured and simulated reflection coefficient agrees well besides a little frequency shift that is caused by the machining accuracy and test environment. As shown in Fig. 8, the measured bandwidth of the array is 0.045 GHz (0.9 GHz – 0.945 GHz) at $|S_{11}| < -10$dB, which can fully satisfy the UHF RFID standard in China.

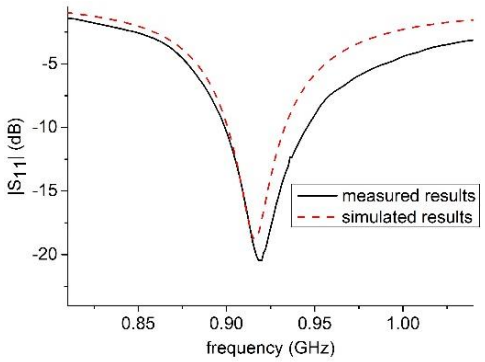

Fig. 8. Simulated and measured $|S_{11}|$ of the prototype antenna.

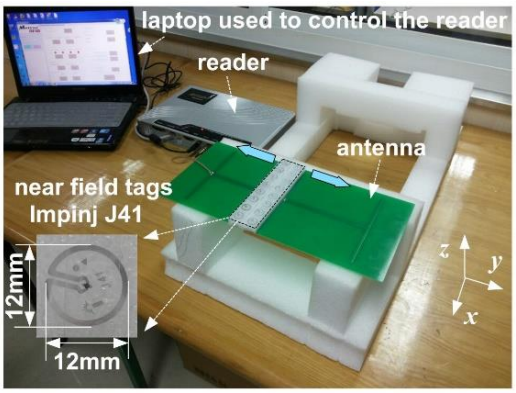

Fig. 9. Experiment setup.

To be used in a real RFID system, the reading performance of the prototype is evaluated using a commercial RFID reader (Marktrace RFID UHF Four Channel Fixed Reader MR6100) and near-field tags (impinj J41). As shown in Fig. 9, the array is connected to the reader by a coaxial-cable, the output power of the reader is set as 30dBm. The tags are placed parallel to the FR-4 board. Figure 10 (a) shows the simulated $|H_z|$ distribution at different observing height, where the area of $|H_z| > -20$ dBA/m is the interrogation area in this paper. The measured interrogation area of the proposed array at different observing height is given in Fig. 10 (b) for comparison. As can be seen, all of the tags are read successfully when the observing height is 10mm with an interrogation area of 300mm × 144mm. When the observing height increases, not all of the tags can be detected and the "weak H_z regions" of $|H_z| < -20$dBA/m will appear. One can see that the "weak H_z regions" in simulated results agree well with those measured results (dark blocks). In the bandwidth of 0.9 GHz to 0.945 GHz, the reading performance of the proposed array is examined and the array works well.

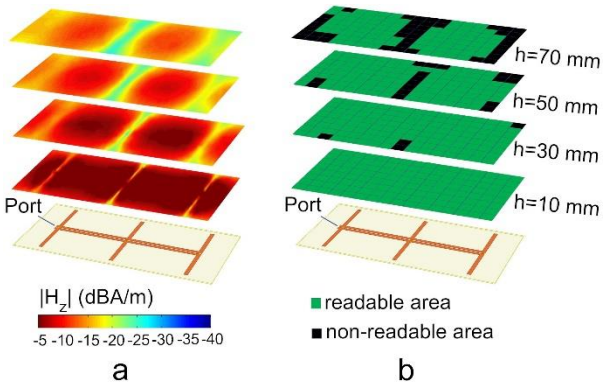

Fig. 10. Simulated $|H_z|$ distribution and measured reading area of the prototype antenna at different observing height: (a) simulated $|H_z|$ distribution, and (b) measured reading area of the proposed array.

IV. CONCLUSION

In this paper, the series-fed dipole array is proposed and studied for near-field UHF RFID application. The method of calculating the current distribution and the near-field distribution of the series-fed array is presented. A prototype that contains three dipoles is designed, fabricated and measured. The simulations and experiments agree well and it is proved that the series-fed dipole is capable of generating a strong magnetic over a rectangular area, which is very useful in near-field UHF RFID applications.

ACKNOWLEDGMENT

This work is supported by the National Key Research and Development Program of China (Grant No. 2017YFB0503500) and the National Natural Science Foundation of China (Grant No. 61571232).

REFERENCES

[1] P. V. Nikitin, K. V. S. Rao, and S. Lazar, "An overview of near field UHF RFID," *Proc. IEEE Int. Conf. RFID*, Grapevine, pp. 167-174, 2007.

[2] A. R. Partridge. "Accuracy in action: Item-level RFID takes off," *Apparel Magazine*, 2013.

[3] D. M. Dobkin, S. M. Weigand, and N. Iye, "Segmented magnetic antennas for near-field UHF RFID," *Microwave Journal*, vol. 56, no. 6, pp. 872-873, 2007.

[4] X. Qing, Z. Chen, J. Shi, and C. K. Goh, "Zero-phase-shift line antennas," *International Workshop on Antenna Technology (iWAT)*, pp. 179-182, 2013.

[5] X. Qing, C. K. Goh, and Z. Chen, "A broadband UHF near-field RFID antenna," *IEEE Transaction on Antennas and Propagation*, vol. 58, no. 12, pp. 3829-3838, 2010.

[6] J. Shi, X. Qing, and Z. N. Chen, "Electrically large zero-phase-shift line grid-array UHF near-field RFID reader antenna," *IEEE Trans. Antenna Propag.*, vol. 62, no. 4, pp. 2201-2207, 2014.

[7] A. Sharma, I. J. G. Zuazola, J. C. Batchelor, et al., "Dual purpose near- and far-field UHF RFID coil antenna with non-uniformly distributed-turns," *IEEE Antennas & Wireless Propagation Letters*, vol. 14, pp. 1342-1345, 2015.

[8] C. Cho, J. Ryoo, I. Park, and H.Choo, "Design of a novel ultra-high frequency radio-frequency identification reader antenna for near-field communications using oppositely directed currents," *IET Microw. Antennas Propag.*, vol. 4, pp. 1543-1548, 2010.

[9] D. Xumin, W. Qun, Z. Kuang, and F. Chunnan, "A magnetic coupling dipole for UHF near-field RFID reader," *IEEE Trans. Magn.*, vol. 48, no. 11, pp. 4305-4308, 2012.

[10] L. Shen, W. Tang, H. Xiang, and W. Zhuang, "A novel antenna achieving null-less magnetic field distribution for near-field UHF RFID," *Antennas and Propagation (ISAP), 2014 International Symposium on*, Kaohsiung, pp. 547-548, 2014.

[11] L. Shen, W. Zhuang, W. Tang, and J. Ma, "Achieving uniform perpendicular magnetic field distribution for near-field UHF RFID," *IET Microw. Antennas Propag.*, vol. 10, no. 2, pp. 215-222, 2016.

[12] R. Duhamel and D. Isbell, "Broadband logarithmmically periodic antenna structures," *Ire International Convention Record IEEE*, pp. 119-128, 1966.

[13] H. E. King, "Mutual impedance of unequal length antennas in echelon," *IEEE Trans. Antennas Propag.*, vol. AP-5, pp. 306-313, 1957.

[14] C. A. Balanis, *Integral Equations, Moment Method, and Self and Mutual Impedances, in Antenna Theory: Analysis and Design*, 3rd ed., New Jersey: John Wiley & Sons, pp. 461-473, 2005.

[15] ANSYS High Frequency Structure Simulator, http://www.ansys.com/

Yi Wang (M' 15) received the B.S. and Ph.D. degrees in Communication and Information System from Nanjing University of Aeronautics and Astronautics (NUAA), Nanjing, China, in 2006 and 2012. In 2012, he joined the College of Electronic and Information Engineering, NUAA, as an Assistant Professor. Currently he is working there as an Associate Professor. His research interests include computational electromagnetics, and the earthquake electromagnetics.

Laiwei Shen was born in Anhui Province, China, in 1990. He received the B.S. degree from Nanjing University of Science and Technology in 2011. Currently, he received the Ph.D. degree From Nanjing University of Science and Technology in 2017. His research interests include RF/microwave circuit, and modeling and optimization of RFIC, antennas.

Cheng Huang was born in Jiangsu Province, China, in 1989. He received the B.S. degree from Nanjing University of Science and Technology, Nanjing, China in 2011. Currently, he is working towards the Ph.D. degree at Nanjing University of Science and Technology. His current research interests include RF/microwave circuit, and modeling and optimization of RFIC, antennas.

Jianping Zhu was born in Anhui Province, China, in 1986. He received the B.S. degree from Anhui University, Hefei, in School of Electronics and Information Engineering in 2010. Currently, he is working towards the Ph.D. degree at Nanjing University of Science and Technology. His current research interests include RF/microwave circuit, through silicon via and frequency-selective surfaces.

Wanchun Tang (M'04) was born in China in 1967. He received the B.S. degree from Tsinghua University, Beijing, China, in 1990, the M.S. degree from the Nanjing University of Science and Technology (NJUST), Nanjing, China, in 1995, and the Ph.D. degree from the City University of Hong Kong, Hong Kong, in 2003, all in electrical engineering.

He was a Full Professor with the Department of Communication Engineering, NJUST, and is currently a Specially Invited Full Professor with the Jiangsu Ley Laboratory on Optoelectronic Technology, School of Physics and Technology, Nanjing Normal University, Nanjing. He has authored or coauthored over 100 journal and conference papers. His current research interests include modeling and optimization of RFIC antennas, signal integrity, and power integrity design in package.

Compact Antenna Array with Newly Designed Decoupling Network

Tao Dong [1], Yantao Yu [2], Meng Li [2], and Hao Zeng [2]

[1] State Key Laboratory of Space-Ground Integrated Information Technology
Beijing Institute of Satellite Information Engineering, Beijing, 100095, China

[2] College of Communication Engineering
Chongqing University, Chongqing, 400044, China
yantaoyu@cqu.edu.cn

Abstract ─ The design of a compact two-element antenna array with highly isolated ports is presented in this paper. The high port isolation is achieved by inserting a decoupling network between the ports of the antenna elements. The decoupling network is designed based on the method of eigen-mode analysis and is realized by the simple microstrip lines. The systematic design procedure of the decoupling network is presented. The achieved microstrip decoupling network is simple and easy to fabricate. The measured results show that the isolation between the antenna ports has been increased by more than 13 dB for a two-element monopole array with the element spacing of 0.1λ.

Index Terms ─ Compact array, decoupling network, eigen-mode analysis, microstrip line.

I. INTRODUCTION

The multiple-input multiple-output (MIMO) technology, which is considered as one of the key technologies of the next generation communication system, has been proven to be effective in improving the channel capacity and throughput. The study of MIMO antenna arrays has received tremendous attention from the researchers all over the world. When multiple antennas are implemented in a platform with limited size, the array has to be kept compact. However, the small separation between the array elements in MIMO systems causes strong mutual coupling effect, which results in severe degradation of the radiation performance [1] and diminishes the benefits of a multiple antenna system [2].

The problem of mutual coupling has attracted a lot of research interest and many contributions have been made to remove or reduce the mutual coupling effect in recent years [3-6]. Electromagnetic band-gap (EBG) structures and defected ground structures (DGS), both with the bandstop features, were proposed to suppress the mutual coupling [7-10]. However, the EBG technology requires enough periodic unit structures to be placed between the antenna elements, which may occupy much space and is not suitable for the arrays with closely spaced elements. While for the defected patterns etched on the ground plane, it may lead to strong backward radiation [11]. Another promising technique using the neutralization lines (NL) was reported to reduce the mutual coupling between two antennas [12, 13]. Although the NLs are simple and require little space, they are usually designed intuitively and must be redesigned for different antennas.

Design of a decoupling network (DN) connecting to the antenna array is another effective and systematic method to increase the isolation between the antenna ports. Decoupling networks have been achieved by connecting the simple reactive elements or a section of transmission line between the input ports and antenna ports, but with the constraint that the mutual impedances of the array must be made to be reactive [14, 15]. After that, various DNs composed of the lumped elements [16-18] were proposed to obtain high port isolation without the abovementioned constraint. However, there is a practical problem with those DNs that there may be no such commercial lumped components with the theoretically calculated values when realizing the networks.

In this paper, a decoupling network using only the microstrip lines for a compact two-element array is proposed. In Section II, the design theory of the decoupling network is explained. In Section III, the design example of a two-element monopole array is presented with the discussion of the simulated and measured results. Finally, Section IV concludes the paper.

II. DESIGN THEORY OF THE DN

The configuration structure of the proposed microstrip decoupling network for a two-element antenna array is shown in Fig. 1. A section of microstrip transmission line with the characteristic impedances of Z_1 and the electrical length of θ_1 is

Submitted On: January 21, 2018
Accepted On: October 19, 2018

connected in serial to each port of the array. Another section of microstrip line with the characteristic impedances of Z_2 and the electrical length of θ_2 is connected in parallel between the two ports. With the addition of the three sections of microstrip lines, the two-element array can be decoupled. The values of the parameters Z_1, Z_2, θ_1 and θ_2 can be calculated by the method of eigen-mode analysis [15].

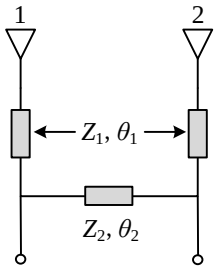

Fig. 1. Configuration structure of the decoupling network for a two-element antenna array.

The impedance matrix Z^a of an antenna array with two identical elements is given by:

$$Z^a = \begin{bmatrix} Z_{11}^a & Z_{12}^a \\ Z_{12}^a & Z_{11}^a \end{bmatrix}. \quad (1)$$

The eigenvalues of the impedance matrix are given by $Z_a = Z_{11}^a + Z_{12}^a$ and $Z_b = Z_{11}^a - Z_{12}^a$, while the corresponding orthogonal eigenvectors are $\mathbf{e}_a = [1\ ,\ 1]^T$ and $\mathbf{e}_b = [1, -1]^T$, respectively. According to the theory of eigen mode, the equivalent circuits of the DN can be analyzed as in Fig. 2.

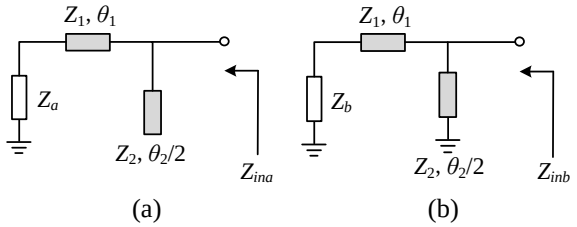

Fig. 2. Equivalent circuits of the DN for different modes: (a) odd mode; (b) even mode.

The input admittances of each mode are given by:

$$Y_{ina} = \frac{(Z_1 + jZ_a \tan\theta_1)}{Z_1(Z_a + jZ_1 \tan\theta_1)} + j\frac{\tan(\theta_2/2)}{Z_2}, \quad (2)$$

$$Y_{inb} = \frac{(Z_1 + jZ_b \tan\theta_1)}{Z_1(Z_b + jZ_1 \tan\theta_1)} - j\frac{1}{Z_2 \tan(\theta_2/2)}. \quad (3)$$

Then, the real and imaginary parts of (2) and (3) are as follows, respectively:

$$G_{ina} = \frac{(Z_1 - X_a \tan\theta_1) Z_1 R_a + R_a \tan\theta_1 \left(Z_1 X_a + Z_1^2 \tan\theta_1\right)}{\left(Z_1 R_a\right)^2 + \left(Z_1 X_a + Z_1^2 \tan\theta_1\right)^2}, \quad (4)$$

$$B_{ina} = \frac{Z_1 R_a^2 \tan\theta_1 - \left(Z_1 - X_a \tan\theta_1\right)\left(Z_1 X_a + Z_1^2 \tan\theta_1\right)}{\left(Z_1 R_a\right)^2 + \left(Z_1 X_a + Z_1^2 \tan\theta_1\right)^2} + \frac{\tan(\theta_2/2)}{Z_2}, \quad (5)$$

$$G_{inb} = \frac{(Z_0 - X_b \tan\theta_1) Z_0 R_b + R_b \tan\theta_1 \left(Z_0 X_b + Z_0^2 \tan\theta_1\right)}{\left(Z_0 R_b\right)^2 + \left(Z_0 X_b + Z_0^2 \tan\theta_1\right)^2}, \quad (6)$$

$$B_{inb} = \frac{Z_1 R_b^2 \tan\theta_1 - \left(Z_1 - X_b \tan\theta_1\right)\left(Z_1 X_b + Z_1^2 \tan\theta_1\right)}{\left(Z_1 R_b\right)^2 + \left(Z_1 X_b + Z_1^2 \tan\theta_1\right)^2} - \frac{1}{Z_2 \tan(\theta_2/2)}. \quad (7)$$

The array can be decoupled when the modal impedances/admittances are equal. Set

$$Y_{ina} = Y_{inb}, \quad (8)$$

and evaluate the real and imaginary parts, respectively, which results in two equations with four variables, that is:

$$f_1 = G_{ina} - G_{inb} = 0, \quad (9)$$

$$f_2 = B_{ina} - B_{inb} = 0. \quad (10)$$

If the characteristic impedances Z_1 and Z_2 are chosen, the functions are a group of binary nonlinear equations which can be solved by the 'gamultiobj' function in MATLAB. Then, the values of the electrical lengths θ_1 and θ_2 can be obtained. Finally, the decoupled ports can be matched by using the conventional L-section impedance matching networks with the system impedance of $Z_0 = 50\ \Omega$.

Theoretically speaking, the proposed decoupling procedure can be extended to the antenna arrays with more than two antenna elements. The above procedure can be used to decouple two different eigen modes at each time. Then, repeat the same procedure until all the modes are decoupled. However, if the number of array elements is large, then the resulted decoupling network will be complicated, which makes it difficult to be implemented. Therefore, the proposed decoupling network is typically applied to the arrays with four or less elements.

III. DESIGN EXAMPLE AND RESULTS

The monopole antenna is used as the array elements due to its simplicity. The DN for the two-element monopole antenna array operating at 2.4 GHz is designed to verify the proposed method.

A. Two-element monopole antenna array

As shown in Fig. 3, the length of the array element is h = 30.5 mm and the element spacing is d = 12 mm, which is about 0.1λ. It is noted that the proposed DN is applicable to the antenna arrays with different element separations. The monopole elements are mounted on a FR4 substrate, which has a thickness of t = 1.6 mm and the dielectric constant of 4.4. The top surface of the FR4 substrate is copper, which acts as the ground plane of the monopole array. The size of the substrate is $W \times L$ = 70 mm × 70 mm. The monopole elements are fed by microstrip lines with a length of l = 36.5 mm and a

width of w = 3 mm. To keep the constancy and avoid the spurious radiation, both the microstrip feed lines and the subsequently designed DN are printed on the lower surface of the substrate.

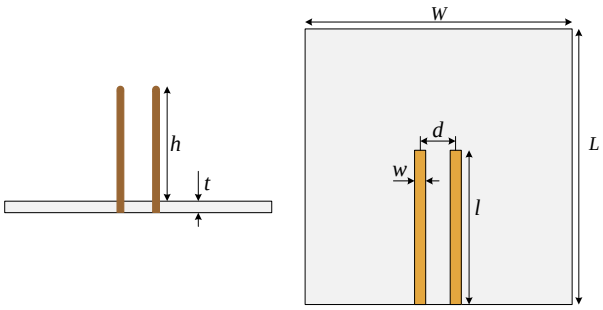

Fig. 3. The geometry of two-element monopole antenna array: (a) side view; (b) bottom view.

The designed monopole array was simulated in HFSS and Fig. 4 shows the simulated *S*-parameters. It can be seen that the S_{12} is as high as -8 dB at 2.4 GHz. The strong mutual coupling makes the antenna array unmatched, where the S_{11} is only -7 dB at the operating frequency. Therefore, a decoupling network is required to reduce the mutual coupling between the array elements.

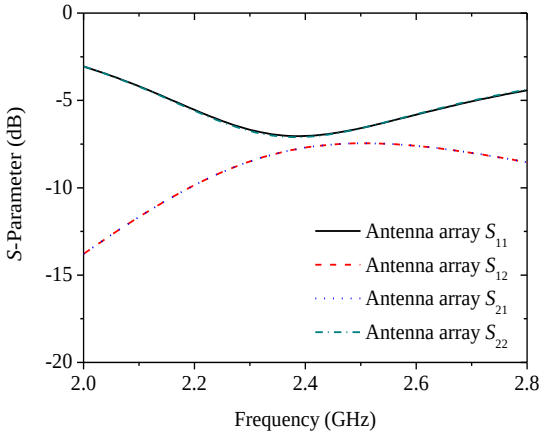

Fig. 4. The simulated *S*-parameters of the two-element monopole array.

B. Design of the decoupling network

The impedance parameters of the antenna array at the operating frequency can be obtained directly from HFSS or from the transformation of the **S** matrix of the array. The conventional 50 Ω microstrip line is used for all the microstrip sections of the design. The values of the electrical lengths θ_1 and θ_2 of the decoupling network are calculated by adopting a simple genetic algorithm, i.e., gamultiobj, in MATLAB. The L-section impedance matching networks are then designed to match the decoupled ports, with θ_3 being the electrical length of the series branch and θ_4 being that of the open stub.

The designed microstrip decoupling and matching network is then connected to the two-element monopole array and simulated in HFSS. After a fine tuning, the obtained values of the parameters are shown in Table 1. Figure 5 shows the simulated results of the *S*-parameters of the array with the decoupling and matching network. It is obvious that both of the S_{11} and S_{12} have been reduced to around -30 dB at the operating frequency of 2.4 GHz. The isolation between the antenna ports has been significantly improved by about 20 dB.

Table 1: Values of the design parameters of the microstrip decoupling and matching network

Parameter	Value
θ_1	133.3°
θ_2	148.6°
θ_3	63.2°
θ_4	72.7°

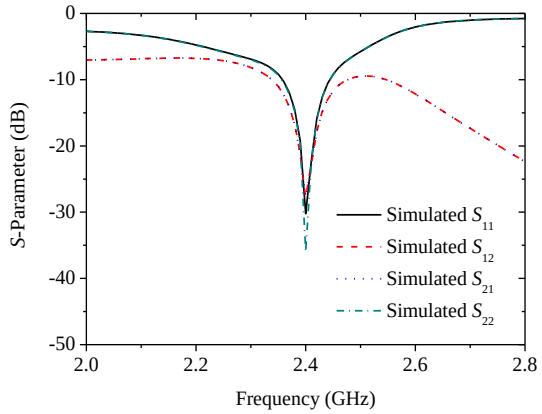

Fig. 5. The simulated *S*-parameter of the array with the decoupling and matching network.

The prototype of the designed monopole array with microstrip decoupling and matching network was fabricated, as shown in Fig. 6. It was measured by using a Keysight E5063A Vector Network Analyzer and the achieved results are plotted in Fig. 7. From the figure, it can be seen that the S_{12} is -21 dB and the S_{11} is around -20 dB at the center frequency, which validates the effectiveness of the decoupling method. Good agreement between the simulated and measured results was obtained.

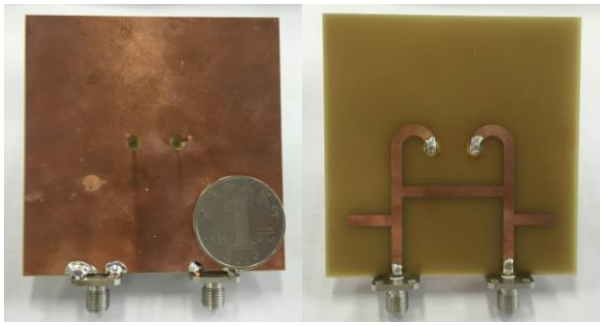

(a) (b)

Fig. 6. The fabricated monopole array with the decoupling and matching network: (a) top view; (b) bottom view.

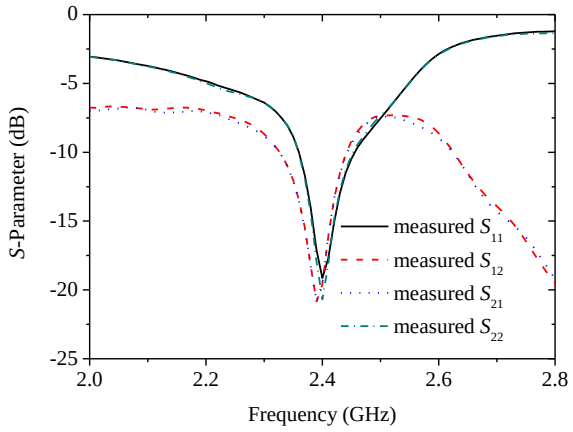

Fig. 7. The measured *S*-parameter of the array with the decoupling and matching network.

The normalized radiation patterns of both the original and decoupled arrays at the operating frequency of 2.4 GHz are illustrated in Fig. 8, respectively. With both of the elements excited, the radiation patterns remain consistent in a certain level.

IV. CONCLUSION

The systematic design procedure of the decoupling network for a two-element antenna array has been presented. The DN contains only simple microstrip lines and is easy to implement. By adopting the method of eigen-mode analysis, the design parameters of the network can be obtained. The measured results of the design example show that the port isolation of a two-element monopole array has been enhanced by more than 13 dB, which illustrates the effectiveness of the proposed decoupling network.

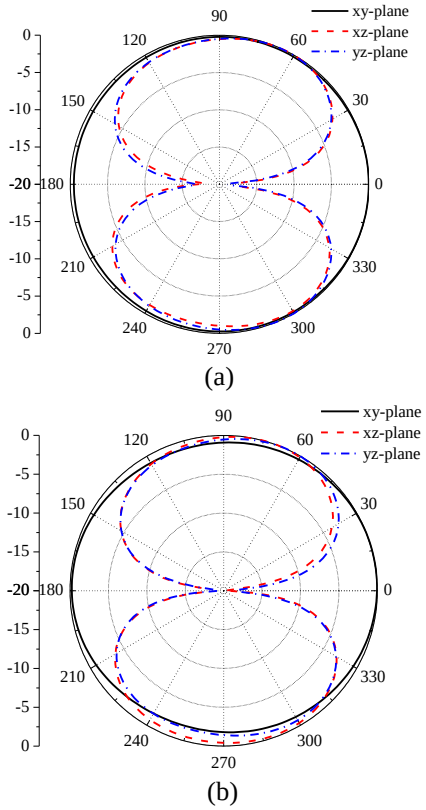

(a) (b)

Fig. 8. The radiation patterns of antenna arrays at operating frequency of 2.4 GHz: (a) original array; (b) decoupled array.

ACKNOWLEDGMENT

This work was supported in parts by the Innovation Funds from China Academy of Space Technology (Grant CAST2016021), the Fundamental Research Funds for the Central Universities (Grant 106112016CDJZR165508, 106112017CDJQJ168817 and 2018CDJDTX0010) and the National Natural Science Foundation of China (Grant 61571069).

REFERENCES

[1] X. Li and Z. Nie, "Mutual coupling effects on the performance of MIMO wireless channels," *IEEE Antennas Wireless Propag. Lett.*, vol. 3, pp. 344-347, 2005.

[2] L. Zhao, L. K. Yeung, and K.-L. Wu, "A coupled resonator decoupling network for two-element compact antenna arrays in mobile terminals," *IEEE Trans. Antennas Propag.*, vol. 62, no. 5, pp. 2767-2776, 2014.

[3] S. Zhang and G. F. Pedersen, "Mutual coupling

reduction for UWB MIMO antennas with a wideband neutralization line," *IEEE Antennas Wireless Propag. Lett*., vol. 15, pp. 166-169, 2016.

[4] Y. Yu, L. Yi, X. Liu, and Z. Gu, "Mutual coupling reduction of dual-frequency patch antenna array," *ACES Journal*, vol. 31, no. 9, pp. 1092-1099, 2016.

[5] M. D. Ardakani and R. Amiri, "Mutual coupling reduction of closely spaced MIMO antenna using frequency selective surface based on meta-materials," *ACES Journal*, vol. 32, no. 12, pp. 1064-1068, 2017.

[6] K. Yu, Y. Li, and X. Liu, "Mutual coupling reduction of a MIMO antenna array using 3-D novel meta-material structures," *ACES Journal*, vol. 33, no. 7, pp. 758-763, 2018.

[7] F. Yang and Y. R. Samii, "Microstrip antennas integrated with electromagnetic band-gap EBG structure: A low mutual coupling design for array applications," *IEEE Trans. Antennas Propag*., vol. 51, no. 10, pp. 2936-2946, 2003.

[8] H. S. Farahani, M. Veysi, M. Kamyab, and A. Tadjalli, "Mutual coupling reduction in patch antenna arrays using a UC-EBG superstrate," *IEEE Antennas Wireless Propag. Lett*., vol. 9, pp. 57-59, 2010.

[9] C.-S. Kim, J.-S. Lim, S. Nam, K.-Y. Kang, and D. Ahn, "Equivalent circuit modeling of spiral defected ground structure for microstrip line," *Electron. Lett*., vol. 38, no. 19, pp. 1109-1110, 2002.

[10] H. A. Atallah, A. B. Abdel-Rahman, K. Yoshitomi, and R. K. Pokharel, "Mutual coupling reduction in MIMO patch antenna array using complementary split ring resonators defected ground structure," *ACES Journal*, vol. 31, no. 7, pp. 737-743, 2016.

[11] R.-L. Xia, S.-W. Qu, P.-F. Li, Q. Jiang, and Z.-P. Nie, "An efficient decoupling feeding network for microstrip antenna array," *IEEE Antennas Wireless Propag. Lett*., vol. 14, pp. 871-874, 2015.

[12] H. Wang, L. Liu, Z. Zhang, Y. Li, and Z. Feng, "Ultra-compact three-port MIMO antenna with high isolation and directional radiation patterns," *IEEE Antennas Wireless Propag. Lett*., vol. 13, pp. 1545-1548, 2014.

[13] S.-W. Su, C.-T. Lee, and F.-S. Chang, "Printed MIMO-antenna system using neutralization-line technique for wireless USB-dongle application," *IEEE Trans. Antennas Propag*., vol. 60, no. 2, pp. 456-463, 2012.

[14] H. J. Chaloupka, X. Wang, and J. C. Coetzee, "Superdirective 3-element array for adaptive beamforming," *Microw. Opt. Technol. Lett*., vol. 60, no. 2, pp. 425-430, 2003.

[15] J. B. Anderson and H. H. Rasmussen, "Decoupling and descattering networks for antennas," *IEEE Trans. Antennas Propag*., vol. 24, no. AP-6, pp. 841-846, 1976.

[16] S.-C. Chen, Y.-S. Wang, and S.-J. Chung, "A decoupling technique for increasing the port isolation between two strongly coupled antennas," *IEEE Trans. Antennas Propag*., vol. 56, no. 12, pp. 3650-3658, 2009.

[17] H. T. Huang, Y. Yu, and L. Yi, "Design of highly isolated compact antenna array for MIMO applications," *Int. Journal Antennas Propag*., vol. 2014, Article ID 473063, 5 pages, 2014.

[18] J. C. Coetzee and Y. Yu, "Closed-form design equations for decoupling networks of small arrays," *Electron. Lett*., vol. 44, no. 25, pp. 1441-1442, 2008.

Tao Dong received the B.S. and Ph.D degrees in Electronics Science and Technology from Beijing Institute of Technology in 1999 and 2004, respectively. He is currently a Professor at State Key Laboratory of Space-Ground Integrated Information Technology, Beijing Institute of Satellite Information Engineering, China. His research interests include antenna, optical phased array, and free space optical communication.

Yantao Yu received the B.Eng degree (1st class honors) and the Ph.D degree both from the National University of Singapore, in 2004 and 2009, respectively. From 2008 to 2009, he worked at Motorola Electronics Pte Ltd, Singapore, as an RF Engineer. From 2009 to 2010, he was a Research Fellow with the National University of Singapore. He is currently an Associate Professor in the College of Communication Engineering, Chongqing University, China. His research interests include analysis and design of antennas and compact antenna arrays.

Meng Li received the B.Eng degree from the Chongqing University, China in 2017. He is now working toward the Master degree in the same university. His research interests include antenna/array design and microwave circuits.

Hao Zeng received the B.S. and Ph.D degrees in Electronics Science and Technology from Chongqing University of China in 2000 and 2006, respectively. He is currently a Professor at the College of Communication Engineering in Chongqing University, Chongqing, China. His research interests include smart antenna, phased array antenna and array signal processing.

Dual-Polarized Antenna Based on Metal Ring and Microstrip Patch

Lizhong Song [1] and Sai Li [2]

[1] College of Information and Electrical Engineering
Harbin Institute of Technology at Weihai, Weihai, 264209, China
songlz@hit.edu.cn

[2] College of Information and Electrical Engineering
Harbin Institute of Technology at Weihai, Weihai, 264209, China
lisai920@163.com

Abstract ─ Based on the principle of the complementary antenna, a kind of dual-polarized antenna element is studied, which combines the metal ring and rectangular microstrip patch. The antenna separates the rectangular microstrip patch and the metal ring on a vertical space, and the metal ring is equivalent to a current radiation source. The rectangular microstrip patch is equivalent to a magnetic flux radiation source, which respectively radiates and receives two orthogonal polarized electromagnetic wave components to achieve dual polarization. A metal reflector ground is introduced to realize the uni-direction radiation pattern, and the front-to-back ratio of the pattern has been improved. The simulation results show that the isolation between two polarization ports is 22dB within the frequency range of 4.94GHz~5.06GHz. The measured results of the fabricated antenna indicate that the Voltage Standing Wave Ratio (VSWR), port isolation degree and the cross polarization level can satisfy technical requirements. And design effectiveness of the dual-polarized antenna in this paper was proved. The dual-polarized antenna studied in this paper has been suitable for some application fields such as phased array radar and the research results lay the technical foundation for the practical engineering application.

Index Terms ─ Cross polarization level, dipole, dual-polarized antenna, microstrip patch antenna, radiation pattern.

I. INTRODUCTION

Phased array antenna which compares with mechanical scanning, phased array antenna, as one of the types of electro-scanning antennas, have advantages in beam scanning without inertia, fast beam scheduling and multi-beam capability [1]. The indexes of antenna element directly affect the overall performance of phased array antenna. Therefore, the design and study on phased array antenna element to be applied in engineering application is very meaningful.

Polarization is an inherently important information for radio waves. The wireless electronics with the ability to sense the polarization of electromagnetic waves have better performance than conventional single-polarization electronic devices. The polarization information has gained widespread attention in the field of radar. Dual-polarized antenna can transmit or receive two orthogonally polarized electromagnetic waves, it can be used to get amplitude and phase or other information from the scattered wave of target. Dual-polarized antennas are the key components of phased arrays and MIMO arrays, the design and implementation of dual-polarized antennas have become a hot research area in the field of antenna technology [2-3]. The research on dual-polarization antenna mainly focuses on the radiation principle, realization plan and feasibility of dual-polarization antenna [4-7]. From the radiation mechanism point of view, the dual-polarized antenna is composed of orthogonal current source and magnetic current source, the two polarized ports respectively radiate or receive the corresponding polarized electromagnetic wave. From the structure point of view, the dual-polarized antenna mainly includes the dual-polarized dipole antenna, the dual-polarized log-periodic antenna, the dual-polarized microstrip patch antenna, the dual-polarized aperture antenna and the dual-polarized vivaldi antenna, etc. For example, Qun and his team studied a dual-polarized antenna based on printed dipole and circular microstrip patch structure, the antenna was designed by a combination of a current source and a magnetic current source to explore its engineering realization technology and its radiation performance [8]. A dual-band dual-polarized log-periodic dipole array for multiple-input-multiple-output WLAN applications is proposed in [9]. The antenna has 12 antennas element: six for horizontal polarization and six for vertical polarization. The proposed array is manufactured and exhibits the characteristics of high isolation, good

Submitted On: February 2, 2018
Accepted On: October 19, 2018

front-to-back ratio. A Ku-band dual-linear polarized broadband aperture-coupled antenna is presented based on substrate integrated waveguide technology in [10]. Experimental results indicated that the isolation is more than 40dB, the bandwidth obtains 21% of return loss less than -20dB. A cross-placed Vivaldi antenna is designed in [11], the working frequency of this antenna is 0.7GHz~7.3GHz when the return loss is less than -10dB.

In engineering applications, dual-polarized microstrip patch antenna is one of the most widely used dual-polarized antenna types [12-13]. The radiation of the microstrip patch antenna can be regarded as the radiation of the gap around the patch. According to the equivalent principle of the electromagnetic field, the radiation of the slot can be understood as the radiation of the magnetic current source. The dual-polarized microstrip patch antenna adopts printed circuit technology processing with the advantages of low profile, small size, light weight and low cost. Besides, the feed method of dual-polarized microstrip antenna is flexible and easy to be achieve microstrip side-fed, microstrip corner-fed and electromagnetic coupling feed [14-15]. However, the working bandwidth of the microstrip antenna is narrow, the polarization port isolation of the dual-polarized antenna and the cross-polarization level of the radiation field are higher. Although the improvement measures can be used to extend the impedance bandwidth of the microstrip antenna and improve the antenna pole, but the structure of the dual-polarized antenna is also complicated and the difficulty of engineering is increased. Printed dipole is a common form of microwave radiators, it can achieve a larger impedance bandwidth. The shape of the metal conductor vibrator can be rectangular, circular, oval, butterfly or many other shapes. The printed dipole antenna is realized by loading the dipole structure on dielectric substrate, its feeding methods include coaxial line, coplanar waveguide (CPW), etc. It is designed to be flexible and can even achieve ultra-wideband (UWB) performance [16-19]. Dual-polarized dipole antenna is composed of two orthogonally placed dipoles, equivalent to two orthogonal current source, this antenna has been widely used in base stations, communications and other fields. A Ku-band dual polarization microstrip array antenna is presented in [20]. The microstrip patch antenna as the array element radiates orthogonally excited by approximate and slot coupling, respectively. The design by simulation indicates that the antenna has a good performance of low cross polarization level within large frequency bandwidth. A compact ultra-wideband diversity monopole antenna with tilted inverted tree branches is proposed in [21]. From the discussion above, the microstrip antenna can be seen as the radiation of the orthogonal magnetic current source, dual-polarized printed dipole antenna can be seen as the radiation of the orthogonal current source. According to the principle of duality, their radiation field structure in space is also dual. As space angle changes, the orthogonal polarization characteristics of the two types of dual-polarized antennas will change greatly, and the technical implementation is relatively mature.

Most dual-polarized antennas are achieved by orthogonal feeding of a single type of antenna, but the freedom of design is low and the isolation is hardly to improve. Therefore, we designed a dual-polarized antenna structure based on metal ring and rectangular patch from the engineering requirements. The antenna separately places the rectangular patch and the metal ring in the vertical space and respectively radiates or receives two orthogonally polarized electromagnetic wave components to realize a dual-polarized working mode; Due to the laminated structure, the feeding of the two polarized ports is introduced from the bottom of the antenna element without affecting each other. This structure improves the isolation of the polarization ports of the antenna and is more suitable for the installation of phased array antennas. The rectangular chip can be equivalent to the radiation of the current source, while the metal ring can be equivalent to the radiation of the magnetic source. Therefore, the radiation principle of the dual-polarized antenna proposed in this paper is based on the radiation of the orthogonal electromagnetic source, which is different from the traditional dual-polarized antenna in principle and has strong innovation.

II. ANTENNA DESIGN

According to the principle of the metal circular antenna, the metal ring can be equivalent to two half-wave dipole, while the microstrip rectangular patch antenna is equivalent to two half-wave slot antennas with equal amplitude and phase. The half-wavelength slot antenna and the half-wave dipole are complementary antennas to each other, which satisfies the duality principle. So the two complementary antennas have the same radiation pattern in the ideal case. Therefore, based on the complementary principle of the half-wave dipole and the half-wavelength slot antenna, the dual-polarzied antenna is proposed in this paper and shown in Fig. 1. The metal ring in the upper layer and the microstrip rectangular patch in the lower layer form a basic structure of antenna. The two ports of antenna are fed directly by the coaxial, so that it will facilitate the feed when the array composed. As for the antenna simulation, we use the finite difference method based on three-dimensional electromagnetic simulation software CST for rigorous numerical calculations to get the best results. The dual-polarized antenna designed is a combination of two types of antennas, so how to reduce the mutual coupling between them during the design process is a design difficulty. First, we need to determine the structure of the antenna and feeding method, then consider the influence of the size of the substrate and the dielectric constant, the size of the rectangular patch and

the radius of the metal ring, etc. finally get the dual polarized antenna.

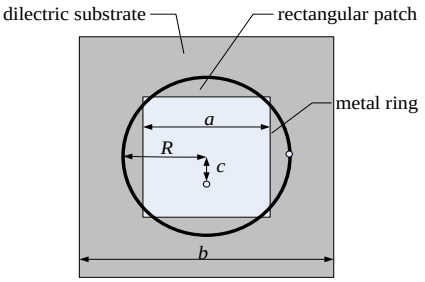

(a) Top view

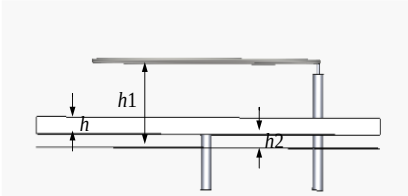

(b) Side view

Fig. 1. Schematic view of antenna.

Choosing wavelength ring to be the metal ring. At first, we use a copper wire with a diameter of 0.4mm as the material of the metal ring, and then according to the principle of the wavelength ring, the radius of the ring can be approximated by the formula $r = \lambda / 2\pi$ at the center frequency of 5GHz and finely adjusted considering the influence between the antennas.

The length of rectangular patch ($\boldsymbol{a}$) can be approximated by the formula:

$$\boldsymbol{a} = \frac{\boldsymbol{c}}{\boldsymbol{2f}}\left(\frac{\boldsymbol{\varepsilon_r+1}}{\boldsymbol{2}}\right)^{-\frac{\boldsymbol{1}}{\boldsymbol{2}}}, \tag{1}$$

$$\boldsymbol{a} = \frac{\boldsymbol{c}}{\boldsymbol{2f\sqrt{\varepsilon_e}}} - \boldsymbol{2\Delta l}, \tag{2}$$

$$\boldsymbol{\Delta l = 0.412h}\frac{\boldsymbol{(\varepsilon_e+0.3)(a/h+0.264)}}{\boldsymbol{(\varepsilon_e+0.258)(a/h+0.8)}}. \tag{3}$$

At modeling, the size of the antenna can be calculated by the formula, but the calculated sizes are theoretical value. In fact, those calculated antenna sizes need be optimized by the simulation software.

In this paper we use the commonly FR4 dielectric substrate with ε_r=4.3. In order to reduce the workload of the rectangular patch in the simulation, we set the height and width of the dielectric substrate is 35mm×35mm.

When the rectangular patch is fed by the coaxial, the antenna's input impedance consists of two parts, the impedance Z_R is caused by the main transmission mode in the antenna, and the probe impedance X_L is caused by higher order mode, so the input impedance of the antenna $Z_{in}=Z_R+jX_L$.

By adjusting the distance c from the feeding point to the center, the square patch can achieve 50Ω matching to reduce the return loss of the port. The changing curve of return loss of rectangular patch port with feed distance *c* is shown in Fig. 2. It can be clearly seen from the figure that the return loss of the rectangular patch port is the smallest when the feeding point is 3mm away from the center of the patch, and the best resonance effect is obtained. However, the matching effect of the distance too close or too far are not very good.

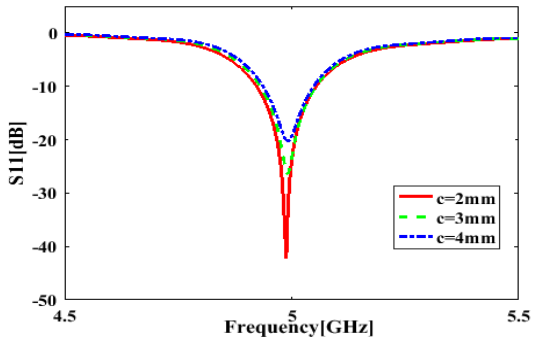

Fig. 2. The change curve of return loss of rectangular patch port with feed position.

The rectangular microstrip patch has resonant characteristics, which can be used as an antenna, but its working frequency band is only about 1%. The main methods to increase the microstrip antenna working frequency band include: (1) Increase the thickness of the dielectric substrate *h*, which is equivalent to increase the width of the radiation slot or reduce characteristic impedance of the microstrip structure, so that the input impedance of the antenna decreases with the frequency changes. But the effect of this method is limited, which is not conducive to the miniaturization of the microstrip antenna, and the requirements of increasing the thickness and decreasing the height are conflicting. This problem can be solved by using substrate with higher relative permittivity, but it will also increase the loss of the antenna. (2) By changing the form of radiation patch, for example, increasing the number of radiation patches and adopting special patches such as E-type, they can be respectively resonated at different frequencies, so that the total working frequency band can be widened.

Without changing the antenna feeding method and the overall structure, the bandwidth of the rectangular microstrip patch antenna is increased by adding slot below the dielectric substrate. The slot structure can make the antenna have close but different resonant frequencies, so the impedance bandwidth is widened. The change curve of S11 with the slot width is shown in Fig. 3.

The bandwidth of rectangular patch has increased nearly double by using slot structure, and the rectangular patch antenna can get the optimal resonance effect by adjust the slot width h2.

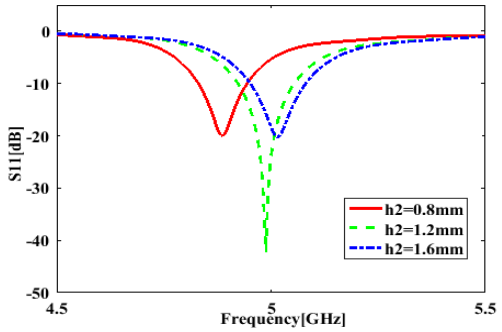

Fig. 3. The change curve of return loss of rectangular patch with the slot width.

The rectangular patch and the metal ring composed the dual-Polarized antenna. When the antenna is working, there are some coupling effect between the rectangular patch and the metal ring. Those coupling effect can cause S-parameters worsen, and radiation 3dB beam width narrowing.

III. SIMULATION AND ANALYSIS

In this paper, the full wave electromagnetic simulation software is used to optimize the performance and structure of the antenna. A set of parameters were obtained to meet the design requirements: *a*=17.8mm, *b*=35mm, *c*=3mm, *R*=11.5mm, *h*=1.5mm, *h*1=6.7mm, *h*2=1.2mm. The simulated curves of S-parameters are obtained by using CST. Figure 4 shows that port 1 is rectangular patch port and port 2 is metal ring port. When the return loss of the dual-polarized antenna is less than -10dB, the working frequency band of the metal ring port is 4.87GHz~5.11GHz and the working frequency band of the rectangular patch port is 4.94GHz~5.06GHz. The overall bandwidth of the antenna is 4.94GHz~5.06GHz. The isolation between ports is less than -22dB within the bandwid.

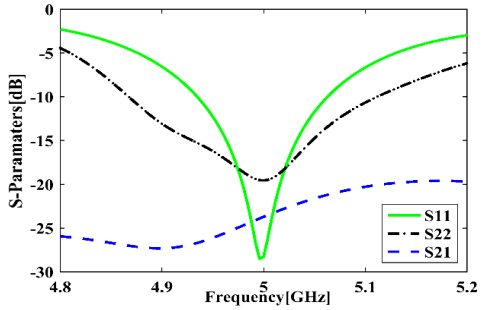

Fig. 4. S-parameter curve of dual-polarized antenna based on metal ring and rectangular patch.

Figure 5 shows the far-field radiation pattern of the two ports of the dual-polarized antenna at the center frequency of 5GHz. As can be seen from the figure, the radiation pattern of the rectangular patch is very regular, and the maximum gain of the radiation far-field is 7.17dB. The 3dB beam width of the $\varphi = 0^{\circ}$ plane is 83.7°. The 3dB beam width of the $\varphi = 90^{\circ}$ plane is 82.2°. The maximum gain of the metal ring part is 7.31 dB in the radiation far-field. The 3dB beam width of the $\varphi = 0^{\circ}$ plane is 56.5°, and the 3dB beam width of the $\varphi = 90^{\circ}$ plane is 80.2°. The gain of the two polarized antennas is relatively close, but the difference of the beam width is large. This is because there is a certain difference in the binary half-wave oscillator spacing between that equivalent by the rectangular patch and metal ring.

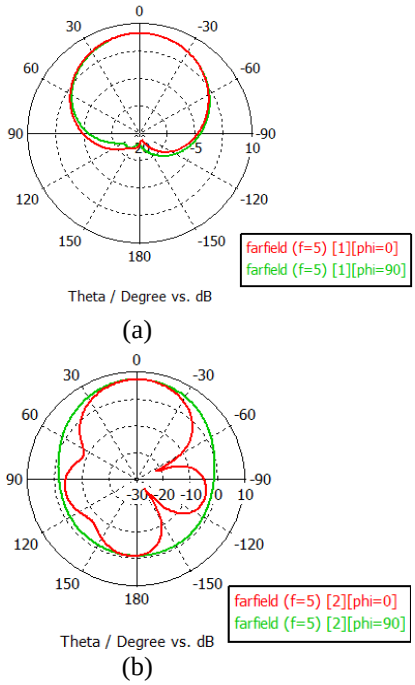

Fig. 5. Radiation pattern of dual-polarized antenna at a frequency of 5GHz: (a) rectangular microstrip patch, and (b) metal ring.

The cross polarization level of the antenna is also a very important performance parameter for dual-polarized antennas. The general communication system requires that the absolute value of the cross polarization level should be greater than 15dB. It can be seen from Fig. 6 that the cross polarization level of the two ports is less than -15dB at the main radiation direction.

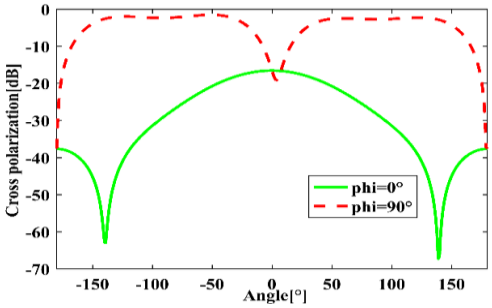

(a) The cross polarization level of metal rings

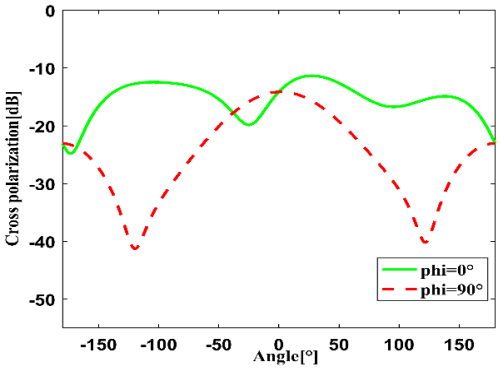

(b) The cross polarization level of rectangular patch

Fig. 6. Simulation results of cross polarization level of dual-polarized antenna.

IV. MEASUREMENT RESULTS

According to the design of the antenna structure and size, the dual-polarized antenna based on metal ring and microstrip patch is processed, assembled and tested.

Figure 7 shows the physical photos after antenna processing. We use the second substrate with little influence on antenna. Therefore, the second layer substrate has little effect on the processed antenna performance.

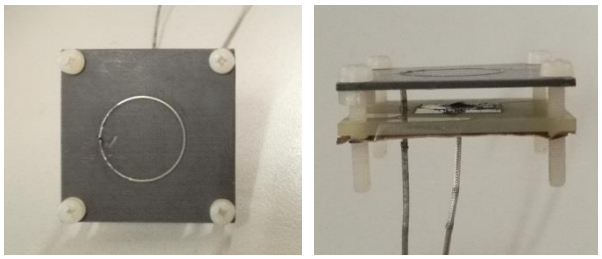

Fig. 7. Prototype of the dual-polarized antenna based on metal ring and microstrip patch.

The measured and simulated results are depicted in Fig. 8. In Fig. 8 (a), at the center frequency of 5GHz, the measured and simulated S11 are less than -15dB. Figure 8 (a) also shows that the measured resonance frequency is less than the simulated resonance frequency. In Fig. 8 (b), at the center frequency of 5GHz, the measured and simulated S22 are less than -13dB. Figure 8 (b) also shows that the measured resonance frequency is greater than the simulated resonance frequency. From the above comparison, we can see that the measured S-Parameters of the two polarized ports are slightly larger than the simulation results. In Fig. 8 (c), at the center frequency of 5GHz, the measured and simulated S21 are less than -20dB. Figure 8 (b) also shows that the measured result is less than the simulated result. According to the analysis, the difference between the measured results and the simulation results is mainly caused by the machining accuracy and assembly error.

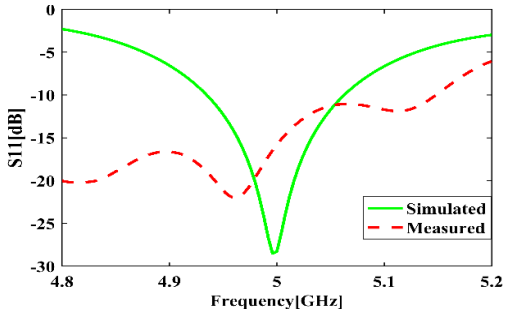

(a) The S11 of the polarization port 1

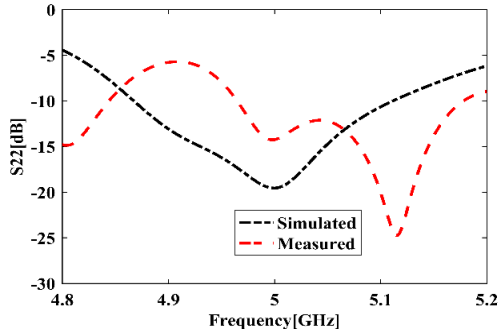

(b) The S22 of the polarization port 2

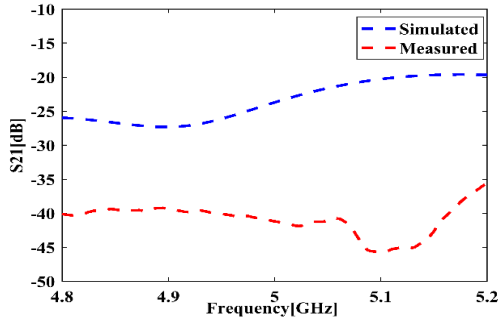

(c) The isolation between two polarization ports

Fig. 8. The circuit characteristics of the machined dual-polarized antenna.

In the microwave darkroom, the radiation pattern of the dual-polarized antenna based on metal ring and microstrip patch is measured. Figure 9 and Fig. 10 show the measured and simulated results of the polarized port

1 (rectangular patch port) and the polarized port 2 (metal ring port) at the center frequency of 5GHz respectively.

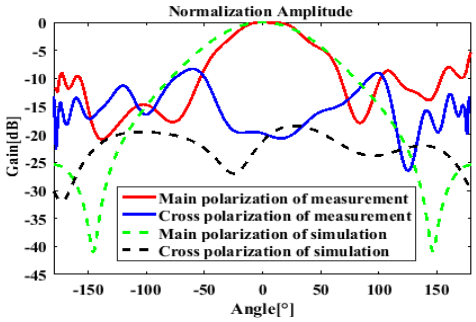

(a) The E-plane pattern of port 1

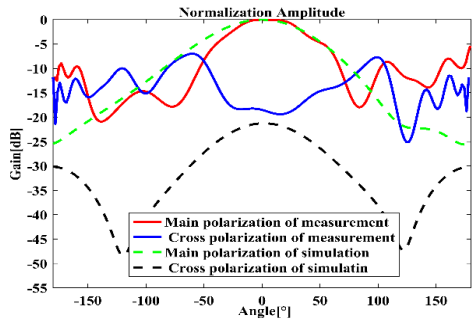

(b) The H-plane pattern of port 1

Fig. 9. The measured pattern of rectangular patch port at 5GHz.

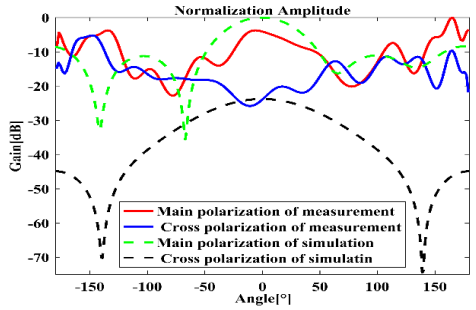

(a) The E-plane pattern of port 2

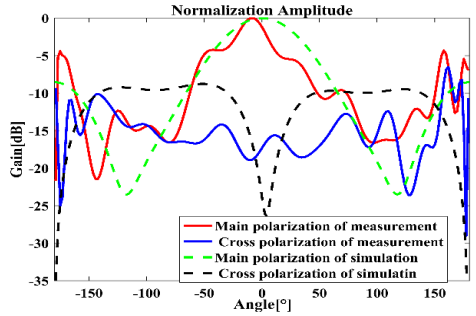

(b) The H-plane pattern of port 2

Fig. 10. The measured pattern of metal ring port at 5GHz.

It can be seen from Fig. 10 that the measured main polarization cure is similar to the simulated results, but the measured cross polarization curve and the simulated cross polarization curve are not slightly similar.

Table 1: Measured 3dB beam width and simulated 3dB beam width at co polarization

			Simulation	Measurement
Port1	E-plane	Main	83.1°	82°
		Cross	66°	44°
	H-plane	Main	82.3°	82°
		Cross	72.1°	72°
Port2	E-plane	Main	56.4°	55°
		Cross	83.9°	82°
	H-plane	Main	68.8°	68°
		Cross	132.2°	17°

Table 1 shows that the measured main polarization beam width is similar to the simulated polarization beam width.

The measured results of the antenna indicate that the two polarization ports of the dual-polarized antenna have wide beam performance and a wide polarization pattern, which is suitable for practical applications. At the same time, the design of the dual-polarized antenna based on electromagnetic radiation source is correct. The measured result is slightly different to the simulation result, which is caused by the antenna machining and testing error.

V. CONCLUSION

As an important part of dual-polarized phased array radar, the technical indicators of dual-polarized antenna element directly influences the performance of the whole system. Based on the principle of complementary antenna radiation, this paper presents a dual-polarized antenna design based on a combination of a current source and a magnetic current source, which provides a new technical approach for the design of a dual-polarized antenna. According to the equivalent principle of the electromagnetic field, the metal ring and the rectangular microstrip patch are respectively equivalent to the current radiation source and the magnetic current radiation source. Both polarized ports of the antenna are introduced from the bottom of the antenna structure, which is suitable for phased array antenna elements. The electromagnetic simulation and optimization design of the dual-polarized antenna are carried out by using the full wave electromagnetic simulation software. In the bandwidth of 4.94GHz~5.06GHz range, the technical indicators such as port isolation degree, cross polarization level and beam width of the antenna can meet the requirements of general dual-polarized antenna, especially the dual-polarized antenna which has a wide directional pattern. That is to say, the two polarization channels

have good orthogonality over a wide range of spatial angles and can be used in phased array radar and communications systems. Through the processing and testing of the designed dual-polarized antenna, the measured results verify the effectiveness of the scheme.

ACKNOWLEDGMENT

This work is sponsored by the National Natural Science Foundation of China (Grant No. 61571154), the Science Foundation of Aeronautics of China (Grant No. 20160177005).

REFERENCES

[1] M. I. Ibrahim, M. G. Ahmed, M. El-Nozahi, A. M. E. Safwat, and H. El-Hennawy, "Design and performance analysis of a miniature, dual-frequency, millimeter wave linear phased array antenna," *IEEE Transactions on Antennas and Propagation*, vol. 65, no. 12, pp. 7029-7037, Dec. 2017.

[2] H. Zhai, L. Xi, Y. Zang, and L. Li, " A low-profile dual-polarized high-isolation MIMO antenna arrays for wideband base-station applications," *IEEE Transactions on Antennas and Propagation*, vol. 66, no. 1, pp. 191-202, Jan. 2018.

[3] A. Elsherbini, J. Wu, and K. Sarabandi, "Dual polarized wideband directional coupled sectorial loop antennas for radar and mobile base-station applications," *IEEE Transactions on Antennas and Propagation*, vol. 63, no. 4, pp. 1505-1513, Apr. 2015.

[4] Y. Wang and Z. Du, "Dual-polarized slot-coupled microstrip antenna array with stable active element pattern," *IEEE Transactions on Antennas and Propagation*, 63(9): 4239-4244, 2015.

[5] K. Ding, C. Gao, Y. Wu, D. Qu, B. Zhang, and Y. Wang, "Dual-band and dual-polarized antenna with endfire radiation," *IET Microwaves, Antennas & Propagation*, vol. 11, no. 13, pp. 1823-1828, Oct. 20, 2017.

[6] W. Li, Z. Zeng, B. You, L. Ye, Y. Liu, and Q. H. Liu, "Compact dual-polarized printed slot antenna," *IEEE Antennas and Wireless Propagation Letters*, vol. 16, pp. 2816-2819, 2017.

[7] H. Lee and B. Lee, "Compact broadband dual-polarized antenna for indoor MIMO wireless communication systems, "*IEEE Transactions on Antennas and Propagation*, vol. 64, no. 2, pp. 766-770, Feb. 2016.

[8] Q. Xu, S. Liu, Y. Wang, L. Song, and H. Cao, "Dual-polarized antenna based on printed dipole and microstrip patch," *Journal of Electronics & Information Technology*, vol. 39, no. 7, pp. 1764-1768, July 2017.

[9] J. J. Liang, J. S. Hong, J. B. Zhao, and W. Wu, "Dual-band dual-polarized compact log-periodic dipole array for MIMO WLAN applications," *IEEE Antennas and Wireless Propagation Letters*, vol. 14, pp. 751-754, 2015.

[10] S. J. Li, J. Gao, X. Cao, Z. Zhang, and D. Zhang, "Broadband and high-isolation dual-polarized microstrip antenna with low radar cross section," *IEEE Antennas and Wireless Propagation Letters*, vol. 13, pp. 1413-1416, 2014.

[11] F. Lin, Y. Qi, J. Fan, and Y.-C. Jiao, "0.7-20GHz dual-polarized bilateral tapered slot antenna for EMC measurements," *IEEE Transactions on Electromagnetic Compatibility*, 56(6):1271-1275, 2014.

[12] D.-L. Wen, D.-Z. Zheng, and Q.-X. Chu, "A dual-polarized planar antenna using four folded dipoles and its array for base stations," *IEEE Transactions on Antennas and Propagation*, 64(12):5536-5542, 2016.

[13] H. Nawaz and I. Tekin, "Dual-polarized, differential fed microstrip patch antennas with very high interport isolation for full-duplex communication," *IEEE Transactions on Antennas and Propagation*, vol. 65, no. 12, pp. 7355-7360, Dec. 2017.

[14] Y. Wang and Z. Du, "Dual-polarized slot-coupled microstrip antenna array with stable active element pattern," *IEEE Transactions on Antennas and Propagation*, 63(9):4239- 4244, 2015.

[15] X. Chen, P. Y. Qin, Y. J. Guo, and G. Fu, "Low-profile and wide-beamwidth dual-polarized distributed microstrip antenna," *IEEE Access*, vol. 5, pp. 2272-2280, 2017.

[16] J. Oh and K. Sarabandi, "Low profile, miniaturized, inductively coupled capacitively loaded monopole antenna," *IEEE Transactions on Antennas and Propagation*, 60(3):1206-1213, 2012.

[17] D. Hua, S. S. Qi, W. Wu, and D. G. Fang, "CPW-fed printed antenna array with conical beam," *IEEE Transactions on Antennas and Propagation*, vol. 64, no. 3, pp. 1096-1100, Mar. 2016.

[18] A. Dastranj, "Very small planar broadband monopole antenna with hybrid trapezoidal–elliptical radiator," *IET Microwaves, Antennas & Propagation*, 11(4):542-547, 2017.

[19] S. X. Ta, H. Choo, and I. Park, "Broadband Printed-Dipole Antenna and Its Arrays for 5G Applications," *IEEE Antennas and Wireless Propagation Letters*, vol. 16, pp. 2183-2186, 2017.

[20] Y. Chong, L. Juan, W. Yang, and Y. Daixu, "Design of a Ku-band dual polarized microstrip array antenna," *Journal of Microwaves*, 2014.

[21] R. Kumar and N. Pazare, "Compact printed ultra-wideband diversity monopole antenna with slant inverted tree-shaped stub," *IET Microwaves, Antennas & Propagation*, 9(14): 1595-1604, 2015.

Lizhong Song was born in 1975. He received master degree and Ph.D. degree from Harbin Institute of Technology in 2001 and 2005, respectively. He is a Professor and Doctoral Supervisor of Harbin Institute of Technology. He focuses his academic interests on antenna design, wireless electromagnetic wave propagation, microwave technology and radar signal processing.

Sai Li received the B.E. degree in Electronic and Information Engineering from Harbin University of Science and Technology, China, in 2016. Currently, she is a master student in the School of Information and Electrical Engineering at Harbin Institute of Technology, China. Her research interests include antenna design and microwave technology.

Reconfigurable Array Designed for Directional EM Propagation using Energy Band Theory of Photonic Crystals

Yanming Zhang, Zhi Cao, Guizhen Lu, Dongdong Zeng, Mingde Li, and Ruidong Wang

Department of Information Engineering
Communication University of China, Beijing, 100024, China
zhangyanming2368@126.com, caozhi0625@aliyun.com, luguizhen1957@qq.com,
dongdong@cuc.edu.cn, 1109268713@qq.com, wangruidong3366@163.com

Abstract ─ A type of reconfigurable array consisting of metal rods was designed for directional electromagnetic (EM) wave propagation at microwave frequency. By adding or removing a part of metal rods, the designed array can be reconfigured between a hexagonal-lattice array and a rectangular-lattice array. As a result, the directional radiation pattern can be changed. In this study, the method of designing metal photonic crystals array is proposed. Dispersion curves of Energy band theory of photonic crystals were computed and integrated with the theory of finite thickness periodic arrays. Measurement results are well consistent with the simulation results, suggesting that the antenna as a radiation source located in the center of the hexagonal-lattice array could reach good directionality at the designed frequency. When the array is transformed into the rectangular-lattice array by adding or removing a part of metal rods, the directional radiation pattern can be changed ±30 degrees at the same frequency.

Index Terms ─ Antennas, directional EM propagation, metal photonic crystals, reconfigurable array.

I. INTRODUCTION

In recent years, the researches and applications of photonic crystals in the microwave domains have become increasingly extensive, e.g., electromagnetic band gap (EBG) antenna [1], photonic crystal directional coupler switch [2], EBG waveguide [3] and EBG filter [4]. With the continuous development of the communication system, the research about the directional EM wave propagation comes to have great significance and practical application value. A periodic structure composed of dielectric material rods with triangle lattices is designed to improve the directivity of emitting devices at optical frequency [5]. But the directivity only vary by rotating the entire array. At microwave frequency, many photonic crystals are made of metal materials. In accordance with the Energy band theory, the dispersion curves of metal photonic crystals also differ from those of dielectric photonic crystals at optical frequency.

In this study, the method of designing metal photonic crystals array for directional EM propagation at microwave frequency was proposed, which is different from that of dielectric photonic crystals at optical frequency. The rough operating frequency range could be determined by the constant-frequency dispersion curves of metal photonic crystals. Subsequently, the optimal operating frequency could be found in the frequency range after the array was simulated. A type of reconfigurable metal array is designed for directional EM wave propagation at microwave frequency, and the directional radiation pattern can vary by changing the structure of the array rather than rotating the entire array, it is an innovative design. By adding or removing a part of metal rods, the designed array can be reconfigured between the hexagonal-lattice array and the rectangular-lattice array, so that the directional radiation pattern can be changed. In accordance with the Bloch Theorem and Energy band theory of photonic crystals, the constant-frequency dispersion curves of photonic crystals with rectangular lattices were analyzed, and Computer Simulation Technology (CST) were employed for modeling and simulations. Based on the simulation results, actual metal arrays were constructed for measurement validation. The measurement results were compared with the simulation results, and the analysis had a high degree of anastomosis. The antenna as a radiation source located in the center of the hexagonal-lattice array could reach the good directionality at 3.1GHz. The array could be transformed into a rectangular-lattice array by adding or removing a part of metal rods, so that the directional radiation pattern could vary by ±30 degrees at the same frequency.

II. DESIGN PRINCIPLE

A rectangular coordinate system (O,X,Y,Z) is used in this paper ,the unit vectors of the axes are $\boldsymbol{e}_x$, $\boldsymbol{e}_y$, and $\boldsymbol{e}_z$. Harmonic fields are expressed using a time dependence in $\exp(-i\omega t)$, with $\omega = 2\pi c/\lambda = ck_0$, c being the speed of light in vacuum, λ the wavelength and k_0 the wavenumber in vacuum. Two-dimensional photonic

Submitted On: February 24, 2018
Accepted On: October 19, 2018

crystals are made with lossless materials (dielectric or perfectly conducting (PEC)) and invariant by translation along the z-axis.

From the Bloch theorem, in the infinite periodic structure, there are two invariant and independent translation vectors $d = d\boldsymbol{e}_x$ and $\Delta = \Delta x\boldsymbol{e}_x - \Delta y\boldsymbol{e}_y$. We denote the related components of the total field with $U(x, y)$. The Bloch theorem shows that each component $U_k(\boldsymbol{r})$ of an electromagnetic wave propagating in the crystal can be expressed as:

$$U_k(\boldsymbol{r}) = exp(i\boldsymbol{k}\cdot\boldsymbol{r})V(\boldsymbol{r}). \quad (1)$$

$\boldsymbol{k}$ is the Bloch wave vector and V(r) is a periodic function:

$$V(\boldsymbol{r}+p\boldsymbol{d}+q\Delta) = V(\boldsymbol{r}), \text{ for all integers p and q.} \quad (2)$$

For these Bloch modes, any $p\boldsymbol{d}+q\Delta$ produces only a phase shift:

$$U_k(\boldsymbol{r}+p\boldsymbol{d}+q\Delta) = exp(i\boldsymbol{k}\cdot(p\boldsymbol{d}+q\Delta))U_k(\boldsymbol{r}). \quad (3)$$

The Bloch wave vector $\boldsymbol{k}$ is real in the usual sense of the Bloch theorem, because actual bounded solutions are considered. In all this paper, we keep this usual definition.

Now we consider a finite thickness crystal with a stake of Ny grids (Ny=3), as shown in Fig. 1.

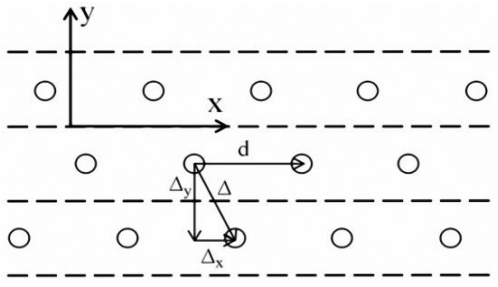

Fig. 1. Photonic crystals with finite thickness (Ny=3).

We suppose that the structure is infinite along the X direction, and it is illuminated by a plane wave:

$$U_{in}(x, y) = exp(i\alpha x - i\beta y). \quad (4)$$

The total field Uα (x, y) is a pseudo-periodic function of x with a pseudo-periodic coefficient α:

$$U_\alpha(x+d, y) = exp(i\alpha d)U_\alpha(x, y). \quad (5)$$

Then, the relationship between the Bloch wave vector propagating in the infinite photonic crystal and the pseudo-periodic coefficient α can be found. The equations (3) and (5) can match together when:

$$k_x = \alpha. \quad (6)$$

In order to consider the second translation vector Δ, we relate Δ to a translation operator T which can transform any function f as flow:

$$Tf(x, y) = f(x+\Delta_x, y-\Delta_y). \quad (7)$$

The model in Fig. 2 is a layer of the photonic crystal array. The T operator can be represented by a **T** matrix. We consider an eigenvectors of the *T*-matrix, with the eigenvalues μ:

$$\mathbf{T}U_\mu = \mu U_\mu. \quad (8)$$

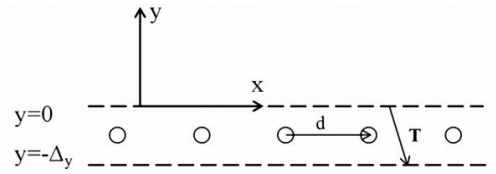

Fig. 2. A single layer extracted from the photonic crystal.

When $|\mu| = 1$, then:

$$U_\mu(x+\Delta_x, y-\Delta_y) = exp(iarg(\mu))U_\mu(x, y). \quad (9)$$

From equations (3) and (9):

$$k_y = (k_x\Delta_x - arg(\mu)) / \Delta_y. \quad (10)$$

When $|\mu| \neq 1$, the restriction to the region $(-\Delta_y \le y \le 0)$ of U_μ associated with the eigenvector cannot be a Bloch solution with real vector **k**.

Equations (6) and (10) indicate the relationship between the finite photonic crystal and the Bloch solution of the infinite structure. For a given value of α, there are two different possibilities for the spectrum of the transfer matrix T. The detailed explanation is given in the references [6].

In any case, the field in the finite structure can never be reduced to a combination of Bloch waves with real Bloch wave vector of the infinite structure. However, for predicting and understanding the complex properties of photonic crystals, the analysis of dispersion diagrams are of great value. Methods based on this assumption may give accurate results in certain cases, but their results should be carefully examined by strict methods [7], [8].

Now, we consider the finite thickness crystal. We assume that this crystal is illuminated by an arbitrary incident electromagnetic field, and the associated field components can be written as a Fourier integral:

$$U(x, y) = \int_{-\infty}^{+\infty} \hat{U}(\alpha, y)exp(i\alpha x)d\alpha. \quad (11)$$

The integration interval $[-\infty,+\infty]$ could be split into subintervals $[(n+\frac{1}{2})\frac{2\pi}{d}, (n-\frac{1}{2})\frac{2\pi}{d}]$. Then, the expression could be changed into:

$$U(x, y) = \int_{-\pi/d}^{\pi/d} U_\alpha(x, y)d\alpha. \quad (12)$$

where the integrand:

$$U_\alpha(x, y) = \sum_{m=-\infty}^{\infty} \hat{U}(\alpha + m\frac{2\pi}{d}, y)exp(i(\alpha + m\frac{2\pi}{d})x), \quad (13)$$

is a pseudo-periodic function of x with pseudo-periodicity coefficient α. Consequently, we can simplify the study of the general field u(x, y) to the study of its pseudo-periodic components $U_\alpha(x, y)$. (For all values of α in the first Brillouin zone $[-\pi/d, \pi/d]$ of the x-periodic problem)

This means that the radiation field propagating in any homogeneous medium outside the crystal can be written as the sum of the plane waves, and the plane wave with significant amplitude should correspond to the smaller value of α, $\alpha \in [-\alpha_{max}, \alpha_{max}]$. Then, according to equation (6), the allowed Bloch mode of the photonic crystal should be located in the region $k_x \in [-\alpha_{max}, \alpha_{max}]$.

If this medium is vacuum, the dispersion curve is a circle defined by $k_x^2 + k_y^2 = k_0^2$, the value of α_{max} is determined by the angle range in the Y direction. Our purpose is to design an array so that the source of radiation can radiate energy in a certain direction. According to the previous principle, we want to design a metal photonic crystal and make a curve of constant-frequency dispersion diagram of the Bloch modes is located in a small region in Fig. 3. Then, the operating frequency of this photonic crystal array could be found, it is the frequency corresponding to the constant-frequency curve.

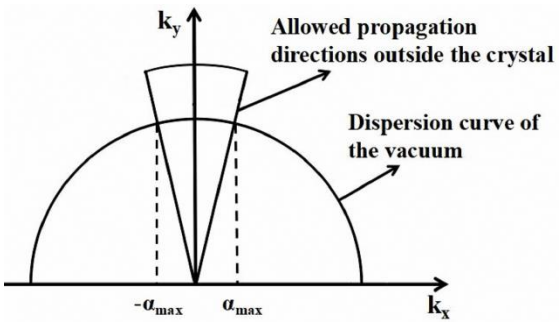

Fig. 3. The Bloch modes which can be propagated in the finite thickness photonic crystal.

III. ANALYSIS OF DISPERSION CURVES

Since experimental tests can be conveniently performed in our laboratory at 3.1GHz, we designed an appropriate structure of the array so that its working frequency is 3.1GHz. As shown in Fig. 4, it is a two-dimensional metal photonic crystal array with rectangular periodic lattices in the XOY plane. Our purpose was to embed a radiation source inside the array and to enforce the radiated field inside a small angular range centered around the normal, and the red point in the center of the array is the radiation source. The length of metal rods along the z-axis direction is infinite. The lattice constants were $d_x = 20\sqrt{3}$ mm, $d_y = 20$ mm, $r = 0.75$ mm. The model was built in the electromagnetic field simulation software CST. In the modeling process, the materials of all metal rods were PEC. The Eigenmode Solver was applied for the unit lattice simulation, and Frequency Domain Solver was employed for the entire array simulation.

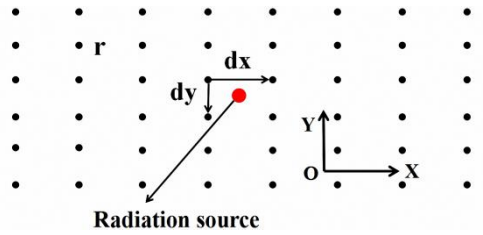

Fig. 4. Two-dimensional metal photonic crystal array with infinite periodic rectangular lattices

As shown in Fig. 5, the model in the left picture represents the rectangular lattice unit and Boundary condition setting in CST. The black area in the right picture ($k_x \in [0, \pi/d_x]$, $k_y \in [0, \pi/d_y]$) is a quarter of the First Brillouin Zone of the metal photonic crystal. Using the Eigenmode Solver of CST, the rectangular lattice unit could be simulated, and the Bloch mode corresponding to each point in the region could be calculated (100 points were calculated here). After the data was imported into MATLAB, the three-dimensional dispersion diagram of the array could be generated. Figure 6 gives the 3D dispersion diagram of a Bloch mode of the metal photonic crystal, the horizontal plane gives the Bloch wave vector *k*, and the vertical axis gives the frequency *f*.

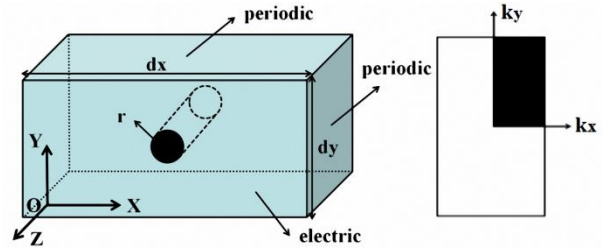

Fig. 5. The rectangular lattice unit and the First Brillouin Zone of the infinite metal photonic crystal.

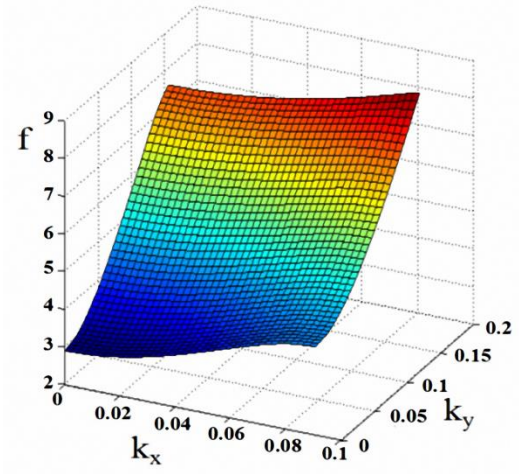

Fig. 6. 3D dispersion diagram of metal photonic crystal.

As shown in Fig. 7, the constant-frequency dispersion curves of the metal photonic crystal with rectangular lattices could help to determine the frequency of directional EM wave propagation. Three constant-frequency dispersion curves are presented in Fig. 7, which are all contour lines of the 3D dispersion diagram in Fig. 6. Only three representative curves were listed. The high frequency constant-frequency curves were not given in Fig. 7, because kx of them were not in a small region.

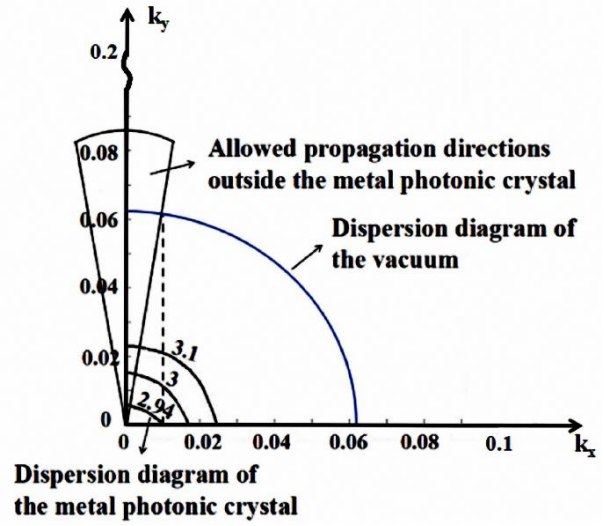

Fig. 7. The constant-frequency dispersion curves.

When the frequency was closer to the cut-off frequency f_0 of this Bloch mode, the constant-frequency dispersion curves would become smaller, and they would be located in a small region of $k_x \in [-\alpha_{max}, \alpha_{max}]$. This suggests that a finite thickness photonic crystal array with such lattice constants could propagate waves directionally in a small frequency band with f_0 as the center frequency. A detailed explanation was given in the reference [5]. We only simply identified an approximate frequency range capable of making the source radiate energy in a certain direction since the field in the finite structure could never be reduced to a combination of Bloch waves with real Bloch wave vector of the infinite structure. To determine the optimal operating frequency, the entire array must be simulated by CST.

IV. SIMULATION MODELS AND RESULTS

In accordance with the previous analysis, the metal photonic crystal array with such lattice constants could make waves propagate directionally in the direction along the short side of the array, and the optimal operating frequency was in the approximate frequency range identified from the constant-frequency dispersion curves. In our previous studies, we explored the impacts of the change of the number of metal rods and frequency on directionality [9]. Based on the previous work, in this study, we directly selected an appropriate number of metal rods and designed a lattice reconfigurable array, which could not only make the source radiate energy in a certain direction but also change the direction of the beam by changing the structure of the array.

As shown in Fig. 8, two same metal finite thickness rectangular-lattice arrays in the XOY plane are composed of 8×6 metal rods, with their horizontal axes intersecting at 60 degrees. The lattice constants were the same as those of the metal photonic crystals in Fig. 1. The length of metal rods in the Z direction was much larger than the radius, which could be approximated as infinite long metal rods. In accordance with the previous analysis, both of the two arrays could make waves propagate directionally in the direction along the short side of each array at a certain frequency as shown in Fig. 9, and the directional patterns of the top array and bottom array were symmetrical about the Y direction. Figure 12 gives the directional patterns of the top array in Fig. 8, at the frequencies of 2.9GHz, 3.1GHz and 3.2GHz, respectively. Here we gave the small frequency range (2.9-3.2GHz) based on the previous analysis of the constant-frequency curves, and in this frequency range we could find a frequency point allowing the new array with lattice reconstruction could make EM waves propagate directionally in the Y direction. Subsequently, the frequency was found as 3.1GHz.

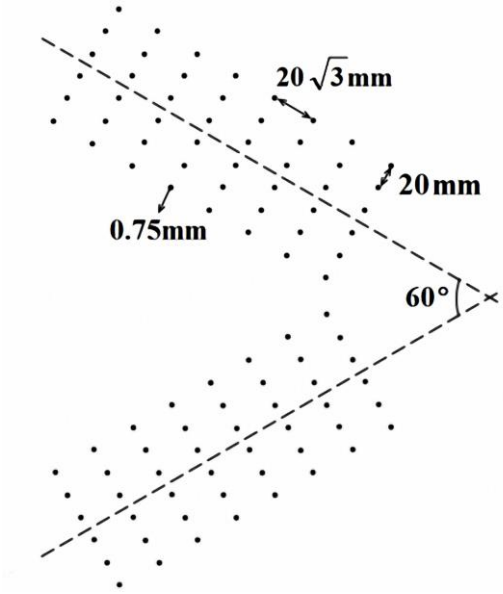

Fig. 8. Two finite thickness rectangular-lattice arrays crossed together at 60 degrees.

As shown in Fig. 10, the array in the red border consists of those two arrays in Fig. 8 crossed together with the angle of 60 degrees, and the crossed part forms a structure with hexagonal lattices. The cross array enabled EM waves from the radiation source to be propagated directionally in the Y direction. We only selected the array in the red box since the metal rods outside the red border would radiate energy in other directions and cause the appearance of excess sidelobes and affect the directionality.

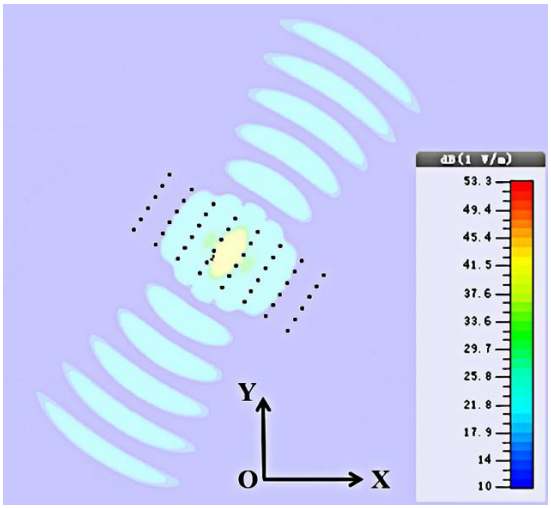

Fig. 9. The electric field distribution of the rectangular-lattice array at 3.1GHz.

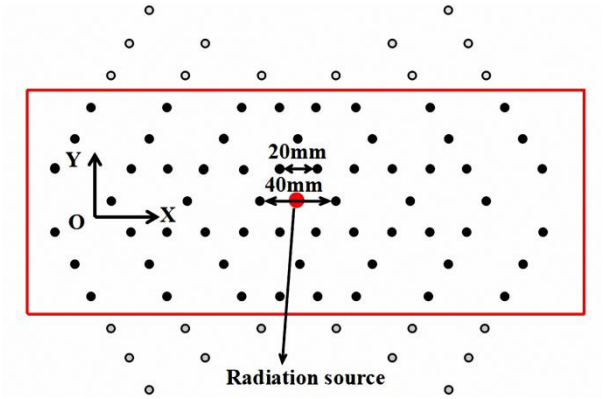

Fig. 10. The crossed part forms a finite thickness array with hexagonal lattices.

The models were simulated with the electromagnetic field simulation software CST. As shown in Fig. 11, the crossed array with hexagonal lattices can make the waves propagate directionally in the Y direction at 3.1GHz. The new crossed array with hexagonal lattices could propagate EM waves directionally in the Y direction since the two rectangular-lattice arrays were superimposed to form the new array with hexagonal lattices, their Bloch wave vectors are also superimposed on each other, and the X-direction components cancel each other.

It is noteworthy that the crossed array was not only composed of hexagonal lattices but of some defective ones. Yet by analyzing constant-frequency dispersion curves, it could be determined that a finite thickness metal array consisting of hexagonal lattices entirely could be designed for directional EM wave propagation at a different frequency by analyzing its constant-frequency dispersion curves. The hexagonal-lattice array could be transformed into either of the two rectangular-lattice arrays in Fig. 8 by adding or removing a part of metal rods, and Fig. 12 presents the directional patterns of the top array with rectangular lattices in Fig. 8, the direction of its main lobe was 30 degrees off the Y direction. Directional patterns of the top array and bottom array were symmetrical about the Y direction. Now we could determine that both the rectangular-lattice array and the hexagonal-lattice array could make EM waves propagate directionally at 3.1GHz, the directional radiation pattern could vary by ±30 degrees through the mutual transformation between the two kinds of array. Arrays of lattice structures which could be transformed were called reconfigurable array.

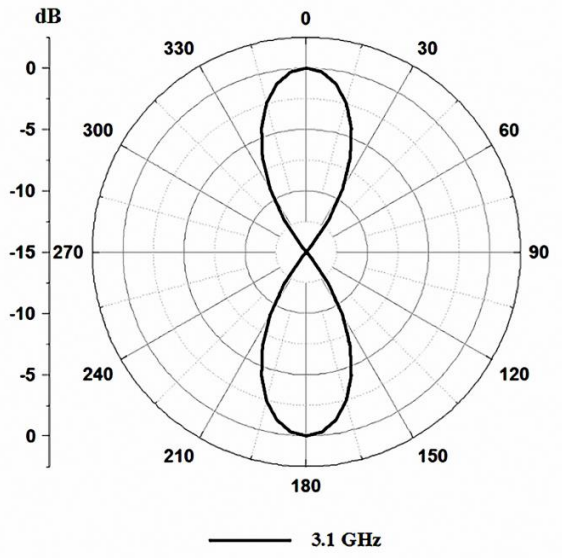

Fig. 11. Directional pattern of the hexagonal-lattice array.

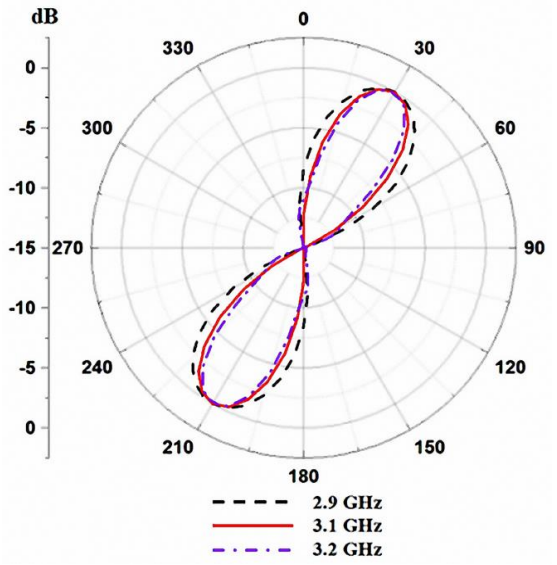

Fig. 12. Directional patterns of the top array in Fig. 8.

V. MEASUREMENT RESULTS

Based on the previous simulation models, actual arrays composed of copper rods were constructed for measurement validation at 3.1GHz. Different structures can also be designed to make it operate at the required frequency by the method in this paper. Considering the conditions of our laboratory, this frequency band is selected for experimental testing. Figure 13 shows the photographs of the hexagonal-lattice array and the rectangular-lattice array. Foam plates with a dielectric constant close to the air dielectric constant were used to fix copper rods. Copper foils were affixed on the upper surface of the top foam board and the lower surface of the bottom foam board to form the perfect electric conductor (PEC) surface. In accordance with the principle of Mirror Image, the length of copper rods in the Z direction could be approximately equal to infinite length.

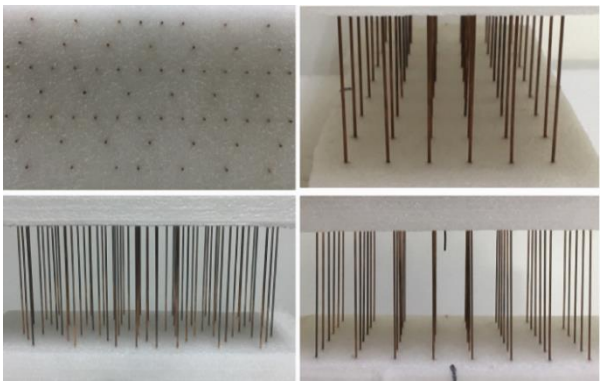

Fig. 13. Actual reconfigurable hexagonal-lattice array and rectangular-lattice array.

As shown in Fig. 14, a rectangular waveguide antenna (WR-284, 2.60-3.95GHz) is employed to receive the radiation power of the monopole antenna in the center of the array. The rectangular waveguide antenna is placed in the far-field area, and the distance between the rectangular waveguide antenna and the array is nearly 2m. Figure 15 shows the picture of the experimental measurement environment. A monopole antenna served as radiation source, inserted from the top of the array into the center of the array and fixed. When measuring, the rectangular waveguide antenna was fixed, and the center point of the array was fixed as the center of a circle. The measured array was rotated 10 degrees each time, and a total of 36 experimental data would be recorded after a lap. The measurement results were compared with the simulation results after normalization at 3.1GHz.

As shown in Fig. 16 and Fig. 17, the black dots were experimental data. The red curves were fitting curves of experimental data generated by the software ORIGIN. The blue dotted lines were simulation results. It could be seen that both of the two arrays could give the monopole antenna good directionality, and the differences between the gains in the two vertical directions of each array could reach more than 10 dB. The fitting curves are well consistent with the simulation curves, except that there were small sidelobes in the direction perpendicular to the main radiation direction of each array.

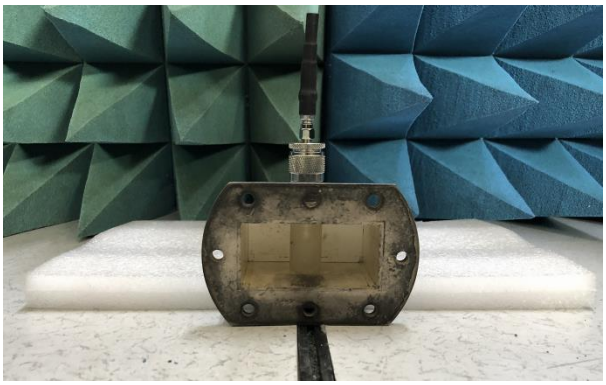

Fig. 14. The rectangular waveguide antenna.

Fig. 15. Experimental measurement environment.

The experimental results suggest that the sidelobes of the rectangular-lattice array was smaller than those of the hexagonal-lattice array. This was because they have different lattice structures. Moreover, there were some defect lattices of hexagonal-lattice array, while the rectangular-lattice array completely consisted of rectangular lattices. Accordingly, the inhibitory effect of the former on sidelobes was weaker than that of the latter. Small variations of the sidelobes were allowed to achieve the reconfigurable properties of the array. Sidelobes could be reduced by increasing the number of metal rods of the arrays, specific methods were described in our previous paper [9]. In general, not only the two types of arrays could be employed for directional EM wave propagation at 3.1GHz, but also the directional radiation pattern could be changed through the mutual transformation between the two structures.

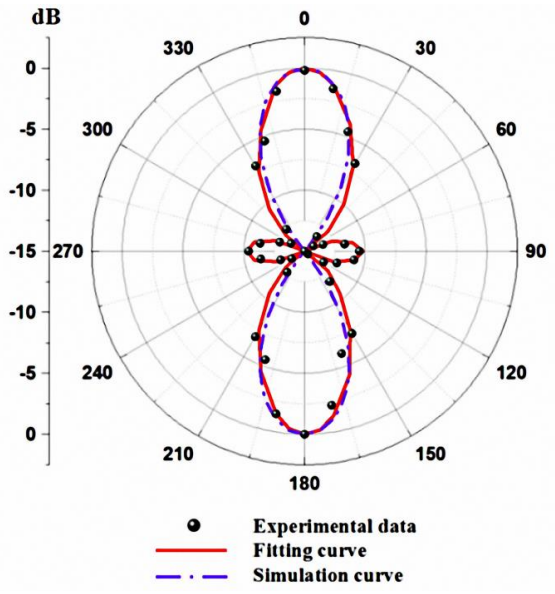

Fig. 16. The comparison of measurement results and simulation results of hexagonal-lattice array at 3.1GHz.

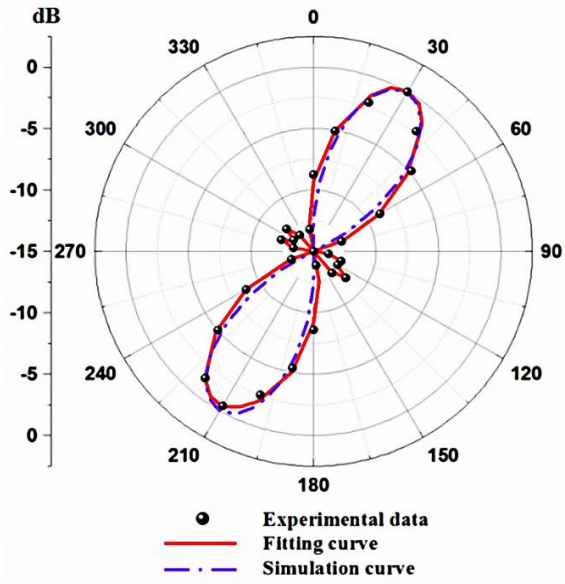

Fig. 17. The comparison of measurement results and simulation results of rectangular-lattice array at 3.1GHz.

VI. CONCLUSION

In this study, a type of reconfigurable array consisting of metal rods was designed for directional EM propagation at microwave frequency. The method of designing the metal array was proposed. Measurement results are well consistent with the simulation results, which shows that the antenna as a radiation source located in the center of the hexagonal-lattice array can get good directionality at the designed frequency. Meanwhile, the array can be reconfigured into a rectangular-lattice array by adding or removing a part of metal rods. And the directional radiation direction can vary by ±30 degrees at the same frequency. Different structures could also be designed to make it operate at required frequencies by the method in this paper.

REFERENCES

[1] S. Ceccuzzi, L. Pajewski, C. Ponti, and G. Schettini, "Directive EBG antennas: a comparison between two different radiating mechanisms," *IEEE Trans. Antennas Propag*., vol. 62, no. 10, pp. 5420-5424, 2014.

[2] S. Maktoobi and S. Bahadori-Haghighi, "Investigation and simulation of photonic crystal directional coupler switch," *Electron. Lett*., vol. 51, no. 13, pp. 1016-1018, 2015.

[3] H. Ouassal, J. Shaker, L. Roy, M. R. Chaharmir, and K. Hettak, "Multi-layer EBG slab waveguide based on open square rings," *IET Microw. Antennas Propag*., vol. 11, no. 9, pp. 1241-1247, 2017.

[4] Y. Guo, S. Kim, X. Liu, H. Gao, and G. P. Li, "A compact configurable EBG filter on PCB," *IEEE Trans. Compon. Packag. Technol*., vol. 5, no. 5, pp. 668-674, 2015.

[5] S. Enoch, G. Tayeb, and D. Maystre, "Dispersion diagrams of Bloch modes applied to the design of directive sources," *PIER*, vol. 41, no. 1, pp. 61-81, 2003.

[6] B. Gralak, S. Enoch, and G. Tayeb, "Anomalous refractive properties of photonic crystals," *J. Opt. Soc. AM. A*., vol. 17, no. 6, pp. 1012-1020, 2000.

[7] P. R. Villeneuve, S. Fan, and J. D. Joannopoulos, "Microcavities in photonic crystals: Mode symmetry, tunability, and coupling efficiency," *Phys. Rev. B Condens. Matter*, vol. 54, no. 11, pp. 7837-7842, 1996.

[8] Z. Yuan, J. Haus, and K. Sakoda, "Eigenmode symmetry for simple cubic lattices and the transmission spectra," *Optics Express*, vol. 3, no. 1, pp. 19-27, 1998.

[9] Y. Zhang, G. Lu, and D. Zeng, "Design of directionality of the antenna using two-dimensional metal photonic crystal," *International Symposium on Electromagnetic Compatibility IEEE*, 2017.

Yanming Zhang received the B.S. degree in Communication Engineering from Communication University of China, Beijing, China, in 2016. He is currently studying for the M.S. degree of Electromagnetic Field and Microwave Technology, at Communication University of China. His current research interests include antennas, electromagnetic wave propagation and photonic crystals.

Zhi Cao received the M.S. degree in Communication Engineering from Communication University of China, Beijing, China. He is currently pursuing the Ph.D. degree of Electromagnetic Field and Microwave Technology, at Communication University of China. His current research interests include electromagnetic wave propagation, antennas pattern synthesis and high dimensional optimization.

Guizhen Lu graduated from University of Science and Technology Beijing in 1982 with a B.S. degree in Physics. He graduated from Peking University in 1984 with a M.S. degree in Solid State Physics. He received his Ph.D. degree at Beihang University in 2001. He was assigned to Communication University of China in 1984, engaged in teaching and research work. The main courses include: Functional Analysis, Mobile Communications, Electromagnetic Theory, Microwave Technology, Wave propagation.

He is a Professor at China Communication University, a Doctoral Supervisor, and a Director of the Department of Communication Engineering. He is a committee member of the Committee for Radio Wave of Chinese Institute of Electronics Propagation, the Electromagnetic Compatibility Committee of the Microwave Society of Chinese Institute of Electronics.

Dongdong Zeng received the Ph.D. degree in Electromagnetic Field and Microwave Technology from Communication University of China, Beijing, China. Now she works as a Professor at Communication University of China. Her main lectures include analog circuits and electromagnetic fields. Her research interests include antennas, electromagnetic wave propagation and computational electromagnetic.

Mingde Li received the B.S. degree in Communication Engineering from Communication University of China, Beijing, China, in 2016. He is currently studying for the M.S. degree of Electromagnetic Field and Microwave Technology, at Communication University of China. His current research interests include antennas, electromagnetic wave propagation and terahertz.

Ruidong Wang received the M.S. degree in Electromagnetic Field and Microwave Technology from Communication University of China, Beijing, China, in 2014. He is currently pursuing the Ph.D. degree of Electromagnetic Field and Microwave Technology, at Communication University of China. His current research interests include electromagnetic wave propagation, antennas, microwave technologies, computational electromagnetics, electromagnetic compatibility, scattering.

Coverage Prediction for Triple Diffraction Scenarios

Mehmet B. Tabakcioglu

Electrical and Electronics Engineering Department
Bursa Technical University, Bursa, 16330, Turkey
mehmet.tabakcioglu@btu.edu.tr

Abstract — Electromagnetic waves emanating from the transmitter can reach to the receiver by reflection, direct or diffraction mechanism. In urban areas, dominant mechanism is diffraction. Thanks to using of high frequency, the obstructions can be modeled as a knife-edge. Coverage prediction is vital to install reliable and high-quality communication systems. In this study, a triple diffraction coefficient is derived for Uniform Theory of Diffraction (UTD) model and used for coverage problem. Coverage problems could be solved by the developed program in MATLAB computationally. Simulation results obtained in developed program are compared with FEKO electromagnetic wave propagation simulation software.

Index Terms — Coverage mapping, diffraction coefficient, FEKO, radio wave propagation, ray-tracing.

I. INTRODUCTION

Predicting the electric field strength and extracting the coverage maps are very important in order to install more efficient and reliable digital communication system in urban or rural areas including multiple obstructions. Ray-tracing based electromagnetic wave propagation models are introduced to predict the field strength accurately at the receiving point [1-9] and to extract the coverage map [10].

Geometrical optic (GO) model had used for some physical events like reflection and refraction before Geometrical theory of diffraction was introduced [11]. Geometrical optic model fails to calculate the electric field behind an obstruction. Keller introduced Geometrical theory of diffraction (GTD) model in 1962 [12]. The GTD model is an extension to the GO model with including diffracted wave terms [13]. If a source, diffraction and observation points are close to the same line, the GTD model is not succeeded in calculating the field strength accurately [14,15]. In order to remove the discontinuity problem of GTD model in the vicinity of the shadow, another high frequency asymptotic technique, called Uniform theory of diffraction (UTD) model, introduced [1].

In the rest of paper, firstly UTD model is explained briefly for single, double and triple diffraction, respectively. Then simulation results for the scenario including single, double and triple obstructions are given and compared with FEKO. FEKO, developed by Altair, is a comprehensive computational electromagnetics code used widely in the telecommunications, space and defense industries [16].

II. UTD MODEL

Buildings, hills, trees and cars etc. are obstructions and can cause reflection, refraction and/or diffraction. Due to ultra-high frequency (UHF), these obstructions are modeled as a knife edge or wedge. Electric field can be calculated behind an obstruction [14] by:

$$E = [E_i D]A(s)e^{-jks}, \tag{1}$$

where E_i is incident electric field, *A(s)* represents spreading factor, D stands for amplitude diffraction coefficient, k and s refers to wave number and travelling distance, respectively. The simplest case in outdoor or indoor propagation in the real environment is single diffraction case. The diffraction coefficient for single obstruction case is given by:

$$D = \frac{e^{-j\frac{\pi}{4}}F(L_{123})}{2\sqrt{2\pi k}\sqrt{\cos(\alpha_{123})/2}}, \tag{2}$$

where, F is transition function given in [17], k is the wave number, L is distance parameter and α is diffraction angle as shown in Fig. 1. The spreading factor for a single diffraction case is given by:

$$A(s) = \sqrt{\frac{s_1}{s_2(s_1+s_2)}}, \tag{3}$$

where, s_1 and s_2 are distance before and after diffraction point as illustrated in Fig. 1.

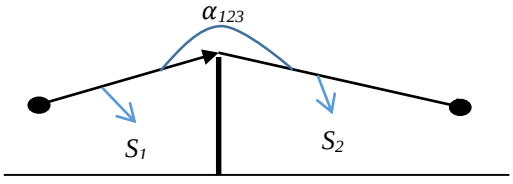

Fig. 1. Single diffraction case.

Submitted On: March 17, 2018
Accepted On: September 24, 2018

The diffraction coefficient for double obstruction case is given by:

$$DD = \frac{e^{-j\frac{\pi}{2}} F(L_{123}) F(L_{1234})}{8\pi k \sqrt{\cos(\alpha_{123})/2} \sqrt{\cos(\alpha_{1234})/2}}, \quad (4)$$

where, F is the transition function, k is the wave number, L_{123} and L_{1234} are the distance parameters and α_{123} and α_{1234} are the diffraction angles as shown in Fig. 2. The spreading factor for double diffraction case is given by:

$$AA(s) = \sqrt{\frac{s_1}{s_2 s_3 (s_1 + s_2 + s_3)}}, \quad (5)$$

where, s_1 is the distance between the transmitter and first obstruction, s_2 is the distance between obstructions, and s_3 is the distance between second obstruction and the receiver as depicted in Fig. 2.

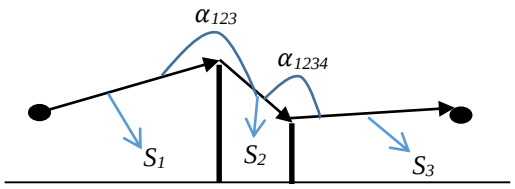

Fig. 2. Double diffraction case.

The diffraction coefficient for triple obstruction case is given by:

$$DDD = \frac{e^{-j\frac{3\pi}{4}} F(L_{123}) F(L_{1234}) F(L_{12345})}{2^3 (\sqrt{2\pi k})^3 \sqrt{\cos(\alpha_{123})/2} \sqrt{\cos(\alpha_{1234})/2} \sqrt{\cos(\alpha_{12345})/2}}, \quad (6)$$

where, F is the transition function, k is the wave number, L_{123}, L_{1234} and L_{12345} are the distance parameters and α_{123}, α_{1234}, α_{12345} are the diffraction angles as shown in Fig. 3. The spreading factor for triple diffraction case is given by:

$$AAA(s) = \sqrt{\frac{s_1}{s_2 s_3 s_4 (s_1 + s_2 + s_3 + s_4)}}, \quad (7)$$

where, s_1 is the distance between the transmitter and the first obstruction, s_2 is the distance between first and second obstructions, s_3 is the distance between the second and third obstructions, and s_4 is the distance between the third obstruction and the receiver as demonstrated in Fig. 3.

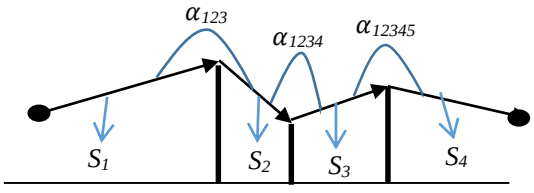

Fig. 3. Triple diffraction case.

III. SIMULATION RESULTS

UTD model can be used in coverage prediction before base station installation. Optimization of base station location is so important to increase the QoS. For a test case following scenario is considered. Operation frequency is 900 MHz. The distance between the antennas is 35 m. At 10, 20 and 30 m from the origin there are 3 knife-edge type obstructions. The transmitter is 5 m away from the origin and has an altitude of 6 m. The receiver height changes between 0 and 30 m. In the developed program, firstly all the data is entered and then ray paths are determined as follow.

- 1-4-5: In that case there is only single diffraction (the ray emanates from the transmitter, diffracts from the third obstruction and reaches to receiver).
- 1-2-4-5: In that case there is double diffraction (the ray emanates from the transmitter, diffracts from the first and then the third obstruction and reaches to receiver).
- 1-2-3-4-5: In that case there is triple diffraction (the ray emanates from the transmitter, diffracts from the first, then the second and then the third obstruction and reaches to receiver).

There will be 4 different cases for simulations. In the first case there is only single knife edge, whose height is 10 m, and 15 m away from the receiver in the scenario as mentioned previously. As both direct and reflected waves are considered, coverage map of single diffraction is depicted in Fig. 4.

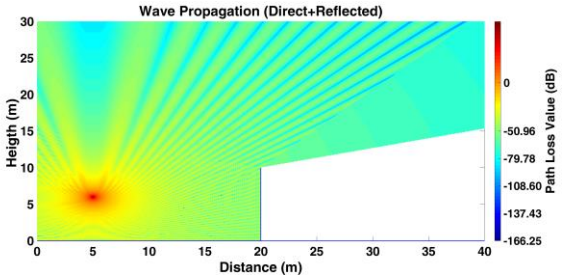

Fig. 4. Single diffraction (direct and reflected waves).

As can be seen in Fig. 4, there are two regions, which are lit and dark regions, separated with shadow boundary line in the coverage map of the single diffraction case. Due to not considering diffraction, there is no twilight region. Path loss decreases to -166.25 dB on the receiver side. If only diffraction phenomena is considered coverage map is demonstrated in Fig. 5.

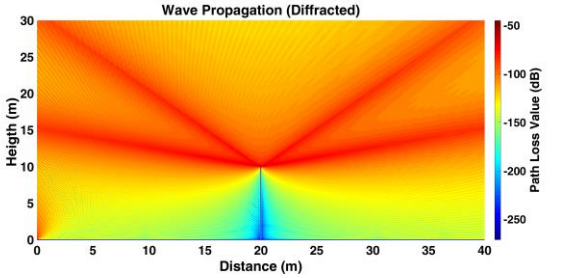

Fig. 5. Single diffraction (diffracted waves).

As can be seen in Fig. 5, there is diffracted wave behind the obstruction. The diffracted field effect is at the utmost along the shadow boundary line. Diffracted field contribution is at most -50 dB and decreases to -250 dB as far away from the shadow boundary line. In order to approve the results, the same scenario is run with FEKO software and obtained results are given in Fig. 6.

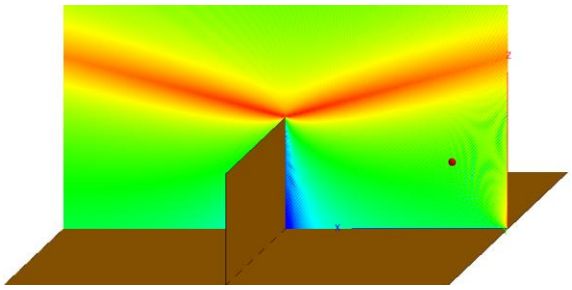

Fig. 6. Single diffraction (diffracted waves, FEKO).

As can be seen in Fig. 6, FEKO software gives almost the same diffraction pattern with developed program. Full coverage map for single obstruction case is obtained by using direct, reflected and diffracted waves as it is shown in Fig. 7.

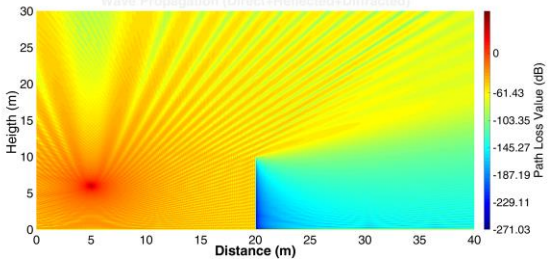

Fig. 7. Single diffraction (full coverage).

As it is shown in Fig. 7, there is a shadow line and diffracted field below and above this line. Also it is seen, there is a deep shadow region just behind the obstruction and diffracted field reduces to -271.03 dB in this region. Moreover, there is an interference pattern due to phase difference of direct, reflected and diffracted fields. Comparison results with FEKO software are demonstrated in in Fig. 8.

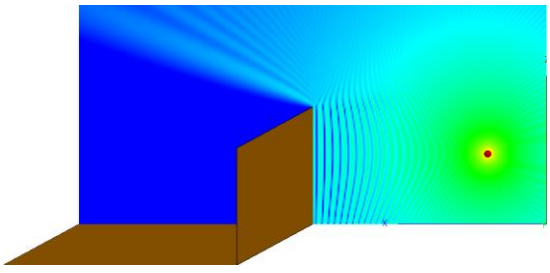

Fig. 8. Single diffraction (full coverage, FEKO).

As can be seen in Fig.8, FEKO software gives approximately the same diffraction and reflection pattern with developed program.

In the second case, an extra knife-edge, whose height is 6 m, is appeared at a distance of 25 m from the transmitter in the scenario. Both direct and reflected waves are considered, and coverage map is depicted in Fig. 9.

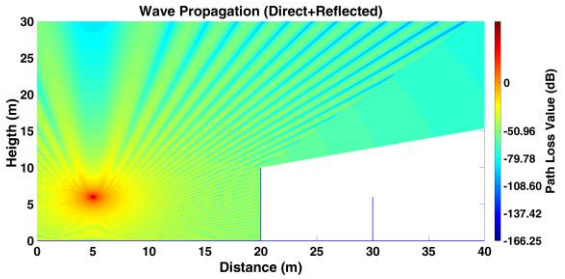

Fig. 9. Double diffraction (direct and reflected waves).

As can be seen in Fig. 9, there is a shadow region below the shadow boundary line of the first obstruction. There is no electromagnetic wave behind the first obstruction thanks to that geometrical optic model cannot explain the diffraction phenomena. Due to that there is no contribution of diffracted field from the first and second obstruction; coverage prediction is the same with first case as it is shown in Fig. 4. As only diffracted waves are considered, the coverage map is plotted in Fig. 10.

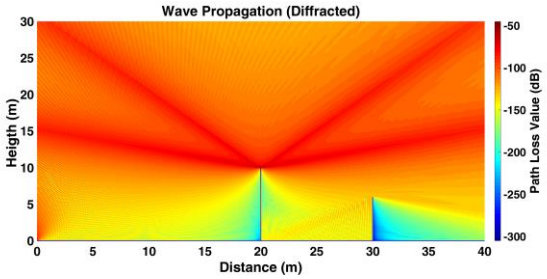

Fig. 10. Double diffraction (diffracted waves).

As can be seen in Fig. 10, unlike to geometrical optic model there is diffracted wave behind the obstructions. Also, the diffracted field effect is maxima (-50 dB) in vicinity of the shadow boundary lines of obstruction. Owing to double diffraction, electric field strength reduced -300 dB in deep shadow region behind the second obstruction. In order to validate the results of UTD model, the same scenario has been run with FEKO software and images of result is given in Fig. 11.

As can be seen in Fig. 11, FEKO software gives approximately the same electromagnetic field pattern and shadow boundary lines with developed program. Besides, electric field strength is reduced with far away

from the transmitting antenna. Moreover, after two diffraction electric field strength decrease radically. Full coverage map for double obstruction case is got by using direct, reflected and diffracted waves as it is indicated in Fig. 12.

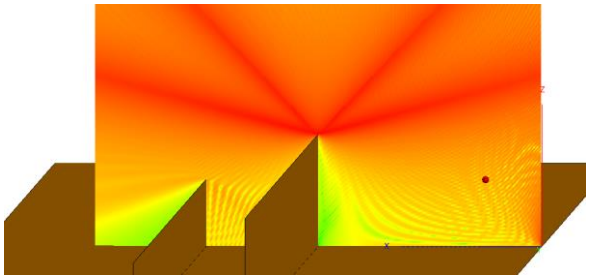

Fig. 11. Double diffraction (diffracted waves, FEKO).

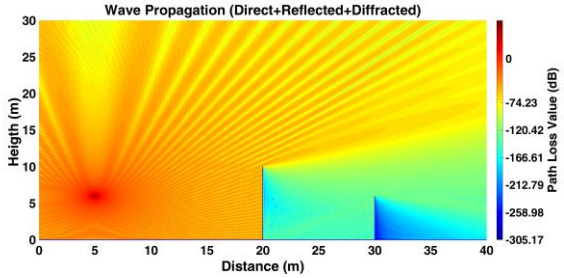

Fig. 12. Double diffraction (full coverage).

As it is indicated in Fig. 12, there are diffracted waves below and above the shadow boundary lines of first and second obstruction. Also it is seen, there is a shadow (-166 dB) and deep shadow (-305 dB) region just behind the first and second obstruction, respectively. Moreover, a diffraction and interference pattern has been composed by diffracted, reflected and direct fields due to phase difference of fields. In order to confirm the results of UTD model for double diffraction case, FEKO software has been run for the same scenario and images of the results are given in Fig. 13.

As can be seen in Fig. 13, FEKO software gives almost the same interference pattern with developed program.

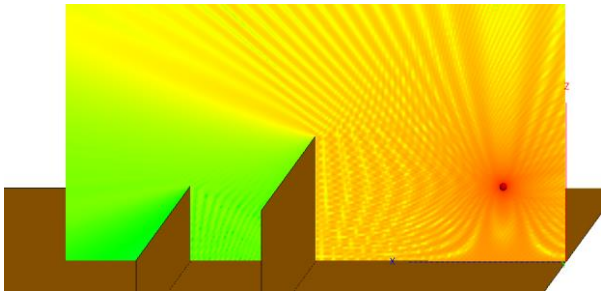

Fig. 13. Double diffraction (full coverage, FEKO).

In the third case, an extra knife-edge, whose height is 10 m, is appeared at a distance of 5 m from the transmitter in the second scenario. Both direct and reflected waves are considered, and coverage map is demonstrated in Fig. 14.

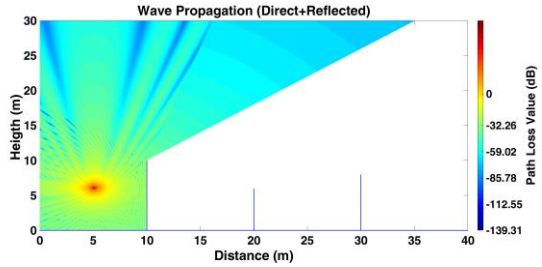

Fig. 14. Triple diffraction (direct and reflected waves).

As it is demonstrated in Fig. 14, there is a shadow region below the shadow boundary line of the first obstruction. There is no electromagnetic field behind the first obstruction owing to that there is no diffracted field in geometrical optic model.

As only diffracted waves are considered, the coverage map is plotted in Fig. 15.

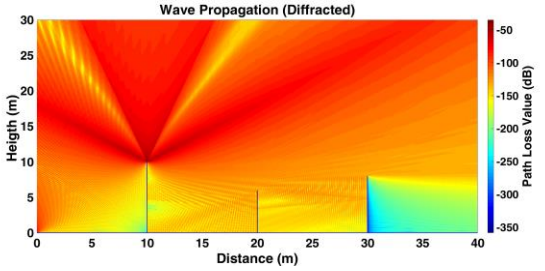

Fig. 15. Triple diffraction (diffracted waves).

As can be seen in Fig. 15, in contrast to geometrical optic model there is diffracted wave behind the obstructions. Also, the diffracted field effect is maxima (-50 dB) in the case of plane angle diffraction. Owing to triple diffraction, electric field strength reduced -350 dB in deep shadow region behind the third obstruction. In order to attest the results of UTD model, the same scenario has been run with FEKO software and plot of result is given in Fig. 16.

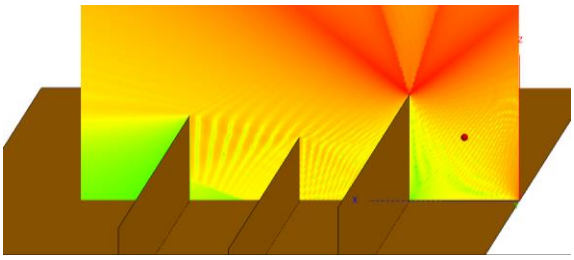

Fig. 16. Triple diffraction (diffracted waves, FEKO).

As can be seen in Fig. 16, FEKO software gives well-nigh the same diffraction pattern with developed program. Full coverage map is obtained by using direct, reflected and diffracted waves as it is indicated in Fig. 17.

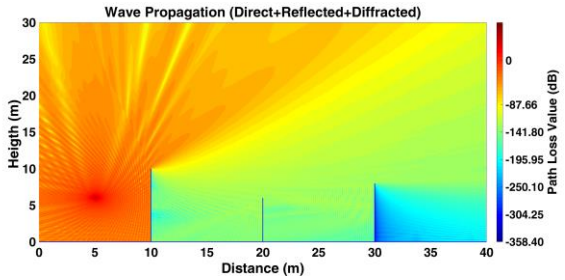

Fig. 17. Triple diffraction (full coverage).

As it is indicated in Fig. 17, there are diffracted waves below and above the shadow boundary lines of first, second and third obstruction. Also it is seen, there is a shadow (-87 dB), deep shadow (-195 dB) and the deepest shadow (-358 dB) region just behind the first, second and third obstruction, respectively. Moreover, an interference pattern has been generated by phase difference of diffracted, reflected and direct fields. In order to validate the results of UTD model for triple diffraction case, FEKO software has been run for the same scenario and images of the results are given in Fig. 18.

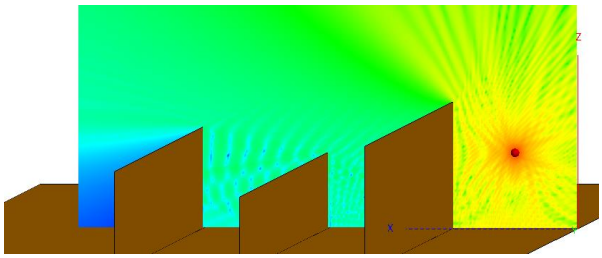

Fig. 18. Triple diffraction (full coverage, FEKO).

As can be seen in Fig. 18, FEKO software gives approximately the same diffraction and reflection and interference pattern with developed program.

IV. CONCLUSIONS

In real environment, there is almost no free space LOS and/or single diffraction in broadcasting systems. Geometrical optic model fails to calculate the field strength behind an obstruction because of diffraction. UTD model can be used in calculation of field strength and coverage prediction in multiple diffraction scenario including buildings, trees, hills, cars etc. In order to verify the results of developed program, detailed comparison results with FEKO software are represented. Coverage prediction should be made before base station installation in order to make more reliable broadcasting systems.

ACKNOWLEDGMENT

This work is partially supported by TUBITAK (The Scientific and Technological Research Council of Turkey) under the Grant No. 215E360.

REFERENCES

[1] R. G. Kouyoumjian and P. H. Pathak, "Uniform geometrical theory of diffraction for an edge in a perfectly conducting surface," *Proceedings of IEEE*, vol. 62, no. 11, pp. 1448-1461, 1974.

[2] J. B. Andersen, "UTD multiple-edge transition zone diffraction," *IEEE Transactions on Antennas and Propagation*, vol. 45, no. 7, pp. 1093-1097, 1997.

[3] C. Tzaras and S. R. Saunders, "Comparison of multiple-diffraction models for digital broadcasting coverage prediction," *IEEE Transactions on Broadcasting*, vol. 46, no. 3, pp. 221-226, 2000.

[4] K. Rizk, R. Valenzuela, D. Chizhik, and F. Gardiol, "Application of the slope diffraction method for urban microwave propagation prediction," *IEEE Vehicular Technology Conference*, Ottawa, Ont., vol. 2, pp. 1150-1155, May 1998.

[5] M. B. Tabakcioglu and A. Kara, "Comparison of improved slope UTD method with UTD based methods and physical optic solution for multiple building diffractions," *Electromagnetics*, vol. 29 no. 4, pp. 303-320, 2009.

[6] M. B. Tabakcioglu, "S-UTD-CH model in multiple diffractions," *International Journal of Electronics*, vol. 103, no. 5, pp. 765-774, 2015.

[7] M. B. Tabakcioglu, "A top-down pproach to S-UTD-CH model," *ACES Journal*, vol. 32, no. 7, pp. 586-592, 2017.

[8] J. V. Rodríguez, J. M. Molina-García-Pardo, and L. Juan-Llácer, "An improved solution expressed in terms of UTD coefficients for the multiple-building diffraction of plane waves," *IEEE Antennas and Wireless Communications*, vol. 4, pp. 16-19, 2005.

[9] J. V. Rodríguez, J. M. Molina-García-Pardo, and L. Juan-Llácer, "UTD-PO formulation for the multiple-diffraction of spherical waves by an array of multimodeled obstacles," *IEEE Antennas and Wireless Propagation Letters*, vol. 8, pp. 379-382, 2009.

[10] E. Arik and M. B. Tabakcioglu, "Uniform kırınım teorisi ve geometrik optik modeliyle kapsama alanı haritalanması," *Akademik Bilişim Konferansı*, pp. 1-6, 2017.

[11] V. A. Borovikov and B. E. Kinber, *Geometrical Theory of Diffraction*. Institution of Electrical

Engineers, London, UK, 1994.
[12] J. B. Keller, "Geometrical theory of diffraction," *Journal of the Optical Society of America*, vol. 52, no. 2, pp. 116-130, 1962.
[13] C. A. Balanis, L. Sevgi, and P. Y. Ufimtsev, "Fifty years of high frequency diffraction," *International Journal of RF and Microwave Computer-Aided Engineering*, vol. 23, no. 4, pp. 1-6, 2013.
[14] M. Schneider and R. J. Luebbers, "A uniform double diffraction coefficient," *Antennas and Propagation Society International Symposium*, San Jose, CA, vol. 3, pp. 1270-1273, June 1989.
[15] R. J. Luebbers, "Finite conductivity uniform GTD versus knife edge diffraction in prediction of propagation path loss," *IEEE Transactions on Antennas Propagation*, vol. 32, no. 1, pp. 70-76, 1984.
[16] https://altairhyperworks.com/FEKO/
[17] D. A. McNamara, C. V. Pistorious, and J. A. G. Malherbe, *Introduction to the Uniform Geometrical Theory of Diffraction*. Boston, MA: Artech House, 1990.

Mehmet Baris Tabakcioglu He was born in 1981. He received B.S. degree in Physics from Middle East Technical University in 2005. Then he received the M.S. degree in Electrical and Electronics Engineering from Atılım University in 2009. After that he received the Ph.D. degree in Electrical and Electronics Engineering from Atatürk University in 2013. His currently research area is wave diffraction, reflection and propagation. He is currently working at Bursa Technical University in Electrical and Electronics Engineering department.

Circular Concentric-Ring Reflectarray Design Using a Coaxial Wedge Unit Cell

Joshua S. Roper and Andrew F. Peterson

School of Electrical and Computer Engineering
Georgia Institute of Technology, Atlanta, GA 30332, USA
jroper33@gatech.edu, afpeterson@gatech.edu

Abstract ─ This paper presents a design methodology for a concentric ring reflectarray using angular periodic structures. This paper also examines the coaxial wedge unit cell using the waveguide simulator method and contrasts it to the coaxial unit ring approach. The coaxial wedge unit cell approach is seen to offer a more efficient and more extendable means of simulation than the coaxial unit ring approach.

Index Terms ─ Coaxial waveguide, frequency selective surface, periodic structures, reflectarray, waveguide, waveguide simulator method.

I. INTRODUCTION

The reflectarray, an antenna concept that combines design and analysis techniques from reflector antennas, periodic microwave structures and antenna array theory, has been around since at least the 1960s [1]. Early research was focused on waveguide elements. Planar elements such as spirals, discs, and patches were explored in the 1970s [2-4]. The first reflectarray patent was filed in the 1980s [5]. This early research was mainly conducted by private companies and the U.S. Air Force for military applications.

In the 1990s microstrip reflectarray design concentrated on analyzing the phase behavior as a function of patch size through full wave analysis [6-9]. Essential reflectarray capacities were also investigated including: beamsteering [10], multiple polarizations [11], bandwidth improvement [12], and dual-frequency band operation [13]. Recent advancements have been focused on improving upon these capabilities and enhancing performance metrics.

The reflectarray is a flat surface supporting many elements (usually microstrip patches) that are not connected with power division lines. This antenna has the benefit of being high gain and high efficiency like the reflector antenna or antenna array, while being flat (unlike the reflector) and not having an expensive, high-loss beamformer (unlike the antenna array). Additionally, low-loss phase shifters can be incorporated to add an electronic beam steering capability (like the antenna array) [14-15]. The reflectarray can also be used as a subreflector, instead of a solid subreflector [16].

The reflectarray will usually have non-uniformly sized elements to produce a non-constant reflected phase. At a basic level, the design must provide a phase shift at each element such that the phase delay at that element will produce a uniform reflected phase after path length delay effects are taken into account. A plot of the phase delay or phase shift for a normal angle of incidence will show a series of peaks and nulls around the center of the reflectarray.

One way to produce the phase delay that is needed is to alter the element size as a function of distance from the center of the array. To design a reflectarray of this type, full wave simulations of many element sizes are conducted and then the resulting resonant frequencies are mapped into a "backwards-S" phase reflection curve. This curve is used to fit the required phase delay for the reflectarray. A detailed design overview is presented in the literature [17-18].

Initial work on simulating periodic structures began in the 1960s using the waveguide simulator (WGS) method [19]. This method relied on exciting a radiating element in a waveguide. Because of the surrounding perfect electric conductor (PEC) walls, a method of images environment is formed which extends the element into an infinite array.

The WGS method can be applied to any arbitrary shaped waveguide. In the following, the well-known cylindrical waveguide is used [20-21]. The waveguide simulator method was not applied to simulating structures of this sort until recently [22-24].

It is important to point out that advances have come for planar periodic structure simulation using Floquet conditions to account for the linear phase shifting along the elements in an infinite environment [25]. This approach is a staple of modern array simulations, but assumes a linear phase shifting of the frequency. Due to this fact, for curved or cylindrical designs where the phase shifting is not linear, the Floquet condition cannot be used and other methods must be explored.

Another design consideration is the reflectarray

Submitted On: June 24, 2018
Accepted On: October 13, 2018

feed. Feed design uses efficiency plots and the chosen focal-to-diameter (F/D) ratio of the array. A detailed design overview can be found from classical reflector antenna theory [26-27].

Once the phase behavior of the reflectarray element is determined and the feed designed, the far field characteristics of the antenna can be approximated using array theory. An array geometry of particular interest is the concentric ring array geometry as it has circular periodicity. This array has the drawback of relatively high sidelobes in the uniform case; therefore an amplitude taper or some optimization procedure must be employed. Reference [28] presents techniques to mitigate the sidelobes by as much as 10dB. An actual design would need to employ these techniques as the uniform case would violate FCC 25.209 regulations for Ku-band.

Other approaches and applications to this problem have been considered. A locally planar unit cell analysis can be conducted to get the reflectance and transmittance parameters and then these can be placed on the surface of a reflector for a diffraction analysis [29]. The square geometry of a patch can be warped into a quasi-trapezoidal shape and analyzed [30-31]. Planar results can be simulated for a rectangular patch and then rotated tangentially around a curved surface using the characteristic basis method and spectral rotation approach [32-33].

II. MODEL SETUP

A. Design geometry

In this work, the WGS method is used with Ansys HFSS to analyze angular planar periodic unit cells. A resonant frequency of 6.15GHz (C-Band Uplink) is chosen for this application. In satellite communications, C-Band typically uses circular polarization. Furthermore, C-Band involves a lower frequency than Ka or Ku-Bands and therefore imposes an easier simulation. A copper clad dielectric substrate of Rogers RO3003 with a standard thickness of 1.52mm is used as the medium of design.

The same geometry is used for both the unit ring and the unit cell, with the unit cell stacking rotationally about the center of the coax to form the unit ring. As an example, the angular width of the unit cell is set to 36° in order to make a full 360° unit ring with ten unit cells. The angular width of the patch is set to 24°. The inner and outer spacing above and below the patch is set to 5.9mm. The total length of the design is 0.43 wavelengths. The geometries of the unit cell and unit ring can be seen in Fig. 1.

The geometry is configured with a PEC back plate and is topped with a vacuum layer with a height of 2 wavelengths. The top of the vacuum is set to be a modally driven port, making this design a one-port device. It can be found analytically or via HFSS that the coaxial unit ring has 9 propagating modes and the unit cell has 1. To determine the number of propagating modes in HFSS the user must set the maximum number of allowable modes, run a few passes of the adaptive mesh, and then inspect the propagation constants (gamma) to see which modes have positive real (lambda) and imaginary (epsilon) values.

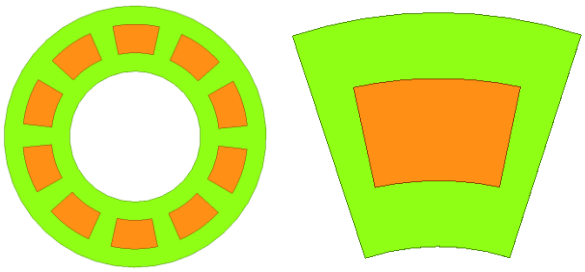

Fig. 1. (Left) Coaxial unit ring; (Right) coaxial wedge unit cell.

B. Boundary conditions

The boundary conditions for this design are depicted in Fig. 2. For the coaxial unit ring, the inner and outer coaxial walls are set to perfect magnetic conducting (PMC) boundary conditions to produce angularly polarized fields, as desired for this illustration. This type of polarization approximates illumination by a circularly polarized source. The boundaries can be also set to perfect electric conducting (PEC) boundary conditions to yield radially polarized fields (not depicted).

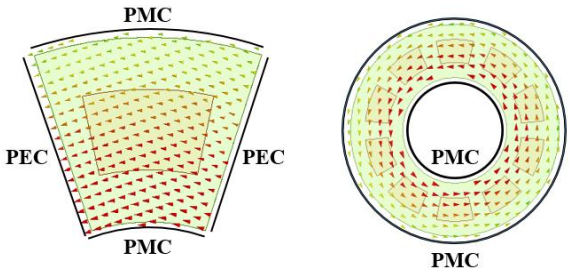

Fig. 2. (Left) Principal propagating mode on a coaxial unit cell; (Right) principal propagating mode on a coaxial wedge unit ring.

The coaxial unit cell (also depicted in Fig. 2) has the PMC boundary condition as well on the radial walls. Additionally, PEC boundary conditions are added to the side walls as a primitive periodic boundary condition. This can be thought about intuitively in two ways: 1) this will create images on these side walls to artificially extend the cell; 2) having the PEC on both side walls will make the fields want to jump from one to the other, creating the same fields in the cell as can be seen in the unit ring.

C. Meshing convergence

The coaxial wedge unit cell has only one propagating mode, and thus the mesh convergence optimization scheme is simple. This simulation is run as a modal solution of a one port cavity in the HFSS software, so the mesh refinement process is based on a single S-Parameter value S11 (magnitude and phase). For accuracy, the mesh is considered to have converged when there is a maximum change of no greater than 0.001 for the magnitude and 1 degree for the phase of S_{11}. Additionally, a minimum number of 8 passes is required to ensure an adequate initial mesh is generated and that the convergence doesn't preemptively exit.

For the coaxial unit ring, the convergence criteria must be a function of all of the diagonal entries of the S-Parameter matrix, i.e., the S11 values for all 9 propagating modes of the coaxial cavity. For the principal TEM mode, which is the mode that will be looked at for the reflected phase delay, the same convergence limit is set: a maximum change of no greater than 0.001 for the magnitude and 1 degree for the phase. For the other 8 modes the criteria require a maximum change of no greater than 0.01 for the magnitude and do not depend on phase.

For full convergence, 26 adaptive passes are needed for the coaxial unit ring, but in order to reduce simulation time, a maximum cut-off of 24 passes was used. This corresponds to a delta phase convergence of 1.28° instead of the desired 1°. Table #1 compares the performance of the unit cell and unit ring approaches. The unit ring results could be improved by allowing the adaptive process to go to 26 passes to match the unit cell criteria.

D. The PEC control case

An additional model must be created that is identical to those previously discussed, but with the radiating element replaced with a PEC block. In this way, a perfectly linear reflected phase shift can be obtained to compare to the reflected phase shift of the radiating element. The total reflected phase plot – which can be thought of as a "backwards S" curve (see Fig. 3) – can be found from subtracting the reflected phase of the PEC control case from the reflected phase of the radiating element.

III. SIMULATION RESULTS

Table 1 summarizes the findings and Fig. 3 presents the reflected phase plot produced by the two approaches. As might be expected, the unit cell is a much more computationally efficient way of calculating the reflected phase of the radiating patch. One important observation to note is that as the ring number increases the b/a ratio (where a is the inner and b is the outer radius of the coaxial unit cell) approaches unity, the physical area of the ring increases, and the number of propagating modes will approach infinity. Thus, another important quality of the unit cell model is that it will involve the same number of propagating modes as its location changes and the design is much easier to simulate for large radial locations.

Table 1: Mesh information for the coaxial wedge unit cell and the coaxial unit ring approach (2nd ring)

Mesh Statistics	Coaxial Wedge Unit Cell	Coaxial Unit Ring
Total mesh size	67,091	427,054
Simulation time	20 min	36 hours
Number of adaptive passes	19	24
Number of modes	1	9
Operational freq. band (GHz) {±90°}	5.870-6.309	5.862-6.299
Resonant phase frequency (GHz)	6.114	6.106
Bandwidth	7.15%	7.15%
Phase difference at 6.11 GHz	4.46°	

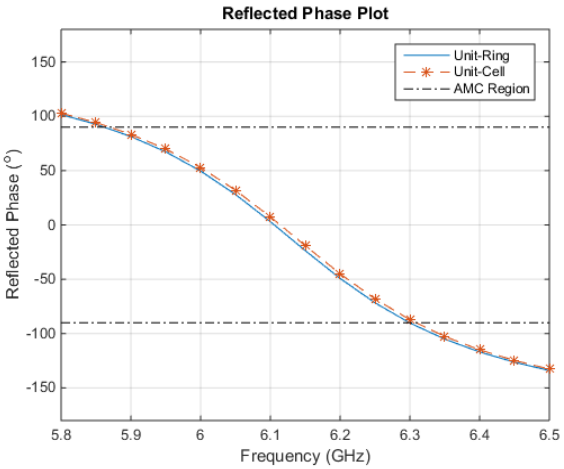

Fig. 3. Reflected phase curve for the two methods.

IV. REFLECTARRAY APPLICATION

As an example, consider a reflectarray for satellite communications in the commercial Ka-Band for an uplink frequency of 29 to 30 GHz and circular polarization. This antenna will be considered as a very small aperture terminal (VSAT) as it will have a total size of ~40cm. For this example, we design a reflectarray with a concentric ring topology. The design uses 47 rings, a spacing of 0.43 wavelengths between the rings, and 5α elements per ring where α is the integer ring index. The radius of the reflectarray is 20 wavelengths, for a total of 5,640 elements. The geometry of the reflectarray is shown in Fig. 4. This design has the minimum beamwidth required to meet the FCC 25.209 envelope, with a

gain of 42dB at 29.5GHz. A design with the unit cell parameters is presented in Table #2.

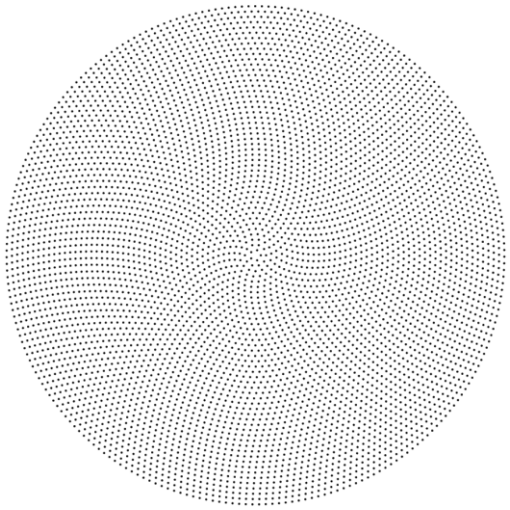

Fig. 4. Reflectarray geometry.

Table 2: Design table for the Ka-band unit cell

Design Table Ka-Band Unit cell	**Value**
Design frequency	29.5GHz
Substrate material	Roger RO3003
Substrate thickness	1.52mm
Radial (inner and outer) spacing	265μm
Angular spacing (cell, patch)	(36°, 28°)
Convergence criteria (mag, phase)	(0.001, 2.5°), 18 Passes
Resonant phase frequency (GHz)	29.54GHz
Bandwidth	1.42%

As discussed in the introduction, the phase shift ψ_i at an element must ensure that the phase delay at that element will produce a uniform reflected phase after path length delay effects are taken into account. This is equivalent to the constraint [36]:

$$k_0(R_i - \bar{r}_i \cdot \hat{r}_o) - \psi_i = 2\pi N, \quad (1)$$

where k_0 is the propagation constant, N is an integer, R_i is the distance to a patch, $\hat{r}_o$ is the unit vector of the reflected ray, and $\bar{r}_i$ represents the geometry of the array. A visual representation – from the geometry of this example – is depicted in Fig. 5.

In order to produce the phase shift required at an element by Fig. 5, the resonant phase as a function of patch size is needed. Notice that when the patch length is grown or shrunk, the resonant frequency will grow or shrink based on the trend depicted in Fig. 6, where patch length is defined as the radial length of the PEC patch within the unit cell. For frequency 29.5 GHz, and the set of resonant phase curves in Fig. 6, another backwards-S type curve can be produced for use as a design equation, as depicted in Fig. 7.

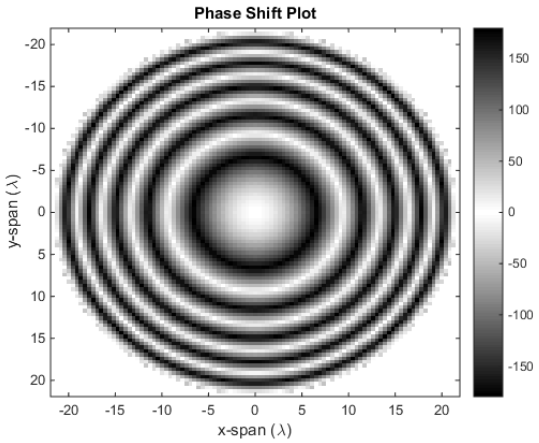

Fig. 5. Required element phase delay to produce a collimated beam using Equation #1.

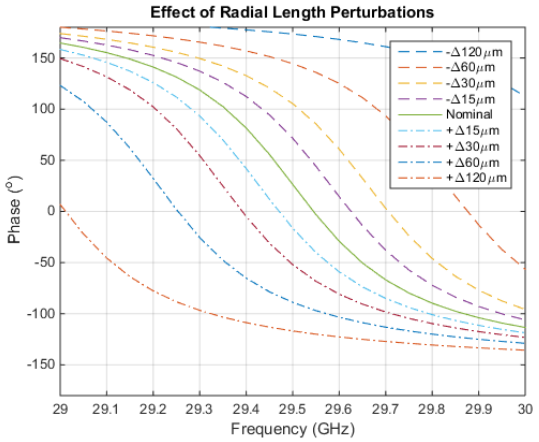

Fig. 6. Individual reflected phase plots for varying length elements.

After the resonant phase characteristics are determined and applied to the phase shift plot to produce a uniform reflected phase, the feed must be designed. The feed can be designed using simple reflector equations to find the optimal quality factor, where the optimal Q-factor is the maximum of the total aperture efficiency curve when combining spillover and illumination efficiencies. For this example, the F/D ratio was fixed at 1. The 3dB Beamwidth of the feed can be found using the following equations:

$$\theta_e = \tan^{-1}\left(\frac{1}{2F/D}\right) \rightarrow u = \cos(\theta_e), \quad (2)$$

$$\eta_{spillover} = 1 - u^{2(q+1)}, \quad (3)$$

$$\eta_{illumination} = \frac{4(q+1)(1-u^q)^2}{q^2 \eta_{spillover} \tan(\theta_e)^2}, \quad (4)$$

$$\eta_{total} = \eta_{spillover} \eta_{illumination}, \quad (5)$$

$$q_{max} = \max(\eta_{total}), \quad (6)$$

$$\Rightarrow BW_{3dB}(Feed) = 2\cos^{-1}\left(\exp\left\{\frac{\log\left(\frac{1}{2}\right)}{2q_{max}}\right\}\right), \quad (7)$$

$$with\ BW_{3dB}(Feed) \approx 30^\circ \left(for \frac{F}{D} = 1\right), \quad (8)$$

These equations produce the plots in Fig. 8, and the optimal Q-factor can be found as the maximum of the total aperture efficiency curve.

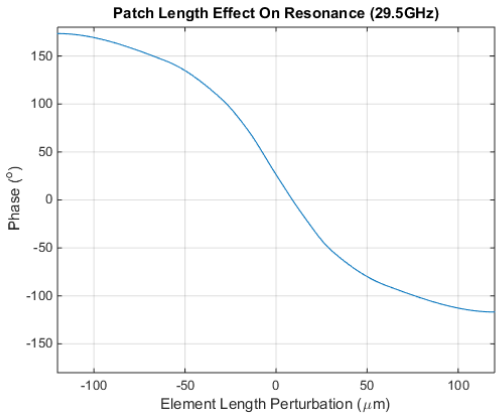

Fig. 7. Resonant phase plot for 12.4GHz versus element lengths.

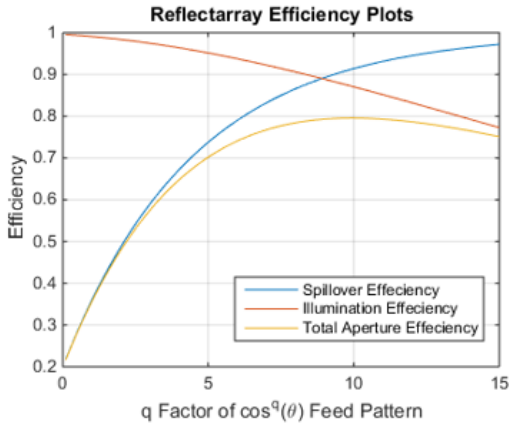

Fig. 8. Reflectarray efficiency plot.

Now that both the array and the feed are designed, the far-field pattern can be found using array theory with the feed and element patterns being applied as amplitude tapers (shown in Fig. 9). Assuming all elements are designed such that the phase delay requirement is met, the far-field plot will be that given in Fig. 10. The initial antenna pattern in Fig. 10 has a few sidelobes close to the main beam that violate regulatory requirements, but these can be mitigated using array optimization as described in [28].

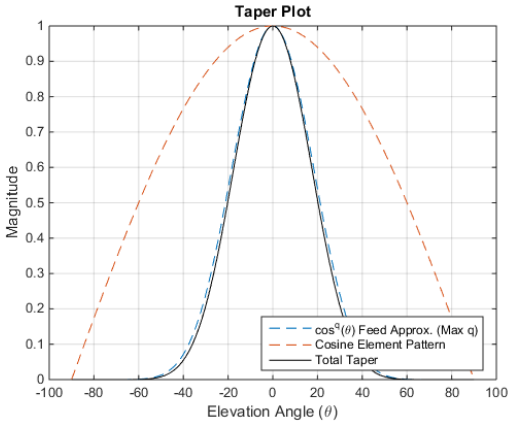

Fig. 9. Amplitude taper plot.

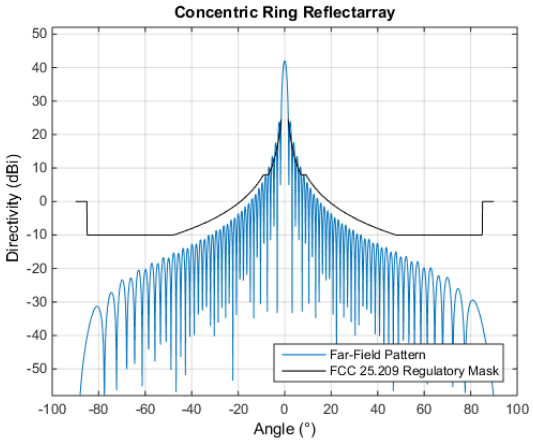

Fig. 10. Far-field pattern of the reflectarray antenna.

V. CONCLUSION

A method of designing a concentric ring reflectarray is presented. EM field simulation is used to determine the phase profiles of the unit cell. It is found that the coaxial wedge unit cell gives nearly identical results, in terms of bandwidth and resonant frequency of the reflected phase curve, compared to the coaxial unit ring. The coaxial wedge unit cell requires an order of magnitude smaller simulation time. A preliminary concentric-ring reflectarray design is presented.

REFERENCES

[1] D. Berry, R. Malech, and W. Kennedy, "The reflectarray antenna" *IEEE Transactions on Antennas and Propagation*, vol. 11, no. 6, pp. 645-651, Nov. 1963.

[2] H. R. Phelan, "Spiralphase reflectarray for multi-target radar," *Microwave Journal*, vol. 20, pp. 67-

73, July 1977.

[3] C. S. Malagisi, "Microstrip disc element reflect array," *Electronics and Aerospace Systems Convention*, pp. 186-192, Sept. 1978.

[4] J. P. Montgomery, "A microstrip reflectarray antenna element," *Antenna Applications Symposium*, University of Illinois, Sept. 1978.

[5] R. E. Munson and H. Haddad, "Microstrip reflectarray for satellite communication and RCS enhancement and reduction," U.S. Patent 4,684,952, Washington, D.C., Aug. 1987.

[6] J. Huang, "Microstrip reflectarray," *IEEE AP-S/URSI Symposium*, London, Canada, pp. 612-615, June 1991.

[7] T. A. Metzler, "Design and Analysis of a Microstrip Reflectarray," *Ph.D. Dissertation*, University of Massachusetts, Sept. 1992.

[8] Y. Zhang, K. L. Wu, C. Wu, and J. Litva, "Microstrip reflectarray: Full-wave analysis and design scheme," *IEEE AP-S/URSI Symposium*, Ann Arbor, Michigan, pp. 1386-1389, June 1993.

[9] D. M. Pozar and T. A. Metzler, "Analysis of a reflectarray antenna using microstrip patches of variable size," *Electronics Letters*, pp. 657-658, April 1993.

[10] R. D. Javor, X. D. Wu, and K. Chang, "Beam steering of a microstrip flat reflectarray antenna," *IEEE AP-S/URSI Symposium*, Seattle, Washington, pp. 956-959, June 1994.

[11] D. C. Chang and M. C. Huang, "Multiple polarization microstrip reflectarray antenna with high efficiency and low cross - polarization," *IEEE Trans. Antennas Propagat*., vol. 43, pp. 829-834, Aug. 1995.

[12] J. Huang, "Bandwidth study of microstrip reflectarray and a novel phased reflectarray concept," *IEEE AP - S/URSI Symposium*, Newport Beach, California, pp. 582-585, June, 1995.

[13] J. A. Encinar, "Design of a dual - frequency reflectarray using microstrip stacked patches of variable size," *Electronic Letters*, vol. 32, no. 12, pp. 1049-1050, June 1996.

[14] D. F. Sievenpiper, J. H. Schaffner, H. J. Song, R. Y. Loo, and G. Tangonan, "Two-dimensional beam steering using an electrically tunable impedance surface," *IEEE Transactions on Antennas and Propagation*, vol. 51, no. 10, pp. 2713-2722, Oct. 2003.

[15] S. V. Hum, M. Okoniewski, and R. J. Davies, "Modeling and design of electronically tunable reflectarrays," *IEEE Transactions on Antennas and Propagation*, vol. 55, no. 8, pp. 2200-2210, Aug. 2007.

[16] S. Xu, Y. Rahmat-Samii, and W. A. Imbriale, "Subreflectarrays for reflector surface distortion compensation," *IEEE Transactions on Antennas and Propagation*, vol. 57, no. 2, pp. 364-372, Feb. 2009.

[17] D. M. Pozar, S. D. Targonski, and H. D. Syrigos, "Design of millimeter wave microstrip reflect-arrays," *IEEE Transactions on Antennas and Propagation*, vol. 45, no. 2, pp. 287-296, Feb 1997.

[18] J. Huang and J. Encinar, *Reflectarray Antennas*. New York, United States: Wiley-IEEE Press, 2008.

[19] P. Hannan and M. Balfour, "Simulation of a phased-array antenna in waveguide," *IEEE Transactions on Antennas and Propagation*, vol. 13, no. 3, pp. 342-353, May 1965.

[20] W. L. Barrow and W. W. Mieher, "Natural oscillations of electrical cavity resonators," *Proceedings of the IRE*, vol. 28, no. 4, pp. 184-191, Apr. 1940.

[21] R. A. Kirkman and M. Kline, "The transverse electric modes in coaxial cavities," *Proceedings of the IRE*, vol. 34, no. 1, pp. 14p-17p, Jan. 1946.

[22] J. Sarrazin, A. C. Lepage, and X. Begaud, "Circular high-impedance surfaces characterization," *IEEE Antennas and Wireless Propagation Letters*, vol. 11, no., pp. 260-263, 2012.

[23] A. C. Durgun, C. A. Balanis, and C. R. Birtcher, "Reflection phase characterization of curved high impedance surfaces," *IEEE Transactions on Antennas and Propagation*, vol. 61, no. 12, pp. 6030-6038, Dec. 2013.

[24] M. A. Amiri, C. A. Balanis, and C. R. Birtcher, "Analysis, design, and measurements of circularly symmetric high-impedance surfaces for loop antenna applications," *IEEE Transactions on Antennas and Propagation*, vol. 64, no. 2, pp. 618-629, Feb. 2016.

[25] A. F. Peterson, S. L. Ray, and R. Mittra, *Computational Methods for Electromagnetics*. New York: IEEE Press, 1998.

[26] W. L. Stutzman and G. A. Thiele, *Antenna Theory and Design*. 3rd ed., New York: John Wiley & Sons, 2013.

[27] C. A. Balanis, Antenna *Theory: Analysis and Design*. 3rd ed., New York: John Wiley & Sons, 2005.

[28] R. L. Haupt, "Optimized element spacing for low sidelobe concentric ring arrays," *IEEE Transactions on Antennas and Propagation*, vol. 56, no. 1, pp. 266-268, Jan. 2008.

[29] Y. Rahmat-Samii and A. N. Tulintseff, "Diffraction analysis of frequency selective reflector antennas," *IEEE Transactions on Antennas and Propagation*, vol. 41, no. 4, pp. 476-487, Apr. 1993.

[30] L. A. Costa, O. M. d. C. Pereira-Filho, and F. J. S. Moreira, "Quasi-trapezoidal microstrip spherical patches and arrays," *IET Microwaves, Antennas & Propagation*, vol. 10, no. 1, pp. 53-60, Jan. 9, 2016.

[31] D. J. Gregoire, "3-D conformal metasurfaces,"

IEEE Antennas and Wireless Propagation Letters, vol. 12, pp. 233-236, 2013.

[32] G. Tiberi, S. Bertini, A. Monorchio, G. Mazzarella, and G. Montisci, "A spectral rotation approach for the efficient calculation of the mutual coupling between rectangular apertures," *IEEE Antennas and Wireless Propagation Letters*, vol. 10, pp. 131-134, 2011.

[33] R. F. Harrington, *Cylindrical Wave Functions, Time-Harmonic Electromagnetic Fields*. Wiley-IEEE Press, 2001.

Joshua S. Roper received two B.S. degrees in Electrical engineering and Physics from Georgia Southern University in 2016 and an M.S. degree in Electrical and Computer Engineering from the Georgia Institute of Technology in 2017. He is currently working towards his Ph.D. degree in Electrical and Computer Engineering at the Georgia Institute of Technology. Since January 2018, he has been a member of Technical Staff at Viasat Inc., where his work focuses on electromagnetics for satellite communication applications.

Andrew F. Peterson received the B.S., M.S., and Ph.D. degrees in Electrical Engineering from the University of Illinois, Urbana-Champaign in 1982, 1983, and 1986 respectively. Since 1989, he has been a member of the faculty of the School of Electrical and Computer Engineering at the Georgia Institute of Technology, where he is now a full Professor. Within ACES, he has served at various times as a member of the Board of Directors, the Finance Committee Chair, the Publications Committee Chair, and the President. He also served as a Technical Co-chair for the 25th Annual Review of Progress in Applied Computational Electromagnetics (ACES 2009). He was elevated to ACES Fellow in 2008.

APPENDIX I. ANALYTICAL MODE PREDICTION

Cylindrical waveguide geometries have a wave function (the solution to the Helmholtz equation) of the form:

$$\psi = B_n(k_\rho \rho) h(n\phi) e^{\pm j k_z z}, \tag{9}$$

where $B_n(k_\rho\rho) \sim J_n(k_\rho\rho)$, $N_n(k_\rho\rho)$, $H_n^{(1)}(k_\rho\rho)$, $H_n^{(2)}(k_\rho\rho)$ and $h(n\phi) \sim \sin(n\phi), \cos(n\phi), e^{\pm jn\phi}$.

A. Coaxial waveguide modes

The modes are commonly known for the coaxial waveguide and were derived in the 1940s.

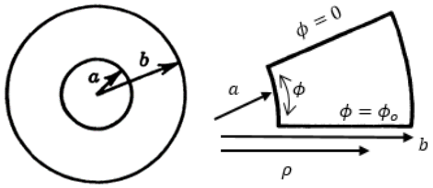

Fig. 11. Cross section of the coaxial waveguide (Left) and coaxial wedge waveguide (Right).

For the coaxial waveguide depicted in Fig. 11, by setting the electric field to zero at ρ = a and b, the propagation constant can be derived from the roots k_ρ of the equation:

$$Y_n(ka)J_n(kb) - J_n(ka)Y_n(kb) = 0, \quad \text{for } n = 0,1,2,\ldots \tag{10}$$

Similarly, for TE modes:

$$Y'_n(ka)J'_n(kb) - J'_n(ka)Y'_n(kb) = 0, \quad \text{for } n = 0,1,2,\ldots \tag{11}$$

The coaxial wedge waveguide is similar to the coaxial waveguide, but there are additional boundary conditions on the angular PEC walls. These require the electric field at φ = 0 and φ_0 to vanish. From these boundary conditions, the propagation constants can be derived from the roots k_ρ of the equation:

$$Y_n(ka)J_n(kb) - J_n(ka)Y_n(kb) = 0, \quad \text{for } n = \frac{k\pi}{\phi_o} \text{ where } k = 1,2,3\ldots \tag{12}$$

Similarly, for TE modes:

$$Y'_n(ka)J'_n(kb) - J'_n(ka)Y'_n(kb) = 0, \quad \text{for } n = \frac{k\pi}{\phi_o} \text{ where } k = 0,1,2,3\ldots \tag{13}$$

Since n is larger in the coaxial wedge waveguide than in the coaxial waveguide, the coaxial wedge waveguide will have fewer modes depending on the value of ϕ_o. We see this in practice – as in Table 1. Additional details on cylindrical wave functions can be found in [33].

Single Layer Reflectarray Antenna with Pie-Shaped Elements for X-band Applications

Tayyab Shabbir [1], Rashid Saleem [1], Sabih U. Rehman [2], and Muhammad Farhan Shafique [3]

[1] Department of Telecommunication Engineering
University of Engineering and Technology, Taxila, 47050, Pakistan
{Tayyab.Shabbir, Rashid.Saleem}@uettaxila.edu.pk

[2] School of Computing and Mathematics, Charles Sturt University, Australia
sarehman@csu.edu.au

[3] Center for Advanced Studies in Telecommunication
COMSATS University Islamabad, Park Road, Tarlai Kalan, Islamabad, 45550, Pakistan
Farhan.Shafique@comsats.edu.pk

Abstract ─ In this paper, a single-layer reflectarray design is presented for X-band applications. The reflectarray comprises of pie-shaped reflective elements. The unit element has compact dimensions of $0.28\lambda_o \times 0.28\lambda_o$. The major segment angle of pie-shaped element controls the reflection phase range and offers a total of 650º phase variation. A reflectarray prototype comprising *23 × 23* elements is realized to demonstrate the necessary reflection characteristics. Different parameters are analyzed for performance evaluation of the reflectarray. The proposed reflectarray offers measured gain of 24 dBi with 1-dB and 3-dB gain bandwidth of 18% and 28% respectively. Moreover, side-lobe-levels and cross-polarizations are less than 22 dB and 35 dB respectively.

Index Terms ─ Radiation patterns, reflectarray antenna (RA), reflection magnitude, reflection phase range.

I. INTRODUCTION

Among various modules of high-speed transceivers, the RF front-end has gained considerable attention over the last two decades. High gain antennas, being the crucial part of front-end, play an important role in long distance communication and other applications like remote sensing. Conventionally, parabolic reflectors and phased-arrays are used for high gain applications. Parabolic reflectors are difficult to realize owing to their curved geometry and phase arrays on the other hand have complicated and lossy feed networks. The phased-arrays and parabolic reflectors can be effectively substituted by reflectarrays. The reflectarrays offer certain advantages over parabolic reflectors as well as phase arrays by combining the features of these two high gain antenna classes. Reflectarrays are low cost, light weight and easy to fabricate and deploy. Reflectarrays have multiple reflective elements printed on a substrate, backed by a ground plane and illuminated by a feed horn antenna. The operating principle of reflectarray is illustrated in Fig. 1. Overall, one of the common limitations of reflectarrays is their narrow operating bandwidth. However, their bandwidth can be improved by employing elements with a broad linear phase range [1 - 3].

Recently, different techniques are proposed to control the reflection phase of reflectarrays. These techniques include but are not limited to variation in geometrical parameters, variable size patches, identical elements with different rotation angles etc. In [4], a modified cross loop reflectarray is presented. A wide phase range of 550º is achieved by varying the length of cross shape. A fractal reflectarray of first and second order with phase range of 354º is presented in [5]. A slotted hollow ring with stacked ground plane is presented recently where the desired gain is achieved by rotating the slotted ring [6]. In [7], a square shaped reflectarray attached with lattice stubs is reported. The stub length is optimized to achieve a broad phase variation of 600º. Parallel dipoles based reflectarray for high gain and broad phase range of 413º is presented in [8]. A single layer qausi-spiral reflectarray with small dispersion in transmission modes is presented in [9]. It is envisioned that the phase range can be further enhanced to improve the design bandwidth with simple geometry and single layer realization as compared to the existing literature.

In this article a single layer pie-shaped reflectarray for X-band applications is proposed. The reflectarray is designed and optimized using a commercially available 3D full-wave electromagnetic solver based on Finite Element Method (FEM) algorithm (Ansys HFSS). The outline of the paper is as follows: unit element design is

Submitted On: January 12, 2017
Accepted On: October 19, 2018

presented in Section II. The reflectarray configuration and measurement setup is elaborated in Section III. Finally, Section IV concludes the paper.

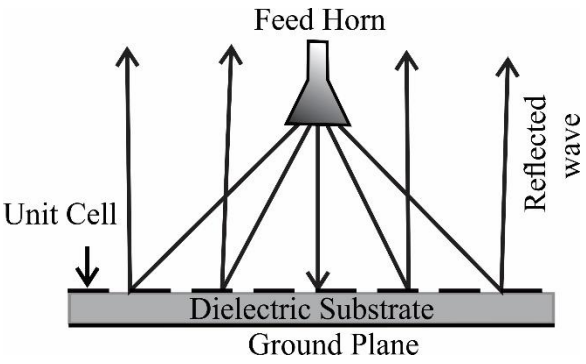

Fig. 1. Reflectarray operational principle.

II. UNIT ELEMENT DESIGN AND ANALYSIS

Unit element is designed and optimized for X-band applications with centre frequency of 10 GHz. The reflectarray unit element geometry is shown in Fig. 2. The design has compact dimensions of $0.28\,\lambda_o \times 0.28\,\lambda_o$, where λ_o is free space wavelength at 10 GHz. The reflectarray is designed on FR-4 substrate with dielectric constant of 4.4 and a loss tangent of 0.02. The top-layer comprises of pie-shaped unit element and the ground plane is placed on the flip side of substrate. The unit element optimized parameters for 10 GHz are shown in Table 1.

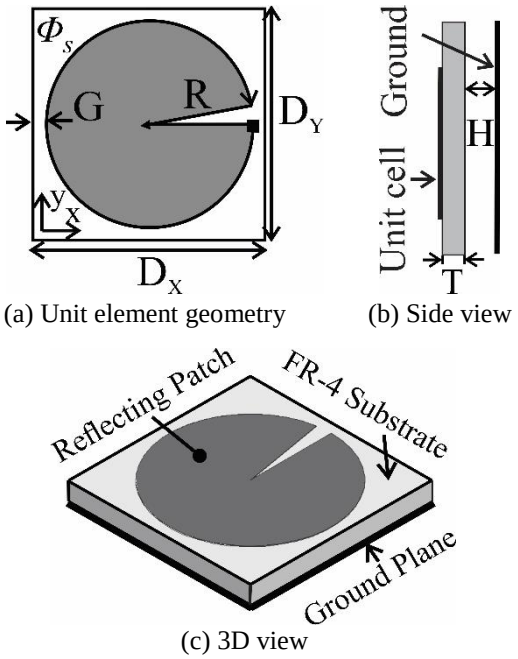

(a) Unit element geometry (b) Side view

(c) 3D view

Fig. 2. Reflectarray unit element configuration.

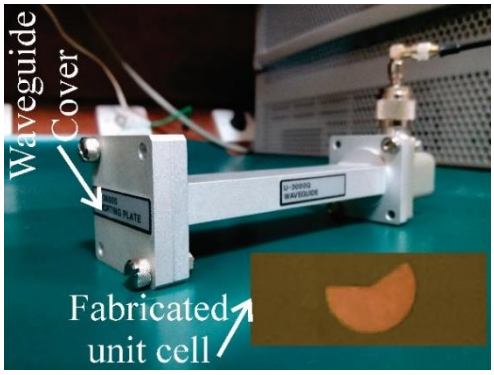

Fig. 3. Unit element measurement through waveguide simulator method.

Table 1 : Unit cell optimized parameters at 10 GHz

Parameter	D_Y	D_X	R	G	T
Value (mm)	8.5	8.5	4	0.25	1.6

A. Unit cell performance parameters

The parametric analysis for simulated reflection magnitude against frequency is shown in Fig. 4. The reflection curve moves towards lower frequencies when the major segment angle of pie-shaped element, ϕ_s, is increased and vice versa. Moreover, reflectarray unit cell prototype for 10 GHz frequency is fabricated, as shown in Fig. 3 and reflection magnitude is measured through waveguide simulator method.

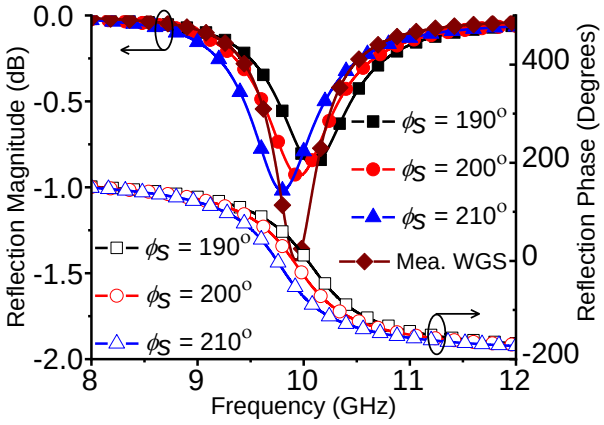

Fig. 4. Reflection magnitude at different segment angles.

The phase range is examined over different parameters, i.e., oblique incident angles in transmission modes and different frequencies. The phase range at 9, 10 and 11 GHz is shown in Fig. 5. By varying the major segment angle, ϕ_s, from 0° to 350°, the design achieves a phase range of 650°. The simulated phase range for TE and TM modes at different oblique incident angles is shown in Figs. 6 (a) and 6 (b). A stable phase response with little shift is obtained at 30° and 45° oblique incident

angles, which is within acceptable limits [10]. Conventionally, the value of real part of impedance should be higher to avoid losses in the reflectarray. The real and imaginary parts of impedance are shown in Fig. 7. The real part of impedance (resistance) is more than 2000 Ω at 10 GHz frequency [11].

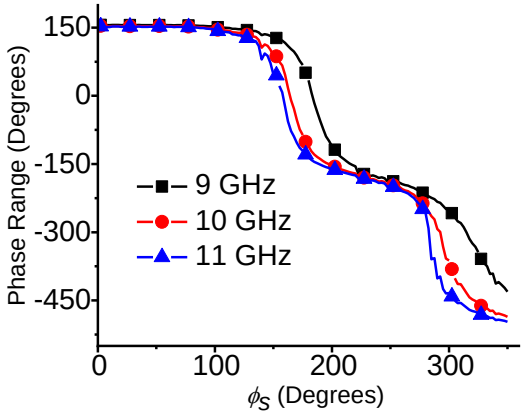

Fig. 5. Reflection phase range at 9, 10 and 11 GHz.

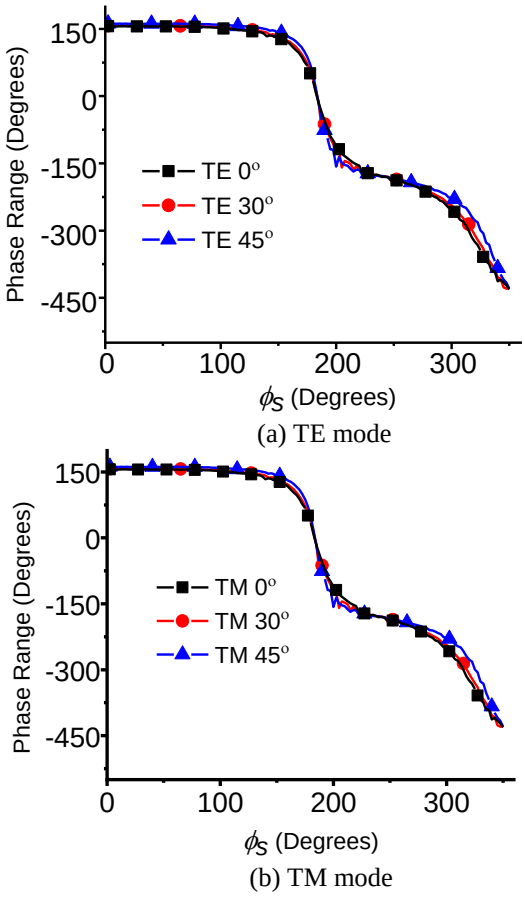

Fig. 6. Performance parameters effect on phase range.

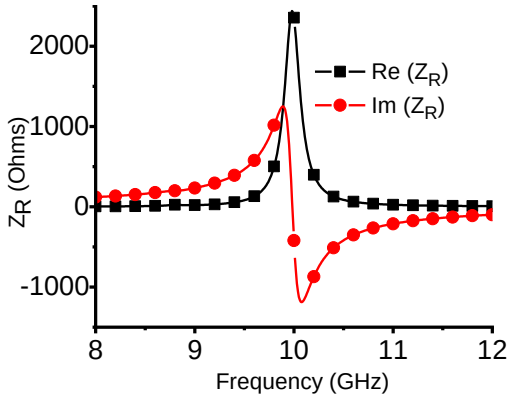

Fig. 7. Input impedance at 10 GHz.

III. REFLECTARRAY REALIZATION AND MEASUREMENT SETUP

A *23×23* element reflectarray is designed on FR-4 substrate. The reflectarray panel has dimensions of $6.5\lambda_o \times 6.5\lambda_o$, where λ_o is the free space wavelength at 10 GHz. The array elements are equally spaced with inter-element spacing of $0.28\lambda_o$. The spacing between elements is commonly kept less than $0.5\lambda_o$, to reduce the presence of grating lobes [1]. Generally, in array configuration, a minor change in the size of unit element produces a large phase shift in the reflected wave. The required phase distribution on each element in reflectarray is attained by using Equation 1:

$$\phi_R = K_o(d_i - (x_i cos\phi_o + y_i sin\phi_o) \times sin\,\theta_o). \quad (1)$$

The parameters used in array Equation (1) are elaborated in [1, 12]. The phase distribution plot is used to calculate the opening angle of each array element. The phase distribution on center-fed pie-shaped reflectarray is depicted in Fig. 8 (a). A stronger phase shift is observed at the center than at the corners/sides. The ratio of focal length to diameter of reflectarray is defined as *F/D* ratio. The fabricated pie-shaped reflectarray has an *F/D* ratio of 1. Reflectarrays have electrically large aperture size and require high computational resources and time. Therefore, a hybrid Finite Element Boundary Integral (FEBI) algorithm is used for reflectarray system simulations. This algorithm combines the Finite Element Method (FEM) with Integral Equation (IE) method [12]. This method efficiently handles the complex and electrically large sized structures. The reflectarray far-field radiation characteristics are obtained by using hybrid FEBI method. Full reflectarray simulations with feed horn and 23×23 reflectarray elements were performed on a ten-core HP Z840 workstation with workable memory of 64 GB. The CPU took about 23 hours to fully simulate the reflectarray. The reflectarray antenna FEBI system model as shown in Fig. 8 (b) is used to obtain far field characteristics.

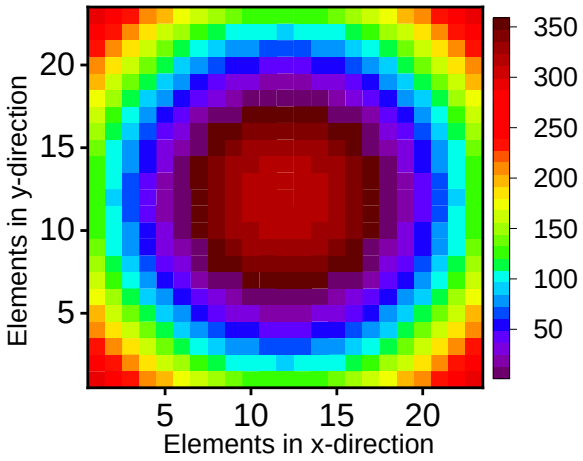

(a) Phase distribution on *23×23* element reflectarray

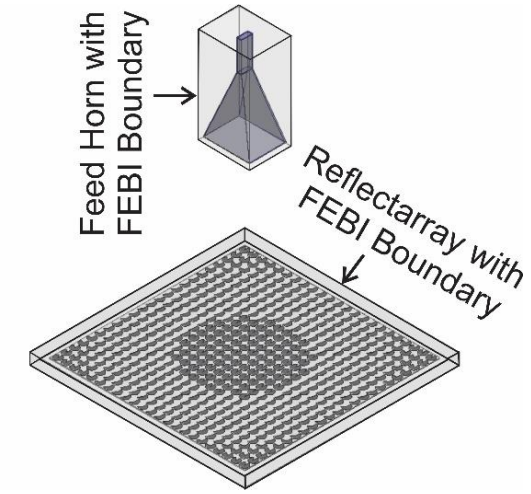

(b) Reflectarray system modeling with FEBI algorithm

Fig. 8. Reflectarray system model along with phase distribution.

The fabricated reflectarray antenna and the measurement setup is shown in Fig. 9. The fabricated 23 × 23 elements reflectarray on FR-4 laminate is placed inside a wooden stand and illuminated by an X-band WR-90 feed horn antenna. The feed horn is placed 194 mm away from the center of array panel. The reflectarray antenna measurements are carried out in an anechoic chamber.

The simulated and measured E and H-plane radiation patterns at 10 GHz are shown in Fig. 10. The side-lobe-levels and cross polarizations are less than 22 dB and 35 dB for the reflectarray. The gain against frequency is shown in Fig. 11. A gain of 24 dBi with aperture efficiency of 48% is achieved at 10 GHz. Moreover, 1-dB and 3-dB gain bandwidths are 18% and 28% respectively. The proposed reflectarray comparison with previously reported reflectarrays is listed in Table 2.

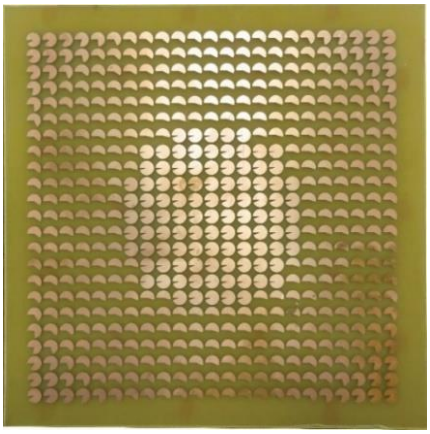

(a) Fabricated 23 × 23 element reflectarray

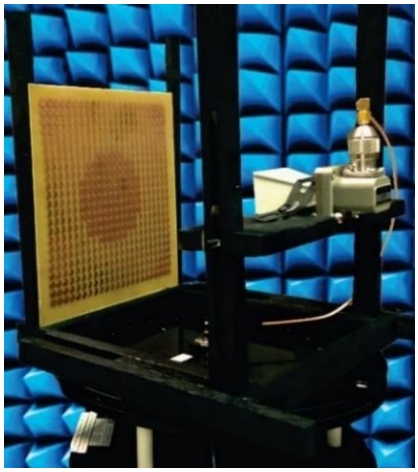

(b) Reflectarray under testing

Fig. 9. Fabricated reflectarray and measurement setup.

Table 2: Comparison with previously reported reflectarrays

References	**This Work**	**[15]**	**[14]**	**[13]**	**[12]**
Middle frequency (GHz)	10	12.5	10	13.5	10
Gain (dBi)	24	26.6	26.1	25	24.5
Aperture efficiency (%)	48	52.5	40.3	39	49.5
1-dB bandwidth (%)	18	8.1	18	20	12.5
3-dB bandwidth (%)	28	19.8	30	—	34
Side-lobe-levels (dB)	-22	—	-16	-25	-35
X-pol (dB)	-35	-21	-23	-30	-40

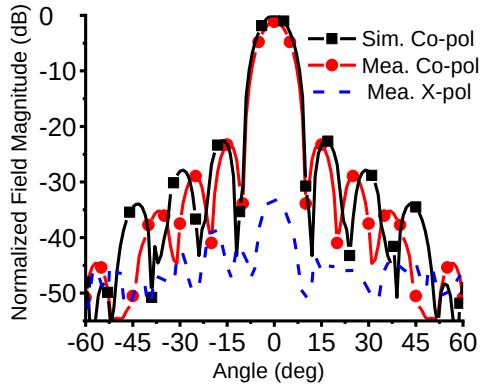

(a) E-plane pattern

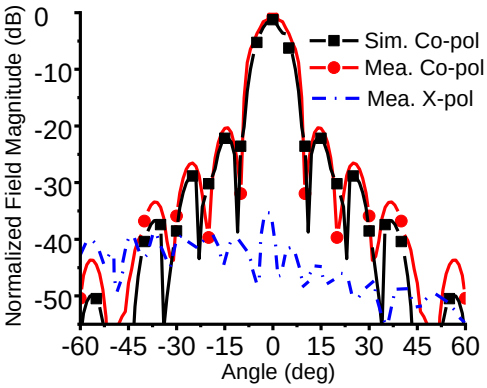

(b) H-plane pattern

Fig. 10. E and H-plane gain patterns at 10 GHz.

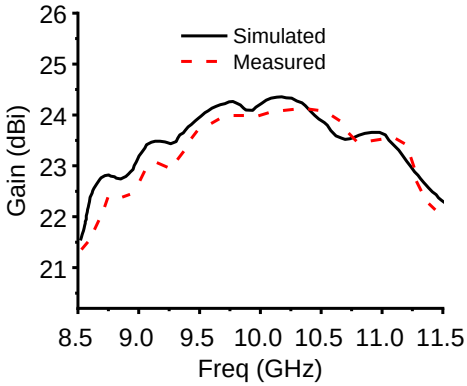

Fig. 11. Gain vs. frequency.

VI. CONCLUSION

Pie-shaped reflectarray for X-band is presented in this paper. Reflectarray prototype of size $6.5\lambda_o \times 6.5\lambda_o$ is fabricated with an *F/D* ratio of 1. The reflectarray performance is analyzed in terms of reflection magnitude, phase range, TE and TM modes. The reflectarray has a measured gain of 24 dBi at 10 GHz frequency. The simulated results are in good agreement with the measured results. The results strongly suggest that the reflectarray is a suitable candidate for high gain X-band applications.

REFERENCES

[1] P. Nayeri, F. Yang, and A. Z. Elsherbeni, "Beam-scanning relectarray antennas: A technical overview and state of the art," *IEEE Antennas and Propagation Magazine*, vol. 57, no. 4, pp. 32-47, 2015.

[2] J. Shaker, M. R. Chaharmir, and J. Ethier, *Reflectarray Antennas: Analysis, Design, Fabrication, and Measurement*. Artech House, 2013.

[3] B. Honarbakhsh, "FR4-only microstrip reflectarray antennas for 5.8 GHz dual-polarized wireless bridges," *Applied Computational Electromagnetics Society Journal*, vol. 31, no. 4, pp. 355-360, 2016.

[4] Q. Wang, Z. Shao, P. Li, L. Li, and Y. Cheng, "A dual polarization, broadband millimeter-wave reflectarray using modified cross loop element," *Microwave and Optical Technology Letters*, vol. 56, no. 2, pp. 287-293, 2014.

[5] S. Costanzo and F. Venneri, "Miniaturized fractal reflectarray element using fixed-size patch," *IEEE Antennas and Wireless Propagation Letters*, vol. 13, pp. 1437-1440, 2014.

[6] H. Chen, G. Zhang, X. Lei, and J. Wu, "A slotted hollow ring element for Ku-band high-efficiency circularly polarized reflectarrays," *Microwave and Optical Technology Letters*, vol. 57, no. 11, pp. 2629-2632, 2015.

[7] S. F. Qotolo, H. R. Hassani, and M. Naser-Moghadasi, "A novel broadband reflectarray antenna with lattice stubs on square element for Ku-band application," *Microwave and Optical Technology Letters*, vol. 57, no. 11, pp. 2699-2702, 2015.

[8] J. H. Yoon, Y. J. Yoon, W. S. Lee, and J. h. So, "Broadband microstrip reflectarray with five parallel dipole elements," *IEEE Antennas and Wireless Propagation Letters*, vol. 14, pp. 1109-1112, 2015.

[9] I. Derafshi, N. Komjani, and M. Mohammadirad, "A single-layer broadband reflectarray antenna by using quasi-spiral phase delay line," *IEEE Antennas and Wireless Propagation Letters*, vol. 14, pp. 84-87, 2015.

[10] E. R. F. Almajali and D. A. McNamara, "Angle of incidence effects in reflectarray antenna design: Making gain increases possible by including incidence angle effects," *IEEE Antennas and Propagation Magazine*, vol. 58, no. 5, pp. 52-64, Oct. 2016.

[11] F. Costa and A. Monorchio, "Closed-form analysis of reflection losses in microstrip reflectarray antennas," *IEEE Transactions on Antennas and Propagation*, vol. 60, no. 10, pp. 4650-4660, Oct.

2012.
[12] T. Shabbir, R. Saleem, S. U. Rehman, and M. F. Shafique, "A compact single layer reflectarray antenna based on circular delay-lines for X-band applications," *Radioengineering*, vol. 27, no. 2, pp. 440-447, 2018.
[13] S. F. Qotolo, H. R. Hassani, and M. Naser-Moghadasi, "A novel broadband reflectarray antenna with lattice stubs on square element for ku-band application," *Microwave and Optical Technology Letters*, vol. 57, pp. 2699-2702, 2015.
[14] J. Wu, X. Da, and K. Wu, "Circularly polarized high efficiency wideband reflectarray using rectangle-shaped patch element," *International Journal of RF and Microwave Computer Aided Engineering*, vol. 27, no. 5, 2017.
[15] X. Da, J. Wu, J. Zhao, L. Baoqin, and K. Wu, "Single-layer circularly polarized wide band reflectarray antenna with high aperture efficiency," *International Journal of Antennas and Propagation*, vol. 2018, Article ID 2403052, 2018.

Tayyab Shabbir received his B.Sc. in Electrical Engineering in 2011 from COMSATS Institute of Information Technology, Islamabad, Pakistan and Masters in Telecommunication Engineering in 2014 from University of Engineering and Technology (UET) Taxila, Pakistan, where he won a studentship. Recently he is again awarded a Ph.D. studentship by UET Taxila. His main research interests are in reflectarrays, Frequency Selective Surfaces and UWB-MIMO systems.

Rashid Saleem received B.S. Electronic Engineering from Ghulam Ishaq Khan Institute of Engineering Sciences and Technology, Pakistan, in 1999. He pursued a career in the telecommunication industry for several years while continuing education. He received M.S. from UET Taxila through Center for Advanced Studies in Engineering, Pakistan, in 2006 and Ph.D. from The University of Manchester, United Kingdom in 2011. In his Ph.D., he worked in Microwave and Communication Systems research group under the supervision of Prof. Anthony K. Brown, then-head of the School of Electrical and Electronic Engineering, The University of Manchester. He worked on antennas, channel modeling and interference aspects of Ultra-Wideband systems during his Ph.D. and was also member of a team designing and testing arrays for the Square Kilometer Array project. Currently, he is working as Assistant Professor at University of Engineering and Technology (UET), Taxila, Pakistan where he is supervising several postgraduate students and heading the MAP (Microwaves, Antennas and Propagation) research group. His research interests include antennas, angle-of-arrival based channel modeling, microwave periodic structures and meta-materials.

Sabih Ur Rahman is Adjunct Lecturer in the School of Computing and Mathematics at Charles Sturt University, Australia. He has combined experience in the field of Telecommunication and Information Technology for over 16 years in both enterprise and educational sector environments. Sabih completed his Ph.D. from Charles Sturt University, in the area of Vehicular Wireless Communication in 2016. He received his Bachelor's degree from University of South Australia, Adelaide in Electronics & Telecommunication Engineering with Honours. Sabih is also the recipient of a competitive scholarship from Charles Sturt University for his doctorate. Sabih's current research interests are in the areas of antennas and propagation.

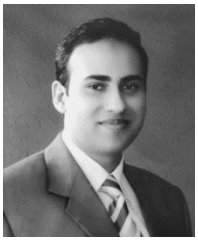

Muhammad Farhan Shafique received B.Eng. degree from Hamdard University, Karachi, Pakistan, in 2003, M.S. degree from the University of Paris East Marne-la-Vallée, Paris, France, in 2005 and Ph.D. in Electronic and Communications Engineering from The University of Leeds, Leeds, U.K in 2010. In 2005, he was an Intern at Conservatoire national des arts et métiers, Paris, France. From 2007 to 2010 he was involved in establishing the LTCC fabrication facility at Institute of Microwave and Photonics, The University of Leeds, UK. His research interests involve multilayered-microwave device fabrication on LTCC and thick-film technology, RF antenna and antenna arrays, Ultra-Wideband diversity antennas and MEMS packaging. He is also involved in dielectric characterization of materials using microwave techniques and fabrication of ceramic microfluidic devices. He is the founding head of Microwave Components and Devices (MCAD) research group, Associate Professor and Associate Director at Center for Advanced Studies in Telecommunications (CAST).

Efficient Computation of SAR and Temperature Rise Distributions in a Human Head at Wide Range of Frequencies Due to 5G RF Field Exposure

Fatih Kaburcuk [1] and Atef Z. Elsherbeni [2]

[1] Electrical and Electronic Engineering Department
Erzurum Technical University, Erzurum, 25700, Turkey
fkaburcu@syr.edu – fatih.kaburcuk@erzurum.edu.tr

[2] Electrical Engineering Department
Colorado School of Mines, Golden, CO, 80401, USA
aelsherb@mines.edu

Abstract ─ In this paper, the effects of radio frequency electromagnetic fields produced by base stations on a human head are investigated with the aid of a multiphysics model at multiple frequencies using a single simulation. This multiphysics model is based on integrating the Debye model of human head dispersive tissues parameters into the finite-difference time-domain method by using the auxiliary differential equation approach and then calculating the specific absorption rate and temperature rise distributions in the head with the use of bioheat equation. The effects of frequency and incident angle of radio frequency electromagnetic fields on the specific absorption rate and temperature rise distributions in the head are analyzed.

Index Terms ─ Biologic effects of electromagnetic radiation, dispersive head, FDTD method, multiphysics model, specific absorption rate, temperature rise.

I. INTRODUCTION

In recent years, the number of the base stations mounted on towers and rooftops has increased with the use of mobile phones. As a consequence, it is important to consider the possible harmful effects on human tissues due to radio frequency (RF) electromagnetic fields by the base station antennas. The maximum permissible exposure limits from the base station antenna are determined for occupational and general public exposures. For the occupational exposure, RF worker needs to work very close to the base station antennas, whereas, for the public exposure, people received RF fields stay far away from the base station antennas. Many international protection organizations [1-3] have presented safety standards for limiting RF exposure. These standards have basic restriction and reference levels for occupational and public exposures which are dependent on the frequency ranges.

The thermal effect of the RF electromagnetic fields on a human head has been studied due to far-field [4-8] and near-field exposures [8-12] from different types of the antennas using the traditional finite-difference time-domain (FDTD) method. Additionally, several researchers have investigated the thermal effect on a human eye, one of the most sensitive organs in the human head for the RF field exposure, due to far-field exposure [13-16] and near-field exposure [16-18]. In the previous works [4-18], temperature rise and specific absorption rate (SAR) distributions in the human head or eye were calculated at only one frequency of interest in a single simulation because of frequency dependent of the electromagnetic properties of the biological tissues. Therefore, these distributions cannot be calculated for multiple frequencies of interest in a single simulation. A multiphysics model based on the FDTD method proposed in [19] allows to calculate these distributions at multiple frequencies in the human head due to a wideband antenna using a single FDTD simulation.

During the last few years, a fifth generation (5G) mobile communication has gained enormous popularity and extensive research interest. Its possible effects on a human head are not studied significantly. In this paper, the interaction between a human head and the RF electromagnetic fields due to the 5G base stations for the occupational and public exposures are investigated using the multiphysics model. Thus, SAR and temperature rise distributions in the head are obtained at possible operating frequencies of the 5G base stations using a single simulation. In this investigation, the frequency ranges of the RF electromagnetic fields radiated by the 5G base stations are 3.4-3.8 GHz and 4.4-4.9 GHz.

In the multiphysics model, the Debye model is integrated into the FDTD method using the auxiliary differential equation (ADE) as presented in [20], then the SAR and temperature rise with the use of Pennes bioheat equation [21] are calculated. In the Debye model, the three-term Debye coefficients (the relative permittivity

Submitted On: June 12, 2018
Accepted On: November 4, 2018

of medium at infinite frequencies, the static relative permittivity, and the relaxation time) calculated and tabulated in [22] are used as the dispersive EM properties of the human head tissues for a wide range of frequencies (500 MHz to 20 GHz).

In this paper, a realistic head model [23] under RF electromagnetic fields exposure due to the 5G base stations is analyzed to prove the validity of the multiphysics model. The SAR and temperature rise distributions in the head at multiple frequencies 3.4, 3.8, 4.4, and 4.9 GHz are calculated using the multiphysics model in a single simulation as well as using the traditional FDTD method in multiple simulations. The effect of incident angle of the RF fields on the SAR and temperature rise distributions in the head is also investigated.

II. MULTIPHYSICS MODEL

A. Human head model with dispersive tissues

A three dimensional realistic head model generated in [23] is used in this work. The head model used here consists of eight tissues (skin, muscle, bone, blood, fat, lens, and white and grey matter) and 172(width)× 208(depth)×240(height) cubic cells. In order to ensure the numerical stability in the FDTD method, the cell size should be less than $\lambda_{\min}/10$, where $\lambda_{\min}$ is the wavelength of the highest frequency in the head model. Therefore, the head model is divided into 0.9 mm cells in all directions to satisfy this criterion.

The complex relative permittivity $\left(\varepsilon_r^*(\omega)\right)$ for the three-term Debye coefficients is defined [22] as:

$$\varepsilon_r^*(\omega) = \varepsilon_\infty + \sum_{k=1}^{3} \frac{\Delta\varepsilon_k}{1 + j\omega\tau_k}. \tag{1}$$

where $\Delta\varepsilon_k = \varepsilon_{s_k} - \varepsilon_\infty$, ε_∞ is the relative permittivity at infinite frequencies, ε_{s_k} and τ_k are the static relative permittivity and the relaxation time constant of *k*th term, respectively. They were obtained using a numerical technique developed in [22] for the frequency range 500 MHz to 20 GHz.

B. FDTD method and incident plane wave

The RF electromagnetic fields radiated by the 5G base stations are considered as far-field sources generated somewhere outside of the FDTD problem domain. The FDTD problem domain involved the head model is illuminated by the incident plane wave produced from these sources. The power density of the incident plane wave are set to 50 W/m^2 and 10 W/m^2 which are maximum permissible exposure limits for occupational and public exposures [1-2], respectively. The incident plane wave is a Gaussian waveform containing each frequency of interest. The total-field/scattered-field formulation [20] used here generates the incident plane wave in the FDTD problem domain. The convolution perfect matching layer (CPML) [20] as an absorbing boundary is applied at the borders to truncate the FDTD problem domain.

C. SAR calculation

The RF energy absorbed per unit mass of biological tissue is defined as SAR. The spatial peak SAR value over any 1g tissue (SAR_{1g}) for the occupational and public exposures cannot be exceeded 8 and 1.6 W/kg [1], respectively. After EM simulation is done and the steady-state fields are achieved using the discrete Fourier transform (DFT), the magnitudes of the averaged *E* field components are used for the calculation of the steady-state SAR distribution at each frequency of interest. The SAR is defined at a given location as:

$$SAR(i,j,k) = \frac{\sigma(i,j,k)}{2\rho(i,j,k)}\left(\left|E_x(i,j,k)\right|^2 + \left|E_y(i,j,k)\right|^2 + \left|E_z(i,j,k)\right|^2\right), \tag{2}$$

where $\sigma(i,j,k)$ and $\rho(i,j,k)$ are the electric conductivity and mass density [kg/m^3] of the tissue at a given location, respectively. In equation (2), an averaging of E fields in all directions is performed to obtain the corresponding values at the exact location of interest. For calculating the peak SAR_{1g} in the head, the IEEE standard C95.3-2002 is considered [24]. These SAR_{1g} values are considered as RF heat source in the temperature rise calculation.

D. Temperature rise calculation

After the SAR_{1g} distribution in the head is calculated and recorded, the temperature analysis with the use of bioheat equation [21] is performed in two steps. In the first step, the steady-state temperature distribution in the head is calculated by solving the bioheat equation with no RF heat source (SAR_{1g}=0). In the second step, the final temperature distribution is calculated by substituting the SAR_{1g} distribution into the bioheat equation. The difference between the final and steady-state temperature distribution provides the temperature rise distribution in the head.

The bioheat equation is given by:

$$\rho \cdot C \cdot \frac{\partial T}{\partial t} = K \cdot \nabla^2 T + \rho \cdot SAR_{1g} - B \cdot \left(T - T_b\right), \tag{3}$$

where T is the temperature of the tissue at time t, ρ is the mass density of the tissue [kg/m^3], C is the heat capacity of the tissue [J/(kg·°C)], K is the thermal conductivity of the tissue [J/(m·°C)], B is the blood perfusion rate [W/(m^3.°C)], and T_b is the blood temperature. The convective boundary condition [9] for the bioheat equation in (3) applied to the external and internal surface of the human head is expressed as:

$$K \cdot \frac{\partial T}{\partial n} = -h \cdot \left(T - T_{air}\right), \tag{4}$$

where T_{air} is the air temperature, n is the unit normal

vector to the skin surface or internal cavity, and h is the convection heat transfer coefficient [W/(m^2·^{o}C)]. The finite difference approximation of the bioheat equation in (3) and the convective boundary condition in (4) is given in [19]. The mass density and thermal parameters of the head tissues are given in [19]. The convection heat transfer coefficients (h) is set to 10.5 between the skin surface and external air and 50 between the internal cavity surface and internal air [5]. The air temperature (T_{air}) and initial head temperature (T_b) were set to 20 and 37 ^{o}C, respectively. In order to ensure the numerical stability, the temperature time-step (Δt) must satisfy the following criterion [9]:

$$\Delta t \le \frac{2\rho C d^2}{12K + Bd^2}. \quad (5)$$

III. NUMERICAL RESULTS

In the first part of this section, the maximum SAR_{1g} and temperature rise in the head are calculated at 1.5 GHz using the multiphysics model and traditional FDTD method. The obtained results are compared with the results obtained in [5-6] in order to prove the validity of the multiphysics model. In the second part of this section, the effects of frequency and incident angle of the RF fields on the SAR and temperature rise distributions in the head are investigated using the multiphysics model. Finally, in the last part of this section, the performance of the multiphysics model is presented. The computer being used in this paper has Intel® Core™ i7-4790 CPU and 16 GB DDR RAM. The program is written and compiled in 64-bit MATLAB version 8.2.0.701 (R2013b). The total number of cells used in the simulations is 14,007,552.

A. Comparison of results obtained using the multiphysics model and traditional FDTD method

In order to confirm the validity of the multiphysics model, the maximum temperature rise and SAR_{1g} values in the head calculated at 1.5 GHz using the multiphysics model are compared with those obtained using the traditional FDTD method and those reported in [5-6] for the occupational and public exposures. In this simulation, the human head with a cell size of 2 mm is illuminated by a θ polarized plane wave with the incident angles of θ^{inc}=90^o and ϕ^{inc}=90^o (from the front to rear of the head). The comparison in Table 1 shows that the results obtained using the multiphysics model agree very well with the results obtained using the traditional FDTD method. It is also realized that the maximum SAR_{1g} value in the head is reasonably in good agreement whereas the maximum temperature rise in the head is slightly different with those reported in [5-6]. The reason for the difference in the compared results is due to the use of different head model.

Table 1: Comparison of maximum SAR_{1g} and maximum temperature rise in the head at 1.5 GHz

Exposure Type	Methods	Max. SAR_{1g} (W/kg)	Max. Temp. Rise (°C)
Occupation RF Exposure	Multiphysics model	5.55	0.49
	Traditional FDTD	5.55	0.49
	Reported in [5]	**5.62**	**0.35**
Public RF Exposure	Multiphysics model	1.11	0.09
	Traditional FDTD	1.11	0.09
	Reported in [6]	**1.12**	**0.069**

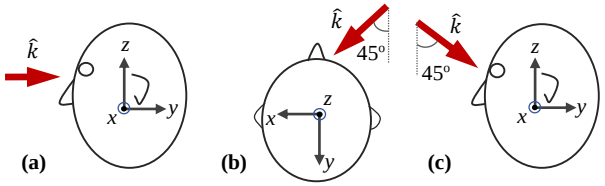

Fig. 1. (a) Front, (b) front-right, and (c) front-above.

B. Effect of frequencies and incident angles on the SAR and temperature rise distributions in the head

The temperature rise and SAR_{1g} distributions in the head due to the occupational RF field exposure are calculated using the multiphysics model at 5G frequencies below 6 GHz (3.4, 3.8, 4.4, and 4.9 GHz) in a single simulation. In order to excite the human head, a θ polarized plane wave is considered with three different incident angles: first is called front incident with the angles of θ^{inc}=90^o and ϕ^{inc}=90^o, second is called front-right incident with the angles of θ^{inc}=90^o and ϕ^{inc}=45^o, and third is called front-above incident with the angles of θ^{inc}=135^o and ϕ^{inc}=90^o, as shown in Fig. 1.

For the front incident, the SAR_{1g} and resulting temperature rise distributions in the x-y cross section of the head model at the listed frequencies are shown in Fig. 2. For the front-right and front-above incidence, the SAR_{1g} and resulting temperature rise distributions in the x-y cross section of the head model at the listed frequencies are shown in Figs. 3-4, respectively. It can be realized from the figures that SAR_{1g} distributions are correlated well with the temperature rise in the head. It can be seen from Fig. 3 that the SAR_{1g} and temperature rise values in the right eye are higher than those in the left eye because the nose prevents the RF fields from penetrating in the left eye. The electric conductivities of the tissues become larger as the frequency is increased, then the magnitude of EM waves in the head decreases exponentially. Therefore, the SAR_{1g} and resulting temperature rise values in the head decrease at higher frequencies.

The maximum SAR_{1g} value and temperature rise in the head at the listed frequencies are shown in Table 2 for front, front-right, and front-above incidence. It is realized that the maximum values of the SAR and temperature rise obtained from the front-above incident are smaller than those obtained from other two incidence. The maximum temperature rise and SAR_{1g} in the head are less than 1 ^{o}C and 8 W/kg for the occupational exposure, respectively.

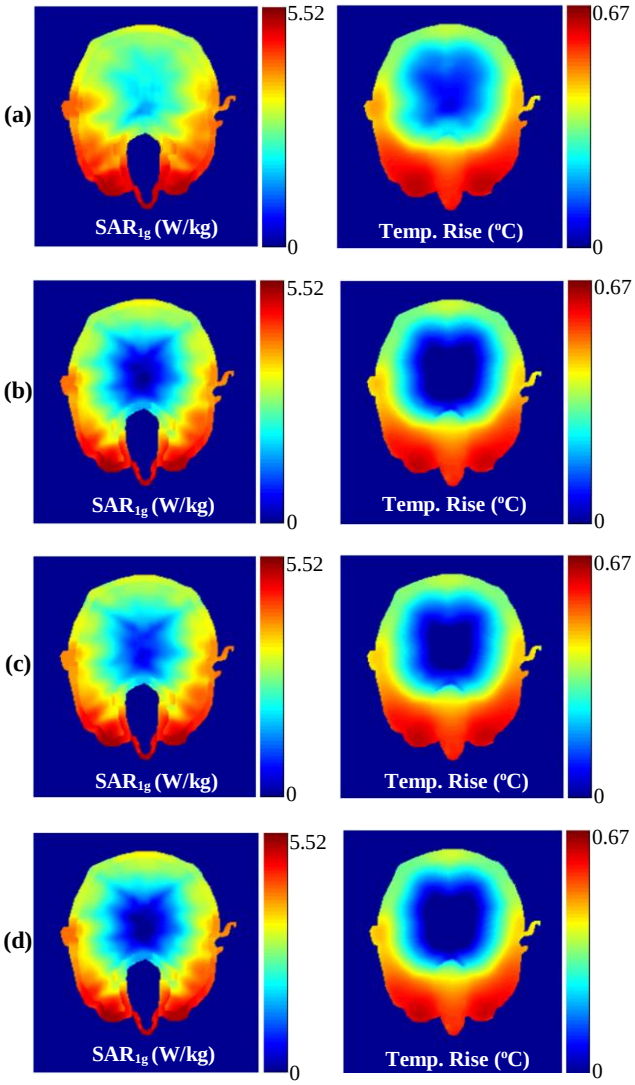

Fig. 2. SAR_{1g} and temperature rise distributions due to front incident at: (a) 3.4, (b) 3.8, (c) 4.4, and (d) 4.9 GHz.

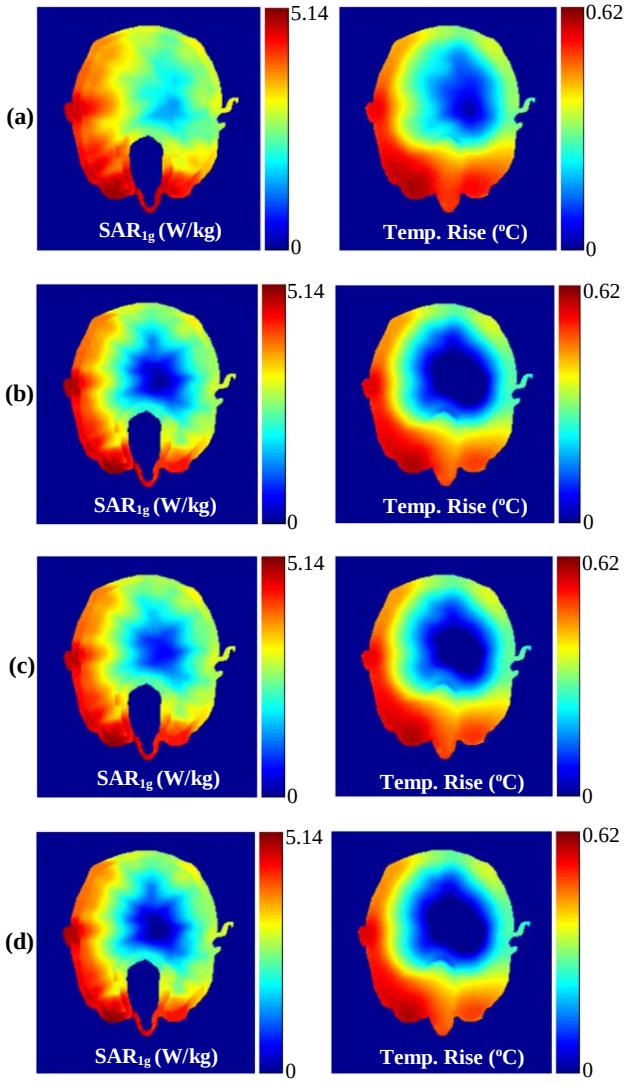

Fig. 3. SAR_{1g} and temperature rise distributions due to front-right incident at: (a) 3.4, (b) 3.8, (c) 4.4, and (d) 4.9 GHz.

The maximum temperature variation in the head at 3.4 GHz as a function of time is shown in Fig. 5 for the front, front-right, and front-above incidence. It can be seen from Fig. 5 that the temperature increases rapidly over the first 6 minutes, then temperature increase slows down, and the maximum (steady-state) temperature is reached after 30 minutes of exposure. The temperature rise due to the RF electromagnetic fields exposure is not significantly much to change the EM and thermal properties of the tissues.

Table 2: Maximum SAR_{1g} and temperature rise at listed frequencies for three different incidence

Freq.	**Max. SAR_{1g} (W/kg)**			**Max. Temperature Rise (°C)**		
(GHz)	Front	Front-right	Front-above	Front	Front-right	Front-above
3.4	5.52	5.14	2.98	0.67	0.62	0.37
3.8	4.01	3.66	2.99	0.56	0.45	0.31
4.4	3.33	4.08	3.16	0.45	0.49	0.31
4.9	3.24	3.65	2.82	0.44	0.43	0.31

C. Performance of multiphysics model

The SAR_{1g} and temperature rise values at the listed frequencies obtained using the multiphysics model in a single simulation are found to be exactly the same as those obtained using the traditional FDTD method using multiple simulations. The complexity of the traditional FDTD method [20] is less than that of the multiphysics model. However, the traditional FDTD method provides solutions at a single frequency in a single simulation because of frequency dependent of the biological tissues, whereas the multiphysics model can provide solutions at multiple frequencies using a single simulation. To show the performance of the multiphysics model, the relative percentage time saving between the multiphysics model and the traditional FDTD method is shown in Fig. 6 when the number of frequencies of interest is increased.

The relative percentage of CPU time saving between the multiphysics model and the traditional FDTD method is defined as:

$$t_{saving} = \left(\frac{t_{FDTD} - t_{multiphysics}}{t_{FDTD}} \right) \times 100\%, \qquad (6)$$

where $t_{multiphysics}$ and t_{FDTD} are the computation time of multiphysics model and the traditional FDTD method, respectively. It is realized that the multiphysics model is more efficient than the traditional FDTD method while obtaining solutions at more than one frequency. The solutions at frequencies above 20 GHz can be obtained using the multiphysics model once the three-term Debye coefficients of the tissues are determined using a numerical technique similar to that developed in [22].

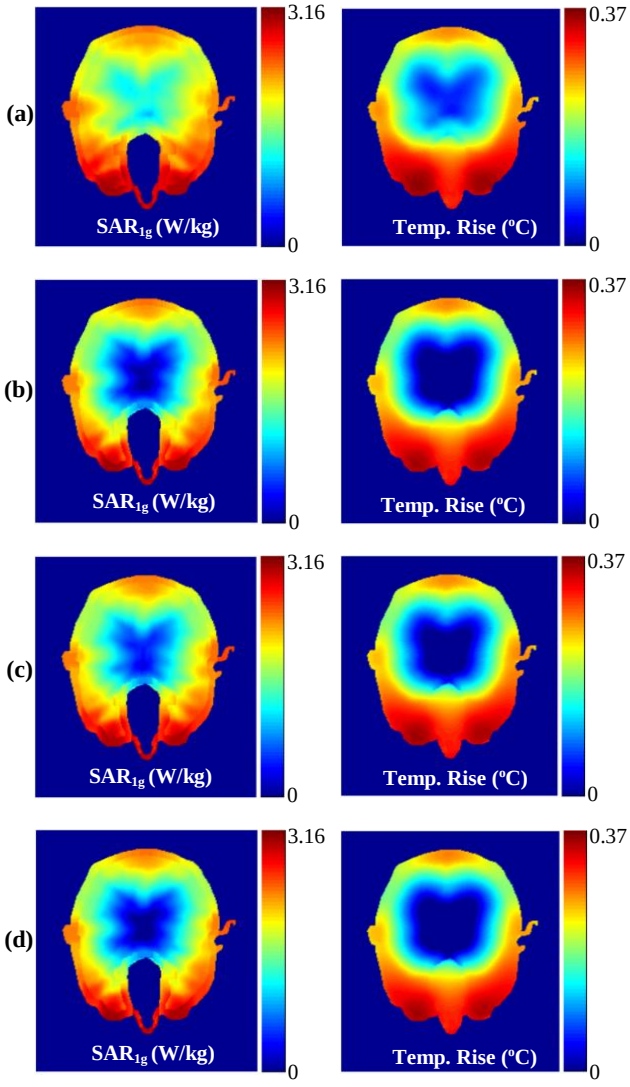

Fig. 4. SAR_{1g} and temperature rise distributions due to front-above incident at: (a) 3.4, (b) 3.8, (c) 4.4, and (d) 4.9 GHz.

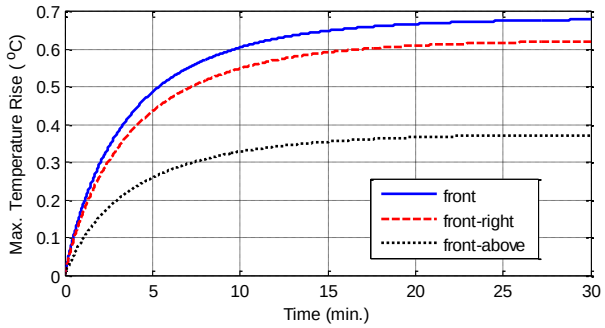

Fig. 5. Maximum temperature rise in the head at 3.4 GHz for front, front-right, and front-above incidence.

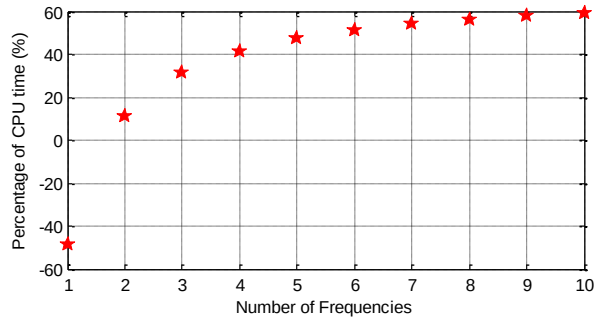

Fig. 6. Relative percentage of CPU time saving.

IV. CONCLUSION

The interaction between a dispersive human head and RF electromagnetic fields radiated by 5G base station is investigated using the multiphysics model at multiple frequencies in a single simulation. The SAR_{1g} and resulting temperature rise distributions in the head are calculated at 5G frequencies (3.4, 3.9, 4.4, and 4.9 GHz) in a single simulation with the use of multiphysics model. Numerical results show that the SAR_{1g} and temperature rise distributions in the human head are dependent on the frequency and incident angle of the RF fields. It is also realized that the maximum SAR_{1g} and temperature rise values occur in the eyes of the head. The multiphysics model provides remarkable saving in the computation time when the analysis is performed at more than one frequency.

REFERENCES

[1] Federal Communications Commission, "Evaluating compliance with FCC guidelines for human exposure to radio frequency electromagnetic fields," Rep., Washington, DC, Tech. Rep. OET Bull. 65, 1997.

[2] International Commission on Non-Ionizing Radiation Protection (ICNIRP), "Guidelines for limiting exposure to time-varying electric, magnetic,

and electromagnetic fields (up to 300 GHz)," *Health Phys.*, vol. 74, pp. 494-522, 1998.

[3] IEEE C95.1. IEEE standard for safety levels with respect to human exposure to radio frequency electromagnetic fields, 3 kHz to 300 GHz, IEEE Standard C95.1-2005, 2006.

[4] Y. Lu, J. Ying, T-K. Tan, and K. Arichandran, "Electromagnetic and thermal simulations of 3-D human head model under RF radiation by using the FDTD and FD approaches," *IEEE Transactions on Magnetics*, vol. 32, no. 3, pp. 1653-1656, 1996.

[5] O. Fujiwara, M. Yano, and J. Wang, "FDTD computation of temperature rise inside a realistic head model for 1.5-GHz microwave exposure," *Electron. Comm. Jpn. Pt. I*, vol. 82, no. 3, pp. 240-247, 1999.

[6] M. Yano, J. Wang, and O. Fujiwara, "FDTD computation of temperature rise in a realistic head models simulating adult and infant for 1.5-GHz microwave exposure," *Electron. Comm. Jpn. Pt. I*, vol. 84, no. 4, pp. 57-66, 2001.

[7] I. Laakso, "Assessment of the computational uncertainty of temperature rise and SAR in the eyes and brain under far-field exposure from 1 to 10 GHz," *Physics in Medicine and Biology*, vol. 54, pp. 3393-3404, 2009.

[8] S. Kodera, J. Gomez-Tames, and A. Hirata, "Temperature elevation in the human brain and skin with thermoregulation during exposure to RF energy," *BioMedical Engineering Online*, vol. 17, no. 1, pp. 1-17, Jan. 2018.

[9] J. Wang and O. Fujiwara, "FDTD computation of temperature rise in the human head for portable telephones," *IEEE Trans. Microwave Theory Tech.*, vol. 47, pp. 1528-1534, Aug. 1999.

[10] P. Bernardi, M. Cavagnaro, S. Pisa, and E. Piuzzi, "Specific absorption rate and temperature increases in the head of a cellular-phone user," *IEEE Trans. Microwave Theory Tech.*, vol. 48, pp. 1118-1126, July 2000.

[11] P. Bernardi, M. Cavagnaro, S. Pisa, and E. Piuzzi, "Power absorption and temperature elevations induced in the human head by a dual-band monopole-helix antenna phone," *IEEE Trans. Microwave Theory Tech.*, vol. 49, no. 12, pp. 2539-2546, Dec. 2001.

[12] A. Hirata, M. Morita, and T. Shiozawa, "Temperature increase in the human head due to a dipole antenna at microwave frequencies," *IEEE Trans. Electromag. Compat.*, vol. 45, no. 1, pp. 109-116, Feb. 2003.

[13] A. Hirata, G. Ushio, and T. Shiozawa, "Calculation of temperature rises in the human eye exposed to EM waves in the ISM frequency bands," *IEICE Trans. Commun.*, vol. E83-B, no. 3, pp. 541-548, Mar. 2000.

[14] A. Hirata, S. Matsuyama, and T. Shiozawa, "Temperature rise in the human eye exposed to EM waves in the frequency range 0.6-6 GHz," *IEEE Trans. Electromag. Compat.*, vol. 42, no. 4, pp. 386-393, Nov. 2000.

[15] A. Hirata, H. Watanabe, and T. Shiozawa, "SAR and temperature increase in the human eye induced by obliquely incident plane waves," *IEEE Trans. Electromag. Compat.*, vol. 44, no. 4, pp. 592-594, Nov. 2002.

[16] A. Hirata, "Temperature increase in human eyes due to near-field and far-field exposures at 900 MHz, 1.5 GHz, and 1.9 GHz," *IEEE Trans. Electromag. Compat.*, vol. 47, no. 1, pp. 68-76, Feb. 2005.

[17] P. Bernardi, M. Cavagnaro, S. Pisa, and E. Piuzzi, "SAR distribution and temperature increase in an anatomical model of the human eye exposed to the field radiated by the user antenna in a wireless LAN," *IEEE Trans. Microwave Theory Tech.*, vol. 46, no. 12, pp. 2074-2082, Dec. 1998.

[18] C. Buccella, V. D. Santis, and M. Feliziani, "Prediction of temperature increase in human eyes due to RF sources," *IEEE Trans. Electromag. Compat.*, vol. 49, no. 4, pp. 825-833, Nov. 2007.

[19] F. Kaburcuk and A. Z. Elsherbeni, "Temperature rise and SAR distribution at wide range of frequencies in a human head due to an antenna radiation," *ACES Journal*, vol. 33, no. 4, pp. 367-372, April 2018.

[20] A. Z. Elsherbeni and V. Demir, *The Finite-Difference Time-Domain Method for Electromagnetics with MATLAB Simulations*, second edition, ACES Series on Computational Electromagnetics and Engineering, SciTech Publishing, an Imprint of IET, Edison, NJ, 2016.

[21] H. H. Pennes, "Analysis of tissue and arterial blood temperature in resting forearm," *J. Appl. Physiol.*, vol. 1, pp. 93-122, 1948.

[22] M. A. Eleiwa and A. Z. Elsherbeni, "Debye constants for biological tissues from 30 Hz to 20 GHz," *ACES Journal*, vol. 16, no. 3, pp. 202-213, Nov. 2001.

[23] http://noodle.med.yale.edu/zubal/ [Online website 2017].

[24] *IEEE Recommended Practice for Measurements and Computations of Radio Frequency Electromagnetic Fields With Respect to Human Exposure to Such Fields, 100 kHz-300 GHz*, IEEE Standard C95.3-2002, Annex E, 2002.

Fatih Kaburcuk received both the M.Sc. and Ph.D. degrees in Electrical Engineering from Syracuse University, Syracuse, New York, USA, in 2011 and 2014, respectively. He was a visiting research scholar in the Electrical Engineering Department at Colorado School of Mines in 2014. Currently, Kaburcuk is an Assistant Professor at the Department of Electrical and Electronics Engineering at Erzurum Technical University, Turkey. His research interest includes numerical methods in electromagnetics, bioelectromagnetic, and microwave systems.

Atef Z. Elsherbeni received his Ph.D. degree in Electrical Engineering from Manitoba University, Winnipeg, Manitoba, Canada, in 1987. Elsherbeni was with the University of Mississippi from 1987 to 2013. He was a Finland Distinguished Professor from 2009 to 2011. He joined the Electrical Engineering and Computer Science Department at Colorado School of Mines in August 2013 as the Dobelman Distinguished Chair Professor. His research interest includes the scattering and diffraction of EM waves, finite-difference time-domain analysis of antennas and microwave devices, field visualization and software development for EM education, interactions of electromagnetic waves with the human body, RFID and sensor integrated FRID systems, reflector and printed antennas and antenna arrays, and measurement of antenna characteristics and material properties. His academic achievements includes: Funded Research Grants with a total amount of $11,413,903, 13 books, 29 book chapters, 171 journal publications, 15 developed software packages, 56 (35 M.S. and 21 Ph.D.) graduate students advised, 40 invited presentations, 221 proceedings publications, 174 conference abstracts, 74 technical reports, 35 short courses offered, 43 invited talks. Elsherbeni is a Fellow Member of IEEE and ACES. He is the Editor-in-Chief for ACES Journal. He was the General Chair for the 2014 APS-URSI Symposium and was the President of ACES Society from 2013 to 2015.

A Novel Adaptive Tracking Algorithm for the Resonant Frequency of EMATs in High Temperature

Xiaojuan Jia [1], Qi Ouyang *[1], Tao Zhang [1], and Xinglan Zhang [2]

[1] School of Automation
Chongqing University, Chongqing 400044, China
jiaxiaojuan@cqu.edu.cn, yangqi@cqu.edu.cn

[2] Department of Computer Science and Engineering
Chongqing University of Technology, Chongqing 400050, China
zxlan@cqut.edu.cn

Abstract ─ Resonant frequency drift of electro-magnetic acoustic transducers (EMATs) is a common phenomenon in high temperature, resulting in a low conversion efficiency. In this work, for tracking the resonant frequency of EMATs automatically, a novel adaptive radial basis function neural network (RBFNN) with guaranteed transient is proposed. First, the configuration and dynamic behavior of EMATs are introduced at room temperature. Then, the initial system under the constraint of transient performance index is converted into a new unconstrained equivalent system by the error conversion mechanism. Furthermore, the adaptive tracking control for the resonant frequency is analyzed in detail. Finally, the validity and effectiveness of the proposed novel method are verified by numerical simulations.

Index Terms ─ Adaptive neural network, EMATs, RBFNN, resonant frequency, transient performance.

I. INTRODUCTION

At present, the nondestructive evaluation (NDE) methods are mainly electromagnetic acoustic transducers (EMATs) and eddy current (EC) testing in high temperature [1-4]. However, the EC testing method is only suitable for the detection of the surface or near-surface of metallic materials. Due to the non-contact and couple-free features, EMATs are used widely in industry, biomedical science and other high temperature environment, such as the solidified shell and absorber tubes of solar power [5-6]. At room temperature, the influence of temperature on the resonant frequency of EMATs is small enough to be ignored. However, the conversion efficiency will be effected under high temperature, while leading to the resonant frequency drift. For instance, the surface temperature of solidified shell directly radiates to EMATs, causing the temperature of EMATs to rise sharply. In addition, the vibration of the solidified shell contributes to the variation of lift-off distance. These factors have a great influence on the electric parameters of EMATs, such as inductance, capacitance, and resistance [7].

Therefore, under high temperature, the resonance frequency will drift, which makes the EMAT matched in the initial state mismatches again. Furthermore, this will cause the power loss and seriously fever of EMATs, thus greatly decrease the conversion efficiency and damage the drive circuit. Hence, it is better to drive EMATs at its resonant frequency under high temperature as the maximum power conversion is achieved at this point. It is urgent to find a method to realize non-error tracking resonant frequency.

To date, various tracking methods have been proposed to track the working frequency around the resonant frequency, such as phase-locked automatic tracking methods, audio tracking methods, and electric tracking methods. Qu et al. proposed a strategy combining the orthogonal correlation method and PID control algorithm, which realizes the frequency tracking and vibration stabilization of transducers [8-9]. Tang et al. adopt a frequency automatic tracking scheme, which combines with the current method and phase method to achieve the resonance frequency control [10]. Zhang et al. used a binary search algorithm to track the resonance frequency in the specified search range and fuzzy logic method was combined to improve the tracking algorithm performance [11]. However, the studies on resonance frequency tracking mainly focus on the piezoelectric ultrasonic transducer. For EMATs, there is almost no literature with respect to the resonance frequency tracking used in high temperature environment.

In this paper, the aim is to present a novel adaptive

Submitted On: January 19, 2017
Accepted On: September 29, 2018

neural network (NN) method, which can automatically track the resonance frequency and maintain the stability of EMATs. Firstly, the dynamic impedance characteristic of EMATs is analyzed, and the impedance matching is deduced at the room temperature. Then, an adaptive NN control scheme is presented. To improve the accuracy and performance of the tracking algorithm, an improved method combined with transformation mechanism of transient performance index is proposed to track the resonance frequency of EMATs system in a varying temperature. Finally, numerical simulations verify that the improved scheme can perfectly track the resonance frequency while achieving a perfect transient performance of EMAT systems.

II. DYNAMIC BEHAVIOR OF EMATs

Figure 1 (a) illustrates the configuration of an EMAT, which composes of a spiral coil, a cylindrical magnet placed vertically and a metallic specimen. To obtain a higher energy efficiency, the EMAT generally driven by an external high-frequency excitation power.

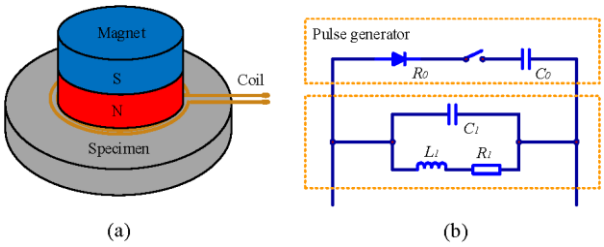

Fig. 1. (a) The configuration and (b) equivalent circuit of an EMAT.

An EMAT system at frequencies near resonance can be modeled as a simple equivalent circuit, as showed in Fig. 1 (b), which consists of a coil circuit and a driving circuit of the pulse generator. The coil equivalent circuit is a parallel RLC (Resistor-Capacity-Inductor) resonant circuit that includes three components, i.e., the equivalent resistance R_1, equivalent distributed capacitance C_1 and equivalent inductance L_1. The driving equivalent circuit consists of the internal resistance of signal source R_0 and capacitance C_0 of the signal source port. Since the connection wire of the coil and signal source is short, thus the capacitance value is small and neglected in this work. Based on the equivalent circuit of EMATs, the admittance can be written as:

$$Y = G + Bj = \frac{R_1}{R_1^2 + (\omega L_1)^2} + \left(\omega C_1 + \frac{\omega L_1}{R_1^2 + (\omega L_1)^2} \right) j , \quad (1)$$

where ω is the angular frequency. G and B denote the conductance and susceptance, respectively, which can be calculated as:

$$G = \frac{R_1}{R_1^2 + (\omega L_1)^2} , \quad (2)$$

$$B = \omega C_1 + \frac{\omega L_1}{R_1^2 + (\omega L_1)^2} . \quad (3)$$

Based on Eqs. (2) and (3), the following equation can be obtained:

$$\left(G - \frac{1}{2R_1} \right)^2 + (B - \omega C_1)^2 = \left(\frac{1}{2R_1} \right)^2 . \quad (4)$$

The admittance locus of EMATs can be described as a circle, whose center is in $(1/2R_1, \omega C_1)$ and radius is $1/2R_1$, as shown in Fig. 2. f_m is the frequency corresponding to the maximum admittance or minimum impedance. f_p is the parallel resonance frequency corresponding to the maximum conductance, which can be calculated as:

$$f_p = \frac{1}{2\pi\sqrt{L_1 C_1}} . \quad (5)$$

In addition, f_r and f_a are also important marked frequency, which are the resonance frequency of the whole system, with zero phase. When f_m, f_p, f_r are equal to each other, the best resonance performance can be obtained. In this work, f_r is defined as the tracking target because the impedance phase is easily measured relatively in the operation process of EMATs.

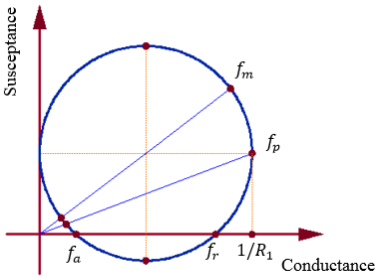

Fig. 2. The admittance locus diagram of EMATs.

To obtain the maximum energy and minimum impedance phase, the impedance matching of coil circuit is required. Hao et al. [4] proposed that the method of coil impedance matching is to parallel a proper capacitor on both ends of the coil. For a better effect, the circuit is matched by series capacitance and shunt inductance in this work. The total impedance after electrical matching can be expressed as:

$$Y_s = G_s + B_s j = \frac{R_1}{R_1^2 + (\omega L_1)^2} + \left[\left(\omega C_m - \frac{1}{\omega L_S} \right) + \frac{\omega L_1}{R_1^2 + (\omega L_1)^2} \right] j , \quad (6)$$

where C_m is the sum of the matching capacitance and

C_1, and L_S is the matching inductance.

The conductance G_s and susceptance B_s are:

$$G_s = \frac{R_1}{R_1^2 + (\omega L_1)^2}, \tag{7}$$

$$B_S = (\omega C_m - \frac{1}{\omega L_S}) + \frac{\omega L_1}{R_1^2 + (\omega L_1)^2}. \tag{8}$$

Based on Eqs. (7) and (8), when

$$\omega C_{\mathrm{m}} - \frac{1}{\omega L_S} = 0, \tag{9}$$

we get,

$$\left(G_s - \frac{1}{2R_1}\right)^2 + (B_s)^2 = \left(\frac{1}{2R_1}\right)^2. \tag{10}$$

Near the resonance frequency, the transducer admittance locus after impedance matching is a circle with the center of $(1/2R_1, 0)$ and radius of $1/2R_1$. Thus, the admittance circle is symmetrical about the conductance-axis, indicating that the f_p, f_m and f_r are equal to each other, respectively. At that moment, the best resonant characteristics can be achieved. When the initial frequency f_0 is given, the relationship between the matching inductance and capacitance is:

$$C_m = \frac{1}{4\pi^2 f_0^2 L_s}. \tag{11}$$

Therefore, the desired results can be achieved if C_m and L_s are selected appropriately.

III. ADAPTIVE TRACKING CONTROL

Intuitively, the adaptive controller can adapt to the dynamic characteristics of the control object and disturbance by changing its parameters automatically. More importantly, this control method is suitable for the unknown or time-varying parameters, do not need to know the mathematical model of controlled object. In many schemes, the system is usually assumed to be affine, i.e., the system is linear with respect to the control input [12-13]. However, most of the actual systems, such as the chemical reaction [14], aircraft systems [15] and EMATs system to study in this work, are non-affine, which has no affine appearances of control input. Therefore, designing an adaptive tracking method for EMATs is a meaningful and challenging problem.

A. Mathematical model of EMATs

Based on Eqs. (7) and (8), the impedance phase θ can be evolved by:

$$\theta = \tan^{-1}\left(-\frac{B_s}{G_s}\right) = \tan^{-1}\left[\frac{\left(L_1^2 - C_m L_s R_1^2 - L_1 L_s\right)\omega}{L_s R_1} - \frac{C_m L_1^2 \omega^3}{R_1} + \frac{R_1}{L_s \omega}\right]. \tag{12}$$

Defining,

$$\theta = f(\omega, L_1, C_1, R_1) = F(\omega, T, h), \tag{13}$$

where ω, L_1, C_1, R_1 are the angular frequency, equivalent inductance, equivalent distributed capacitance and equivalent resistance, respectively. Differentiating Eq. (13) with respect to time, we get:

$$\dot{\theta} = \frac{\partial F}{\partial \omega}\dot{\omega} + \frac{\partial F}{\partial T}\dot{T} + \frac{\partial F}{\partial h}\dot{h}. \tag{14}$$

The control input ω that we design is produced by a low pass filter driven by the input v [16], it can be expressed by:

$$\dot{\omega} = -\mathrm{a}\omega + v, \tag{15}$$

where $\mathrm{a} \in R^+$ is a design parameter. By substituting Eq. (15) to (14), we get:

$$\begin{aligned}\dot{\theta} &= \frac{\partial F}{\partial \omega}(-\mathrm{a}\omega + v) + \frac{\partial F}{\partial T}\dot{T} + \frac{\partial F}{\partial h}\dot{h} \\ &= \frac{\partial F}{\partial \omega}v - \mathrm{a}\frac{\partial F}{\partial \omega}\omega + \frac{\partial F}{\partial T}\dot{T} + \frac{\partial F}{\partial h}\dot{h} \\ &= \mathrm{g}(\omega)v + H(\omega, T, h),\end{aligned} \tag{16}$$

where $\mathrm{g}(\omega) = \frac{\partial F}{\partial \omega}$, $H(\omega, T, h) = -\mathrm{a}\frac{\partial F}{\partial \omega}\omega + \frac{\partial F}{\partial T}\dot{T} + \frac{\partial F}{\partial h}\dot{h}$. In Section IV.B, the sign of $\mathrm{g}(\omega)$ is proved to be greater than 0. While $H(\omega, T, h)$ is an unknown function.

B. Adaptive tracking control

Radial basis function neural network (RBFNN) can approximate any nonlinear functions and deal with the regularity of systems, which has a good generalization ability and learning convergence rate. It has three layers, that is, the input, hidden and output layers. The hidden layer is for nonlinear transformation between the input and output. The input are mapped to the hidden layer, then the hidden layer nodes are linearly summed to get the output.

Based on the universal approximation property of RBFNN [17], the unknown function $H(\omega, T, h)$ can be approximated as:

$$\mathrm{H}(Z) = W^T \varnothing(Z) + \eta(\mathrm{Z}), \tag{17}$$

where W is an unknown and constant weight vector of the output layer, $\varnothing(Z)$ is the so-called radial basis function in hidden layer nodes, $\mathrm{Z} = [\omega, T, h]^T$ is the input vector of RBFNN, $\eta(\mathrm{Z})$ is the corresponding reconstruction error.

In terms of above analysis, the EMAT system can be abstracted as a second order nonlinear system, whose mathematical model can be expressed by:

$$\begin{cases} \dot{\omega} = -\mathrm{a}\omega + v \\ \dot{\theta} = \mathrm{g}(\omega)v + H(Z) \end{cases}, \tag{18}$$

where the input ω of the initial system and v are

considered as the state and input of the new system respectively. Noted that this is an augmented system. Therefore, the main goal is to stabilize the new system and maintain zero impedance phase. Thence, the implementable controller is proposed as:

$$v = -K\theta - \hat{W}^T \varnothing(Z). \tag{19}$$

The update law of $\hat{W}$ is determined as:

$$\dot{\hat{W}} = -\sigma_1 \hat{W}|\theta| + \sigma_2 \theta \varnothing(Z), \tag{20}$$

where $K > 0$, $\sigma_1 > 0$, $\sigma_2 > 0$ are free design parameters. $\hat{W}^T$ is the estimation of W^T and $\hat{W}^T \varnothing(Z) = \hat{H}(Z)$ is the estimation of $H(Z)$. The estimation error is defined as $W = W - \hat{W}$. Controller parameters are set as $a = 1$, $K = 3550$, $\sigma_1 = 2$, $\sigma_2 = 10$.

Based on the analysis Lyapunov theory, W and θ are both uniformly ultimately bounded (UUB) [22]. Since $W = W - \hat{W}$ and W is bounded, so that $\hat{W}$ is UUB. In addition, in accordance with that $\varnothing(Z)$ of RBFNN is bounded and Eq. (19), v is proved UUB. Furthermore, the input ω of the initial system is considered to be a stable linear time-invariant system driven by v. Since v is bounded, we can conclude that the control signal ω is bounded based on the BIBO (Bounded-Input Bounded-Output) property of linear time invariant systems. Thus, all states of the EMAT system have been proved to be bounded.

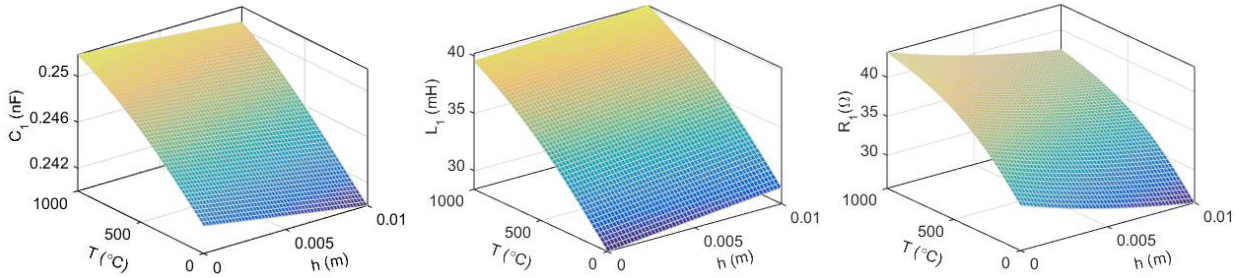

(a) (b) (c)

Fig. 3. (a) Capacitance, (b) inductance, and (c) resistance varying with temperature and lift-off distance.

C. Improved adaptive tracking control

The stability of systems is usually considered in the design of adaptive controllers, rarely involving the transient performance. However, many systems need to preset the transient performance index to ensure the effectiveness of systems [17]. For EMAT systems, if the impedance phase is too large, the system output will be small, resulting in inefficient generation and transmission of ultrasonic waves. The low energy conversion efficiency seriously affects the accuracy and efficiency of NDE. Therefore, we propose an improved method considering the transient performance index, which transforms the constrained transient performance index into a non-constrained error function. Furthermore, the error satisfies the preset transient performance index by proving the boundedness of the conversion error [18].

The impedance phase θ is limited within two curves to ensure it is not too large [16]:

$$-\underline{\alpha}\rho(t) < \theta(t) < \bar{\alpha}\rho(t), t \geq 0, \tag{21}$$

where $\underline{\alpha}, \bar{\alpha} \geq 0$ are the pre-set range. $\rho(t)$ is a performance function, which is smooth and belongs to $\{\rho(t): R_+ - \{0\}\}$. $\rho(0) = \rho_0, \rho(\infty) = \rho_\infty$. Based on the demands of different systems on the transient performance, different $\rho(t)$ is chosen to meet the requirement of rising time and error convergence rate. $\underline{\alpha}, \bar{\alpha}$ are assigned different values to meet the vibration error and overshoot. Then, the initial system under the constraint of transient performance index is converted into a new unconstraint one by the error transformation. We define:

$$\theta(t) = \rho(t) S(\varepsilon), \tag{22}$$

where $S(\cdot)$ is a strictly increasing smooth function, ε is the transform error, which can be written as:

$$\varepsilon = S^{-1}\left(\frac{\theta}{\rho}\right) = \frac{1}{2}\ln\left[\frac{\bar{\alpha}(\theta/\rho) + \bar{\alpha}\underline{\alpha}}{\bar{\alpha}\underline{\alpha} - \underline{\alpha}(\theta/\rho)}\right]. \tag{23}$$

Differentiating Eq. (23) with respect to time we get:

$$\dot{\varepsilon} = r\dot{\theta} + m\theta, \tag{24}$$

where $r = \frac{\partial S^{-1}}{\partial(\theta/\rho)} = \frac{1}{2}\left(\frac{\bar{\alpha}}{\bar{\alpha}\theta + \bar{\alpha}\underline{\alpha}\rho} + \frac{\underline{\alpha}}{\bar{\alpha}\underline{\alpha}\rho - \underline{\alpha}\theta}\right)$, and $m = -\frac{1}{2}\left(\frac{\bar{\alpha}\dot{\rho}}{\bar{\alpha}e\rho + \bar{\alpha}\underline{\alpha}\rho^2} + \frac{\underline{\alpha}\dot{\rho}}{\bar{\alpha}\underline{\alpha}\rho^2 - \underline{\alpha}e\rho}\right)$.

Substituting Eqs. (13) and (16) into Eq. (24):

$$\dot{\varepsilon} = rgv + rH + mF. \tag{25}$$

Let,

$$J(Z) = rH + mF. \tag{26}$$

Thence, the mathematical model of EMAT systems after error transformation is expressed as:

$$\begin{cases} \dot{\omega} = -a\omega + v \\ \dot{\varepsilon} = rgv + J(Z) \end{cases}, \tag{27}$$

where $Z = [\omega, T, h]^T \in R^3$ is the observable state. r is a design parameter. Since the unknown nonlinear part

of systems can be estimated by RBFNN, the unknown function $J(Z)$ can be written as:

$$J(\mathrm{Z}) = P^T \varnothing(Z) + \mu(\mathrm{Z}), \quad (28)$$

where P is an unknown and constant weight vector, $\varnothing(Z)$ is the radial basis function of hidden layer nodes, $\mu(\mathrm{Z})$ is the estimation error. The control input of the transformed system can be expressed as:

$$v = -\frac{1}{r}\left[\mathrm{k}\varepsilon + \hat{P}^T \varnothing(Z)\right]. \quad (29)$$

The update law is expressed as:

$$\dot{\hat{P}} = -\tau_1 \hat{P}|\varepsilon| + \tau_2 \varepsilon \varnothing(Z), \quad (30)$$

where $\mathrm{k} > 0, \tau_1 > 0, \tau_2 > 0$ are free design parameters, $\hat{P}^T$ is the estimation of P^T and $\hat{P}^T \varnothing(Z) = \hat{J}(Z)$ is the estimation of $J(Z)$. Then, the estimation error of P is defined as $P = P - \hat{P}$. The controller parameters are set as $\tau_1 = 2$, $\tau_2 = 100$, $\rho(0) = 1.01$, $\rho(\infty) = 0.01$. All states of the transformed system are also proved to be bounded by the same method as Section III.B.

IV. SIMULATION ANALYSIS

A. Contributions of T and h to $\mathbf{L_1}$, $\mathbf{C_1}$ and $\mathbf{R_1}$

It is well known that L_1, C_1 and R_1 are changing along with temperature (T) and lift-off distance (h), and the variation law is shown in Fig. 3, in which T ranges from 0 to 1000°C, and h from 0 to 0.01m.

As can be seen from Fig. 3, L_1, C_1 and R_1 increase nonlinearly with T increases. For instance, as T varies from 25 to 500°C, corresponding to R_1 changing from 21.04 to 35.72 Ω, as shown in Fig. 3 (c). C_1 and R_1 decrease as h increases, while L_1 increases sharply with the increase of h. In addition, the variation law is similar to the exponential law. Hao etc. has given a clear physical explanation about the variation of electric parameters with h [4]. When h between the coil and specimen increases gradually, the skin and adjacent effect become weaker, leading to the more uniform current density distribution in coils and the larger conductor area flowing through the same current. Therefore, the variation of T and h has significant influence on internal electric parameters, such as L_1, C_1 and R_1, which leads to the resonance frequency shift of EMATs.

B. Analysis the sign of $\mathbf{g}(\boldsymbol{\omega})$

To calculate the matching capacitance C_m and inductance L_s of an EMAT, the equivalent capacitance C_1, resistance R_1, and inductance L_1 are measured, which are 0.2424nF, 21.04Ω and 28.39mH. Then, L_s and C_m are taken as 81.3mH and 2.5561nF by Eq. (12), respectively. Based on Eq. (12), when the equivalent impedance phase θ of EMATs is zero, we can obtain:

$$C_m L_s L_1^2 \omega^4 + \left(C_m L_s R_1^2 - L_1^2 - L_1 L_s\right)\omega^2 - R_1^2 = 0. \quad (31)$$

The discriminate Δ of Eq. (31) should be greater than or equal to zero, which means:

$$\Delta = \left(C_m L_s R_1^2 - L_1^2 - L_1 L_s\right)^2 + 4 C_m L_s L_1^2 R_1^2 \geq 0. \quad (32)$$

Based on Eq. (32), the resonance angular frequency ω_r and anti-resonant angular frequency ω_a can be calculated as:

$$\omega_r = \sqrt{\frac{\xi - \sqrt{\gamma^2 - 4\eta}}{2\delta}}, \quad (33)$$

$$\omega_a = \sqrt{\frac{\xi + \sqrt{\gamma^2 - 4\eta}}{2\delta}}, \quad (34)$$

where $\xi = \left(L_1^2 + L_1 L_{s-} C_m L_s R_1^2\right)$, $\eta = C_m L_s L_1^2 R_1^2$, $\gamma = \left(C_m L_s R_1^2 - L_1^2 - L_1 L_s\right)$, $\delta = C_m L_s L_1^2$. Thus, ω_r and ω_a can be calculated. Figure 4 describes the function F varying with ω, which indicates that F is an increasing function with the increase of ω near the ω_r. Thence, we can obtain that $\mathrm{g}(\omega) > 0$. This inference is critical to the controller design. Without loss of generality, for $\mathrm{Z} \in R^3$, we suppose $\mathrm{g}_0 < g < \mathrm{g}_\mathrm{m}$, where g_0, g_m are unsure normal number.

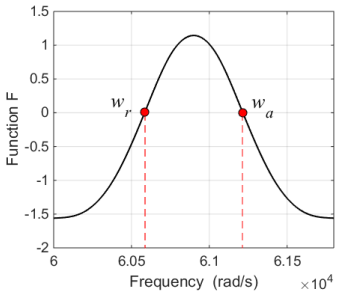

Fig.4. Function F varying with angular frequency.

C. Simulation results

To verify the feasibility of the proposed adaptive NN controller, simulations are carried out for tracking the resonant frequency of EMATs. The basis function applies Gaussian function:

$$\varnothing_i = \exp\left[-\frac{\| Z - c(:,i) \|^2}{b}\right], \quad (35)$$

where b and $c(:,i)$ are the width and center of $\varnothing_i$, respectively.

Figures 5 (a) and (b) illustrate the impedance phase θ and control input v using the adaptive NN method, respectively, which demonstrates their boundedness. The initial state values are $\omega(0) = 436\mathrm{Krad/s}, h(0) = 5\mathrm{mm}$. As can be seen from Fig. 5 (a), θ is stable in [-5°, 5°]. The tracking trajectory using the adaptive NN control algorithm is shown in Fig. 6 (a), which shows a fairly good tracking performance. Solid and dashed lines

denote the inherent resonance frequency f_r and working frequency *f*, respectively. In addition, θ ends up in an emergency collection along with the varying of temperature T and lift-off distance *h*. However, the system has a larger overshoot and steady-state error of θ, leading to a more severe oscillation and unfavorable tracking effect of resonant frequency for the EMATs system.

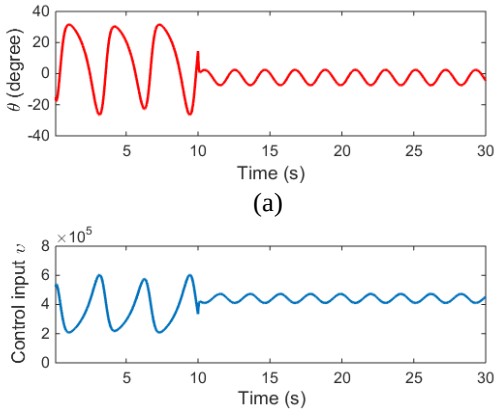

Fig. 5. (a) The impedance phase, and (b) control input using the adaptive NN method.

Figure 6 (b) shows the tracking trajectory using the improved adaptive NN control algorithm, in which the range of frequency is from 45 to 75 KHz. It indicates that the working frequency *f* can track the inherent resonance frequency f_r better than using the adaptive NN control algorithm. In addition, the conversion error is very small and stable in [-0.04, 0.01], as shown in Fig. 7 (a). The variation of θ is shown in Fig. 7 (b), where the solid and dotted lines denote θ and pre-set boundaries $(\bar{\alpha}=20, \underline{\alpha}=-20)$ of $\pm 20\rho(t)$. It indicates that θ is completely within pre-set boundaries and the overshoot is in [-20.2, 20.2]. Noted that θ has a same initial value as Fig. 5 (a), which is due to the same initial conditions and parameters. In addition, θ is in [-10°, 10°] after 5 seconds and eventually stable in [-0.2°, 0.2°]. Furthermore, the convergence rate of θ is greater than $\rho(t)$. Thence, if the design parameters, such as $\bar{\alpha}, \underline{\alpha}$, $\rho(t)$ and *l*, are properly configured, the overshoot, conversion error and convergence rate of EMAT systems can be well controlled by the improved adaptive NN controller.

Thence, it can be seen from Figs. 6 (a) and (b) that the improved adaptive NN algorithm considering transient performance index has a better tracking effect, even when their intrinsic behaviors change due to the varying temperature.

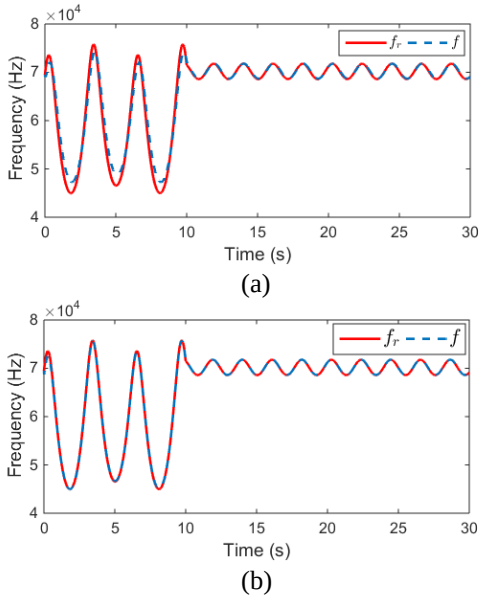

Fig. 6. The result of frequency tracking by: (a) the adaptive NN method, and (b) the improved adaptive NN method.

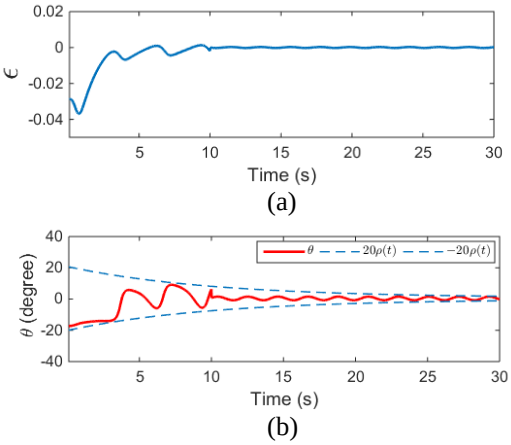

Fig. 7. (a) The conversion error, and (b) the impedance phase using the improved adaptive NN method.

V. CONCLUSION

This paper presents a novel adaptive NN scheme of the resonance frequency tracking for EMATs under high temperature. Based on the equivalent circuit of EMATs near its resonance frequency, the impedance phase θ is calculated after impedance matching. The relationship among L_1, C_1 and R_1 with *T* and *h* are analyzed, indicating that L_1 increases with *T* and *h*, while C_1, R_1 increases with *T* and decreases with *h*. To compensate the resonant frequency drift and low conversion efficiency caused by *T*, the adaptive NN control strategy is adopted to track the resonant frequency automatically.

In addition, an improved scheme considering with transient performance is proposed to ensure the tracking accuracy and efficiency, which shows that θ is stable in [-0.2°, 0.2°], the convergence rate of θ is greater than $\rho(t)$ and the range of conversion error is within [-0.04, 0.01]. The simulation results demonstrate that the proposed novel adaptive NN scheme is feasible and efficient.

ACKNOWLEDGEMENT

This work is supported by the National Natural Science Foundation of China (No. 51374264) and the Entrepreneurship and Innovation Foundation for Returned Overseas Scholars, Chongqing City of China (No. CX2017004).

REFERENCES

[1] B. Fu, "Application Research on Quantitative Detection of Defect in CFST Arch Bridge with Ultrasonic Detecting Technology," *Master Thesis of Chongqing Jiao tong University*, Chongqing, China, 2005.

[2] Y. Zhang, Q. Chen, and Z. G. Sun, "Development of research on electromagnetic acoustic transducer for nondestructive testing," *Nondestructive Testing*, vol. 26, no. 6, pp. 275-279, 2004.

[3] S. J. Wang, L. Kang, Z. X. Zhao, and G. F. Zhai, "Overview of research advances in electromagnetic acoustic transducer," *Instrument Technique and Sensor*, no. 5, pp. 47-50, 2006.

[4] K. Hao, S. Huang, Z. Wei, and W. Shen, "Calculation of new type coil impedance and matched capacitance of electromagnetic ultrasonic transducer," *Chinese High Technology Letters*, no. 8, pp. 845-849, 2010.

[5] L. Scrantz, "System, method and apparatus for the ultrasonic inspection of liquid filled tubular and vessels," U.S, 5619423 A, 1997.

[6] H. J. Salzburger, G. Dobmann, and H. Mohrbacher, "Quality control of laser welds of tailored blanks using guided waves and EMATs," *IEE Proceedings-Science, Measurement and Technology*, vol. 148, no. 4, pp. 143-148, 2001.

[7] X. Jian, S. Dixon, R. S. Edwards, et al., "Coupling mechanism of an EMAT," *Ultrasonics*, vol. 44, pp. e653-e656, 2006.

[8] B. Qu and Z. Han, "Research on a method of frequency tracking and vibration stabilization for transducer," *Piezoelectrics and Acoustooptics*, vol. 36, no. 5, pp. 845-848, 2014.

[9] Q. U. Baida and N. I. Zhenglong, "Frequency automatic tracking system of ultrasonic transducer based on fuzzy–DDS," *Piezoelectrics and Acoustooptics*, vol. 36, no. 1, pp. 156-158, 2014.

[10] X. Tang, "Development of Ultrasonic Power Supply based on Frequency Automatic Tracking and Amplitude Constant Control," *Master Thesis of Beijing Jiao Tong University*, Beijing, China, 2005.

[11] H. Zhang, F. Wang, D. Zhang, L. Wang, Y. Hou, and X. Tao, "A new automatic resonance frequency tracking method for piezoelectric ultrasonic transducers used in thermosonic wire bonding," *Sensors and Actuators A: Physical*, vol. 235, pp. 140-150, 2015.

[12] D. Han and L. Shi, "Guaranteed cost control of affine nonlinear systems via partition of unity method," *Automatica*, vol. 49, no. 2, pp. 660-666, 2013.

[13] I. Kar and L. Behera, "Direct adaptive neural control for affine nonlinear systems," *Applied Soft Computing*, vol. 9, no. 2, pp. 756-764, 2009.

[14] W.-D. Chang, "Nonlinear CSTR control system design using an artificial bee colony algorithm," *Simulation Modeling Practice and Theory*, vol. 31, no. 2, pp. 1-9, 2013.

[15] Q. Zou and S. Devasia, "Precision preview-based stable-inversion for nonlinear nonminimum-phase systems: The VTOL example," *Automatica*, vol. 43, no. 1, pp. 117-127, 2007.

[16] T. Zhang, "The Research on Adaptive Tracking Control of Resonant Frequency of EMAT for High Temperature," *Master Thesis of Chongqing University*, Chongqing, China, 2015.

[17] W. Meng, Q. Yang, S. Jagannathan, and Y. Sun, "Adaptive neural control of high-order uncertain nonaffine systems: A transformation to affine systems approach," *Automatica*, vol. 50, no. 5, pp. 1473-1480, 2014.

[18] C. P. Bechlioulis and G. A. Rovithakis, "Adaptive control with guaranteed transient and steady state tracking error bounds for strict feedback systems," *Automatica*, vol. 45, no. 2, pp. 532-538, 2009.

Microwave Imaging Based on Time Reversal Mirror for Multiple Targets Detection

Tong Mu and Yaoliang Song

School of Electronic and Optical Engineering
Nanjing University of Science and Technology, Nanjing, 210094, China
mutong@njust.edu.cn, ylsong@njust.edu.cn

Abstract ─ Time reversal (TR) is an applicable technique for target detecting and has gained extensive attention due to its self-adaptive focusing ability. However, the imaging performance of the traditional time reversal mirror (TRM) deteriorates in multiple targets cases. A TR imaging approach for multiple targets detection is proposed in this paper. Different from the direct retransmission of the TR signals, the time domain gating is applied to the targets responses to divide them into different groups, and the optimal time frame corresponding to each target which will be utilized in the subsequent step is calculated. After the retransmission of the gated TR signals, the essential zero setting step and the summation step are conducted to construct the imaging function. Numerical simulations are carried out for three multi-targets cases using the finite-different time-domain (FDTD) method. The imaging results are compared with the traditional TRM method and indicate the effectiveness and the superiority of the proposed approach.

Index Terms ─ Multi-targets detecting, optimal time frame, time domain gating, time reversal.

I. INTRODUCTION

Time reversal (TR) technique was first proposed in acoustics [1] and then introduced to electromagnetics [2]. It exploits the invariance of the wave equation in lossless and time-invariant media, and involves physical or synthetic retransmission of signals received by a TR array (TRA) in a time reversed fashion. Time reversal has found applications in various disciplinary fields such as microwave imaging [3,4], wireless communication [5,6] and nondestructive testing [7,8], etc.

Time reversal mirror (TRM) is the direct implementation of time reversal and performs as an effective technique for the detection and localization of targets. Traditional TRM method contains two main steps. In the first step, the probing signal is emitted from the transmitter and the signals scattered from the targets are recorded by the TRA. In the second step, the recorded signals are time reversed and retransmitted by the corresponding receiver in TRA. Then the back-propagated signals will focus around the target positions, and the total field values in the imaging domain at the focusing instant are used for imaging the targets. Although the traditional TRM is easy to accomplish, its performance deteriorates in multiple targets cases. Specifically, images of targets especially the further and weaker ones may be disturbed or swamped by the nearer and stronger ones, and false results will be obtained if the targets are located closely to each other. The iterative TRM method [9] conducts the signal reception, reversal and retransmission iteratively and achieves focusing on the strongest target, but it is still unable to detect the weaker targets. The TR imaging method proposed in [10] uses the grouping technique that divides the TRA into different sub-TRAs and discriminates multiple targets by enhancing the synchronism at target positions. However, the signals need to be retransmitted many times as the number of sub-TRAs should be large enough to ensure the coherence at target positions and the incoherence at non-target positions, which makes it time-consuming to some degree.

The imaging techniques based on the TR operator (TRO) have raised concern in recent years. They include the decomposition of the TR operator (DORT) and the TR multiple signal classification (TR-MUSIC). Selective imaging for different targets can be achieved by the DORT [11,12], and simultaneous multi-targets imaging can be achieved by the TR-MUSIC [13,14]. For the acquisition of the TRO, both the two methods require a large number of measurements to construct the multistatic data matrix (MDM). Specifically, each transceiver transmits signal to the detecting region in sequence, and the scattered signals are recorded by all transceivers after each transmission, causing heavy computation and making it time-consuming for data collection. In addition, the number of targets should not exceed the number of transceivers, limiting the practical applications of these methods.

In this paper, a new TR imaging scheme based on the TRM is proposed for multiple targets detection. First, the signals scattered from the targets are recorded by TRA, and the time domain gating technique is applied at

Submitted On: June 22, 2017
Accepted On: October 19, 2018

each receiver to divide the signals into different groups corresponding to different targets. The time domain gating is able to eliminate unwanted responses from other targets by using a gating filter, and it is also effective for noise reduction [15]. After that the target initial reflection method (TIRM) [16] is used to obtain the focusing instant for each target. Next, the gated signals are time reversed and retransmitted in sequence and the field values in the imaging domain at each time frame are recorded correspondingly. Then, the zero setting is conducted and the recorded field values are added up to construct the imaging function. The images of different targets can be obtained by selecting different time frames, and simultaneous multi-targets imaging can be achieved by applying the normalization and summation steps. Numerical simulations are carried out for three multi-targets cases and the results are compared with the traditional TRM method. It turned out that the proposed approach is simple for implementation and it is able to detect multiple targets synchronously with only one transmitter. It overcomes the near-far problem and the focusing false in multi-targets cases, and also, is more efficient than the TRO based methods.

II. TR IMAGING SCHEME

A. TRM method

Let us consider the 2-D scene with a TRA consisting of N antennas. A probing pulse $x(t)$ is emitted from the transmitter located at $\mathbf{r}_t$ and the signals scattered from the point-like targets are recorded by TRA. The target with the scattering potential ρ_s is located at $\mathbf{r}_s$ and the nth antenna is located at $\mathbf{r}_n$. The incident signal at the target position $\mathbf{r}_s$ in the frequency domain is given by:

$$X_{\text{in}}(\omega) = G(\mathbf{r}_t, \mathbf{r}_s, \omega) X(\omega), \tag{1}$$

where $X(\omega)$ is the Fourier transform of $x(t)$, and $G(\mathbf{r}_t, \mathbf{r}_s, \omega)$ is the Green's function from the transmitter location $\mathbf{r}_t$ to the target position $\mathbf{r}_s$ which represents the "propagator". For notational simplicity the scalar field and Green's function are considered in the theoretical analysis. Extension to the vector case is straightforward in principle but complicated for expression in general form.

The received signal at the nth receiver can be represented as:

$$X_{\text{r}}(\mathbf{r}_n, \omega) = G(\mathbf{r}_s, \mathbf{r}_n, \omega) G(\mathbf{r}_t, \mathbf{r}_s, \omega) X(\omega) \rho_s. \tag{2}$$

If we take the complex conjugate of $X_{\text{r}}(\mathbf{r}_n, \omega)$ which is equivalent to the time reversal in the time domain and then back-propagate it from the nth antenna, we can obtain the total signal at the observation point $\mathbf{r}$ in the imaging domain:

$$X_{\text{TR}}(\mathbf{r}, \omega) = \sum_{n=1}^{N} G(\mathbf{r}_n, \mathbf{r}, \omega) X_{\text{r}}^{*}(\mathbf{r}_n, \omega), \tag{3}$$

where "$*$" denotes the complex conjugate.

Substituting (2) into (3) yields:

$$\begin{aligned} X_{\text{TR}}(\mathbf{r}, \omega) = \sum_{n=1}^{N} & G(\mathbf{r}_n, \mathbf{r}, \omega) G^{*}(\mathbf{r}_s, \mathbf{r}_n, \omega) \\ & G^{*}(\mathbf{r}_t, \mathbf{r}_s, \omega) X^{*}(\omega) \rho_s. \end{aligned} \tag{4}$$

According to the spatial reciprocity principle, we have:

$$G(\mathbf{r}_s, \mathbf{r}_n, \omega) = G(\mathbf{r}_n, \mathbf{r}_s, \omega), \tag{5}$$

and when the observation point $\mathbf{r}$ happens to be the target positon $\mathbf{r}_s$, (4) can be rewritten as:

$$\begin{aligned} X_{\text{TR}}(\mathbf{r}_s, \omega) = \sum_{n=1}^{N} & G(\mathbf{r}_s, \mathbf{r}_n, \omega) G^{*}(\mathbf{r}_s, \mathbf{r}_n, \omega) \\ & G^{*}(\mathbf{r}_t, \mathbf{r}_s, \omega) X^{*}(\omega) \rho_s. \end{aligned} \tag{6}$$

The corresponding time domain representation of (6) can be described as:

$$\begin{aligned} x_{\text{TR}}(\mathbf{r}_s, t) &= \frac{1}{2\pi} \int [\sum_{n=1}^{N} G(\mathbf{r}_s, \mathbf{r}_n, \omega) G^{*}(\mathbf{r}_s, \mathbf{r}_n, \omega) \\ &\quad G^{*}(\mathbf{r}_t, \mathbf{r}_s, \omega) X^{*}(\omega) \rho_s] e^{j\omega t} d\omega \\ &= \sum_{n=1}^{N} G(\mathbf{r}_s, \mathbf{r}_n, t) \otimes G(\mathbf{r}_s, \mathbf{r}_n, -t) \\ &\quad \otimes G(\mathbf{r}_t, \mathbf{r}_s, -t) \otimes x(-t) \rho_s, \end{aligned} \tag{7}$$

where "$\otimes$" denotes the time domain convolution.

Here $G(\mathbf{r}_s, \mathbf{r}_n, t) \otimes G(\mathbf{r}_s, \mathbf{r}_n, -t)$ represents a matched filter which achieves the maximum output at $t = 0$. The signals back-propagated from N antennas will synchronously achieve their maximum values at the target position $\mathbf{r}_s$ at the same instant which is called the optimal time frame. As a result, the field value at the target position is much larger than that of non-target locations thus the target image can be acquired at the optimal time frame by scanning the field value for each point in the imaging domain.

B. Partition of echo signals

According to the analysis above, the target can be detected precisely by the traditional TRM method when there is only one target. If the target positon changes, the optimal time frame changes as well due to the space-time matching property of TR. Now we assume that there are two point-like targets located at $\mathbf{r}_1$ and $\mathbf{r}_2$ respectively. The signals recorded by TRA are the sum of the signals scattered from the two targets and contain the spatial information of both them. If the signals are time reversed and back-propagated directly, the signal components corresponding to the first target will achieve their maximum values synchronously at $\mathbf{r}_1$ at an instant t_1, and the signal components corresponding to the second one will achieve their maximum values synchronously at $\mathbf{r}_2$ at t_2, generally $t_1 \neq t_2$. The intensity of the total field focusing at the first target is also different from that of

the second one.

As a result, if we choose one of the two instants as the optimal time frame, we can only obtain the image of one target which may be disturbed and swamped by the field focusing somewhere else in the imaging domain especially when this target is the weaker or the further one. The deterioration increases as the number of targets grows. To solve this problem, we introduce a new TR imaging scheme, the core idea of which is the partition of the responses from different targets. For this purpose, we apply the time domain gating method that selects a region of interest in the time domain and eliminates unwanted responses by adopting the window function.

It is assumed that there are *K* point-like targets and the multi-path reflections are negligibly small, thus the signal received by each antenna is comprised of *K* responses. As is shown in Fig. 1, if the propagation delay of the signal from the *k*th target is t_k, by using a window function from $t_k-\tau$ to $t_k+\tau$ we can extract the response at t_k as well as the target located between $c(t_k-\tau)/2$ and $c(t_k+\tau)/2$. The principle of choosing the window function is appropriately eliminating unwanted responses without damaging the mainlobe of the desired response. Besides, the use of time domain gating also shows effectiveness in noise suppression.

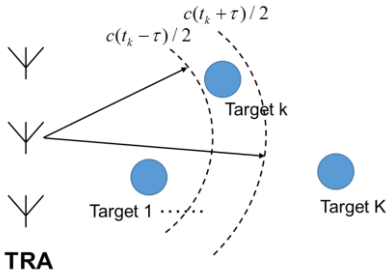

Fig. 1. Illustration of the time domain gating technique.

C. Multiple targets imaging

By applying the time domain gating to all the N received signals, the responses from the *K* targets are divided into *K* groups which can be expressed as

$$\mathbf{Y}=[\mathbf{y}_1,\mathbf{y}_2,...,\mathbf{y}_K], \tag{8}$$

where $\mathbf{y}_k=[\mathbf{s}_{k,1}(t),\mathbf{s}_{k,2}(t),...,\mathbf{s}_{k,N}(t)]^T$, $k=1,2,...,K$ is the *k*th target responses recorded by N receivers, and "T" denotes the transposition. $\mathbf{s}_{k,n}(t)$ with $n=1,2,...,N$ is the 1×*M* signal sequence where *M* is the number of the sampling points in the time domain.

Next, the TIRM algorithm is used to calculate the optimal time frame for each target. The algorithm requires only a few signal parameters and prevails over the traditional methods such as the maximum E-field method and the entropy-based methods. According to the derivation in [16], the optimal time frame is given by:

$$t^{\text{opt}}=\text{maxtime}-\frac{t_r+t_d}{2}, \tag{9}$$

where maxtime is the total duration of the signal propagation, t_r is the instant when the initial reflection from the target arrives at the transmitter antenna, and t_d is the instant when the probing signal reaches its peak value after being excited.

We assume that the transmitter antenna is the n_0th element in the TRA, the instant corresponding to the maximum value of the *k*th target response received by the transmitter antenna is $t_k^{\max}$, and the pulse width of the probing signal is t_p. Therefore (9) can be modified as:

$$t_k^{\text{opt}}=\text{maxtime}-\frac{t_k^{\max}-t_p+t_d}{2}. \tag{10}$$

After the calculation of all the *K* optimal time frames, the *K* groups of signals $\mathbf{y}_1,\mathbf{y}_2,...,\mathbf{y}_K$ are time reversed and retransmitted into the imaging domain in sequence. Thus the field value at each point in the imaging domain is given by:

$$\mathbf{u}_k(\mathbf{r},t)=\sum_{n=1}^{N}\mathbf{s}_{k,n}^{\text{TR}}(\mathbf{r},t)\quad k=1,2,...,K. \tag{11}$$

Now we introduce the essential step: at the optimal time frame we set the elements of $\mathbf{u}_k(\mathbf{r},t)$ corresponding to all the other targets to zero. This step is described as:

$$\mathbf{u}_k(\mathbf{r},t_{k'}^{\text{opt}})|_{k'\neq k}=0\quad k'=1,2,...,K. \tag{12}$$

The zero setting ensures that when the TR signals achieve the maximum value at t_k^{opt} the image of the *k*th target will not be disturbed or swamped by other targets, and it is applicable for both strong and weak targets. Then all the modified $\mathbf{u}_k(\mathbf{r},t)$ are added up to construct the imaging function:

$$\mathbf{U}(\mathbf{r},t)=\sum_{k=1}^{K}\mathbf{u}_k(\mathbf{r},t). \tag{13}$$

Imaging for the *k*th target can be realized by selecting $t=t_k^{\text{opt}}$, and simultaneous multi-targets imaging is given by:

$$\mathbf{F}(\mathbf{r})=\sum_{k=1}^{K}\frac{\mathbf{U}(\mathbf{r},t_k^{\text{opt}})}{U(\mathbf{r}_k,t_k^{\text{opt}})}, \tag{14}$$

where $\mathbf{r}_k$ is the *k*th target position and $U(\mathbf{r}_k,t_k^{\text{opt}})$ is the maximum value of the field intensity recorded in the imaging domain at the focusing instant. The normalization process makes the signals synchronically achieve the value of 1 at each target position. Based on the proposed scheme, the image of each target can be acquired without interference and the images of *K* targets show equal visibility.

The block diagram of the proposed TR imaging approach is depicted in Fig. 2.

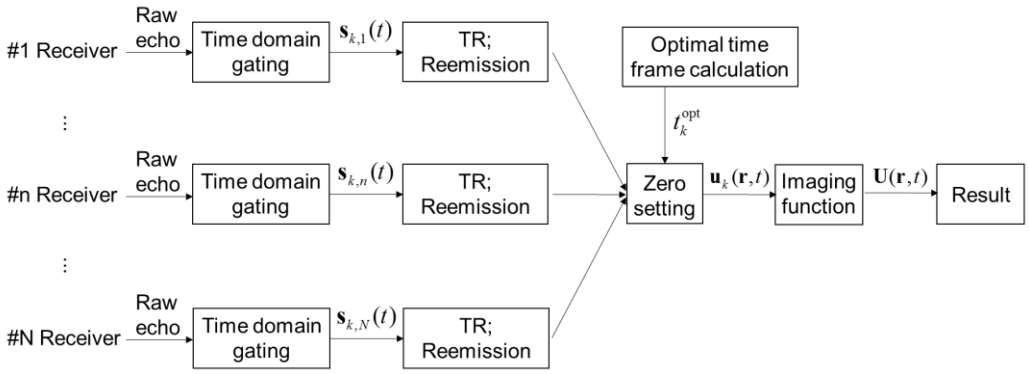

Fig. 2. Block diagram of the proposed approach.

III. SIMULATIONS AND RESULTS

A. Simulation setup

For solving the electromagnetic scattering problem and collecting the waveform data, the TMz polarized 2-D finite-different time-domain (FDTD) method is used in this work. FDTD is a numerical technique that is based on the finite difference approximation of the differential Maxwell's equations [17]. It discretizes the time and space variables in the computational domain by using the Yee cells, and it makes the electric (magnetic) field at each grid point only dependent on the magnetic (electric) field at the adjacent grid point as well as the corresponding component at the last time step. Given the initial value, the future values of the electric and magnetic fields are updated from the previous values at each grid point, thus the spatial distribution of the electromagnetic field can be acquired. The FDTD method calculates the field propagation in the time domain directly and is able to model different objects of study in different coordinates with low computational costs. Therefore, it is appropriate for the numerical solution of forward propagation of the probing signal/target response and back-propagation of the TR signals.

Figure 3 illustrates the setup of the numerical simulation. The imaging domain contains 200×200 FDTD grids and the grid size is set as $\Delta x = \Delta y = 1\,\text{cm}$. The time step is $\Delta t = 16.7\,\text{ps}$ and the maximum iteration time is $\text{maxtime} = 1000\Delta t$. The perfectly matched layers (PML) are applied as the absorbing boundaries to truncate the computational domain and avoid wave reflections on the boundary. Point-like scatterers with radius $r = 3\,\text{cm}$ are located in the detecting region which is considered as the homogeneous medium (free space) in the experiment. The conductivity and the relative permittivity of the scatterers are $\sigma = 0.1\,\text{S/m}$ and $\varepsilon_r = 30$ respectively. It is worth mentioning that in the case of dispersive or lossy medium such as detecting tumor in the breast tissue or sensing target through the brick wall, dispersion or attenuation of the fields caused by the background medium should be taken into account. Also, the corresponding FDTD iterative formulas should be modified depending on the specific case in the modeling, which is out of the scope of this paper. The TRA composed of 10 antennas is equally spaced and located parallel to the Y axis. The interval between adjacent antennas is half of the wave length corresponding to the center frequency of the probing signal. The sinusoidal modulated Gaussian pulse with the center frequency being 2 GHz and the bandwidth being 4 GHz is transmitted by the 5th antenna of the TRA, and the corresponding waveform and frequency spectrum are shown in Fig. 4. The signals scattered from the targets are recorded by the TRA and the Gaussian white noise with the signal-to-noise ratio (SNR) being 25 dB is added to the received signal.

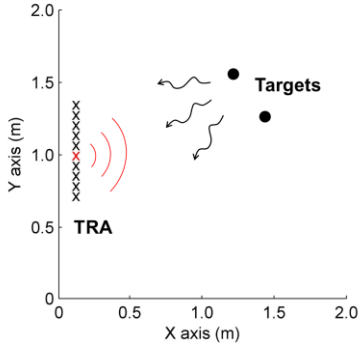

Fig. 3. Setup of the numerical simulation.

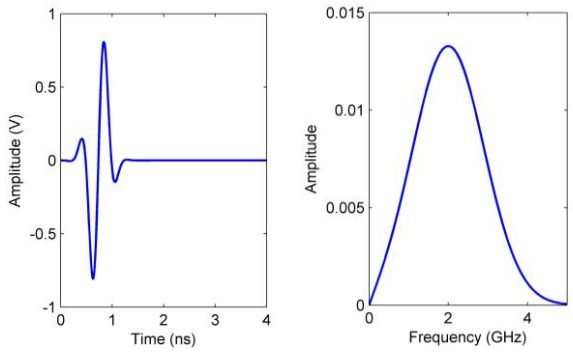

(a) (b)

Fig. 4. Probing signal: (a) time domain waveform and (b) frequency spectrum.

B. Simulation results

Three different multi-targets cases are studied to evaluate the performance of the proposed imaging approach. The numerical results obtained by the proposed method and the traditional TRM method are both provided for comparisons. The TRA is marked with "x" and the actual targets locations are marked with "o" in the resulted images.

In the first case, imaging for two targets located at (0.6 m, 0.8 m) and (1.4 m, 0.8 m) respectively is investigated. After the reception and storage of the echo data, the time domain gating is applied to all the raw signals. The Hanning window is selected as the window function for the numerical experiment. The *k*th time-window for the *k*th target response is given by:

$$f_k(t) = 0.5(1-\cos(\frac{2\pi(t-\delta_k)}{W})), \qquad (15)$$

where δ_k is the time shift and W is the window width. As is analyzed in the second section of the paper, the time shift value is set equal to the propagation delay of the *k*th target response. The window width is chosen depending on the specific circumstance, and it is set as $W = 100\Delta t$ for the numerical experiment.

The raw signal received by the 1st antenna and two corresponding window functions used for target response extraction are shown in Fig. 5. The amplitude values of the actual echo signals are far less than 1, thus the amplitude normalization is applied to the signal to make it visually comparable with the window functions.

Figure 6 shows the imaging results for the targets based on the traditional TRM method. It can be seen that the image of the first target (the nearer one) is accurately obtained while the image of the second target (the further one) is not as bright as the first one, and some interferences can be observed in the image domain. The reason is that the echo from the further target arrives at the TRA later, thus it is emitted from the TRA earlier after being time reversed. When it achieves the maximum value at the further target position, the TR signal for the nearer target is to be emitted or just emitted from the TRA. So if the snapshot is taken at the optimal time frame for the further target, strong fields will appear around the TRA and cause inevitable interferences.

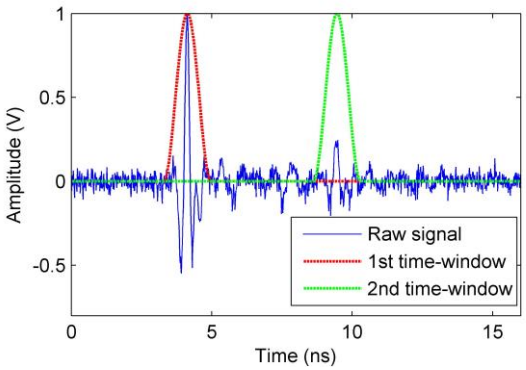

Fig. 5. Raw signal received by the 1st antenna and window functions.

Figure 7 shows the imaging results given by the proposed approach. It can be observed that both of the targets are imaged accurately and clearly without any interference. Besides, the two targets can be imaged synchronously with the same brightness by the normalization process described in (14), as shown in Fig. 7 (c).

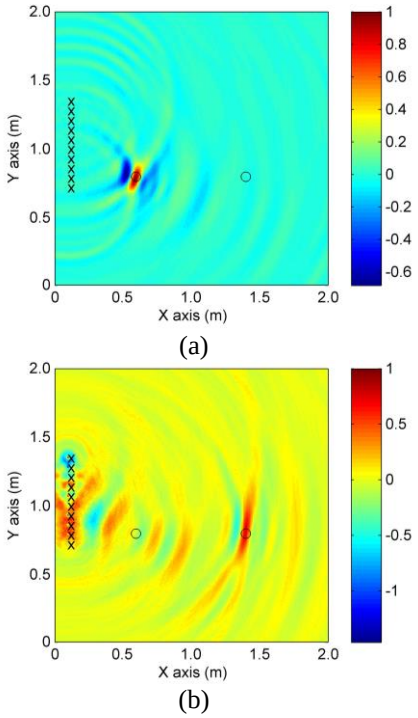

(a)

(b)

Fig. 6. Imaging results for the targets located at: (a) (0.6 m, 0.8 m) and (b) (1.4 m, 0.8 m) by the traditional TRM method.

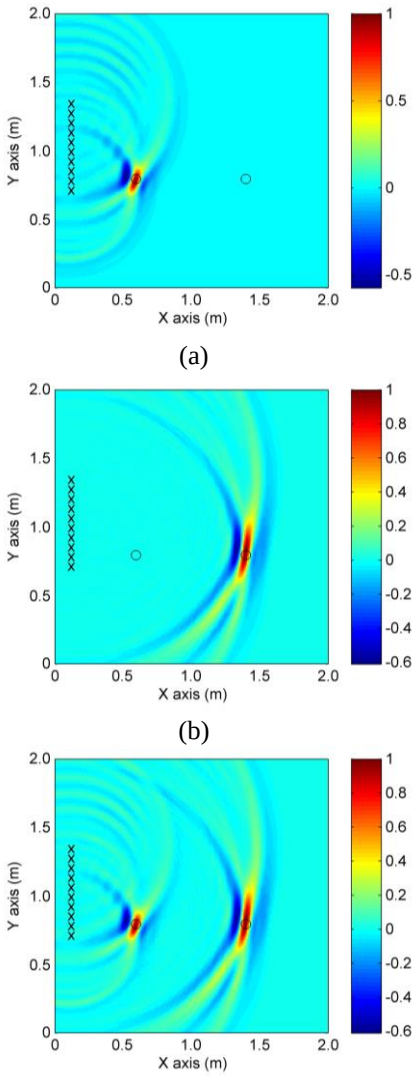

Fig. 7. Imaging results for the targets located at: (a) (0.6 m, 0.8 m), (b) (1.4 m, 0.8 m, and (c) multiple targets by the proposed TR method.

Figure 8 and Fig. 9 show the imaging results for two targets located at (0.6 m, 0.8 m) and (0.75 m, 0.9 m) given by the two methods respectively, representing the case where the targets are located closely to each other. On the one hand, from Fig. 8 (a) we can see that the nearer target is imaged precisely but a darker "ghost image" appears around the further target. It is because that when the back-propagated signals focus at the nearer target, the focusing fields at the further one just diverged. Similarly in Fig. 8 (b), the fields are about to reach the maximum values at the nearer target at the optimal time frame corresponding to the further one, causing a "ghost image" which is even brighter than the image of the further target. Therefore the traditional TRM method fails to detect the further target in this case.

On the other hand, it is shown in Figs. 9 (a), (b) and (c) that the two closely located targets can be both detected successfully and no "ghost image" appears, indicating the effectiveness of the proposed method for the closely-located-targets-case.

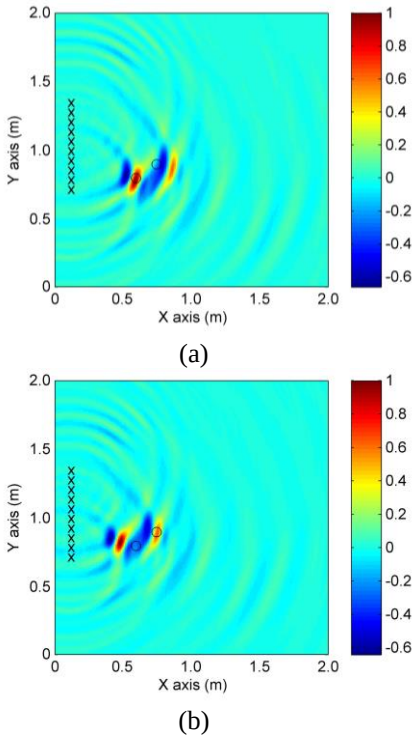

Fig. 8. Imaging results for the targets located at: (a) (0.6 m, 0.8 m) and (b) (0.75 m, 0.9 m) by the traditional TRM method.

In the third case we investigate the detection of three targets located at (0.6 m, 0.8 m), (0.75 m, 0.8 m) and (1.5 m, 1.42 m) respectively. Figure 10 depicts the imaging results given by the traditional TRM method. It is observed that only the first target (the nearest one) can be detected (still with interference). The actual locations of the other two targets can be hardly identified from the resulted images.

On the contrary, successful imaging for all the three targets are achieved based on the proposed method, as shown in Figs. 11 (a), (b), (c) and (d). The results indicate that the proposed TR imaging approach is also applicable for the case where there are more than two targets.

The corresponding optimal time frames obtained by the TIRM algorithm for all the three cases are shown in Table 1.

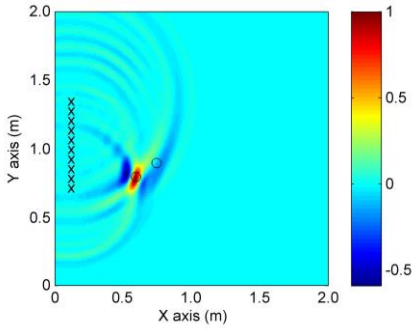

(a)

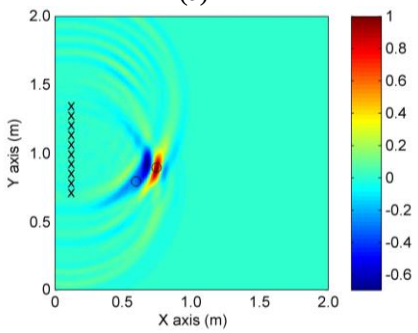

(b)

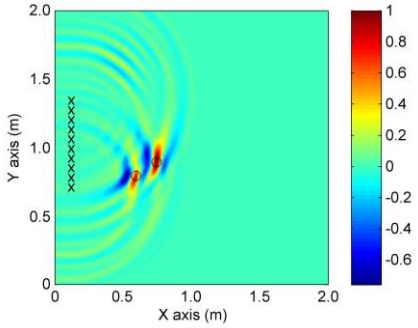

(c)

Fig. 9. Imaging results for the targets located at: (a) (0.6 m, 0.8 m), (b) (0.75 m, 0.9 m), and (c) multiple targets by the proposed TR method.

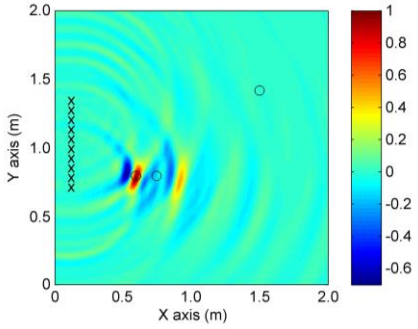

(a)

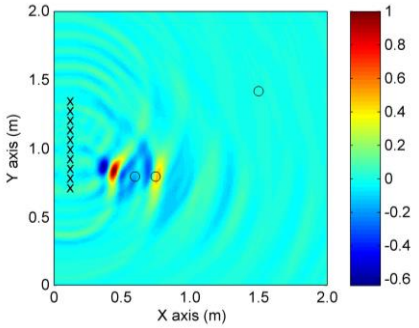

(b)

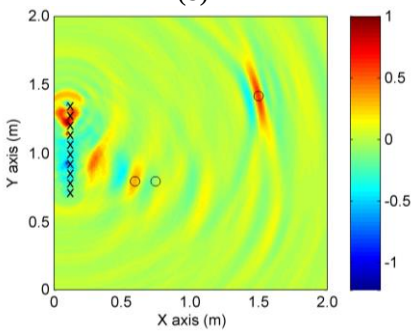

(c)

Fig. 10. Imaging results for the targets located at: (a) (0.6 m, 0.8 m), (b) (0.75 m, 0.8 m), and (c) (1.5 m, 1.42 m) by the traditional TRM method.

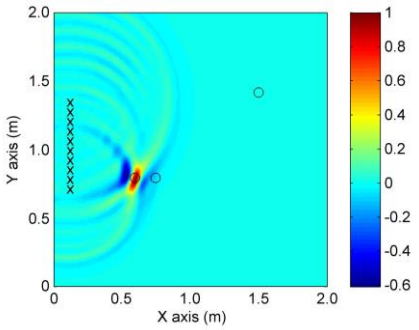

(a)

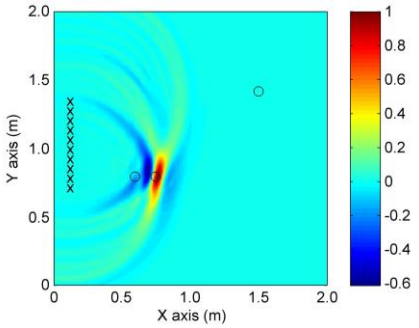

(b)

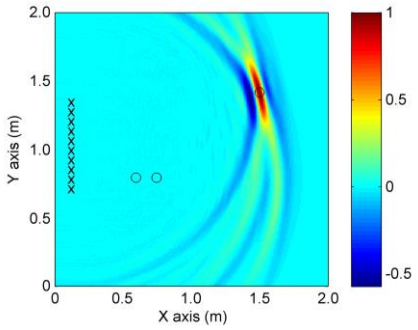

(c)

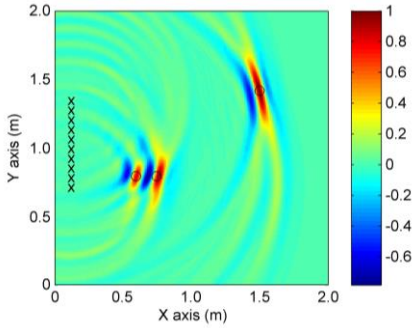

(d)

Fig. 11. Imaging results for the targets located at: (a) (0.6 m, 0.8 m), (b) (0.75 m, 0.9 m), (c) (1.5 m, 1.42 m), and (d) multiple targets by the proposed TR method.

Table 1: Optimal time frames obtained by the TIRM algorithm

Case	Optimal Time Frame/ Δt		
	Target 1	Target 2	Target 3
1	855	698	/
2	855	833	/
3	856	825	670

IV. CONCLUSION

A new TR imaging scheme for multiple targets detection is proposed in this paper. Direct retransmission of the TR signals causes inevitable interferences which are adverse to the identification for the actual targets. To achieve better imaging performance the time domain gating is utilized for the partition of the echo signals. Once the optimal time frame for each target is obtained, all groups of the target responses are time reversed and retransmitted from the TRA. Then the zero setting process is applied to the recorded fields, and imaging for individual target as well as simultaneous multi-targets imaging are carried out based on the new imaging function. Numerical simulation results for three multi-targets cases indicate that satisfactory imaging for the targets can be achieved by the proposed approach which prevails over the traditional TRM method in solving the near-far problem and suppressing the interference fields. Furthermore, it turned out that the proposed scheme is efficient and simple for implementation as it requires only one transmitter and single measurement by the antenna array.

ACKNOWLEDGMENT

This work was supported by the National Natural Science Foundation of China under Grant 61271331 and Grant 61571229.

REFERENCES

[1] M. Fink, D. Cassereau, A. Derode, *et al*., "Time-reversed acoustics," *Reports on progress in Physics*, vol. 63, no. 12, pp. 1933-1995, 2000.

[2] G. Lerosey, J. De Rosny, A. Tourin, *et al*., "Time reversal of electromagnetic waves," *Physical review letters*, vol. 92, no. 19, pp. 193904, 2004.

[3] P. Kosmas and C. M. Rappaport, "Time reversal with the FDTD method for microwave breast cancer detection," *IEEE Trans. Microw. Theory Tech.*, vol. 53, no. 7, pp. 2317-2323, 2005.

[4] S. Sadeghi and R. Faraji-Dana, "A Practical UWB Microwave Imaging System Using Time-Domain DORT for Tumor Detection," *Applied Computational Electromagnetics Society Journal*, vol. 31, no. 6, pp. 692-699, 2016.

[5] R. C. Qiu, C. Zhou, N. Guo, *et al*., "Time reversal with MISO for ultrawideband communications: Experimental results," *IEEE Antennas and Wireless Propagation Letters*, vol. 5, no. 1, pp. 269-273, 2006.

[6] H. T. Nguyen, I. Z. Kovcs and P. C. F. Eggers, "A time reversal transmission approach for multiuser UWB communications," *IEEE Trans. Antennas Propag.*, vol. 54, no. 11, pp. 3216-3224, 2006.

[7] T. Leutenegger and J. Dual, "Non-destructive testing of tubes using a time reverse numerical simulation (TRNS) method," *Ultrasonics*, vol. 41, no. 10, pp. 811-822, 2004.

[8] C. Fan, M. Pan, F. Luo, *et al*., "Multi-frequency time-reversal-based imaging for ultrasonic non-destructive evaluation using full matrix capture," *IEEE Trans. Ultrason., Ferroelectr., Freq. Control*, vol. 61, no. 12, pp. 2067-2074, 2014.

[9] X. Zhu, Z. Zhao, W. Yang, *et al*., "Iterative time-reversal mirror method for imaging the buried object beneath rough ground surface," *Progress In Electromagnetics Research*, vol. 117, pp. 19-33, 2011.

[10] Y. Li and M. Xia, "Time Reversal Imaging Based on Synchronism," *IEEE Antennas and Wireless Propagation Letters*, vol. 16, pp. 2058-2061, 2017.

[11] M. E. Yavuz and F. L. Teixeira, "Full time-domain DORT for ultrawideband electromagnetic fields in dispersive, random inhomogeneous media," *IEEE Trans. Antennas Propag.*, vol. 54, no. 8, pp. 2305-

2315, 2006.

[12] T. Zhang, P. C. Chaumet, A. Sentenac, *et al*., "Improving three-dimensional target reconstruction in the multiple scattering regime using the decomposition of the time-reversal operator," *Journal of Applied Physics*, vol. 120, no. 24, pp. 243101, 2016.

[13] E. A. Marengo and F. K. Gruber, "Subspace-based localization and inverse scattering of multiply scattering point targets," *EURASIP Journal on Advances in Signal Processing*, vol. 2007, no. 1, pp. 017342, 2006.

[14] R. Solimene and A. Dell'Aversano, "Some remarks on time-reversal MUSIC for two-dimensional thin PEC scatterers," *IEEE Geoscience and Remote Sensing Letters*, vol. 11, no. 6, pp. 1163-1167, 2014.

[15] H. Choi, Y. Ogawa, T. Nishimura, *et al*., "Iterative angle-and-time-domain gating technique for time-reversal MUSIC imaging," *Signal processing*, vol. 111, pp. 39-49, 2015.

[16] A. B. Gorji and B. Zakeri, "Time-reversal through-wall microwave imaging in rich scattering environment based on target initial reflection method," *Applied Computational Electromagnetics Society Journal*, vol. 30, no. 6, pp. 626-637, 2015.

[17] K. Yee, "Numerical solution of initial boundary value problems involving Maxwell's equations in isotropic media," *IEEE Trans. Antennas Propag.*, vol. 14, pp. 302-307, 1966.

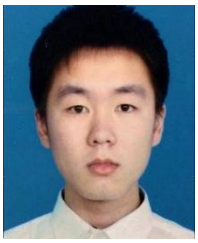

Tong Mu received the B.Eng. degree in Electronic Information Engineering from the Nanjing University of Science and Technology, Nanjing, China, in 2014, where he is currently pursuing the Ph.D. degree in Information and Communication Engineering. His current research interests include microwave imaging and radar signal processing.

Yaoliang Song received the B.Eng., the M.Eng. and the D.Eng. degrees in Electrical Engineering from the Nanjing University of Science and Technology, Nanjing, China, in 1983, 1986 and 2000 respectively. He has been a Researcher Fellow at the Department of Engineering Science at the University of Oxford from Sept. 2004 to Sept. 2005. At present, he is a Professor at Nanjing University of Science and Technology. His major research interests include UWB communications, UWB radar imaging and advanced signal processing.

Optimal Design of Microwave Devices by Fitness-estimation-based Particle Swarm Optimization Algorithm

Xiao-hong Fan, Yu-bo Tian, and Yi Zhao

School of Electronics and Information
Jiangsu University of Science and Technology, Zhenjiang 212003, Jiangsu, P. R. China
18362895409@163.com, tianyubo@just.edu.cn, 422554361@qq.com

Abstract ─ As important parts of modern communication systems, microwave devices play a decisive role in communication quality. When optimizing the complex microwave devices, the global optimization algorithm is generally used exploiting full-wave electromagnetic simulation software. The full-wave electromagnetic simulation software evaluates the performance of the microwave device. Based on this evaluation result, the global optimization algorithm is used to design the microwave device. This ordinary method can achieve high accuracy, but the main disadvantage is time-consuming. It takes a long time and sometimes takes days or even weeks. In order to improve the efficiency of the optimization of microwave devices, this research presents a method called fitness-estimation-based particle swarm optimization (fePSO). According to the explicit evolution formula of particle swarm optimization (PSO), the particles fitness predictive model is constructed. From the third generation, the fitness value is estimated by the predictive model, so as to replace the time-consuming full-wave electromagnetic simulation when optimizing complex microwave devices. Thereby it can greatly reduce the evaluation time of the fitness, shorten the entire optimization process, and improve the design efficiency. This method is validated by optimizing Yagi microstrip antenna (MSA) and hairpin SIR band-pass filter. The results show that the efficiency can be increased by about 90% with the assurance of design accuracy, so the purpose of rapid optimization has been achieved.

Index Terms ─ Antenna, filter, particle swarm optimization.

I. INTRODUCTION

With the rapid development of modern communication systems, microwave devices, as an important part of communication systems, play an important role in civil and military communications. Therefore, the demand for various microwave devices with complex structures is also growing. In order to meet the needs of development of microwave devices, it is an important research area to improve the performance of microwave devices through optimization. When optimizing complex microwave devices, global optimization algorithms are used exploiting full-wave electromagnetic simulation software [1]. The commonly used global optimization algorithms include genetic algorithm (GA) [2], particle swarm optimization (PSO) [3], etc. The commonly used full-wave electromagnetic simulation softwares include High Frequency Structure Simulator (HFSS), IE3D, Computer Simulation Technology (CST), etc. In this process, full-wave electromagnetic simulation software evaluates the performance of microwave devices. The evaluation result is as fitness of global optimization algorithm to design microwave devices. Although this method can achieve high precision, it is very time-consuming. It may take days or even weeks to design a microwave device that meets the design specifications, and it has high requirements for the computer performance. Therefore, it has some limitations when designing complex microwave devices. Under this research background, how to reduce the computing time to design microwave devices has become a hot topic.

In order to solve this problem, machine learning methods have been applied in designing and optimizing microwave devices. Through constructing surrogate models and reducing the evaluation number of full-wave electromagnetic simulation, the methods can decrease the optimizing time. Currently, the most common and popular methods are artificial neural network (ANN), support vector machine (SVM) and Gaussian process (GP), etc. Zhang described the design process of radio frequency and microwave devices from theory to practice using ANN in [4]. In [5], ANN was proposed to predict the resonant frequency of a single-feed corner-sliced circularly polarized microstrip antenna (MSA). In [6], the authors used the particle behavior parallelization of PSO to accelerate ANN training, and modeled the resonant frequency of rectangular MSA under compute unified device architecture (CUDA). Yi et al. in [7] proposed a knowledge-based neural network (KBNN) based on Advanced Design System (ADS) and applied

Submitted On: February 1, 2018
Accepted On: August 11, 2018

it to design filters. Angiulli proposed SVM-based microwave device modeling in [8]. Al Sharkawy et al. in [9] proposed a new CAD system for the detection of breast cancer in mammograms. The discrete wavelet transform (DWT), the contourlet transform, and the principal component analysis (PCA) were all used for feature extraction; while the SVM was used for classification. Sun et al. in [10] proposed a SVM combined with a hybrid kernel function (HKF) for accurately modeling the resonant frequencies of the compact microstrip antenna (MSA). Kayabasi in [11] presented a SVM based analysis and synthesis models for the equilateral triangular ring microstrip antennas (ETRMAs) that operated at ultrahigh band applications. Villier modeled ultra-wideband and dual-frequency coplanar waveguides fed slot antennas using GP [12-13]. Chen et al. in [14] proposed a KBNN based on GP and applied it to design microstrip antenna. In general, the construction of these prediction models consists of two parts, sampling and modeling. These prediction models usually don't have a direct formula, so it is not built by looking for model parameters. Instead, it approximates the function by learning a large number of samples. The correctness of the model has a great relationship with the sample selection. As the dimension increases, the difficulty of constructing a prediction model also increases. ANN training requires a large number of samples and the model structure is not easy to be determined, and it usually suffers problems of over-fitting or under-fitting. For SVM and GP, it is difficult to find a suitable kernel function and optimal hyper parameters.

The fitness inheritance method is another approach to predict the fitness, that is, the fitness of the children inherits that of the parents in a certain way. In [15], Smith proposed that in the evolutionary process of GA, inherited fitness could be used instead of the true fitness. The fitness of some individuals in the population was directly assigned to the average value of their parents' fitness, reducing the actual evaluation of the number of evaluations. Salami and Hendtlass [16] proposed a fast evolutionary algorithm. The fitness of the offspring was directly assigned by the weighted average of the fitness of the parent. Sun [17] proposed a fitness inheritance and estimation technique to reduce the number of fitness evaluations by using different linear combinations of historical location fitness and directly assigning recent historical location fitness. Xiao [18] proposed a novel fitness estimation based particle swarm optimization algorithm with an adaptive penalty function approach (FEPSO-AP) to handle the problem of expensive computational cost of truss analysis. Cui [19] proposed a fast PSO algorithm based on the change of particle velocity and position. Only when the confidence of the particle fitness was lower than a certain threshold, the true fitness was needed to calculate. Different from the sample prediction model, the inheritance prediction model does not need a large number of sample selection, it can save a large number of sample acquisition time. Simultaneously, it can avoid the prediction model error caused by the improper sampling.

As we all know, PSO is a typical swarm intelligence optimization algorithm that is simulated bird swarm in search of food processes, which was proposed by Kennedy, a social psychologist, and Eberhart, an electrical engineer [1, 20-21]. The theory is that collaboration among the particles generates group intelligence to guide search. PSO considers each individual as a particle without weight and volume in space and flies at a certain speed in the search space with reference to the flight experience of the group and the flight experience of the particle itself. As an effective parallel search method, the algorithm preserves the global search strategy based on population, and does not need to rely on the feature information of the problem itself. It adopts a simple velocity-shift evolution model to avoid complicated genetic operations. PSO has the advantages of simple operation, fewer parameters to be adjusted and faster convergence, which are quite effective for the optimization of nonlinear problems, combinatorial problems and hybrid nonlinear problems [22]. PSO algorithm has many successful applications in designing microwave devices, such as filters [23-25] and antennas [26-27]. The evolutionary process of PSO is an iterative optimization process. As the number of iterations increases, individuals in the population gradually converge to the optimal solution of the problem. If the individual fitness prediction model can be constructed according to the characteristics of the algorithm, not only the time consumption of sampling can be avoided, but also the optimization ability of the algorithm can be kept while greatly reducing the calculation times of the real fitness. Therefore, based on the PSO evolutionary formula, this paper constructs a PSO algorithm with predictive mechanism to design complex microwave devices with high efficiency.

The specific content of this paper is structured as follows. Section II presents a brief introduction of the standard PSO and theory of the proposed fitness-estimation-based PSO (fePSO). In Section III, the method is introduced in the optimization of microstrip Yagi MSA. In Section IV, the method is introduced in the optimization of hairpin-type SIR band-pass filter. Finally, summarizes are provided in section V.

II. THE FePSO ALGORITHM

A. Standard PSO algorithm

In PSO, the state vector of each particle usually contains the position and velocity. At the beginning of the search, the state of particles is given randomly within the search range. During the search there are two important

pieces of information that be retained, one is the best location named *pbest* for each particle, the other is the best location named *gbest* for the entire population. The best location is measured by fitness function. Each particle is driven toward its best location and the optimal location of the population. There are fewer parameters to be adjusted, but these parameters directly affect the performance and convergence. One of the parameters is the inertia weight factor ω. A large ω can jump out of the local optimum, which is in favor of looking for the global optimum. A small ω is beneficial to the local optimization and accelerates the convergence of the algorithm.

The PSO can be described in mathematical language. Assuming that the particles search space is *n*-dimension, and the entire particle swarm $\boldsymbol{x}=\left(x_1,x_2,\cdots,x_m\right)^T$ contains m particles. The location of the particle i is $\boldsymbol{x}_i=\left(x_{i,1},x_{i,2},\cdots,x_{i,n}\right)^T$. At this time, the particle velocity is $\boldsymbol{v}_i=\left(v_{i,1},v_{i,2},\cdots,v_{i,n}\right)^T$ and the best individual particle is $\boldsymbol{p}_i=\left(p_{i,1},p_{i,2},\cdots,p_{i,n}\right)^T$. When particles find the best individual locations and the global best location, we can use equation (1) and (2) to update their velocity and positions:

$$\begin{aligned} v_{i,d}^{(k+1)} &= \omega v_{i,d}^{(k)} + c_1 rand()(pbest_{i,d}^{(k)} - x_{i,d}^{k}) \\ &\quad + c_2 rand()(gbest_{i,d}^{(k)} - x_{i,d}^{(k)}) \end{aligned}, \tag{1}$$

$$x_{i,d}^{(k+1)} = x_{i,d}^{(k)} + v_{i,d}^{(k+1)}, \tag{2}$$

where c_1 and c_2 are accelerating constants; $rand()$ is used to generate a random number between (0,1); $v_{i,d}^{(k)}$ and $x_{i,d}^{(k)}$ are the velocity and positions of the *d*th dimension of particle i in the k iteration; $pbest_{i,d}^{(k)}$ is the best individual position of a particle and $gbest_{i,d}^{(k)}$ is the best position of the global particles.

B. The description of the proposed fePSO algorithm

For particle i in the population, the standard PSO velocity update formula (1) is substituted into the position update formula (2), we have:

$$\begin{aligned} x_{i,d}^{(k+1)} &= x_{i,d}^{(k)} + \omega v_{i,d}^{(k)} \\ &\quad + c_1 rand()(pbest_{i,d}^{(k)} - x_{i,d}^{k}) \\ &\quad + c_2 rand()(gbest_{i,d}^{(k)} - x_{i,d}^{(k)}) \end{aligned}. \tag{3}$$

From (2), we know that:

$$x_{i,d}^{(k)} = x_{i,d}^{(k-1)} + v_{i,d}^{(k)}. \tag{4}$$

Thus,

$$v_{i,d}^{(k)} = x_{i,d}^{(k)} - x_{i,d}^{(k-1)}. \tag{5}$$

Substituting (5) into (3), after rearrangement, it becomes:

$$\begin{aligned} x_{i,d}^{(k+1)} &= (1+\omega - c_1 rand() - c_2 rand())x_{i,d}^{(k)} \\ &\quad - \omega x_{i,d}^{(k-1)} + c_1 rand()\, pbest_{i,d}^{(k)} \\ &\quad + c_2 rand()\, gbest_{i,d}^{(k)} \end{aligned}. \tag{6}$$

From (6), we know that the (k+1)-th generation position $x_{i,d}^{(k+1)}$ of particle i can be obtained by linear combination of $x_{i,d}^{(k)}$, $x_{i,d}^{(k-1)}$, $pbest_{i,d}^{(k)}$ and $gbest_{i,d}^{(k)}$. Thus, the (k+1)-th generation fitness $f\left(x_{i,d}^{(k+1)}\right)$ of particle i can be obtained by these four locations fitness linearly weighted, where weight coefficients can be determined by the distances from the (k+1)-th generation position $x_{i,d}^{(k+1)}$ of particle i to $x_{i,d}^{(k)}$, $\boldsymbol{x}_{i,d}^{(k-1)}$, $pbest_{i,d}^{(k)}$ and $gbest_{i,d}^{(k)}$. Suppose $d_i^{(k)}$, $d_i^{(k-1)}$, $d_{ip}^{(k)}$ and $d_{ig}^{(k)}$, respectively, denote the distances from the (k+1)-th generation position $x_{i,d}^{(k+1)}$ of particle i to $x_{i,d}^{(k)}$, $\boldsymbol{x}_{i,d}^{(k-1)}$, $pbest_{i,d}^{(k)}$ and $gbest_{i,d}^{(k)}$. The (k+1)-th generation fitness $f\left(x_{i,d}^{(k+1)}\right)$ of particle i can be calculated as follows:

$$\begin{aligned} f(x_{i,d}^{(k+1)}) &= \frac{1}{\alpha}\frac{1}{d_i^{(k)}} f(x_{i,d}^{(k)}) + \frac{1}{\alpha}\frac{1}{d_i^{(k-1)}} f(x_{i,d}^{(k-1)}) \\ &\quad + \frac{1}{\alpha}\frac{1}{d_{ip}^{(k)}} f(pbest_{i,d}^{(k)}) \\ &\quad + \frac{1}{\alpha}\frac{1}{d_{ig}^{(k)}} f(gbest_{i,d}^{(k)}) \end{aligned}, \tag{7}$$

where

$$\alpha = \frac{1}{d_i^{(k)}} + \frac{1}{d_i^{(k-1)}} + \frac{1}{d_{ip}^{(k)}} + \frac{1}{d_{ig}^{(k)}}. \tag{8}$$

Obviously, if the fitness of the particle i in (k-1)-th generation and k-th generation are known, the fitness in (k+1)-th generation can be predicted by the formula (7). Like the standard PSO, the best position of population in this method is also selected from the best position of all individuals.

It must be mentioned that in formula (7) distances $d_i^{(k)}$, $d_i^{(k-1)}$, $d_{ip}^{(k)}$, and $d_{ig}^{(k)}$ have an very important impact on the fitness value $f\left(x_{i,d}^{(k+1)}\right)$. If one of them is too small, its reciprocal will be very large, and it will be the main part of the fitness value. Moreover, if one of them is zero, the expression (7) has no meaning. So, we have to avoid this happened. Usually, we should give a certain threshold. If the distance is less than the threshold, the algorithm will be terminated. Of course, as we all know as the PSO algorithm evolutes, the $x_{i,d}^{(k+1)}$ will approaches the $gbest_{i,d}^{(k)}$. In this situation, the termination is normal. Otherwise, the termination is abnormal, which we should avoid it. In this paper, the threshold is 0.0001.

C. Proposed PSO algorithm

The flowchart of the fePSO algorithm is shown in Fig. 1, and the main steps of the proposed algorithm for optimizing complex microwave devices are as follows.

(1) Modeling the microwave device in HFSS;

(2) PSO initialization, including population size, inertia weight, cognitive coefficient and social coefficient, number of iterations;

(3) For the first two generations of the population, calculate particles fitness using the model in HFSS, which is the true fitness, and update particles velocity and positions according to formula (1) and (2);

(4) According to the previous two generations particles position and fitness, we can calculate the next generation particle fitness using formula (7), which is the estimated fitness, and then update the particles position using formula (6);

(5) Return to step (4) until the number of iterations is reached, then the algorithm stops.

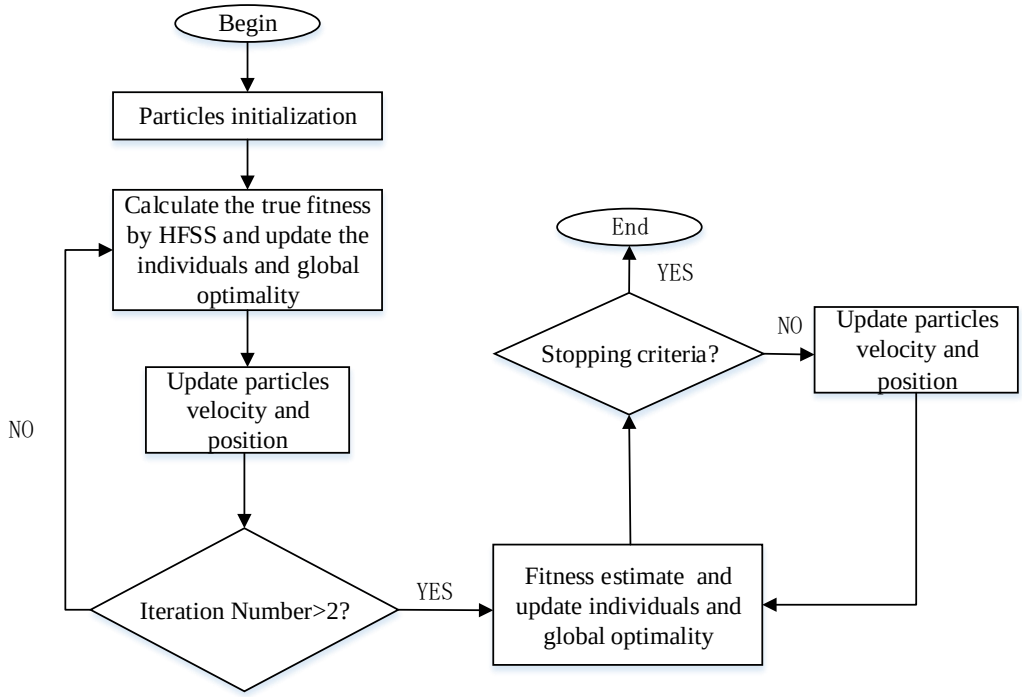

Fig. 1. Flowchart of the proposed fePSO algorithm.

III. OPTIMAL DESIGN OF YAGI MSA BASED ON THE PROPOSED fePSO ALGORITHM

Yagi-Uda antenna was developed by two Japanese scholars Shintaro Uda and Hidetsugu Yagi in 1920, and it is called "Yagi Antenna" for short [28]. Yagi antenna is composed of a feeder oscillator and several passive parasitic oscillator side by side, and it is a commonly used for radar, television and meter, decimeter band end-fire antenna in communication. In 1989, Huang designed a Yagi MSA for mobile satellite equipment [29]. Yagi MSA has get high attention due to its small size, light weight, compact structure, easy processing and integration features. In 1998, Qian proposed a Yagi MSA with broadband characteristics [30]. The broadband impedance matching was performed on the antenna through microstrip line to a broadband balun structure with coplanar strip line [31], and it used a truncated floor acting as a reflector. As a result, it gained 17% relative bandwidth and 6.5 dB gain. The Yagi MSA is widely used in tunnels, narrow mines due to its high gain and wide beam width. In this section, we will optimize a Yagi MSA by the proposed fePSO algorithm.

The structure of the Yagi MSA is shown in Fig. 2 (a) and its HFSS model is shown in Fig. 2 (b). The antenna uses a tapered microstrip balun for feeding, and uses a tapered structure to connect the microstrip line and the excitation array. There is a reflection array, an excitation array and a lead array on the substrate. The parameters related to the performance of the antenna include the length of the reflection element W, the diameter of the cylinder d, the length of the excitation element d_r and the width W_1, the length and width of the lead element d_1 and W_2, the distance between the excitation element and the reflection element g_1, the distance between the excitation element and the lead

element g_2, the distance between the lead elements g_3, the width of the feed microstrip line S_2 and the width of the ground plane S_1. The dielectric board material is FR4, which length is L, width is W, thickness is h, the relative dielectric constant ε_r = 4.4 and dielectric loss tangent $\tan\delta$ = 0.02.

The design specifications of the antenna is that the center frequency is 2.45GHz covering 2.4 ~ 2.483GHz WiFi frequency band. Totally, there are 12 variables except the dielectric board. We select 4 variables to optimize, and the other fixed sizes are shown in Table 1. The optimized size parameters are $\boldsymbol{v}$=[d_r g_1 g_2 g_3], where the range of each parameter is d=[40, 45], g_1=[15, 20], g_2=[8, 14], g_2 = g_3.

Table 1: Fixed parameters of the Yagi MSA

Names	Value (mm)
W	60
d	2
W1	4.96
d1	37
W2	3.7
S2	1.5
h	0.8
L	120

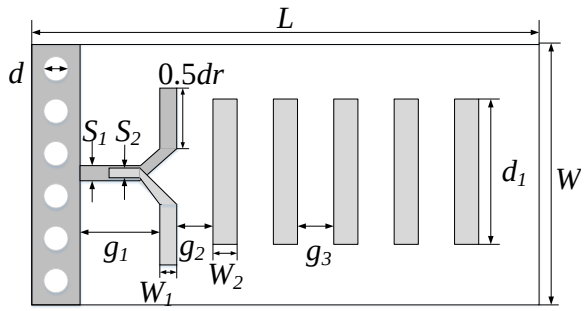

(a) Structure of the Yagi MSA

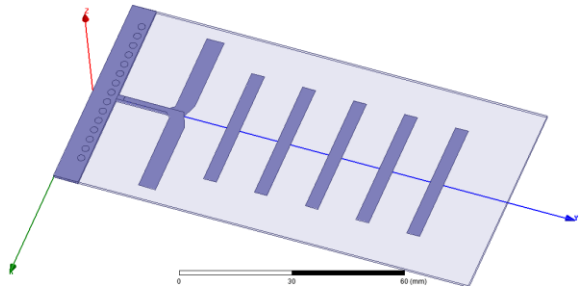

(b) Model of the Yagi MSA in HFSS

Fig. 2. The Yagi MSA.

Select 24 groups $\boldsymbol{v}$ =[d_r g_1 g_2 g_3] as the initial population using orthogonal design method, which means the number of particles is 24. The maximum number of iterations is 500. For the first two generations of the population, calculate reflection coefficient S_{11} in HFSS, which is the true fitness, and update particles velocity and positions according to equation (1) and (2), where c_1=c_2=2, ω =1. According to the previous two generations particles position and fitness, we can calculate the next generation particle fitness using equation (7) and update the particles position using equation (6). When the number of iterations is reached, we may save the optimal size combination. Then, we model the Yagi MSA with the optimal sizes into HFSS to calculate exact solution for comparison.

In this example, the fitness function of the fePSO is given by:

$$Fit = \max\left|S_{11@2.45GHz}\right|. \tag{9}$$

According to the proposed fePSO algorithm and equation (9), we get the optimal result, which is $\boldsymbol{v}$ = [41.6252 18.3370 12.1976 12.1976].

After optimization, the accuracy of the model is evaluated using the average absolute error (ABE). Assume $y_{pred,i}$ is calculated by equation (7), and its precision value computed by HFSS is y_i. We select T data points for each group of data, so the ABE is given by:

$$ABE = \frac{1}{T}\sum_{i=1}^{T}\left|y_{pred,i} - y_i\right|. \tag{10}$$

Table 2: ABE of different test samples

Test Sample Number	ABE
1	0.2013
2	0.2955
3	0.1981
4	0.2480
5	0.3314

In order to demonstrate the accuracy of formula (7), in this example, we select five sets of sizes randomly in the 3rd generation as test samples for comparison with computing results by HFSS, and the results are in Table 2. There are 41 points selected for the S_{11}, that is, T = 41 in (10), then the ABE is calculated. It can be seen from Table 2 that the ABE of the five test samples are around 0.2. Also, according to (10), we compute the ABE of the optimized result, which is 0.2610. Therefore, we can conclude that the results given by the fePSO algorithm are very close to the accuracy values in HFSS, which means the method is effective.

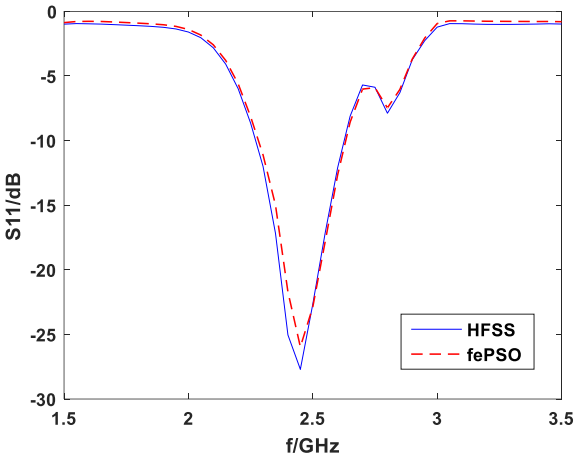

(a) S_{11} of the optimized Yagi MSA

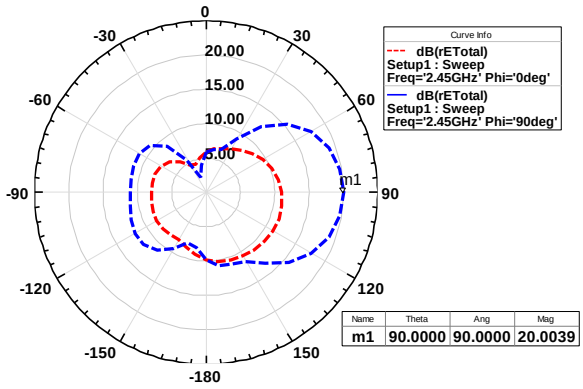

(b) Pattern of the optimized Yagi MSA

Fig. 3. Optimal results of the Yagi MSA.

The performance of the optimized Yagi MSA is given in Fig. 3. From Fig. 3 (a) we know that the resonant frequency is 2.45GHz, the attenuation is -27dB, and covers the WiFi frequency band from 2.4 to 2.483GHz with -10dB. Figure 3 (b) shows the radiation pattern. It can be seen that the maximum gain of the optimized Yagi MSA can reach 20dB at 2.45 GHz, which meets the requirements. Therefore, the fePSO algorithm can be used to optimize the Yagi MSA, and the performance is excellent.

When optimizing the Yagi MSA by using standard PSO exploiting HFSS, it takes about 150s for a particle, therefore 24 particles need around 1800000s after 500 iterations. When optimizing the Yagi MSA by GP, establishing a precise GP model needs at least 28 sets of data after many trials. Only calculating HFSS to acquire 28 sets of data requires 4004s. But before modeling, it needs tedious manual extraction and arrangement of the data. When establishing a precise ANN model for the Yagi MSA, it requires more than 28 sets of data, the total time will be more time-consuming than optimization by GP model. Moreover, the training time either GP or ANN is necessary. However, it only needs 7210s using the proposed fePSO algorithm after 500 iterations. Therefore, the optimization of the Yagi MSA using the fePSO algorithm can greatly shorten the optimization time.

IV. OPTIMAL DESIGN OF SIR MICROSTRIP BANDPASS FILTER BASED ON THE PROPOSED fePSO ALAGORITHM

In microwave communications, microstrip bandpass filter directly affects the performance of the system. There are many kinds of microwave bandpass filters, such as capacitive gap coupling transmission line bandpass filters, comb bandpass filters, interdigital filters and half-wavelength resonators parallel coupled bandpass filters. Straddy Impedance Resonator (SIR) parallel coupled bandpass filter is a unique parallel coupled bandpass filter. It was first proposed by Mitsuo Makimoto and Sadahiko Yamashita in 1980 [32], which is an essential components between the low-noise final amplifier and Mixer. Compared with the traditional microstrip filters, the hairpin SIR microstrip bandpass filter has the advantages of small size, easy integration and low cost. By controlling the coupling and non-coupling segments, the position of the parasitic passband can be controlled. The problem of harmonic suppression is solved, so it has been widely used in the L-band and S-band.

The structure of the L-band hairpin SIR microstrip band-pass filter is shown in Fig. 4 (a), and the HFSS model is shown in Fig. 4 (b). The parameters for a single resonator are as follows: l_1 and l_c are the length of the different microstrip lines; w_t and w_c are the width of the different microstrip lines; l_2 is the width of a single resonator unit and l-l_2 is the spacing of adjacent resonator units; The thickness of dielectric substrate is h and the relative dielectric constant ε_r = 9.5.

The design specifications of the SIR microstrip bandpass filter are that the center frequency is 1.2GHz, -3dB bandwidth is greater or equal to 50MHz, $S_{21} \le -40$ dB in 1.05GHz and 1.35GHz. In this example, two sizes are selected for optimization. The optimized size parameter is $\boldsymbol{v}=[w_t\ l_1]$, where the range of each parameter is w_t=[0.5, 0.9], l_1=[6.5, 8.5]. Other dimensions are fixed, as shown in Table 3.

Select 24 groups $\boldsymbol{v} = [w_t\ l_1]$ as the initial population using orthogonal design, in which the number of particles is 24. The maximum number of iterations is 500. For the first two generations of the population, calculate transmission coefficient S_{21} in HFSS, which is the true fitness, and update particles velocity and positions according to equation (1) and (2), where c_1=c_2=2, ω =1. According to the previous two generations particles position and fitness, we can calculate the next generation particle fitness using equation (7) and update the particles position using equation (6). When the number of iterations is reached, we get the optimal size

combination. After that, the SIR microstrip band-pass filter with the optimized parameters is modeled in HFSS to calculate its exact solution for comparison.

In this example, the fitness function of the fePSO for the filter is given by:

$$Fit = \left(S_{21@1.185GHz} < 3\right) \&\& \left(S_{21@1.235GHz} < 3\right) \&\& \left(S_{21@1.05GHz} > 40\right) \&\& \left(S_{21@1.35GHz} > 40\right). \quad (11)$$

According to the proposed fePSO algorithm and equation (11), we get the optimal result, which is $\boldsymbol{v}$ = [0.8074 8.3717].

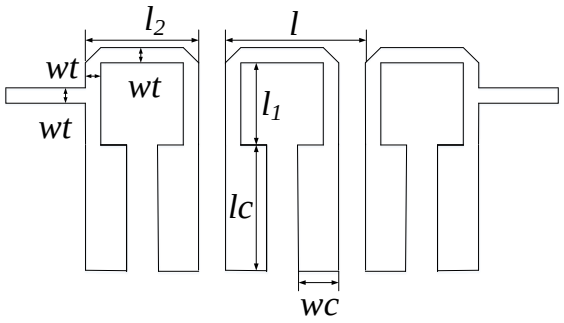

(a) SIR microstrip band-pass filter structure

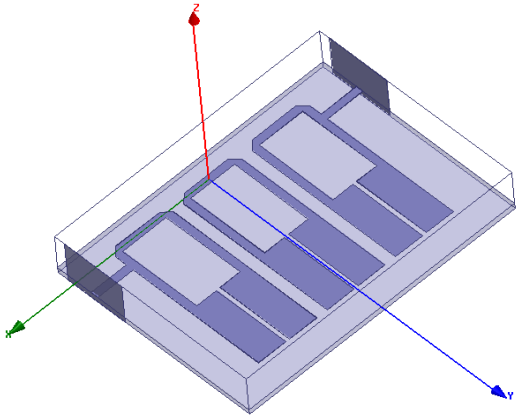

(b) SIR microstrip band-pass filter model in HFSS

Fig. 4. The SIR microstrip bandpass filter.

Table 3: Fixed parameters of the SIR microstrip bandpass filter

Names	Value (mm)
wc	2.76
lc	7.25
l_2	5.2
l	7
h	0.254

In order to demonstrate the accuracy of formula (7), in this example, we select five sets of sizes randomly in the 3rd generation as test samples for comparison with computing results by HFSS, and the result is in Table 4.

There are 61 points selected for the S_{21}, that is, T = 61 in (10), then the ABE is calculated. It can be seen from Table 4 that the ABE of the five test samples are around 0.5. Also, according to (10), we compute the ABE of the optimized result, which is 0.6792. Therefore, we can conclude that the results given by the fePSO algorithm are very close to the accuracy values in HFSS, which means the method is effective.

Table 4: ABE of different test samples

Test Sample Number	ABE
1	0.4792
2	0.5602
3	0.4125
4	0.7939
5	0.4489

From the optimized result in Fig. 5 we can see that the SIR microstrip bandpass filter center frequency is 1.2GHz and the 3dB cutoff bandwidth reached 50MHz. At 1.05 GHz and 1.35 GHz, the decay have reached 40dB. It can meet the design requirements.

When optimizing a SIR microstrip bandpass filter by using standard PSO exploiting HFSS, it takes about 40s for a particle in HFSS and 24 particles need around 480000s after 500 iterations. When optimizing design the SIR microstrip band-pass filter by GP, we find it needs at least 10 sets of data after many trials for establishing a precise GP model. Only calculating HFSS to acquire 10 sets of data requires 400s. Also, we need some time to train the GP. When establishing a precise ANN model of the SIR microstrip band-pass filter, it requires more than 10 sets of data, the total time will be more time-consuming than optimization by GP model. However, it only needs 1930s using the proposed fePSO algorithm after 500 iterations. The optimization of the SIR microstrip bandpass filter using the fePSO algorithm can greatly increase the optimization design efficiency.

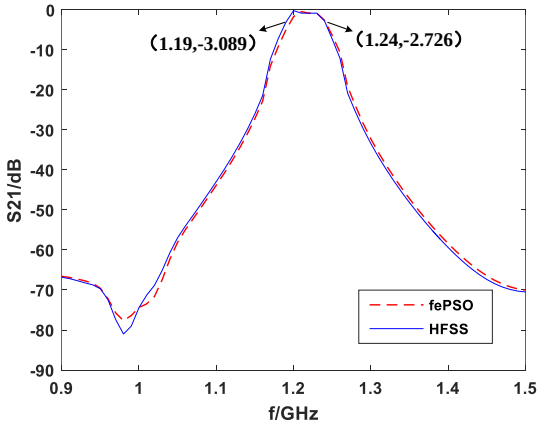

Fig. 5. S_{21} of the optimized SIR bandpass filter.

V. CONCLUSION

When optimizing complex microwave devices, it takes a lot of time to use global optimization algorithms exploiting full-wave electromagnetic simulation software. The most commonly used fitness prediction methods such as neural networks, support vector machines and Gaussian processes require sample acquisition and training. And the choice of sample affects the correctness of the constructed model. The fitness estimation method proposed in this paper is derived from the explicit evolutionary formula of particle swarm optimization, that is, the fitness of the offspring is obtained through the weighted average of the fitness of the parents. Therefore, only the first and the second generation true fitness are needed. The third generation fitness can be obtained by weighting the position and fitness of the first and the second generation particles, and the fourth generation fitness can be obtained by weighting the position and fitness value of the second and the third generation particle, and so on. When optimizing the microwave devices, only the first two generations of particles need to be solved in the full wave electromagnetic simulation software, and then the prediction formula is used in the subsequent iterative optimization, which can greatly improve the optimization efficiency. In this paper, the Yagi microstrip antenna and hairpin SIR bandpass filter are optimized respectively. From the results, it can be seen that this method can achieve good optimization design in a short time, so this method provide theoretical guidance for the optimal design of complex microwave devices.

ACKNOWLEDGMENT

This work is supported by the National Natural Science Foundation of China (NSFC) under No. 61771225, the Key Research and Development Program Project of Social Development in Jiangsu Province under No. BE2016723, the Postgraduate Research & Practice Innovation Program of Jiangsu Province China under No. KYCX18_2326, and the Qinglan Project of Jiangsu Higher Education.

REFERENCES

[1] Y. B. Tian, *Particle Swarm Optimization Algorithm and Electromagnetic Applications*. Beijing: Science Press, 2014. (in Chinese).

[2] J. Zolghadr, Y. Cai, and N. Ojaroudi, "UWB slot antenna with band-notched property with time domain modeling based on genetic algorithm optimization," *Applied Computational Electromagnetics Society Journal*, vol. 31, no. 8, pp. 926-932, 2016.

[3] A. A. Adly and S. K. Abd-El-Hafiz, "Utilizing particle swarm optimization in the field computation of non-linear magnetic media," *Applied Computational Electromagnetics Society Journal*, vol. 18, no. 3, pp. 202-209, 2003.

[4] Q. J. Zhang, K. C. Gupta, and V. K. Devabhaktuni, "Artificial neural networks for RF and microwave design - From theory to practice," *IEEE Transactions on Microwave Theory & Techniques*, vol. 51, no. 4, pp. 1339-1530, 2003.

[5] Z. Wang, S. Fang, Q. Wang, et al., "An ANN-based synthesis model for the single-feed circularly-polarized square microstrip antenna with truncated corners," *IEEE Transactions on Antennas & Propagation*, vol. 60, no. 12, pp. 5989-5992, 2012.

[6] F. Chen and Y. B. Tian. "Modeling resonant frequency of rectangular microstrip antenna using CUDA-based artificial neural network trained by particle swarm optimization algorithm," *Applied Computational Electromagnetics Society Journal*, vol. 29, no. 12, pp. 1025-1034, 2014.

[7] Y. Chen, Y. B. Tian, and M. J. Le, "Modeling and optimization of microwave filter by ADS-based KBNN," *International Journal of RF and Microwave Computer Aided Engineering*, vol. 27, no. 2, 2017.

[8] G. Angiulli, M. Cacciola, and M. Versaci, "Microwave devices and antennas modelling by support vector regression machines," *IEEE Transactions on Magnetics*, vol. 43, no. 4, pp. 1589-1592, 2007.

[9] M. Al Sharkawy, M. Sharkas, and D. Ragab, "Breast cancer detection using support vector machine technique applied on extracted electromagnetic waves," *Applied Computational Electromagnetics Society Journal*, vol. 27, no. 4, pp. 292-301, 2012.

[10] F. Y. Sun, Y. B. Tian, and Z. L. Ren, "Modeling the resonant frequency of compact microstrip antenna by the PSO-based SVM with the hybrid kernel function," *International Journal of Numerical Modelling: Electronic Networks, Devices and Fields*, vol. 29, no. 6, pp. 1129-1139, 2016.

[11] A. Kayabasi, "Analysis and synthesis of equilateral triangular ring microstrip antenna using support vector machine," *Applied Computational Electromagnetics Society Journal*, vol. 33, no. 6, pp. 616-624, 2018.

[12] J. P. D. Villiers and J. P. Jacobs, "Gaussian process modeling of CPW-fed slot antennas," *Progress in Electromagnetics Research*, vol. 98, no. 4, pp. 233-249, 2009.

[13] J. P. Jacobs and J. P. D. Villiers, "Gaussian-process-regression-based design of ultrawide-band and dual-band CPW-fed slot antennas," *Journal of Electromagnetic Waves & Applications*, vol. 24, no. 13, pp. 1763-1772, 2010.

[14] Y. Chen, Y. B. Tian, Z. Qiang, and L. Xu, "Optimization of reflection coefficient of microstrip antennas based on KBNN exploiting GPR model," *IET Microwaves, Antennas & Propagation*,

vol. 12, no. 4, pp. 602-606, 2018.
[15] R. E. Smith, B. A. Dike, and S. A. Stegmann, "Fitness inheritance in genetic algorithms," *ACM Symposium on Applied Computing. DBLP*, pp. 345-350, 1995.
[16] M. Salami and T. Hendtlass, "A fast evaluation strategy for evolutionary algorithms," *Applied Soft Computing*, vol. 2, no. 3, pp. 156-173, 2003.
[17] C. L. Sun, J. C. Zeng, et al., "A new fitness estimation strategy for particle swarm optimization," *Information Sciences*, vol. 221, no. 2, pp. 355-370, 2013.
[18] A. Xiao, B. Wang, C. Sun, S. Zhang, and Z. Yang, "Fitness estimation based particle swarm optimization algorithm for layout design of truss structures," *Mathematical Problems in Engineering*, 2014.
[19] Z. Cui, J. Zeng, and G. Sun, "A fast particle swarm optimization," *International Journal of Innovative Computing Information & Control*, vol. 2, pp. 148-155, 2009.
[20] J. Kennedy and R. Eberhart, "Particle swarm optimization," *IEEE International Conference on Neural Networks, 1995. IEEE Proceedings*, vol. 4, pp. 1942-1948, 2002.
[21] R. Eberhart and J. Kennedy, "A new optimizer using particle swarm theory," *IEEE International Symposium on Micro Machine and Human Science*, pp. 39-43, 2002.
[22] M. Clerc, "From theory to practice in particle swarm optimization," *Simulation Transactions of the Society for Modeling & Simulation International*, vol. 86, no. 3, pp. 181-197, 2011.
[23] W. Wang, Y. Lu, J. S. Fu, et al., "Particle swarm optimization and finite-element based approach for microwave filter design," *IEEE Transactions on Magnetics*, vol. 41, no. 3, pp. 1800-1803, 2005.
[24] B. S. Darki and N. Granpayeh, "Improving the performance of a photonic crystal ring-resonator-based channel drop filter using particle swarm optimization method," *Optics Communications*, vol. 283, no. 20, pp. 4099-4103, 2010.
[25] Y. B. Tian, D. Yue, Z. B. Xie, S. Sha, and T. Peng, "Frequency characteristics of electromagnetic band-gap structure with bow-tie cells and its optimal design based on particle swarm optimization," *IEEE Transactions on Electrical and Electronic Engineering*, vol. 8, no. 1, pp. 63-68, 2013.
[26] M. H. Ho, C. C. Chiu, and S. H. Liao, "Optimization of channel capacity for multiple-input multiple-output smart antenna using a particle swarm optimizer," *IET Communications*, vol. 6, no. 16, pp. 2645-2653, 2012.
[27] P. Nayeri, F. Yang, and A. Z. Elsherbeni, "Design of single-feed reflect array antennas with asymmetric multiple beams using the particle swarm optimization method," *IEEE Transactions on Antennas & Propagation*, vol. 61, no. 9, pp. 4598-4605, 2013.
[28] H. Yagi and S. Uda, "Projector of the sharpest beam of electric waves," *Proc. of the Imperial Academy of Japan*, vol. 2, no. 2, pp. 49-52, 1926.
[29] J. Huang, "Planar microstrip Yagi array antenna," *IEEE International Symposium*, vol. 2, pp. 894-897, 1989.
[30] Y. Qian, W. R. Deal, N. Kaneda, et al., "Microstrip-fed quasi-Yagi antenna with broadband characteristics," *Electronics Letters*, vol. 34, no. 23, pp. 2194-2196, 1998.
[31] Y. Qian and T. Itoh, "A broadband uniplanar microstrip-to-CPS transition," *Microwave Conference Proceedings, 1997. APMC '97, 1997 Asia-Pacific. IEEE Xplore*, vol. 34, pp. 609-612, 1997.
[32] M. Makimoto and S. Yamashita, "Bandpass filters using parallel coupled strip-line stepped impedance resonators," *Microwave Symposium Digest, 1980 IEEE MTT-S International. IEEE*, pp. 141-143, 1980.

Xiao-hong Fan (1994-), Graduate student. Her main research is rapid design of microwave devices. Address: School of Electronics and Information, Jiangsu University of Science and Technology, Zhenjiang 212003, P. R. China.

Yu-bo Tian (1971-), received his Ph.D. in 2004 from Nanjing University. Now, he is a Full Professor at Jiangsu University of Science and Technology. His main research concerns computational intelligence and swarm intelligence technologies and applications in electronics and electromagnetism. Address: School of Electronics and Information, Jiangsu University of Science and Technology, Zhenjiang 212003, P. R. China.

An Irregular Ground Oriented Miniaturized Antenna for UWB Industrial Applications

Md Z. Mahmud [1,2], T. Alam [2], M. Samsuzzaman [2], A. Ullah [2], and Mohammad T. Islam [2]

[1] Department of AIS
Jagannath University, Dhaka 1000, Bangladesh
zulfikerm@yahoo.com

[2] Centre of Advanced Electronic and Communication Engineering (PAKET)
Universiti Kebangsaan Malaysia, 43600, Bangi
tauhid13@yahoo.com, samsuzzaman@ukm.edu.my, amanath.ullah@gmail.com, tariqul@ukm.edu.my

***Abstract* –** In this paper, a new small UWB antenna for different UWB industrial applications is presented. The proposed prototype comprises of a simple structure with a modified triangular patch and a sawtooth ground plane. The electrical size of the proposed antenna is 0.15λ× 0.13λ×0.014λ, at lower end frequency. The patch and ground plane is optimized and analyzed. The antenna shows 116% of VSWR<2 impedance bandwidth from 2.8 to 10.5 GHz with a peak gain of 5.6 dBi and 75% of the average radiation efficiency. The proposed design established a nearly omnidirectional radiation characteristic over the operating frequency band. The proposed antenna was successfully simulated, prototyped, and measured. The uniqueness of the proposed antenna is the miniaturization of the antenna for the UWB frequency band, which can be applied for different portable and convenient UWB applications.

***Index Terms* –** Antenna, partial ground plane, UWB, wideband, wireless communication.

I. INTRODUCTION

The demand for a high-performance antenna with wider bandwidth is increasing exponentially due to the rapid growth of the global wireless communication industry. UWB has become a promising technology and area of interest in different industrial applications like short-range communication, ranging and localization, tracking, and data relay satellite (TDRSS), removable media in computers, etc. This is due to some of its striking features like high data rate, small spectral power density, high precision, low cost, robust to multi-path fading, very low interference etc. The Federal Communications Commission (FCC) has assigned 7.5 GHz spectrum from 3.1 to 10.6 GHz for UWB radio applications since February 2002 [1]. Typically, UWB antennas should be electronically small and inexpensive while maintaining desirable wideband performance for different industrial applications. UWB has wide applications in short range and high-speed wireless systems, such as ground penetrating radars, medical an imaging system, high data rate wireless local area networks (WLAN), communication systems for military and short pulse radars for automotive even or robotics [2-5]. Thus, one of the main challenges of designing UWB antennas is to get higher bandwidth, efficiency, and low profile within allocated smaller dimensions.

UWB antenna characteristics can improve by changing the shape of the radiating patch. The patch may be rectangular, circular, heart-shaped, elliptical, etc. The antenna performance also can be improved by manipulating the ground structure [6-12]. In the work of Gokmen et al. [13], a compact size UWB antenna with heart shape using triangular patches with dimensions of 25×26×0.5 mm^3, operating from 4 GHz to 19.1 GHz, is proposed. Liu and Yang [14] presented a hook-shaped UWB antenna operating from 3 GHz to 10.7 GHz with dimensions of 10×10×1.6 mm^3. In the work of Ojaroudi et al. [15], UWB monopole antenna for 3.12 to 11.2 GHz bandwidth with an inverted T-shaped notch in the ground plane is presented with a compact size of 12×18 mm^2. A Tapered-shaped slot antenna [16] with an area of 22×24 mm^2 is presented with operational frequencies from 3 GHz to 11.2 GHz. In another study [17], the antenna is designed with a heart-shaped patch and a defected ground plane. This antenna is proposed and optimized for ultra-wideband applications. To increase the impedance bandwidth and reduce the reflection coefficient, three semi-circular slots were proposed in the ground plane. T. Yang and X. J. Tian [18], proposed a heart-shaped monopole patch and a couple of rectangular ground plane on the same side of a substrate. A standard impedance bandwidth is achieved from 2.1 to 11.5 GHz. Some designs are presented in literature, some of them are large in size, and some of them obtain law gain or low radiation efficiency.

Submitted On: March 4, 2018
Accepted On: June 24, 2018

In this work, a new and ultra-small (13×16mm^2) UWB antenna with enhanced impedance bandwidth is presented. The main objective of the work is to reduce the dimensions of the antenna and increase the bandwidth to make it applicable for portable and convenient UWB applications. This antenna consists of a sawtooth orientation ground plane on the back side of the substrate with a rectangular shape and a patch with the modified triangular shape. The inner parts of the patch are partially etched away to increase the bandwidth especially for covering the lower end of the UWB frequency spectrum. By using the triangular patch and defected ground plane, wide input impedance matching is achieved over the entire 2.9 to 10.5 GHz band with relatively stable omnidirectional radiation patterns. Simulated results of different frequencies for VSWR, gain, efficiency, radiation pattern, Surface Current distribution are presented along with the measured results. The simulation is performed by Computer Simulation Technology (CST) Microwave studio.

II. ANTENNA DESIGN

The geometric layout of the proposed UWB antenna is depicted in Fig. 1. The dimension of the antenna is 13×16 mm^2 of 1.6 mm thickness. Substrate Flame Retardant (FR4) is used with a dielectric constant of 4.3 and loss tangent is 0.025. FR4 is commonly used in the industry because of its low cost and convenient to make from one-layer to multi-layer PCBs. The proposed antenna is composed of a partial radiating patch on one side and ground plane on the opposite side of the substrate. The orientation of the ground plane and shape of the patch has a strong effect on the impedance matching. Therefore, by properly selecting ground orientation and patch shape, good impedance bandwidth and radiation characteristics are achieved. A triangular shape patch is developed on the front side of the antenna. In the middle of the patch, a triangular pattern is etched away. This is mainly done for covering larger bandwidth especially to cover lower frequencies. A microstrip feed line of 1 mm width and 5 mm long is printed on top of the substrate. The gap from patch to end of the substrate in left and the right side is not same. It is much larger on the left side (G) than the right side (g), as shown in Fig. 1. The ground plane of the antenna is a rectangular shape. The height of the ground plane is 4 mm and width is the same as antenna width. The ground consists of a sawtooth configuration on the upper side by etching a number of triangles from a partial rectangular ground plane to improve the performance at higher frequencies. Without this irregularity, discontinuities appear in the operational bandwidth shown in Fig. 3. The proposed prototype use microstrip feed using 50 Ω SMA connectors located at the edge of the lower part of the antenna. At this point, the electromagnetic energy, which is in the form of voltage and current waves, is split into two parts. One flows along the strip line while the other continues through the edge that acts as an open transmission line. The overall size of the antenna is W×L mm^2 and the ground plane has an area of W×L_g mm^2. In Table 1 details of the optimized design, parameter are summarized.

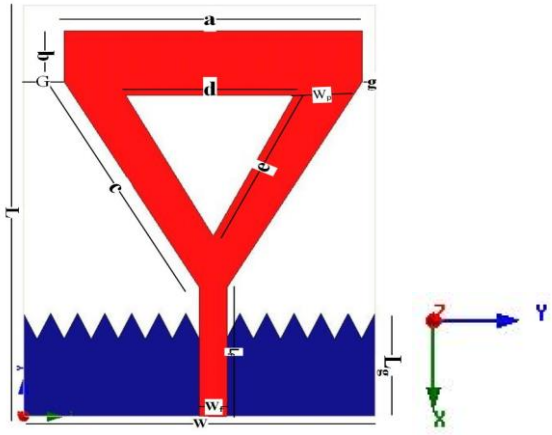

Fig. 1. The geometric layout of the proposed antenna (all dimensions are in mm).

Table 1: Optimized dimension of antenna prototype

Para.	Value (mm)	Para.	Value (mm)	Para.	Value (mm)
W	13	L	16	L_g	4
W_f	1	a	11	b	2
W_p	3.1	G	1.5	g	0.5
c	9.43	d	6.25	e	6.26

The uniqueness of the proposed antenna is its size. The comparison of the proposed antenna with a few recently proposed antennas [6-10] is presented in Table 2. The size of the antenna is significantly reduced in the proposed design.

Table 2: Comparisons of the proposed antenna with existing antenna dimension

Existing Work	Antenna Configuration	Size Decreases (Proposed/ Literature)
[6] Sharma and Shrivastava	Fractal elliptical	97%
[7] Shaalan and Ramadan	Hexagonal monopole	76%
[8] Yang et al.	CPW-fed planar	69%
[9] Liu et al.	Circular-ring	71%
[13] Isik and Topaloglu	Heart shape triangular patch	68%

III. PARAMETRIC STUDY

For investigating the effect of different parameters on antenna performance, some crucial antenna parameters were studied. At a time, a single parameter is changed while others remained unchanged. All the parameters were studied using a CST microwave studio.

A. Effect of ground and patch structure

In order to optimize the patch and ground plane, the proposed design was compared to five other structures as shown in Fig. 2. Their comparative antenna performance in terms of reflection co-efficient S_{11} are shown in Fig. 3. It is evident that the proposed antenna layout achieves much better performance than the other configurations. When full substrate used as a ground, as shown in Fig. 2 (c), no reasonable operating frequency was found. When half of the substrate was used as a ground, as illustrated in Fig. 2 (a), the almost same result was recorded. In other cases, like without the middle triangle, without sawtooth orientation of the ground and without both, there has some band under -10dB but not contiguous. Some parts go higher than -10 dB, hence they do not cover the entire UWB bandwidth. Same parametric study for gain is depicted in Fig. 4. For the gain, it is seen that the proposed layout achieves better gain than other configurations.

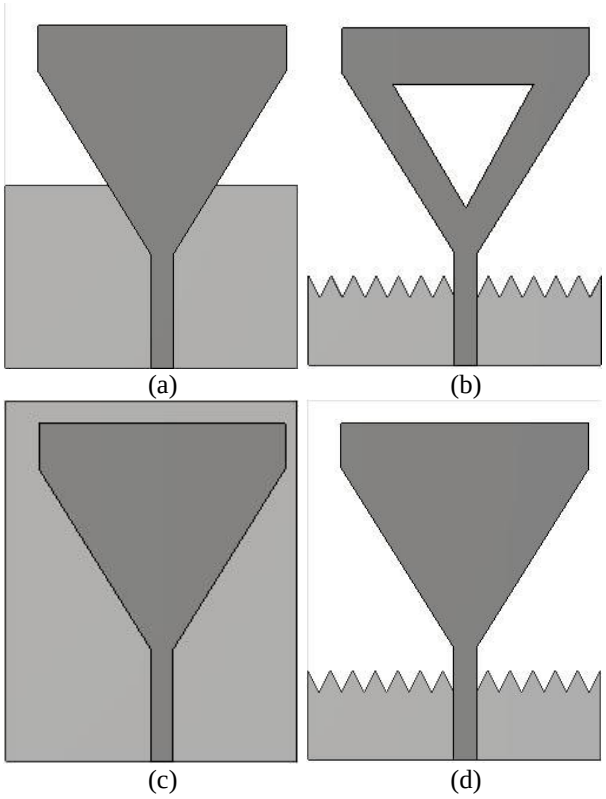

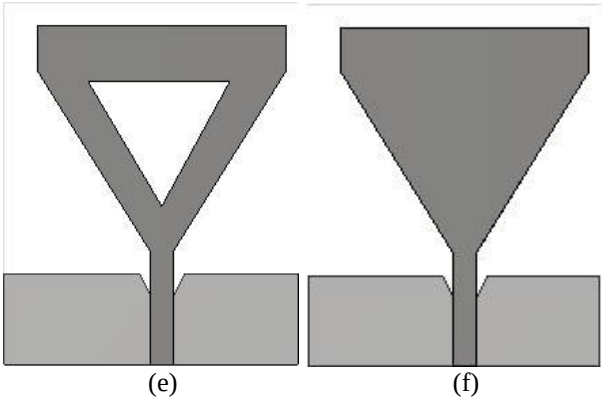

Fig. 2. Different geometric layout: (a) with half ground plane, (b) proposed, (c) full ground, (d) without middle triangle, (e) without saw-tooth ground orientation, and (f) without both saw-tooth ground orientation and middle triangle.

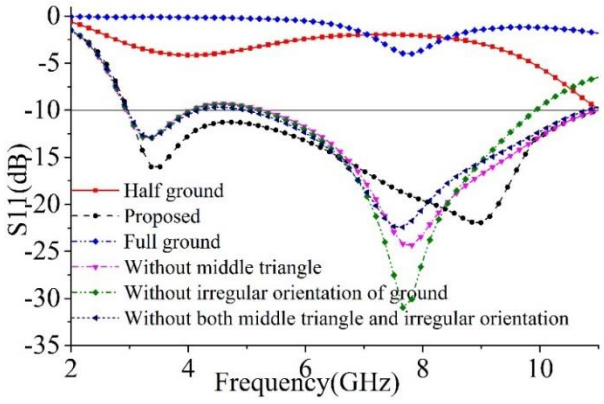

Fig. 3. Simulated reflection coefficient (S_{11}) for a different structure of ground plane and patch.

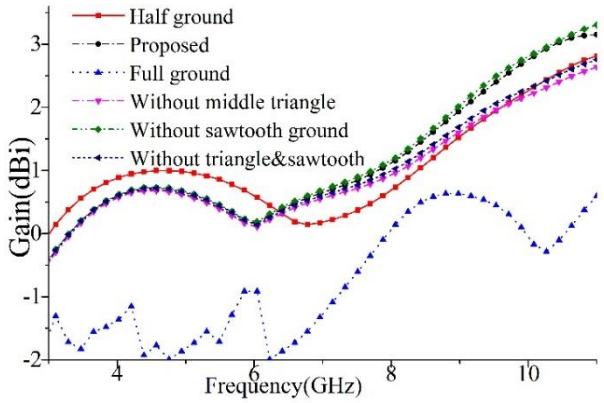

Fig. 4. A simulated gain for a different structure of ground plane and patch.

B. Effect of substrate material

A good selection of substrate will yield superior performance of the antenna. The effect of substrate materials on impedance matching for different dielectric substrates are presented in Fig. 5. The analysis would help to investigate the effects of the different substrate materials on impedance bandwidth. The chosen substrate materials are FR4 (ε_r = 4.3, tanδ = 0.025), Rogers RT 5870 (ε_r = 2.33, tanδ = 0.012), Rogers RT 6010 (ε_r = 10.2, tanδ = 0.0023) and Glass-PTFE (ε_r = 2.33, tanδ = 0.0009). It can be clearly observed from the figure that proposed FR4 composite substrate offers wider bandwidth and lower reflection coefficient for the proposed prototype. Due to good electrical performance, very nice dimensional stability and ideal dielectric constant, FR4 composite materials offer better performance compared to some common substrate materials.

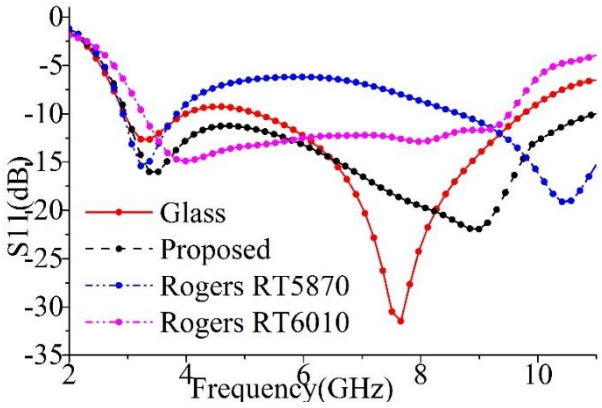

Fig. 5. Simulated reflection coefficient (S_{11}) for different substrate materials

IV. RESULTS AND DISCUSSION

The photograph of the antenna prototyped for experimental verification is shown in Fig. 6. For measurement, the Agilent E8362C vector network analyzer (VNA) shown in Fig. 6 (b) and Satimo near field anechoic chamber (UKM StarLab) shown in Fig. 8 (b) is used. The simulated and experimental Voltage Standing Wave Ratio (VSWR) against the frequency of the proposed antenna are illustrated in Fig. 7. The measured bandwidth for VSWR ≤ 2 ranges from 2.8 GHz to 10.5 GHz and in the simulation from 2.9 GHz to 10.5 GHz. In both cases, it exhibits wideband performance. The measured and simulated results show a good agreement. The minor discrepancies between simulated and measured results can be attributed to imperfect fabrication and the coaxial cable used during measurement. The cable is not considered in the simulation. The size of the proposed antenna is smallest among recently published antenna but it achieves a wide bandwidth. The proposed antenna cover the UWB band (3.1-10.6). A smart average gain of 4.2 dBi presented in Fig. 8. The peak gain is 5.6 dBi at 8.6 GHz. In Fig. 9, the simulated and measured radiation efficiencies of the proposed antenna are presented. The maximum radiation efficiency is achieved at 8.2 GHz of 89% and an average of 75% over the bandwidth. At lower frequency, the efficiency is lower than the average. It is so due to the copper losses of the proposed structure at starting. After a certain level, the losses are minimized and higher order current mode is excited than the efficiency is increased. It also may cause due to the dielectric losses.

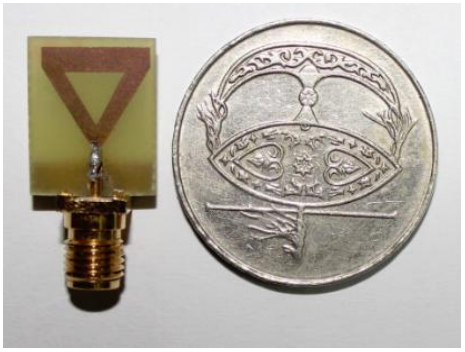

(a)

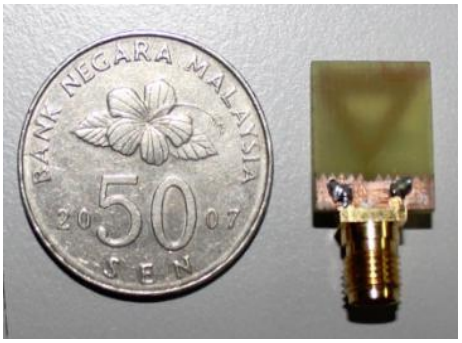

(b)

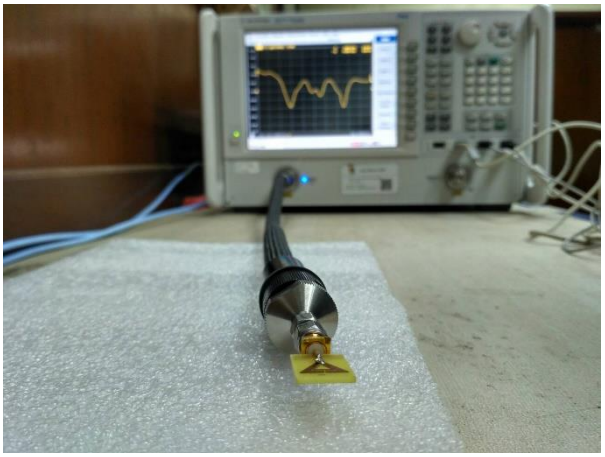

(c)

Fig. 6. Photographs of the fabricated antenna: (a) top layer, (b) bottom layer, and (c) VNA measurement setup.

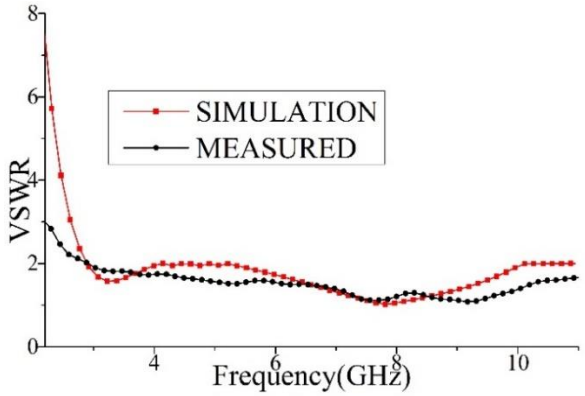

Fig. 7. Simulated and measured VSWR of the proposed antenna.

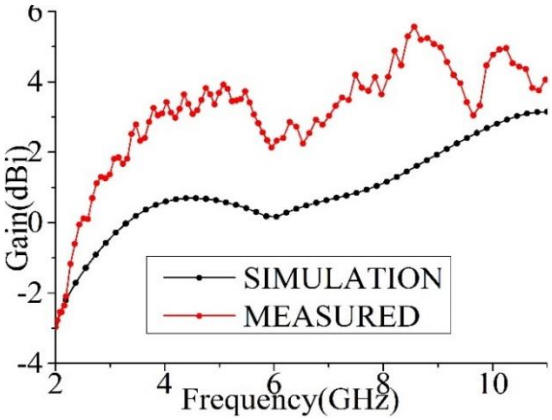

(a)

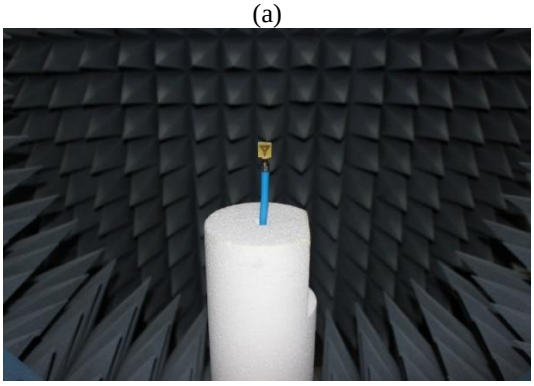

(b)

Fig. 8. (a) Simulated and measured gain of the proposed antenna, and (b) Satimo measurement setup.

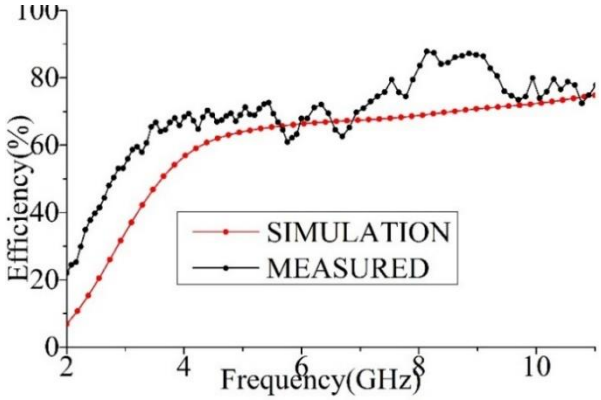

Fig. 9. Simulated and measured efficiency of the proposed antenna.

Measured and simulated radiation pattern, including the cross-polarization and co-polarization of the fabricated antenna for two resonant frequencies 3.25 GHz and 7.8 GHz in both *xz-plane(φ=0)* and *yz-plane(φ=90)*, are shown in Fig. 10. It is seen that, over the desired bandwidth, the proposed antenna exhibits stable radiation pattern characteristics. At lower frequency (3.25 GHz) the radiation pattern is omnidirectional in *xz-plane*. The value of co-polarization is significantly higher than cross-polarization. With the increase of frequency to 7.8 GHz, the cross-polarization increases slightly. At higher frequency in the Fig. 10 (b) in both *xz* and *yz plane* multiple nulls are observed in the radiation pattern as the surface currents are not distributed evenly. This indicates that the radiating element is excited with higher order modes, which typically results in more directional radiation patterns.

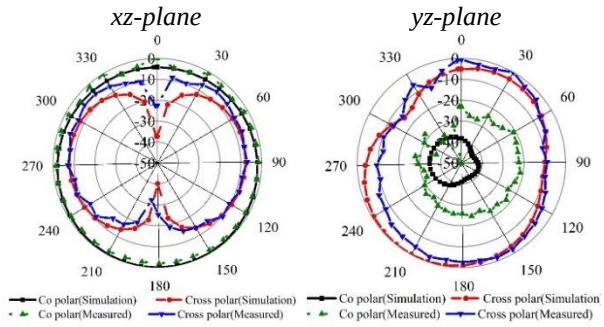

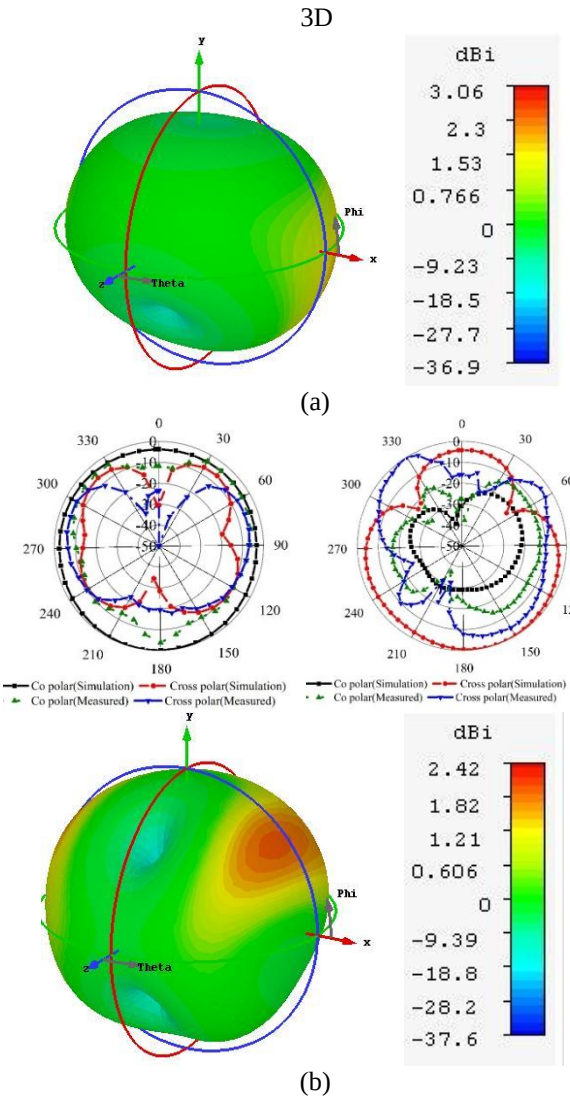

Fig. 10. Measured radiation pattern at different frequencies: (a) 3.25 GHz and (b) 7.8 GHz.

The surface current distribution of proposed defected ground plane antenna is shown in Fig. 11 at 3.2 and 7.8 GHz. The main current conducting area is on the patch and around the middle triangle. The sawtooth on the ground plane change the current path and creates higher order current modes. For this change of ground plane, a remarkable change in the antenna characteristics is found.

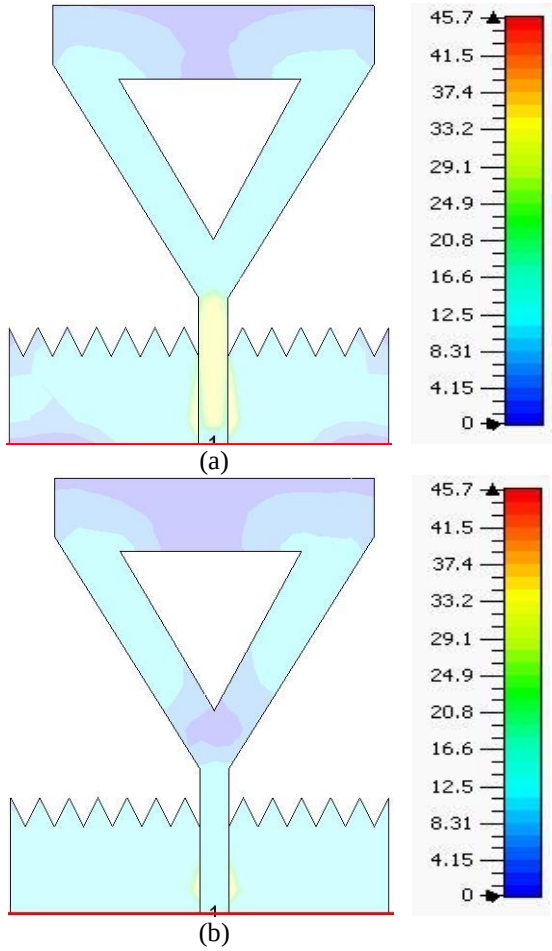

Fig. 11. Current distribution of proposed antenna: (a) 3.2 GHz and (b) 7.8 GHz.

The proposed antenna and the existing antennas (literature review) were studied to ensure an impartial comparison in Table 3, where all reference antennas cover ultra-wideband spectrum. The performances parameters, such as size, applications, less than -10-dB bandwidth, dielectric constant, gain and fractional bandwidth are presented. The proposed antenna is the smallest among all the antenna studied with fair bandwidth and gain. Therefore, the proposed prototype can offer good compact characteristics for different UWB applications.

Table 3: Bandwidth, dielectric constant, fractional bandwidth and gain comparison

Reference	Application	Size (mm^2)	BW (GHz) or VSWR<2dB	ε	FBW (%)	Gain
[13]	UWB	25×26	4-19.1	3.5	100%	3 dBi
[14]	UWB	80×40	3-10.7	4.4	112%	4.5 dBi
[15]	UWB	12×18	3.12-12.73	4.4	120%	--------
[16]	UWB	22×24	3-11.2	4.6	115.5%	4 dBi
[17]	UWB	48×40	2.7-26	4.08	162%	<4 dBi
[18]	UWB & RFID	30×35	2.1-11.5	4.4	110%	<6dBi
Proposed	UWB	13×16	2.8-10.5	4.3	116%	>4.5dBi

V. CONCLUSION

A sawtooth partial ground oriented antenna with an extremely small size of 13×16 mm^2 monopole antenna is proposed for UWB applications. The simulated and measured results comply with the UWB requirements, which is VSWR<2 impedance bandwidth of 116% with stable omnidirectional radiation pattern and 75% of average radiation efficiency over the operating bandwidth. The proposed design is compact in size and can be integrated into limited space around microwave circuitry with low manufacturing cost. The experimental results show that the proposed antenna could be a suitable candidate for industrial UWB Applications.

ACKNOWLEDMENTS

This work was supported by the University Kebangsaan Malaysia, under MI-2017-001.

REFERENCES

[1] F. C. C. FCC, "Revision of Part 15 of the Commission's Rules Regarding Ultra-Wideband Transmission Systems,"First Report and Order," FCC 02," V48, April 2002.

[2] B. Allen, M. Dohler, E. Okon, W. Malik, A. Brown, and D. Edwards, *Ultra Wideband Antennas and Propagation for Communications, Radar and Imaging*. John Wiley & Sons, 2006.

[3] E. Fear and M. Stuchly, "Microwave detection of breast cancer," *Microwave Theory and Techniques, IEEE Transactions on*, vol. 48, pp. 1854-1863, 2000.

[4] H. M. Jafari, M. J. Deen, S. Hranilovic, and N. K. Nikolova, "A study of ultrawideband antennas for near-field imaging," *IEEE Transactions on Antennas and Propagation*, vol. 55, pp. 1184-1188, 2007.

[5] M. Klemm, I. Craddock, A. Preece, J. Leendertz, and R. Benjamin, "Evaluation of a hemi-spherical wideband antenna array for breast cancer imaging," *Radio Science*, vol. 43, 2008.

[6] M. Sharma and V. Shrivastava, "Printed fractal elliptical monopole antenna for UWB application," in *Recent Advances in Microwave Theory and Applications, 2008. MICROWAVE 2008. International Conference on*, pp. 374-376, 2008.

[7] A. A. Shaalan and M. Ramadan, "Design of a compact hexagonal monopole antenna for ultra-wideband applications," *Journal of Infrared, Millimeter, and Terahertz Waves*, vol. 31, pp. 958-968, 2010.

[8] Y. B. Yang, F. S. Zhang, F. Zhang, L. Zhang, and Y. C. Jiao, "A novel compact CPW-fed planar monopole antenna with modified stair-style ground for ultra-wideband applications," *Microwave and Optical Technology Letters*, vol. 52, pp. 2100-2104, 2010.

[9] L. Liu, S. Cheung, R. Azim, and M. T. Islam, "A compact circular-ring antenna for ultra-wideband applications," *Microwave and Optical Technology Letters*, vol. 53, pp. 2283-2288, 2011.

[10] M. Z. Mahmud, M. T. Islam, N. Misran, S. Kibria, and M. Samsuzzaman, "Microwave imaging for breast tumor detection using uniplanar AMC based CPW-fed microstrip antenna," *IEEE Access*, vol. 6, pp. 44763-44775, 2018.

[11] M. Z. Mahmud, M. T. Islam, M. N. Rahman, T. Alam, and M. Samsuzzaman, "A miniaturized directional antenna for microwave breast imaging applications," *International Journal of Microwave and Wireless Technologies*, pp. 1-6, 2017.

[12] M. Mahmud, S. Kibria, M. Samsuzzaman, N. Misran, and M. Islam, "A new high performance hibiscus petal pattern monopole antenna for UWB applications," *Applied Computational Electromagnetics Society Journal*, vol. 31, 2016.

[13] G. Isik and S. Topaloglu, "A vompact size 4-19.1 GHz heart shape UWB antenna with triangular patches," *International Journal of Antennas and Propagation*, vol. 2013, 2013.

[14] H.-W. Liu and C.-F. Yang, "Miniature hook-shaped monopole antenna for UWB applications," *Electronics Letters*, vol. 46, pp. 265-266, 2010.

[15] M. Ojaroudi, C. Ghobadi, and J. Nourinia, "Small square monopole antenna with inverted T-shaped notch in the ground plane for UWB application," *Antennas and Wireless Propagation Letters, IEEE*, vol. 8, pp. 728-731, 2009.

[16] R. Azim, M. T. Islam, and N. Misran, "Compact tapered-shape slot antenna for UWB applications," *Antennas and Wireless Propagation Letters, IEEE*, vol. 10, pp. 1190-1193, 2011.

[17] C. Figueroa Torres, J. Medina Monroy, H. Lobato Morales, R. Chavez Perez, and A. Calvillo Tellez, "Heart shaped monopole antenna with defected ground plane for UWB applications," in *Electrical Engineering, Computing Science and Automatic Control (CCE), 2014 11th International Conference on*, pp. 1-4, 2014.

[18] T. Yang and X. J. Tian, "A novel heart-shaped monopole antenna for UWB and RFID applications," *Microwave and Optical Technology Letters*, vol. 53, pp. 2288-2291, 2011.

Md. Zulfiker Mahmud is an Assistant Professor of AIS Department in Jagannath University Bangladesh. He received the B.Sc. and M.Sc. degree in Computer Science and Engineering from Islamic University Kushtia, Bangladesh. Currently he is working as a Ph.D. student in

the Universiti Kebangsaan Malaysia (UKM), Malaysia. He is currently a Graduate Research Assistant at the Department of Electrical, Electronic and Systems Engineering, UKM, Malaysia. He has authored or co-authored approximately 25 referred journals and conference papers. His research interests include the microwave imaging, antenna design, satellite antennas, satellite communication and wireless communication.

Touhidul Alam is a post graduate student at the Department of Electrical, Electronic and Systems Engineering of the Universiti Kebangsaan Malaysia (UKM). He received B.Sc. in Electrical & Electronic Engineering (EEE) from International Islamic University Chittagong (IIUC) in 2012 and Master of Space Science from Universiti Kebangsaan Malaysia, 2015. From May 2012 to till now, he is working as an Assistant Professor at International Islamic University Chittagong (IIUC). His publications include over 16 research journal papers, nearly 12 conference papers, and two book chapters on various topics related to antennas, microwaves and electromagnetic radiation analysis. His research interests include the antenna, RF, electromagnetic field and propagation, electromagnetic radiation, metamaterial applications and electromagnetic compatibility and microwave imaging.

Md. Samsuzzaman was born in Jhenaidah, Bangladesh in 1982. He received his B.Sc. and M.Sc. degrees in Computer Science and Engineering from the Islamic University Kushtia, Bangladesh in 2005 and 2007, respectively, and the Ph.D. degree from the Universiti Kebangsaan Malaysia, Malaysia 2015. From February 2008 to February 2011, he worked as a Lecturer at the Patuakhali Science and Technology University (PSTU), Bangladesh. From February 2011 to 2015, he worked as an Assistant Professor at the same university. He is now as an Associate Professor at the same university. Samsuzzaman is a Post-Doctoral Fellow of Universiti Kebangsaan Malaysia. He is the author and co-author of about 80 research journal articles, nearly 20 conference articles, and a few book chapters on various topics related to antennas, microwaves and electromagnetic radiation analysis with one inventory patents filed. His Google scholar citation is 546 and H-index is 13. His research interests include the communication antenna design, satellite antennas, and microwave imaging.

Md. Amanath Ullah received B.Sc. in Electrical & Electronic Engineering (EEE) from International Islamic University Chittagong (IIUC) in 2015. Currently, he is pursuing M.Sc. in Electrical, Electronic and Systems Engineering at Universiti Kebangsaan Malaysia (UKM). From September 2016 to till now. His research interests include antenna and propagation, 3D antenna applications, microwave imaging and embedded systems.

Mohammad Tariqul Islam is a Professor at the Department of Electrical, Electronic and Systems Engineering of the Universiti Kebangsaan Malaysia (UKM). He is currently the Group Leader of the Radio Astronomy Informatics Group at UKM. He is the author of over 300 research journal articles, nearly 165 conference articles, and a few book chapters on various topics related to antennas, microwaves and electromagnetic radiation analysis with 11 inventory patents filed. Thus far, his publications have been cited 1990 times and his H-index is 25 (Source: Scopus). He is now handling many research projects from the Malaysian Ministry of Science, Technology and Innovation and Ministry of Education, and some international research grants from Japan. His research interests include communication antenna design, radio astronomy antennas, satellite antennas, and electromagnetic radiation analysis.

A CPW Fed T-shaped Frequency Reconfigurable Antenna for Multi Radio Applications

Sulakshana Chilukuri [1], Keshav Dahal [1], Anjaneyulu Lokam [2], and Wenbing Chen [3]

[1] School of Engineering and Computing
University of West of Scotland, Paisley, PA12LJ, United Kingdom
sulakshana312ster@gmail.com, Keshav.Dahal@uws.ac.uk

[2] Department of Electronics and Communication Engineering
National Institute of Technology, Warangal, 506004, India
anjan.lokam@nitw.ac.in

[3] School of Mathematics and Statistics
Nanjing University of Information Science and Technology, Nanjing, Jiangsu, 210044, China
chenwb@nuist.edu.cn

Abstract ─ This paper deals with design, simulation and experimental analysis of a compact, Coplanar Waveguide (CPW) fed T-shaped reconfigurable antenna with frequency diversity. The antenna mainly comprises of four strips placed in T-shape fed by coplanar waveguide feed which operates at 5.8GHz. The reconfigurability in frequency is achieved by connecting four strips through three switches in main antenna structure by the use of Positive-Intrinsic-Negative (PIN) diodes. By operating the switches in a controlled manner, the antenna is able to operate at seven frequencies namely 5.82GHz, 5.46GHz, 5.26GHz, 5.15GHz, 4.69GHz, 3.93GHz, and 3.21GHz which are suitable for Wi-Fi, WiMAX, WLAN, other C-band, and S-band applications. The antenna aperture area is 35mm × 30mm and it is designed on a FR4 epoxy substrate whose dielectric constant ε_r=4.3, thickness h=0.8mm. A parametric study has been carried to analyze the characteristics of the proposed antenna. The measured results are in good agreement with simulation results and show that the antenna exhibits good radiation behavior in the specified application bands.

Index Terms ─ Antenna gain, CPW feed, frequency diversity, PIN diodes, radiation pattern, reconfigurable antennas.

I. INTRODUCTION

A frequency reconfigurable antenna comprises of elements of the antenna which can be reconfigured to a different physical structure that in turn alters frequency properties of the antenna while maintaining constant radiation behavior. Nevertheless, reconfiguration of one parameter of the antenna affects the rest of the parameters. For example, altering frequency response may affect radiation pattern and vice versa. This inter dependency is one of the main challenges in the area of reconfigurable antennas. This type of reconfiguration includes switching or shifting a resonant frequency, matched impedance bandwidth, or providing multiband and/or stop band characteristics. The most common method of obtaining frequency reconfigurability is by implementing conductor modification reconfiguration mechanism to the microstrip antennas in order to change the effective electrical length which in turn results in change of operating frequency. The operating frequency of the antenna is mainly determined by the antenna's electrical length.

The advantage of the frequency reconfigurable antennas is that by reusing the total antenna volume to function in different operational modes, the size of the antenna can be reduced. The fundamental operating frequency of the antenna depends on its electrical length which can be altered through electronic, mechanical or optical switching. However, electronic tuning is most widely used because of its efficiency and reliability in allocation of bandwidth dynamically. This is achieved by employing switching components such as Positive-Intrinsic-Negative (PIN) diodes, Field Effect Transistors (FETs), Radio Frequency Micro-Electro-Mechanical Systems (RF MEMS) and optical switches. All types of switches have their own advantages and disadvantages and can be used according to the application suitability. For example, in the applications where low power consumption, high linearity and high isolation are needed RF MEMS switches are used [1]. Recently, Wu et al. [2] used reed switch other than the above mentioned switches for the reconfigurable antenna application to eliminate the use of bias and control lines

Submitted On: July 31, 2017
Accepted On: April 21, 2018

near the radiating patch area thus avoiding its impact on antenna radiation performance. So far frequency reconfigurable antennas that alter the physical structure of the antenna through electrical means have been discussed widely. A larger frequency shifts whether used for switched or continuous frequency bands can also be obtained by mechanical means [3]. Reconfigurable antennas that use RF switches like PIN diodes have been extensively researched in the past wherein a folded slot antenna employing two switches operating at two frequencies is proposed in [4], three PIN diodes on a meandered tuning stub which is placed on a half circular patch operating in four modes is presented in [5]. In [6] a multiband antenna with wide band characteristics by employing two switches on feed network of dual patch C-slot patch elements is discussed, a T-shaped switchable slot antenna employing five PIN diodes on ground plane operating at nine different frequencies is proposed in [7]. A CPW fed slot antenna with four PIN diodes is reported in [8]. A MEMS based optimized E shaped patch antenna for cognitive radio is presented in [9]. Also, latest researches [10-12] use different forms of reconfiguration mechanisms. A few antennas based on frequency, polarization and semi compound reconfigurability using PIN diodes with four operating modes are reported in [13-15].

This research proposes a novel and compact T-shaped antenna with frequency reconfigurable capability integrating with three switches functioning in eight different operating bands. The designed antenna finds few applications in wireless communications such as Wi-Fi, WiMAX, and WLAN. The prototype of the antenna is fabricated and tested. The principal aim of designing this frequency reconfigurable antenna is to achieve a wide-bandwidth with a compact size antenna while maintaining the integrity of the radiation pattern when the antenna reconfigures among eight different bands unlike aforementioned reconfigurable antennas with complex structure, use of large number of switches, large dimensions, low impedance bandwidth, feed radiation and low efficiency due to microstrip mechanism. The antenna is carefully designed to meet specific applications in all most all the operating modes. To get enhanced operating bandwidth, the coplanar waveguide (CPW) feeding technique is employed in this study and the experimental results are compared with simulated ones. The structural design aspects are discussed in Section II. The effect of few geometrical parameters on the performance of the antenna is reported in Section III. The simulated and experimental results are presented in Section IV and Section V. Finally, conclusion is presented in the last section.

II. ANTENNA DESIGN AND OPTIMISATION

The structural configuration of the proposed frequency reconfigurable slot antenna is shown in Fig. 1. The antenna is designed on a single layer of FR4 (Flame Retardant epoxy substrate) substrate whose dielectric constant $\varepsilon_r = 4.4$, loss tangent $\tan\delta = 0.027$ and thickness h = 0.8mm with single Coplanar feed. The antenna dimensions are 35 mm × 30 mm. It is longitudinally symmetrical and consists of four unfolded strips creating three slots separated by a distance of 0.5mm attached to CPW feed line. These three slot gaps are connected through three switches S_1, S_2 and S_3 to allow current flow through the metal strips. The optimized antenna parameters after several simulation runs are: L=35mm, W=30mm, the length of one arm of CPW ground L_1=15.3mm, and width W_1=5mm, the width of the feed line L_2=3.6mm, W_2=3.5mm, the length of the radiating strip L_3=8mm, and width W_3=1mm, W_4=0.5mm. The spacing between the ground and feed line, g=0.4mm.

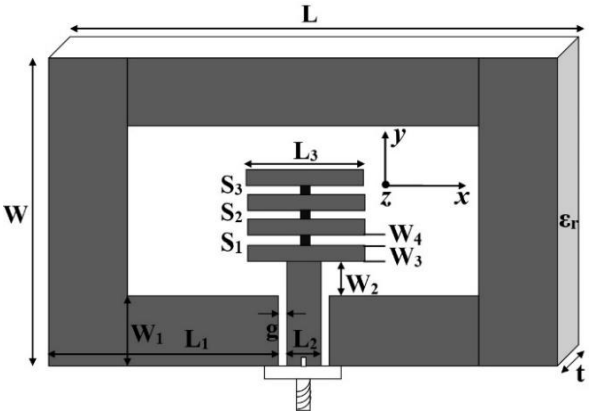

Fig. 1. Geometrical design of the proposed T shaped slot antenna with frequency diversity.

The conductor modification frequency reconfiguration mechanism is obtained by changing the electrical length of the slot and hence its resonant modes by implementing the switching technique using PIN diodes, operated in their ON/OFF condition. Several switches can be employed in the gaps between the strips for generating many resonant mode excitations. We use only three RF switches for the basic proof of concept. The operating conditions of switches are realized by forward (ON state) and reverse (OFF state) biasing of PIN diodes. When the diode is forward biased, the switch acts as short circuit with low impedance allowing current to flow through the switch. This increases the effective electrical length. When it is reverse biased (OFF state), the switch acts as open circuit, exhibiting high impedance and hence there is no connection between the slots. The PIN diodes are realized as short copper paths in the simulation. The ON state of the switch is realized by a small metallic patch of dimensions 0.1mm × 0.5mm and absence of the patch is considered as OFF. In order to obtain frequency reconfiguration, the three diodes are

switched ON and OFF in eight (2^n where n=3 is the number of switches) different configurations as shown in Table 1.

Table 1: Eight cases of switch configurations

Case	Switch 1	Switch 2	Switch 3
1	OFF	OFF	OFF
2	OFF	OFF	ON
3	OFF	ON	OFF
4	OFF	ON	ON
5	ON	OFF	OFF
6	ON	OFF	ON
7	ON	ON	OFF
8	ON	ON	ON

In order to check the changes in the frequency shift or bandwidth, sensitivity studies for each parameter have been carried out. The parameters that show the considerable effect are slot length L_3, slot width W_3 and height of the slots above the center strip, i.e., W_2.

Figure 2 shows the S-parameter curves depicting the variations observed in reflection coefficient (S_{11} in dB) based on variation in the parameter L_3 for all the eight cases keeping W_3 (=1.0mm) and W_2 (=3.5mm) as constant. As the length is increased from 5.0mm to 10.0mm, it is observed that the operating frequency decreases, the bandwidth increases and the gain of the antenna decreases. This is due to the decrease in the frequency with increase in electrical length switching from Case 1 to Case 8. A better characteristic for S_{11} and the bandwidth is obtained when (L_3) is 8.0mm with other parameters fixed, i.e., W_3 = 1.0mm and W_2 = 3.5mm.

By keeping the slot length and height fixed and by varying the slot width W_3, different S_{11} curves are observed for all the eight cases. As the slot width is increased from 0.3mm to 1.5mm, the resonant frequency is decreasing while increasing the bandwidth. The value W_3=1.0mm is found to be the best compromised value for optimized return loss, bandwidth, gain and application frequency among all the cases.

Also, the height at which the patch is positioned above the ground plane is also varied to achieve the best performance of the antenna. The variations to the height are made from 0.5mm to 3.5mm while keeping L_3 (=8mm) and W_3 (=1.0mm) fixed. A better characteristic for S_{11} and the bandwidth is obtained when (W_2) is 3.5mm. Moreover with this value of W_2, in most of the cases, the operating frequency falls in the appropriate application band.

III. SIMULATION RESULTS

A commercially available Method of Moments (MoM) based CAD tool-IE3D, has been used to analyse the performance of the proposed antenna configurations. It uses adaptive symmetric matrix solver for solving Maxwell's boundary equations. The meshing frequency for the solution setup is chosen to be 5.8GHz with 20 number of cells/wavelength. The meshing alignment parameters such as maximum layer distance, regular size and refined size of the cell and refined ratio are set to be 0.0005mm, 2.05357, 0.410713 and 0.2 respectively to obtain more accurate results. The design of the antenna has been simulated with the proper geometrical parameters as shown in Fig. 1 for required numerical analysis.

The simulated S-parameter curves (S_{11} in dB) versus frequency of the proposed reconfigurable antenna in its eight operating modes are shown in Fig. 3. When any two of the switches are made ON, the antenna has single operating band and has low return loss which is desirable. In Case 4, when switches S_2 and S_3 are made ON, the antenna operates at 5.34GHz. The electrical length of the T-shaped patch at this frequency with two strips connected via two switches is about one half of the wavelength ($\approx 0.49\lambda_g$) where $\lambda_g = \frac{\lambda}{\sqrt{\varepsilon_{eff}}}$ and $\varepsilon_{eff} = \frac{\varepsilon_r+1}{2} = 2.7$ and the current flowing in the top two strips is due to the mutual coupling between the first strip and the remaining three strips. In Case 6, when S_1 and S_3 are made ON, it operates at 4.6GHz with electrical length nearly equal to half wavelength ($\approx 0.54\lambda_g$) whereas in Case 7, when S_1 and S_2 are made ON, the antenna resonates at 4.0GHz with electrical length is $\approx 0.53\lambda_g$. It is observed that, when any single switch is made ON, the antenna resonates at two frequencies and exhibits dual band characteristics except in Case 2, switch S_3 is made ON where the antenna operates at single frequency 5.75GHz. In this case, second resonant frequency is not suitable mode of operation because of high return loss, high cross polarization and low gain obtained. In Case 3, when only S_2 is made ON, the antenna resonates at two frequencies namely 5.6GHz and 9.2GHz. The electrical length at 5.6GHz with current flowing in second and third strip is $\approx 0.46\lambda_g$ and at 9.2GHz with current flowing in all three strips is $\approx 0.55\ \lambda_g$. Likewise, in Case 5, when switch S_1 is ON, it operates at two different frequencies namely 4.85GHz and 8.3GHz. It is also observed that the -10dB impedance bandwidth obtained at the first resonant frequency when a single switch is made ON is low compared with the bandwidth obtained when two switches were made ON. Lastly, when all switches are made OFF, the antenna operates at 5.85GHz with electrical length equal to quarter wavelength ($\approx 0.26\lambda_g$) and when all switches are made ON, it resonates at 3GHz with an electrical length of $0.55\ \lambda_g$.

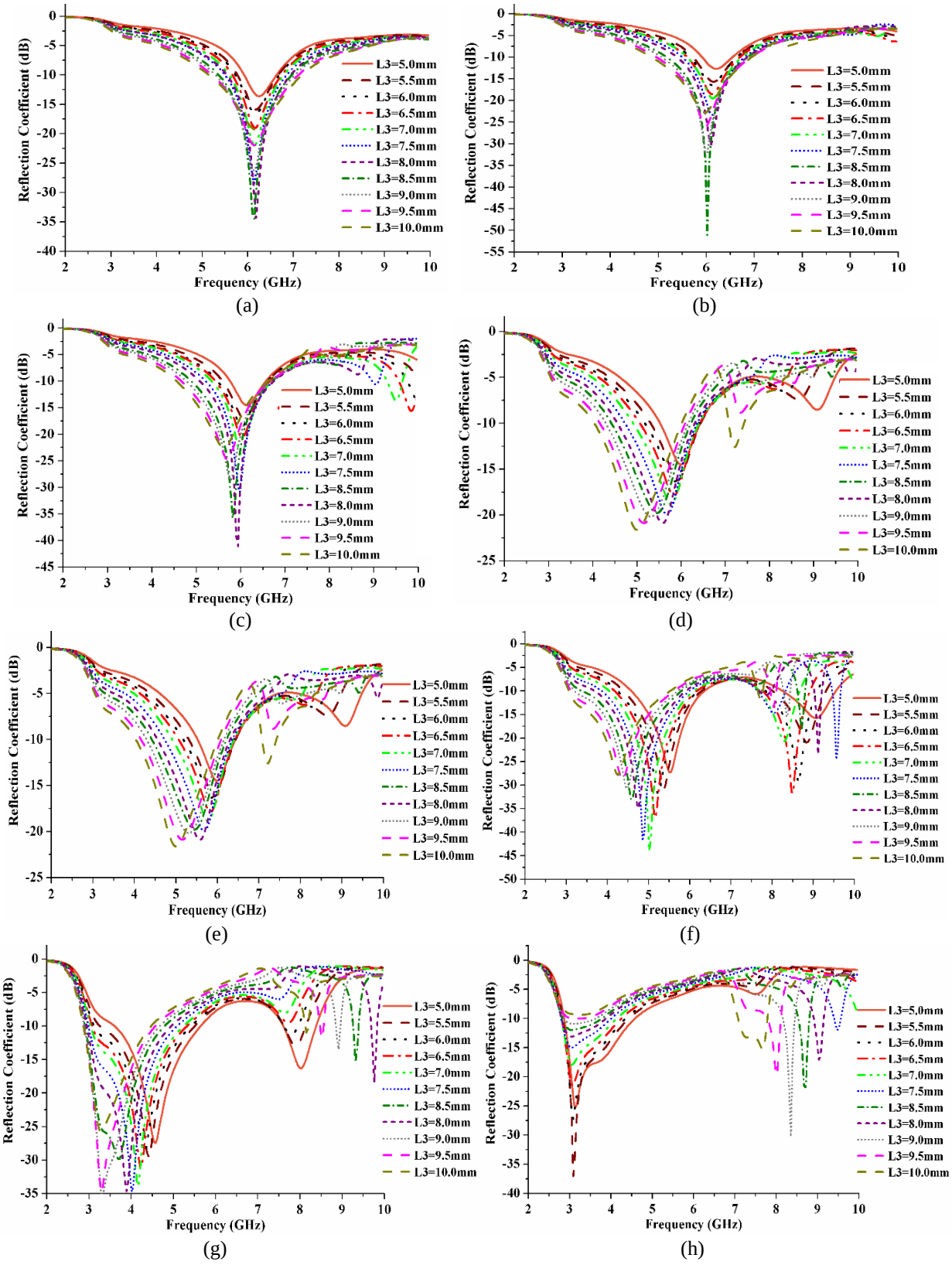

Fig. 2. Simulated S_{11} of proposed reconfigurable antenna for varying slot lengths (L_3) operating in: (a) Case 1, (b) Case 2, (c) Case 3, (d) Case 4, (e) Case 5, (f) Case 6, (g) Case 7, and (h) Case 8.

The operating frequency of the antenna when switched from Case 1 to Case 8 decreases as the electrical length of the antenna from Case 1 to Case 8 is increased.

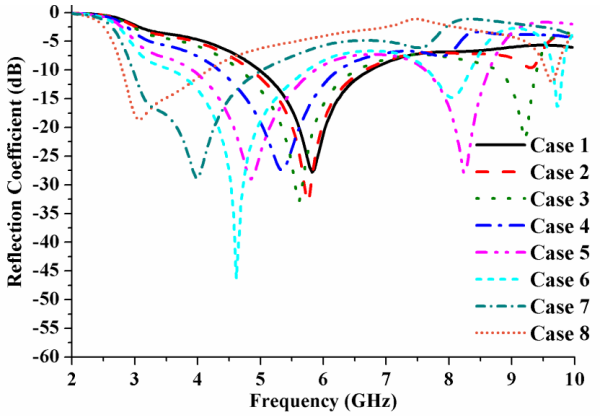

Fig. 3. Simulated reflection coefficients (S_{11}) of proposed reconfigurable antenna.

IV. ANTENNA PROTOTYPE AND EXPERIMENTAL RESULTS

In order to validate the simulated results, the proposed reconfigurable antenna was tested with the optimized geometrical parameters L_3=8.0mm, W_3=1.0mm and W_2=3.5mm. It is fabricated on a FR4 substrate with dielectric constant 4.4 and thickness 0.8mm. In this design, the PIN diode selected is a MADP-008120-12790T from M/A-COM Technology Inc. In ON state it has a very low forward resistance R_S = 2.5Ω and in OFF state it has total capacitance of C_T = 0.15pF and L_S = 0.7nH. Figure 4 shows the DC bias network (on the reverse side of the antenna board) for the practical PIN diodes that are incorporated on the patch. It is biased with forward voltage V_F = 0.73 V.

Two DC blocking capacitors (C_1, C_2), (C_3, C_4), (C_5, C_6) for each diode with 64pF are used to prevent the DC signal but allow RF current to pass through. The inductors L_1, L_2, L_3, L_4, L_5 and L_6 with 56nH are used as RF chokes to provide low impedance for DC signal and high impedance for RF signals. The resistors R_1, R_2, R_3, R_4, R_5 and R_6 are used to control the biasing current to the PIN diodes. The fabricated prototype of the antenna used for the measurement is shown in Fig. 5. An Agilent E8363C PNA Series Microwave Network Analyzer that operates in the frequency range 10 MHz to 40 GHz was used to measure all the return loss parameters.

The measured and simulated return loss graphs are depicted in Figs. 6 (a)-(h) for Case 1 to Case 8. The practical antenna results are in good match with the simulated ones. A very wide bandwidth of around 30%-40% is achieved in all the useful applications and in other cases it is around 50%.

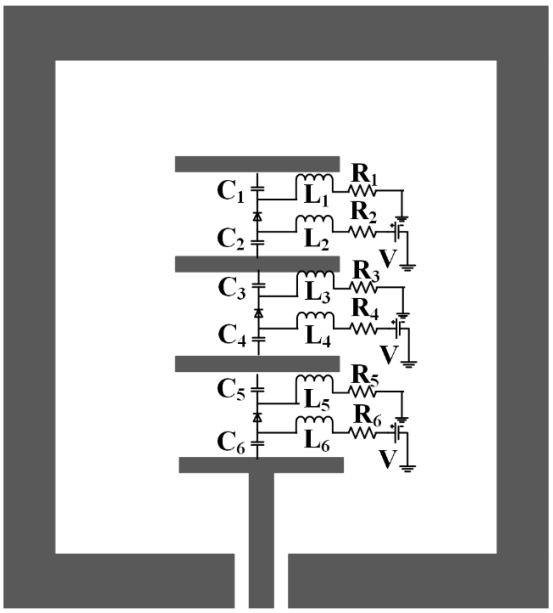

Fig. 4. DC bias network for the PIN diodes.

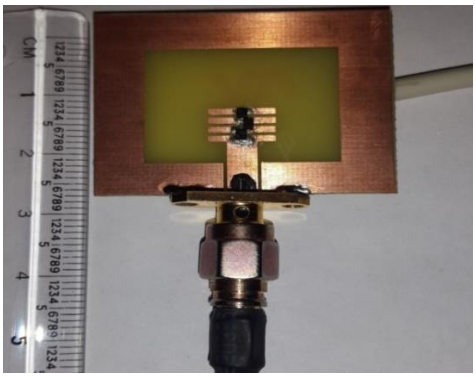

Fig. 5. Prototype of the fabricated T-shaped reconfigurable antenna.

Figure 7 depicts the measured 2D gain radiation patterns in dBi. The figure shows E-total field of the proposed antenna in eight different operating modes in the elevation (E_θ) and azimuth (E_ϕ) planes with $\phi=0^0$ and $\theta=0^0$ referring co-polarization and $\phi=90^0$ and $\theta=90^0$ referring cross-polarization. In all the operating modes, the antenna maintains almost similar and stable (Figure of '8') radiation pattern which satisfies the frequency reconfigurability condition where only frequency has to be changed, not patterns and polarization. It is also observed from the figure that the cross-polarization response is very much below the co-polarization response.

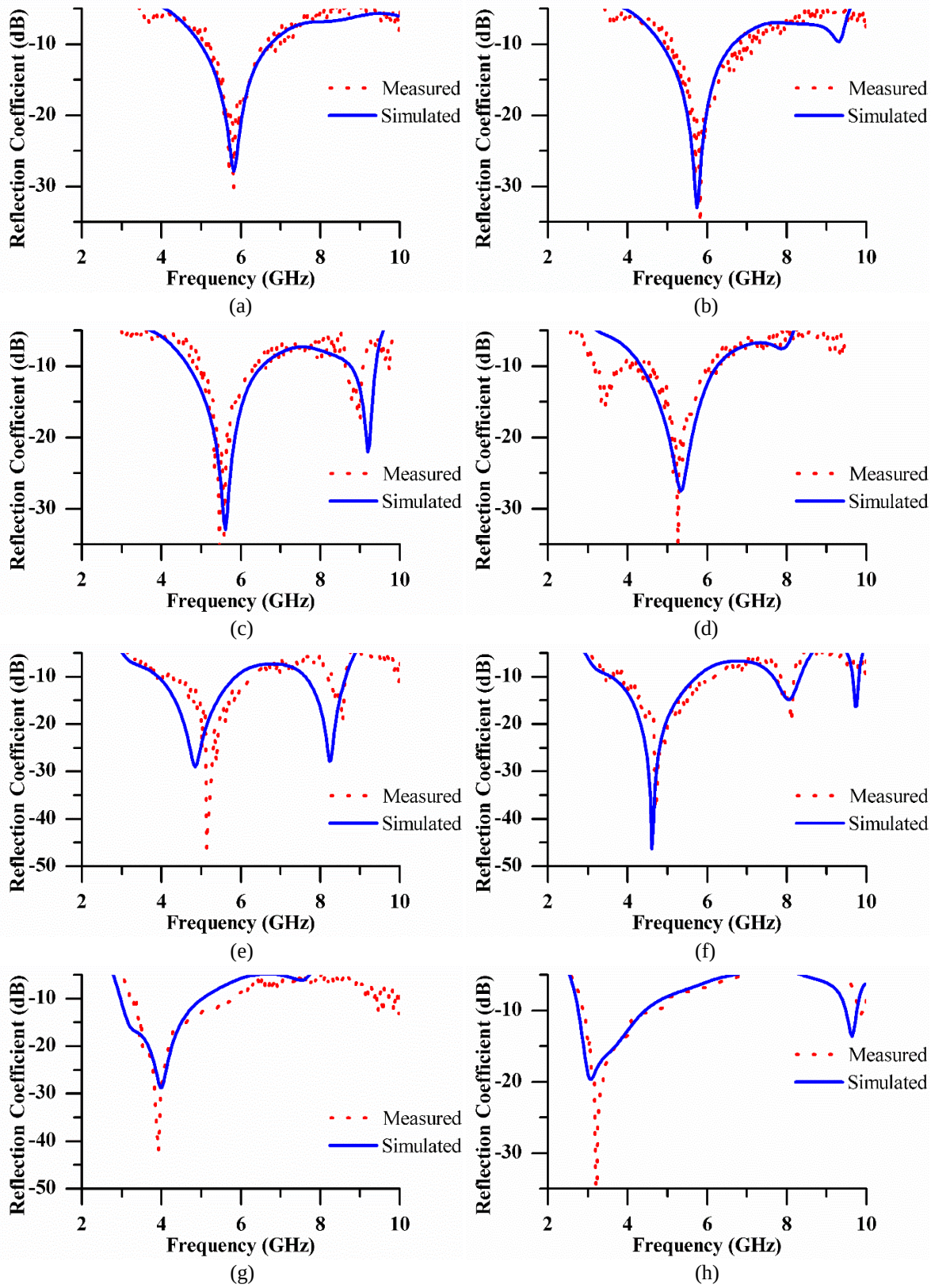

Fig. 6. Simulated and measured reflection coefficients (S_{11}) of proposed reconfigurable antenna operating in: (a) Case 1, (b) Case 2, (c) Case 3, (d) Case 4, (e) Case 5, (f) Case 6, (g) Case 7, and (h) Case 8.

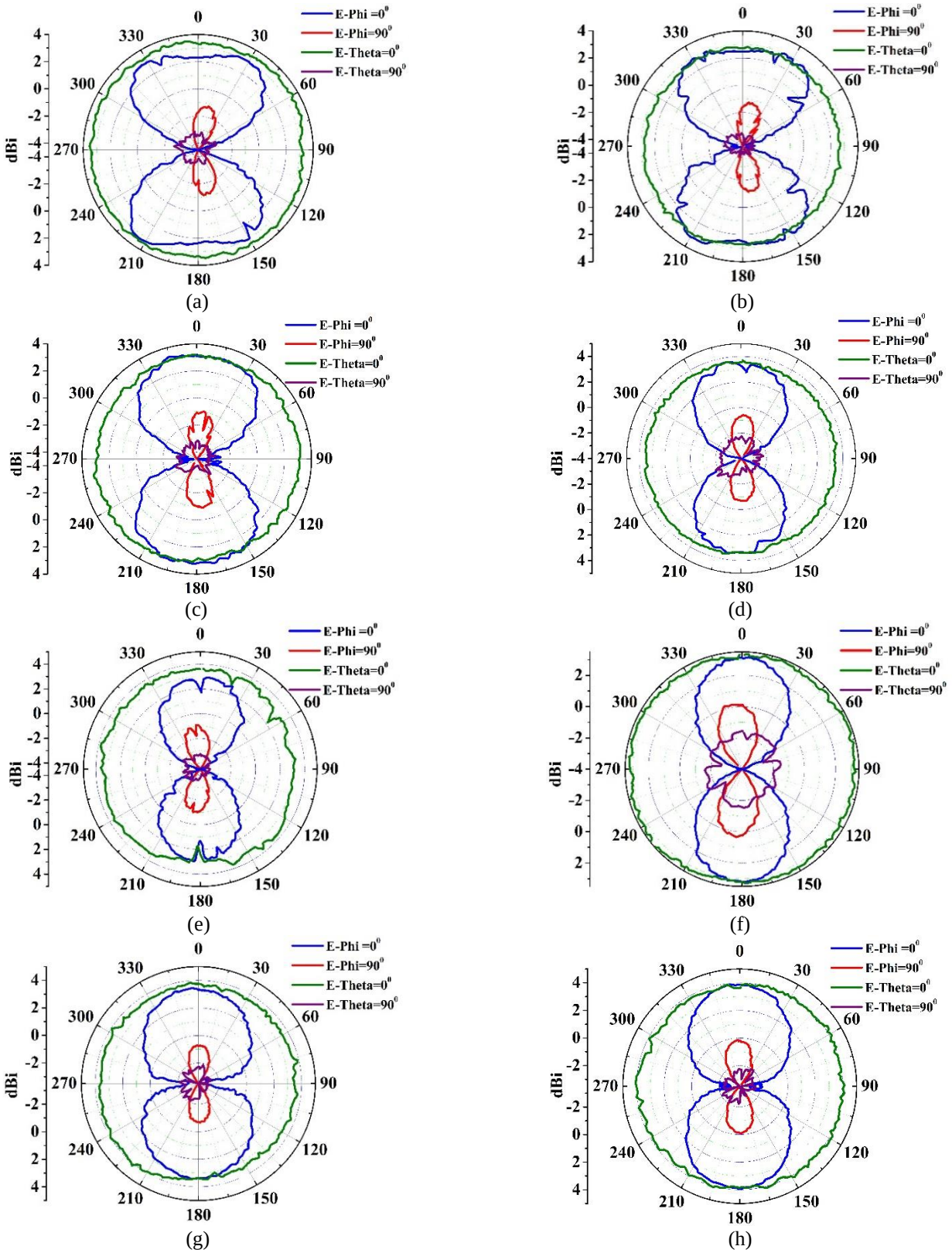

Fig. 7. Measured gain patterns of proposed reconfigurable antenna operating at: (a) 5.78GHz (Case 1), (b) 5.82GHz (Case 2), (c) 5.42GHz (Case 3), (d) 5.24GHz (Case 4), (e) 5.15GHz (Case 5), (f) 4.72GHz (Case 6), (g) 3.95GHz (Case 7), and (h) 3.09GHz (Case 8).

Table 2: Characteristics of reconfigurable antenna in eight operating modes

Antenna Parameters	Mode 1	Mode 2	Mode 3	Mode 4	Mode 5	Mode 6	Mode 7	Mode 8
Operating Frequency (GHz)	5.82 (5.82)	5.75 (5.82)	5.61 (5.46)	5.34 (5.26)	4.85 (5.15)	4.61 (4.69)	4.0 (3.93)	3.07 (3.21)
Return Loss (dB)	27.8 (30.2)	32.83 (36.4)	32.86 (31.9)	27.5 (34.9)	29.0 (46.1)	46.1 (37.9)	28.7 (42.1)	18.63 (41.9)
Measured Operating band (GHz)	5.2-6.7	4.9-6.7	4.8-6.6	4.4-6.2	4.0-6.3	3.6-5.9	3.2-5.7	2.9-4.6
Bandwidth (%)	30.24 (25.61)	31.13 (36.4)	32.97 (31.9)	35.58 (33.8)	40.21 (43.69)	46.63 (51.39)	51.5 (64.12)	44.63 (53.89)
Gain (dBi)	3.22 (3.0)	3.12 (2.9)	3.15 (3.0)	3.44 (3.0)	3.5 (2.4)	3.25 (2.6)	3.35 (3.0)	3.82 (2.9)
VSWR	1.08	1.04	1.04	1.08	1.07	1.009	1.07	1.26
Application	Wireless LAN				Wi-Fi (IEEE 802.11)	C-Band	S-band	WiMAX (IEEE 802.16)

*The values in the braces indicates measured results.

Table 3: Comparison of frequency reconfigurable antennas in literature

Reference Antenna	No. of Switches	Dimensions	Modes	Operating Frequency (GHz)	Bandwidth (%)
Proposed Antenna	3	$0.676\lambda_0 \times 0.58\lambda_0 \times 0.0155\lambda_0$	8	3.21 to 5.82	25 to 64
[6]	2	$0.77\lambda_0 \times 0.58\lambda_0 \times 0.0155\lambda_0$	2	5.25, 5.78	15.5, 13.9
[7]	3	$0.73\lambda_0 \times 0.73\lambda_0 \times 0.023\lambda_0$	4	2.5, 2.9, 3.5, 4.4	5.4, 9.8, 16, 13.7
[8]	2	$1.167\lambda_0 \times 1.167\lambda_0 \times 0.037\lambda_0$	3	(5.55, 5.65) and 5-7	33.5 (wideband)
[9]	5	$0.213\lambda_0 \times 0.337\lambda_0 \times 0.034\lambda_0$	9	1.98 to 3.59	4.6 to 7.7
[13]	4	$0.77\lambda_0 \times - \times 0.018\lambda_0$	3	1.51, 3.27, 3.55	6.0

The average difference between the co-pol and x-pol levels in the main plane (Elevation, x-y plane) direction for most of the frequencies is higher than co-pol and x-pol levels in the Azimuth plane (x-z and y-z plane) direction because of the symmetric shaped strips as the main patch and ground plane that mainly excited all the eight frequencies. In Azimuth plane, a high degree of x-pol is observed for most of the resonant frequencies because of the coupling influences between the T-shaped strips. This is due to the dual mode excitation caused mainly by the nearby four coupled strips which then affected the x-pol levels of these operating frequencies in this plane.

The measured gain of the antenna operating in eight different modes is shown in Fig. 8. The maximum gain of the antenna in all the operating modes is around 3dBi. The detailed simulated and measured values of return loss, bandwidth and other antenna parameters are given in Table 2.

Table 3 compares the results of proposed antenna with conventional frequency reconfigurable antennas in the available literature. It is apparent that the proposed antenna is able to generate all possible modes with the use of limited number of switches when compared to others. The presented antenna provides wider -10dB return loss bandwidth (%) than the existing ones. Also, the total volume occupied by the proposed antenna is less compared to the antennas in the literature. Even though the reconfigurable antenna in [9] occupies less volume and can generate more number of operating modes than the proposed antenna, it has more number of switching elements and less bandwidth when compared to the nominated antenna. The presented antenna provides almost double the -10dB return loss bandwidth when compared to [8].

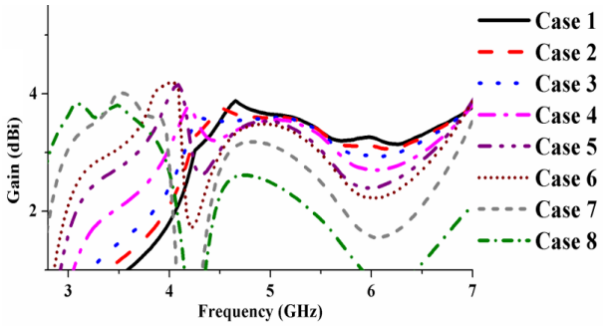

Fig. 8. Measured gain of proposed reconfigurable antenna.

V. CONCLUSION

A frequency reconfigurable slot antenna is designed and evaluated in this paper that operates in eight different operating bands. The coplanar waveguide feeding technique is used to attain wide bandwidths up to 65%. The measured results of the fabricated antenna prototype are found in good agreement with simulated ones with acceptable small deviations which are due to inaccuracies in fabrication process, SMA connector solder losses which causes impedance mismatch at the CPW feed and some imperfections in the dielectric material. The fabricated antenna has found applications in wireless communications such as Wi-Fi, WiMAX and WLAN.

ACKNOWLEDGMENT

The first author acknowledges the funding support provided by EU-Erasmus Mundus Smart Link project to conduct this research under Grant agreement (552077-EM-1-2014-1-UK-ERA) to carry out this research at the University of the West of Scotland, UK.

REFERENCES

[1] D. E. Anagnostou, Guizhen Zheng, M. T. Chryssomallis, J. C. Lyke, G. E. Ponchak, J. Papapolymerou, and C. G. Christodoulou, "Design, fabrication, and measurements of an RF-MEMS-based self-similar reconfigurable antenna," *IEEE Trans. Antennas and Propagation*, vol. AP-54 no. 2, pp. 422-432, 2006.

[2] C. Wu, T. Wang, A. Re, and D. G. Michelson, "Implementation of reconfigurable patch antennas using reed switches," *IEEE Antennas and Wireless Propagation Letters*, vol. 10, pp. 1023-1026, 2011.

[3] J. T. Bernhard, *Reconfigurable Antennas-Synthesis lectures on Antennas*. Morgan & Claypool, 2007.

[4] D. E. Anagnostou and A. A. Gheethan, "A coplanar reconfigurable folded slot antenna without bias network for WLAN applications," *IEEE Antennas and Wireless Propagation Letters*, vol. 8, pp. 1057-1060, 2009.

[5] C. Y. D. Sim, T. Y. Han,. and Y. J. Liao, "A frequency reconfigurable half annular ring slot antenna design," *IEEE Transactions on Antennas and Propagation*, vol. 62, no. 6, pp. 3428-3431, 2014.

[6] H. F. Abutarboush, R. Nilavalan, S. W. Cheung, Karim M. Nasr, Thomas Peter, Djuradj Budimir, and Hamed Al-Raweshidy, "A reconfigurable wideband and multiband antenna using dual-patch elements for compact wireless devices," *IEEE Trans. on Antennas and Propagation*, vol. 60, no. 1, pp. 36-43, 2012.

[7] H. A. Majid, M. K. Abdul Rahim, M. R. Hamid, N. A. Murad, and M. F. Ismail, "Frequency-reconfigurable microstrip patch-slot antenna," *IEEE Antennas and Wireless Propagation Letters*, vol. 12, pp. 218-220, 2013.

[8] Y. B. Chen, X. F. Liu, Y. C. Jiao, and F. S. Zhang, "A frequency reconfigurable CPW-fed slot antenna," *Journal of Electromagnetic Waves and Applications*, vol. 21 no. 12, pp. 1673-1678, 2007.

[9] H. Rajagopalan, J. M. Kovitz, and Y. Rahmat-Samii, "MEMS reconfigurable optimized E-shaped patch antenna design for cognitive radio," *IEEE Trans. on Antennas and Propagation*, vol. 62, no. 3, pp. 1056-1064, 2014.

[10] H. L. Zhu, X. H. Liu, S. W. Cheung, and T. I. Yuk, "Frequency-reconfigurable antenna using metasurface," *IEEE Trans. on Antennas and Propagation*, vol. 62, no. 1, pp. 80-85, 2014.

[11] M. Kelley, C. Koo, H. Mcquilken, B. Lawrence, S. Li, A. Han, and G. Huff, "Frequency reconfigurable patch antenna using liquid metal as switching mechanism," *Electronics Letters*, vol. 49, no. 22, pp. 1370-1371, 2013.

[12] S. Genovesi, A. D. Candia, and A. Monorchio, "Compact and low profile frequency agile Antenna for multistandard wireless communication systems," *IEEE Trans. on Antennas and Propagation*, vol. 62, no. 3, pp. 1019-1026, 2014.

[13] Ch. Sulakshana and L. Anjaneyulu, "A CPW fed rectangular reconfigurable patch antenna with switchable strips for polarization diversity," *Defense Science Journal*, vol. 64, no. 1, pp. 62-66, 2014.

[14] Ch. Sulakshana and L. Anjaneyulu, "A CPW fed reconfigurable patch antenna with circular polarization diversity," *International Journal of Microwave and Wireless Technologies*, vol. 7, no. 6, pp. 753-758, 2015.

[15] Ch. Sulakshana and L. Anjaneyulu, "A compact reconfigurable antenna with frequency, polarization and pattern diversity," *Journal of Electromagnetic Waves and Applications*, vol. 29 no. 15, pp. 1953-1964, 2015.

Sulakshana Chilukuri received the Bachelor's degree in Electronics and Communication Engineering from G. Narayanamma Institute of Technology and Science, Hyderabad, India, in 2007, the Master's degree in Electronics and Communication Engineering with Communication Systems specialization from National Institute of Technology, Tiruchirappalli, Tamilnadu, India in 2010 and received her Ph.D. degree in Electronics and Communication Engineering from national Institute of Technology Warangal, Telengana, India in 2016.

She is presently working as Post-Doctoral Research Fellow at University of West of Scotland. Her field of study is Reconfigurable Antennas and other areas of interest are Microwave Engineering, Electromagnetics and Transmission lines, Wireless Communication Systems and MIMO antennas. She has published her work in 8 peer reviewed International Journals, 10 International conferences.

Keshav P. Dahal is a Professor of Intelligent Systems and the leader of the Artificial Intelligence, Visual Communication and Network (AVCN) Research Centre at the University of the West of Scotland (UWS), UK. He is also affiliated with Nanjing University of Information Science and Technology (NUIST) China. Before joining UWS he was with Bradford and Strathclyde Universities in UK. He obtained his Ph.D. and Master from Strathclyde. His research interests lie in the areas of applied AI to intelligent systems, trust and security modelling in distributed systems, and scheduling/ optimization problems. He has published extensively with award winning papers, and has sat on organizing/ program committees of over 55 international conferences including as the General Chair and Programme Chair. He is a Senior Member of the IEEE.

Lokam Anjaneyulu was born in 1967 in India. He obtained his B.Tech (ECE) in 1989, M.Tech in 1991 and Ph.D. in 2010 from National Institute of Technology, Warangal, India. He worked as Project Officer at Institute of Armament Technology, Pune, India for 5 years from 1991 and involved in the design of Surface borne and Airborne Radar systems for clutter measurement application. Later, he worked as Staff Scientist at Helios Systems, Madras, India for 2 years and engaged in the development of Radio Wave propagation assessment software modules for ship-borne radars. He has been with the Department of Electronics and Communications Engineering at National Institute of Technology, Warangal, India since 1997. His areas of interest include Computer Networks, Electromagnetic Field Theory, Microwave & Radar Engineering, and Neural Networks & Fuzzy Logic Systems. He has completed few Defense R&D Projects and has 31 papers to his credit in National and International Conferences and Journals.

Wenbing Chen is a Senior Engineer and the Head of Department of Information and Computing Science at Nanjing University of Information Science and Technology. He received M.Sc. degree in Applied Mathematics from Nanjing University of Science Information and Technology. He has been regularly visiting the Artificial intelligence, Visual Communications & Networks (AVCN) Research Centre at the University of the West of Scotland. His research interests lie in the areas of machine learning, image processing and pattern recognition, artificial neural network. He has published over 30 peer-reviewed journal/conference papers.

A Resonance Prediction Method for a Shielding Enclosure with Apertures Illuminated by a Plane Wave

Bao-Lin Nie [1], Zhong Cao [2], and Ping-An Du [1]

[1] School of Mechanical and Electrical Engineering
University of Electronic Science and Technology of China, Chengdu, Sichuan 611731, China
blnie@uestc.edu.cn, dupingan@uestc.edu.cn

[2] Chongqing Vehicle Test & Research Institute Co., Ltd.
Chongqing, 401122, China
caozhong@cmhk.com

Abstract ─ Electromagnetic resonances in a shielding enclosure with apertures could result in significant degradation of its shielding performance. In this paper, an analytical method is proposed to predict the resonances of a shielding enclosure with aperture arrays illuminated by a plane wave. Firstly, an obliquely incident and arbitrarily polarized plane wave is decomposed into several normally incident plane waves each polarized in the axis direction. Then, the transmitted fields through each aperture are equivalent to fields radiated by a magnetic current located at the center of the corresponding aperture. Finally, the resonant modes and resonant frequencies of the enclosure are determined according to the direction of the magnetic current and the properties of the radiated fields. This method is verified by comparing its results with the results of full-wave simulations. Compared with numerical methods, the method is easier to implement and more efficient in predicting resonances.

Index Terms ─ Aperture array, electromagnetic shielding, resonances, shielding enclosure.

I. INTRODUCTION

Resonances play an important role in some devices such as microwave resonators and resonant circuits while producing an adverse effect in others. For example, electromagnetic resonances occur in enclosures of electronic equipment, which pronouncedly enhance the amplitude of electromagnetic fields and deteriorate the shielding performance of these enclosures. The shielding performance of an enclosure is quantified by its shielding effectiveness (SE), defined as the ratio of the field strength at observation points in the presence and absence of the enclosure. It is known that an enclosure may have negative SE at resonant frequencies, which means that the presence of the enclosure increases the field strength. Electromagnetic resonances in shielding enclosures thus draw great attention from researcher. Up to present, numerous methods have been reported in predicting SE and resonances of shielding enclosures, including both analytical formulations and numerical methods.

The majority of analytical formulations are based on the equivalent circuit method proposed by Robinson, et al. [1]. In this method, the aperture is represented as a length of shorted coplanar strip transmission line, and the enclosure is modeled as a length of rectangular waveguide shorted at the end. It is expected to be valid beyond the resonant frequency of the next higher order mode of the enclosure [2]. Some attempts strived to extend the original method to handle arbitrary plane wave [3], to account for the thickness [4], and to deal with multiple apertures [5]. Unfortunately, all these methods fail to predict the entire resonances excited in the concerned higher frequency band. Moreover, numerical methods such as the finite-difference time-domain (FDTD) method [6], the transmission-line modeling (TLM) method [7], the finite element method (FEM) method [8, 9], and the method of moments (MoM) [10] can accurately capture the higher order modes propagation effect and deal with arbitrarily complex geometry. However, numerical methods are computationally expensive for this multi-scale configuration.

There are other works reveal the relationship between the resonances of the cavity-slot coupled system and incident plane waves [11-13]. In Ref. [11], the coupling of an incident plane wave through a slot into a lossy rectangular cavity was analyzed by using a generalized network formulation. It was found that, apart from the cavity's natural resonances, two types of cavity-slot coupling resonances may occur. In Ref. [12], explicit formulas for the conditions of cavity-slot resonances were derived based on the duality between a slot and a strip. The formulas are simple to use and do not involve

Submitted On: September 22, 2017
Accepted On: October 23, 2018

the numerical evaluation of derivatives and integrals. In Ref. [13], analytic approximation of the complex resonances of a slot-fed rectangular cavity was derived using just one aperture expansion function. However, most of these efforts were put on one slot case and mainly on the cavity-slot coupling resonances. It has been found that the coupling resonances would not be excited when the diameter of the aperture is very small compared with wavelength [11].

It is known that the electromagnetic fields in a rectangular cavity can be regarded as the superposition of its transverse electric (TE) and transverse magnetic (TM) resonant modes. However, for a rectangular enclosure with aperture arrays excited by an external plane wave, not all the possible resonant modes in the concerned frequency band will be actually excited. So the relationship between the properties of the plane wave and the subsistent resonant modes is important for predicting the resonances in the concerned frequency band. This paper investigates the resonant condition of a shielding enclosure with aperture arrays and provides designers of shielding enclosures with a method to predict resonant frequencies and resonant modes.

II. THE PROBLEM DESCRIPTION

A. Shielding geometry and excitation

As shown in Fig. 1, a shielding enclosure mimics a computer box. The interior dimensions of the enclosure are $a \times b \times d$ mm (360 × 300 × 120 mm) in ***x***, ***y***, and ***z*** directions. The thickness of the enclosure walls is 1.5 mm. The material of the enclosure is aluminum. Two aperture arrays, with aperture radius of 6 mm, center-to-center spacing of 20 mm, and total number of apertures 21 and 27, are residing on the front ***y-z*** wall and the side ***x-z*** wall. A plane wave acting as an excitation source is obliquely incident with propagation vector $\boldsymbol{\beta}$, incident angles ϕ and θ, and polarization angle φ to the θ-axis, as shown in Fig. 2. The monitor point of the electric SE is located at the center of the enclosure (-180mm, 150mm, 60mm). The studied frequency band is 0-2GHz.

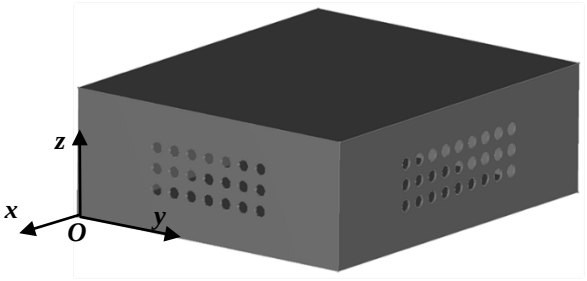

Fig. 1. Geometry of a rectangular enclosure with aperture arrays on multiple walls.

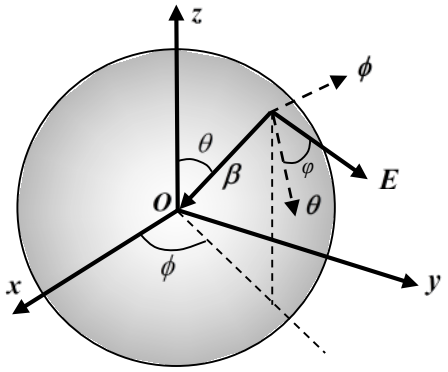

Fig. 2. The coordinate system and the incident plane wave.

As shown in Fig. 2, the propagation vector and the electric field can be decomposed into three components in the rectangular coordinate system as:

$$\boldsymbol{\beta} = -\beta_0[\hat{x}\cos\phi\sin\theta + \hat{y}\sin\phi\sin\theta + \hat{z}\cos\theta], \quad (1)$$

$$\begin{aligned}\boldsymbol{E} = E_0[&\hat{x}(\cos\phi\cos\theta\cos\varphi - \sin\phi\sin\varphi)\\ &+\hat{y}(\sin\phi\cos\theta\cos\varphi + \cos\phi\sin\varphi)\\ &+\hat{z}(-\sin\theta\cos\varphi)],\end{aligned} \quad (2)$$

where β_0 and E_0 are magnitudes of the electric field and the propagation vector, $\hat{x}$, $\hat{y}$, $\hat{z}$ are unit vectors in the direction of each coordinate axis. Then, the oblique incident and arbitrarily polarized plane wave can be decomposed into several normally incident plane waves.

B. Resonant frequency analysis

It is well known that the resonant frequency of each resonant mode in a rectangular cavity of size $a \times b \times d$ can be expressed as:

$$f_{mnp} = \frac{c}{2\pi}\sqrt{(\frac{m\pi}{a})^2 + (\frac{n\pi}{b})^2 + (\frac{p\pi}{d})^2}, \quad (3)$$

where $c = 1/\sqrt{\mu_0\varepsilon_0}$ is the speed of light in free space, ε_0 and μ_0 are the permittivity and permeability in free space, *m*, *n* and *p* are mode indexes in ***x***, ***y***, and ***z*** directions. A resonant frequency usually corresponds to a unique resonant mode of electromagnetic fields in the cavity. Theoretically, the number of modes in a rectangular cavity is a function of the frequency. The number of modes has a smoothed approximation as [14]:

$$N_S(f) = \frac{8\pi abdf^3}{3c^2} - (a+b+d)\frac{f}{c} + \frac{1}{2}. \quad (4)$$

Equation (4) shows that the number of modes and the mode density increase markedly as the frequency increases.

For the shielding enclosure excited by an external plane wave shown in Fig. 1, its shielding performance is,

to a large extent, determined by its resonant properties. Therefore, it is necessary to analyze the resonant properties of the enclosure under specified excitation. For simplicity, we remove the aperture array residing on the side ***x*-*z*** wall, and keep the aperture array residing on the front ***y*-*z*** wall. The related parameters are set to be $\phi = 0^o$, $\theta = 90^o$, and $\varphi = 90^o$, thus the plane wave propagates in -***x*** direction and has its electric field polarized in ***y*** direction.

The Full-wave TLM numerical method in the time domain can accurately deal with arbitrarily complex geometry [15]. Therefore, the TLM method is adopted to compute the electric SE of the enclosure in the following examples. During the TLM simulation, we slowly increase the mesh density until the results converge. The material of the enclosure is assumed to be aluminum with a conductivity of 3.54×10^7 S/m. Take this particular configuration for example, hexahedron absorbing boundary which has all its face 109 mm away from the enclosure is adopted. The whole solution domain is discretized into a Cartesian mesh of grid cells, and the total number of grid cells is 6.34×10^6. The time step is 7.51×10^{-13} s, and the total number of time step is 3.58×10^5.

In Fig. 3, the actual resonant frequencies indicated by the troughs of the electric SE curve are compared with all the possible resonant frequencies. It can be observed from Fig. 3 that only a few of the possible resonant modes are really excited. Specifically, the resonant frequencies for this configuration are 1317 MHz, 1501 MHz, 1600 MHz, 1653 MHz, 1767 MHz, and 1804 MHz. Therefore, this paper investigates the physical mechanism of resonances in shielding enclosures and proposes an effective method for resonance prediction.

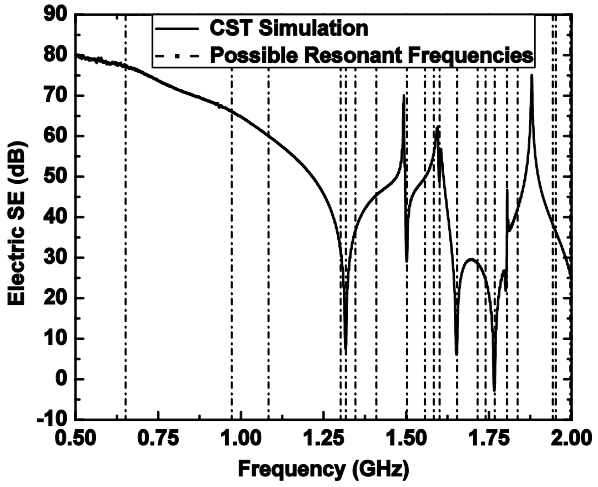

Fig. 3. Electric SE of the enclosure; all possible resonances are indicated with vertical dashed lines.

III. RESONANCE PREDICTION

It is known that the electromagnetic wave transmitted through a small aperture into an enclosure is equivalent to the wave radiated by an infinitesimal electric current and an infinitesimal magnetic current without the aperture present [16],

$$\boldsymbol{J} = j\omega\varepsilon_0\alpha_e\hat{n}E_n\delta(x-x_0)\delta(y-y_0)\delta(z-z_0), \quad (5)$$

$$\boldsymbol{M} = -j\omega\mu_0\alpha_m\boldsymbol{H}_t\delta(x-x_0)\delta(y-y_0)\delta(z-z_0), \quad (6)$$

where α_e and α_m are electric and magnetic polarizability of the aperture, E_n and $\boldsymbol{H}_t$ are the undisturbed normal electric field and transverse magnetic field at the position of the aperture, $\hat{n}$ is the unit vector normal to the surface of the aperture, (x_0, y_0, z_0) are the coordinates of the aperture， and $\delta(x), \delta(y), \delta(z)$ are Dirac delta functions.

The enclosure in Fig. 1 is adopted here to derive the radiated fields and predict the resonances. For simplicity, the apertures residing on the side ***x*-*z*** wall are again removed, the incident angles and polarization angle are set to be $\phi = 0^o$, $\theta = 90^o$, and $\varphi = 90^o$. Since $E_n = 0$ for normal incident case, we need only consider the fields produced by the magnetic current. The magnetic field of the incident plane wave can be expressed as:

$$\boldsymbol{H}^i = -\hat{z}\frac{E_0}{\eta_0}e^{j\beta x}, \quad (7)$$

where $\eta_0 = \sqrt{\mu_0/\varepsilon_0}$ is the intrinsic impedance of free space, β is the phase constant. Equation (7) represents a plane wave polarized in ***y*** direction and propagation in -***x*** direction. The enclosure with apertures closed will approximately cause a total reflection of the incident fields. Thus the total magnetic field outside the enclosure with apertures closed can be expressed as

$$\boldsymbol{H} = -\hat{z}\frac{E_0}{\eta_0}(e^{j\beta x} + e^{-j\beta x}). \quad (8)$$

Then, 21 equivalent magnetic currents each located at the center of the corresponding aperture can be introduced to replace the aperture array. The equivalent magnetic current that represents the aperture located at the center of the ***y*-*z*** wall is analyzed here in detail. The magnetic current density of the equivalent magnetic current is:

$$\boldsymbol{M} = \hat{z}\frac{2j\omega\mu_0E_0\alpha_m}{\eta_0}\delta(x)\delta(y-\frac{b}{2})\delta(z-\frac{d}{2}). \quad (9)$$

In this case, the presence of the conducting wall is easily accounted for using image theory, which has the effect of doubling the current strengths and removing the wall. Thus the electric field radiated by the equivalent magnetic current can be expressed as [17]

$$\boldsymbol{E} = \sum_{n,p} A_{n,p}\boldsymbol{E}^{-x}_{n,p}, \quad (10)$$

where n and p represent the mode indexes in ***y*** direction and ***z*** direction, $\boldsymbol{E}_{n,p}^{-x}$ is the electric field component of the (n, p) mode propagating in ***-x*** direction, $A_{n,p}$ denotes the corresponding coefficient that can be expressed as

$$A_{n,p} = \frac{1}{F_{n,p}} \int_V \boldsymbol{H}_{n,p}^{x} \cdot \boldsymbol{M} dv, \tag{11}$$

where $\boldsymbol{H}_{n,p}^{x}$ denotes the magnetic field component of the (n, p) mode propagating in ***x*** direction, $F_{n,p}$ is a normalization constant proportional to the power flow of the corresponding mode [17].

It can be seen from equation (11) that only the ***z*** component of $\boldsymbol{H}_{n,p}^{x}$ has a contribution to the coefficient $A_{n,p}$, which makes the analysis more straightforward. The ***z*** component of $\boldsymbol{H}_{n,p}^{x}$ has a form of

$$(\boldsymbol{H}_{n,p}^{x})_z = B \cos\frac{n\pi y}{b} \sin\frac{p\pi z}{d} e^{-j\beta x}, \tag{12}$$

where B is a constant. In order to ensure the coefficient $A_{n,p}$ of the (n, p) mode does not vanish when y is set to be $0.5b$ and z is set to be $0.5d$ in evaluation of equation (11), n must be an even number and p must be an odd number. When it comes to the multiple apertures case as shown in Fig. 1, each aperture can be replaced by corresponding equivalent magnetic current. All magnetic currents point in the same direction, thus the conclusion still holds. This is the physical mechanism that only a few of the possible resonant modes are really excited.

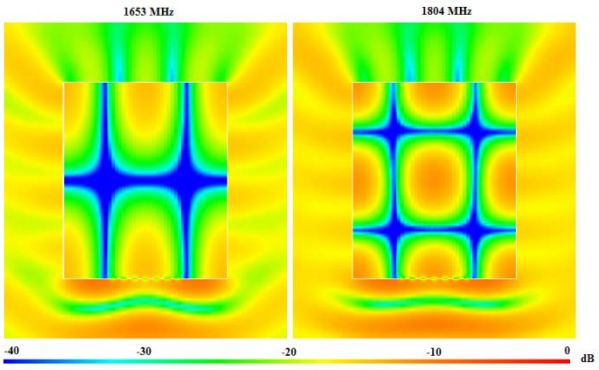

Fig. 4. The RMS magnitude of the magnetic field on the plane z = 60 mm at 1653 MHz and 1804 MHz.

The resonant frequencies shown in Fig. 3 exactly validate this conclusion. The resonant frequencies for this configuration are 1317 MHz for TE_x101, 1501 MHz for TE_x201, 1600 MHz for TM_x021, 1653 MHz for TE_x121, 1653 MHz for TM_x121, 1767 MHz for TE_x301, 1804 MHz for TE_x221, and 1804 MHz for TM_x221. The RMS magnitude of the magnetic field on the plane z = 60 mm in the entire computational domain is shown in Fig. 4, where the horizontal direction and vertical direction correspond to the y-axis direction and x-axis direction in Figure 1. In Fig. 4, the magnetic field distributions at 1653 MHz and 1804 MHz are shown out, which intuitively indicate the mode indexes of these two resonant modes.

IV. VERIFICATION FOR OTHER CONFIGURATIONS

A. Normal incidence in -y direction

In this subsection, we remove the aperture array residing on the front ***y-z*** wall, and keep the aperture array residing on the side ***x-z*** wall. The related parameters are set to be $\phi = 90^\circ$, $\theta = 90^\circ$, and $\varphi = 0^\circ$, thus the plane wave propagates in ***-y*** direction and has its electric field polarized in ***-z*** direction. In this case, the electromagnetic fields transmitted through apertures can be equivalent to fields radiated by magnetic currents in ***-x*** direction. The equivalent magnetic current that represents the aperture located at the center of the ***x-z*** wall is analyzed here in detail. The magnetic current density of the equivalent magnetic current is

$$\boldsymbol{M} = -\hat{x} \frac{2j\omega\mu_0 E_0 \alpha_m}{\eta_0} \delta(x - \frac{a}{2}) \delta(y) \delta(z - \frac{d}{2}). \tag{13}$$

It can be seen from equation (11) that only the ***x*** component of $\boldsymbol{H}_{m,p}^{y}$ has a contribution to the coefficient $A_{m,p}$. The ***x*** component of $\boldsymbol{H}_{m,p}^{y}$ has a form of

$$(\boldsymbol{H}_{m,p}^{y})_x = C \sin\frac{m\pi x}{a} \cos\frac{p\pi z}{d} e^{-j\beta y}, \tag{14}$$

where C is a constant. In order to ensure the coefficient $A_{m,p}$ of the (m, p) mode does not vanish when x is set to be $0.5a$ and z is set to be $0.5d$ in evaluation of equation (11), m must be an odd number and p must be an even number.

It can also be deduced that the resonant frequencies are larger than 2GHz when p is greater than or equal to 2, so p must be equal to 0, thus m must be nonzero. Consequently, the resonant modes must be TE_y type and n must be nonzero. The predicted resonant modes and resonant frequencies are indicated in Table 1 as gray cells. The simulated shielding effectiveness revealing resonances shown in Fig. 5 again confirms the prediction.

Table 1: Resonant frequencies in MHz predicted by the proposed method

m \ n	1	2	3
1	650	1083	1556
2	971	1301	1715
3	1345	1600	1951
4	1739	1942	2241

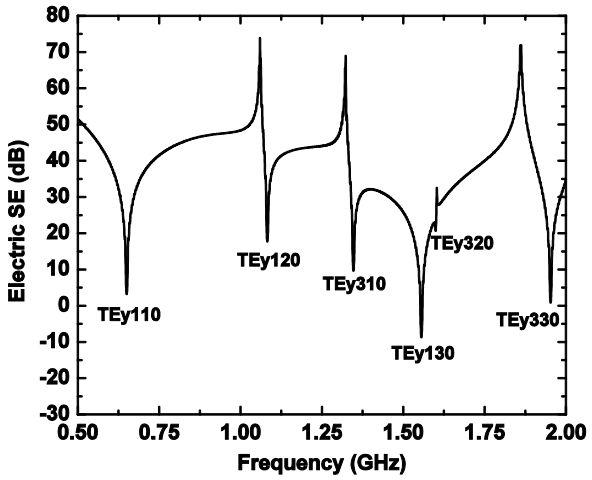

Fig. 5. The resonant frequencies and corresponding modes of the enclosure with aperture array residing on the side ***x*-*z*** wall.

B. Aperture arrays residing on the multiple walls

In this subsection, the aperture arrays residing on the front ***y*-*z*** wall and the side ***x*-*z*** wall are both kept. The related parameters are set to be $\phi = 30^{\circ}$, $\theta = 90^{\circ}$, and $\varphi = 0^{\circ}$, thus the plane wave is obliquely incident and has its electric field polarized in ***-z*** direction. In this case, the plane wave can be decomposed into two plane waves, one propagates in ***-x*** direction and another propagates in ***-y*** direction, both have their electric field polarized in ***-z*** direction.

For the plane wave propagating in ***-y*** direction, its analysis is the same as that in subsection 4.1. Therefore, *m* must be an odd number and *p* must be an even number. For the plane wave propagating in ***-x*** direction, its magnetic field is in ***-y*** direction, thus the electromagnetic fields propagating through apertures can be equivalent to fields radiated by magnetic currents in ***y*** direction. The equivalent magnetic current that represents the aperture located at the center of the ***y*-*z*** wall is analyzed here in detail. The magnetic current density of the equivalent magnetic current is:

$$\boldsymbol{M} = \hat{y}\frac{2j\omega\mu_0 E_0 \alpha_m}{\eta_0}\delta(x)\delta(y-\frac{b}{2})\delta(z-\frac{d}{2}). \qquad (15)$$

It can be seen from equation (11) that only the ***y*** component of $\boldsymbol{H}^{x}_{n,p}$ has a contribution to the coefficient $A_{n,p}$. The ***y*** component of $\boldsymbol{H}^{x}_{n,p}$ has a form of

$$(\boldsymbol{H}^{x}_{n,p})_y = D\sin\frac{n\pi y}{b}\cos\frac{p\pi z}{d}e^{-j\beta x}, \qquad (16)$$

where D is a constant. In order to ensure the coefficient $A_{n,p}$ of the (n, p) mode does not vanish when y is set to be $0.5b$ and z is set to be $0.5d$ in evaluation of equation (11), n must be an odd number and p must be an even number.

In conclusion, for the original obliquely incident plane wave, its mode indexes need to satisfy the following conditions: *m* and *n* cannot be even numbers at the same time, and *p* must be an even number. It can also be deduced that the resonant frequencies are larger than 2GHz when *p* is greater than or equal to 2, so *p* must be equal to 0, thus *m* and *n* must be nonzero. Consequently, the resonant modes must be TE_x type or TE_y type. The predicted resonant modes and resonant frequencies are indicated in Table 2 as gray cells. The simulated shielding effectiveness revealing resonances shown in Fig. 6 again confirms the prediction. It is worth noting that the simulation takes several hours on a desktop to predict the entire resonances.

Table 2: Resonant frequencies in MHz predicted by the proposed method

m \ *n*	1	2	3
1	650	1083	1556
2	971	1301	1715
3	1345	1600	1951
4	1739	1942	2241

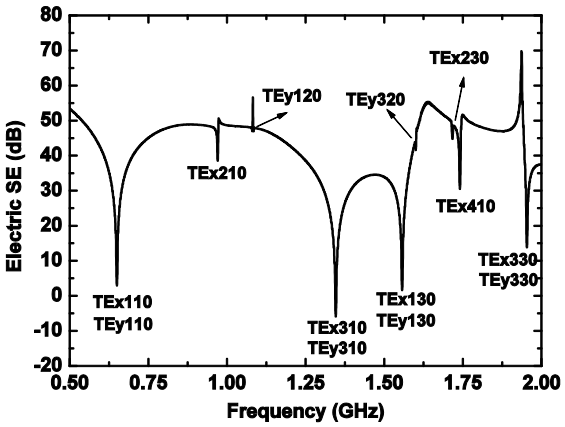

Fig. 6. The resonant frequencies and corresponding modes of the enclosure with aperture arrays residing on the front ***y*-*z*** wall and the side ***x*-*z*** wall.

V. CONCLUSION

In view of the importance of resonance prediction in evaluation of the shielding performance of a shielding enclosure with apertures, an analytical method to determine the resonant modes and resonant frequencies is proposed based on the specified knowledge of the excitation plane wave. This method outperforms the existing methods in several ways. Firstly, once the properties of the excitation plane wave are known, the resonances of the shielding enclosure can be readily

predicted through a simple theoretical derivation. Moreover, this method can predict all the resonant modes and resonant frequencies of shielding enclosures under plane wave excitation without omission of some potential resonances. Furthermore, compared with full-wave methods, the method presented here is easier to use. Although the studied frequency band is below 2GHz in this paper, the method is applicable to higher frequencies.

ACKNOWLEDGMENT

This project was supported in part by the National Natural Science Foundation of China (Grant No. 51705067), the Fundamental Research Funds for the Central Universities of China (Grant No. ZYGX2018J046), and in part by the China Postdoctoral Science Foundation (Grant No. 2015M582534).

REFERENCES

[1] M. P. Robinson, T. M. Benson, C. Christopoulos, J. F. Dawson, M. D. Ganley, A. C. Marvin, S. J. Porter, and D. W. P. Thomas, "Analytical formulation for the shielding effectiveness of enclosures with apertures," *IEEE Trans. Electromagn. Compat.*, vol. 40, no. 3, pp. 240-248, Aug. 1998.

[2] B. L. Nie and P. A. Du, "An efficient and reliable circuit model for the shielding effectiveness prediction of an enclosure with a slot-aperture," *IEEE Trans. Electromagn. Compat.*, vol. 57, no. 3, pp. 357-364, June 2015.

[3] D. Shi, N. Lv, and Y. Gao, "Shielding effectiveness estimation of a metallic enclosure with an off-center aperture for obliquely incident and arbitrary polarized plane wave," *ACES Journal*, vol. 32, no. 4, pp. 352-357, Apr. 2017.

[4] B. L. Nie, Q. S. Liu, and P. A. Du, "An improved thickness correction method of analytical formulations for shielding effectiveness prediction," *IEEE Trans. Electromagn. Compat.*, vol. 58, no. 3, pp. 907-910, June 2016.

[5] C. C. Wang, C. Q. Zhu, X. Zhou, and Z. F. Gu, "Calculation and analysis of shielding effectiveness of the rectangular enclosure with aperture," *ACES Journal*, vol. 28, no. 6, pp. 535-544, June 2013.

[6] J. Chen and J. Wang, "A three-dimensional semi-implicit FDTD scheme for calculation of shielding effectiveness of enclosure with thin slots," *IEEE Trans. Electromagn. Compat.*, vol. 49, no. 2, pp. 354-360, Feb. 2007.

[7] B. L. Nie, P. A. Du, Y. T. Yu, and Z. Shi, "Study of the shielding properties of enclosures with apertures at higher frequencies using the transmission-line modeling method," *IEEE Trans. Electromagn. Compat.*, vol. 53, no. 1, pp. 73-81, Feb. 2011.

[8] W. Abdelli, X. Mininger, L. Pichon, and H. Trabelsi, "Impact of composite materials on the shielding effectiveness of enclosure," *ACES Journal*, vol. 27, no. 4, pp. 369-375, Apr. 2012.

[9] B. L. Nie and P. A. Du, "Electromagnetic shielding performance of highly resonant enclosures by a combination of the FETD and extended Prony's method," *IEEE Trans. Electromagn. Compat.*, vol. 56, no. 2, pp. 320-327, Apr. 2014.

[10] R. Araneo and G. Lovat, "Analysis of the shielding effectiveness of metallic enclosure excited by internal source through an efficient method of moment approach," *ACES Journal*, vol. 25, no. 7, pp. 600-611, July 2010.

[11] C.-H. Liang and D. K. Cheng, "Electromagnetic fields coupled into a cavity with a slot-aperture under resonant conditions," *IEEE Trans. Antennas Propag.*, vol. 30, no. 4, pp. 664-672, July 1982.

[12] B. Ma and D. K. Cheng, "Resonant electromagnetic field coupled into a lossy cavity through a slot aperture," *IEEE Trans. Antennas Propag.*, vol. AP-35, no. 9, pp. 1074-1077, Sep. 1987.

[13] R. W. Scharstein, "Complex resonances of a hard rectangular cavity coupled to a half-space through a narrow aperture," *IEEE Trans. Antennas Propag.*, vol. 57, no. 12, pp. 3835-3846, Dec. 2009.

[14] D. A. Hill, *Electromagnetic Fields in Cavities: Deterministic and Statistical Theories*. John Wiley & Sons, Inc., New Jersey, 2009.

[15] W. J. R. Hoefer, "The transmission-line matrix method—Theory and applications," *IEEE Trans. Microw. Theory Techn.*, vol. MTT-33, no. 10, pp. 882-893, Oct. 1985.

[16] B. L. Nie, P. Xiao, and P. A. Du, "Electromagnetic resonance analysis of a shielding enclosure with apertures excited by a plane wave," *IEEE Int. Symp. on Electromagn. Compat. and Asia-Pacific Symp. on Electromagn. Compat.*, Singapore, pp. 355-358, May 2018.

[17] R. E. Collin, *Foundations for Microwave Engineering, Second Edition*. McGraw-Hill, New York, 1992.

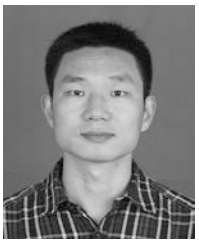

Bao-Lin Nie was born in Shangluo, China, in 1985. He received the B.S. degree and Ph.D. degree in Mechatronics Engineering from the University of Electronic Science and Technology of China, Chengdu, China, in 2007 and 2014, respectively.

From 2010 to 2012, he was a Visiting Student in the Center for Computational Electromagnetics, Department of Electrical and

Computer Engineering, University of Illinois at Urbana-Champaign, Urbana, under the financial support from the China Scholarship Council. Currently, he is an Associate Professor with the University of Electronic Science and Technology of China, Chengdu. His research interests include the analysis of electromagnetic compatibility, EMI in shielding enclosures, multi-physics simulation, and parallel computation.

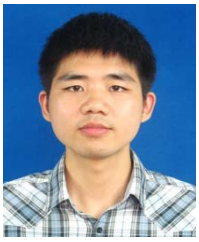

Zhong Cao was born in Chongqing, China, in 1988. He received the Bachelor and Master degrees from the University of Electronic Science and Technology of China, Chengdu, China, in 2011 and 2014. His research interests include electromagnetic simulation, and EMC in shielding enclosures.

Ping-An Du received the M.S. and Ph.D degrees in Mechanical Engineering from Chongqing University, Chongqing, China, in 1989 and 1992, respectively. He is currently a Full Professor of Mechanical Engineering at the University of Electronic Science and Technology of China, Chengdu, China. His research interests include numerical simulation in EMI, vibration, temperature, and so on.

Fast Analysis of Electromagnetic Scattering from a Coated Conductor with the Parabolic Equation

Zi He [1,2], Hong-Cheng Yin [1], and Ru-Shan Chen [2]

Science and Technology on Electromagnetic Scattering Laboratory, BIEF, Beijing, China
zihe@njust.edu.cn, yinhc207@126.com

Department of Communication Engineering
Nanjing University of Science and Technology, Nanjing 210094, China.
eerschen@njust.edu.cn

Abstract — In recent years, the electromagnetic scattering from the coated conductors has been paid more and more attention by many scholars. The parabolic equation (PE) method is firstly utilized to analyze electrically large conductors coated with lossy medium in this paper. The impedance boundary condition is implemented to analyze the lossy medium and the implicit finite difference method of Crank–Nicolson scheme is implemented to solve the parabolic equation. As a result, the computations can be taken in each two-dimensional transverse plane. By this means, both the CPU time and memory requirement are reduced greatly. Numerical results are given to demonstrate the accuracy and efficiency of the proposed method.

Index Terms — electromagnetic scattering, finite difference scheme, impedance boundary condition, parabolic equation method,

I. INTRODUCTION

The electromagnetic (EM) scattering analysis of the conductor has become a research hot due to its wide application in military area. There are a lot of rigorous numerical methods to solve this problem, such as the finite difference time domain (FDTD) [1-3], method of moment (MoM) [4-6], time domain integral equation (TDIE) method [7-8] and so on. In order to reduce the computational requirement, many acceleration techniques were implemented. Firstly, the fast Fourier transform (FFT) has been used to obtain the scattering characteristics [9]. Then the adaptive cross approximate (ACA) algorithm was proposed in [10] to accelerate the surface integral equation-based MoM. Besides, some novel techniques have been applied to reduce the computational complexity, such as adaptive integral method (AIM) [11], equivalent dipole moment (EDM) method [12], thin dielectric sheet (TDS) approximation [13-14]. However, for the rigorous numerical methods, solving electrically large problems takes a great deal of computational resources. As a result, it is necessary to develop the approximation methods to efficiently compute the EM scattering properties of coated conductors.

Parabolic equation (PE) method bridges the rigorous and high frequency methods. It can provide encouraging accuracy along the paraxial direction with limited computational resources. It should be noted that the energy is supposed to propagate in a cone. The PE method was firstly used to analyze the underwater acoustics [15]. Then it was widely applied to calculate the long-range propagation problems of radio wave [16-18]. Many early works have been done by using the split-step Fourier-based PE (SSPE) method. When compared with other PE solvers, the computational efficiency of SSPE is extremely high. However, for the complicated targets, it is not flexible to model the boundary. Therefore, the finite difference (FD) schemes are good choices to deal with targets with complicated boundaries. In recent years, the PE is also introduced to the EM scattering from electrically large conducting targets [19–25]. The Crank-Nicolson-based implicit FD method can be used as an efficient solver for the PE. It should be noted that the rectangular meshes with the mesh size of 1/10th of a wavelength are applied. Nevertheless, when analyzing electrically large targets, there is a supersized sparse matrix equation should be solved in each transverse plane. In recent years, some novel FD schemes are proposed to accelerate the calculation, such as alternating direction implicit (ADI) [17, 22-23, 26], alternating group explicit (AGE) [24, 27-28] schemes. In this way, both the efficiency and the accuracy can be guaranteed. However, there is no report of scattering characteristics for coated targets by using the PE method.

In this paper, the impedance boundary condition is integrated into parabolic equation to fast analyze the electromagnetic scattering from coated conductors. Firstly, the parabolic equation is constructed and the waves in each transverse plane are absorbed with the help of the perfect matching layer (PML). Then Leontovich

Submitted On: August 17, 2018
Accepted On: September 24, 2018

boundary condition is applied on the boundary of perfectly electrical conductor (PEC). It can be found that the error becomes larger with the thickness of the coating material increasing. In other words, the proposed PE method can be used to analyze thin medium-coated conductors. By adopting the Crank-Nicolson scheme to the paraxial direction, PE is implemented in a marching manner. In addition, the bistatic RCS results can be fully obtained by rolling the paraxial direction of PE. Some complex structures, such as missile and plane, are modeled to validate the proposed method.

II. THEORY

A. The standard PE method

Assume *x* axis as the paraxial direction of PE. Then the standard PE in free space can be written as:

$$\frac{\partial u}{\partial x}=\frac{i}{2k}\left(\frac{\partial^2 u}{\partial y^2}+\frac{\partial^2 u}{\partial z^2}\right), \tag{1}$$

where u is the reduced scattered field and can be written as:

$$u(x,y,z)=e^{-ikx}\psi(x,y,z), \tag{2}$$

where ψ represents the scattered field component.

The Crank-Nicolson scheme is introduced to equation (1), and the discretized formula for (1) can be obtained:

$$\begin{aligned}&\left(\frac{i\Delta x}{k\Delta y^2}+\frac{i\Delta x}{k\Delta z^2}+1\right)u_{p,q}^{m+1}-\frac{i\Delta x}{2k\Delta y^2}u_{p-1,q}^{m+1}-\frac{i\Delta x}{2k\Delta z^2}u_{p,q-1}^{m+1}\\&-\frac{i\Delta x}{2k\Delta y^2}u_{p+1,q}^{m+1}-\frac{i\Delta x}{2k\Delta z^2}u_{p,q+1}^{m+1}=u_{p,q}^{m}\end{aligned}, \tag{3}$$

in which, Δx denotes the range step along the paraxial direction, $\Delta y,\Delta z$ are the mesh sizes along the *y*, *z* directions, $u_{p,q}^{m}$ is the reduced scattered fields for $(m\Delta x, p\Delta y, q\Delta z)$.

B. Leontovich impedance boundary condition (IBC)

The electromagnetic field components of u_x,u_y,u_z are coupled by adding the proper boundary conditions on PEC surface. The Leontovich impedance boundary condition is given in terms of surface impedance and can be expressed in the following form

$$\hat{n}\times\mathbf{E}(P)=Z\left[\hat{n}\times\left(\hat{n}\times\mathbf{H}(P)\right)\right], \tag{4}$$

in which $\hat{n}$ is the unit normal vector on the surface of the scattering target, *Z* is the impedance of the object at point *P* and it is defined as:

$$Z=-iZ_0\sqrt{\frac{\mu_r}{\varepsilon_r}}\tan(Nkd), \tag{5}$$

where Z_0 denotes the wave impedance in free space, *d* is the thickness of the coated medium, $N=\sqrt{\mu_r\varepsilon_r}$, μ_r,ε_r represent the permeability and permittivity of the coated medium.

By eliminating the magnetic field, the equation (4) can be rewritten as:

$$\hat{n}\times\mathbf{E}(P)=\frac{Z}{ikZ_0}\left[\hat{n}\cdot\left(\nabla\times\mathbf{E}(P)\right)\hat{n}-\nabla\times\mathbf{E}(P)\right]. \tag{6}$$

The equation (4) can be expressed in terms of the electric fields. Then the magnetic fields can be calculated by taking advantage of the curl equation:

$$\begin{aligned}&n_yu_z-n_zu_y-\frac{Z}{ikZ_0}\begin{bmatrix}n_xn_z\left(iku_y-\frac{1}{2ik}\left(\frac{\partial^2u_y}{\partial y^2}+\frac{\partial^2u_y}{\partial z^2}\right)-\frac{\partial u_x}{\partial y}\right)+\\(n_x^2-1)\left(\frac{\partial u_z}{\partial y}-\frac{\partial u_y}{\partial z}\right)+\\n_xn_y\left(\frac{\partial u_x}{\partial z}+\frac{1}{2ik}\left(\frac{\partial^2u_z}{\partial y^2}+\frac{\partial^2u_z}{\partial z^2}\right)-iku_z\right)\end{bmatrix},\\&=(-n_yE_z^i+n_zE_y^i)e^{-ikx}+\frac{Ze^{-ikx}}{ikZ_0}\begin{bmatrix}(n_x^2-1)\left(\frac{\partial E_z^i}{\partial y}-\frac{\partial E_y^i}{\partial z}\right)+\\n_xn_y\left(\frac{\partial E_x^i}{\partial z}-\frac{\partial E_z^i}{\partial x}\right)+\\n_xn_z\left(\frac{\partial E_y^i}{\partial x}-\frac{\partial E_x^i}{\partial y}\right)\end{bmatrix}\end{aligned} \tag{7}$$

$$\begin{aligned}&n_zu_x-n_xu_z-\frac{Z}{ikZ_0}\begin{bmatrix}n_xn_y\left(\frac{\partial u_z}{\partial y}-\frac{\partial u_y}{\partial z}\right)+\\(n_y^2-1)\left(\frac{\partial u_x}{\partial z}+\frac{1}{2ik}\left(\frac{\partial^2u_z}{\partial y^2}+\frac{\partial^2u_z}{\partial z^2}\right)-iku_z\right)+\\n_yn_z\left(iku_y-\frac{1}{2ik}\left(\frac{\partial^2u_y}{\partial y^2}+\frac{\partial^2u_y}{\partial z^2}\right)-\frac{\partial u_x}{\partial y}\right)\end{bmatrix},\\&=(-n_zE_x^i+n_xE_z^i)e^{-ikx}+\frac{Ze^{-ikx}}{ikZ_0}\begin{bmatrix}n_xn_y\left(\frac{\partial E_z^i}{\partial y}-\frac{\partial E_y^i}{\partial z}\right)+\\(n_y^2-1)\left(\frac{\partial E_x^i}{\partial z}-\frac{\partial E_z^i}{\partial x}\right)+\\n_yn_z\left(\frac{\partial E_y^i}{\partial x}-\frac{\partial E_x^i}{\partial y}\right)\end{bmatrix}\end{aligned} \tag{8}$$

$$\begin{aligned}&n_xu_y-n_yu_x-\frac{Z}{ikZ_0}\begin{bmatrix}n_xn_z\left(\frac{\partial u_z}{\partial y}-\frac{\partial u_y}{\partial z}\right)+\\n_yn_z\left(\frac{\partial u_x}{\partial z}+\frac{1}{2ik}\left(\frac{\partial^2u_z}{\partial y^2}+\frac{\partial^2u_z}{\partial z^2}\right)-iku_z\right)+\\(n_z^2-1)\left(iku_y-\frac{1}{2ik}\left(\frac{\partial^2u_y}{\partial y2}+\frac{\partial^2u_y}{\partial z2}\right)-\frac{\partial u_x}{\partial y}\right)\end{bmatrix},\\&=(-n_xE_y^i+n_yE_x^i)e^{-ikx}+\frac{Ze^{-ikx}}{ikZ_0}\begin{bmatrix}n_xn_z\left(\frac{\partial E_z^i}{\partial y}-\frac{\partial E_y^i}{\partial z}\right)+\\n_yn_z\left(\frac{\partial E_x^i}{\partial z}-\frac{\partial E_z^i}{\partial x}\right)+\\(n_z^2-1)\left(\frac{\partial E_y^i}{\partial x}-\frac{\partial E_x^i}{\partial y}\right)\end{bmatrix}\end{aligned} \tag{9}$$

where (E_x^i, E_y^i, E_z^i) is the incident plane wave.

At last, the discretized form can be obtained by using the FD scheme, which can be derived as:

$$\left(\frac{n_x n_z}{ik\Delta y}-\frac{n_x n_y}{ik\Delta z}\right)u^m_{x,p,q}-\frac{n_x n_z}{ik\Delta y}u^m_{x,p+1,q}+\frac{n_x n_y}{k^2\Delta z^2}u^m_{z,p,q+1}+\frac{n_x n_y}{ik\Delta z}u^m_{x,p,q+1}-\frac{n_x n_z}{k^2\Delta y^2}u^m_{y,p+1,q}+\left(\frac{n_x n_y}{k^2\Delta y^2}+\frac{n_x^2-1}{ik\Delta z}\right)u^m_{z,p+1,q}+\left(\begin{array}{l}\frac{n_x n_z}{2k^2\Delta y^2}+\frac{n_x n_z}{2k^2\Delta z^2}+\\ \frac{n_x^2-1}{ik\Delta z}+n_x n_z+\frac{Z_0}{Z}n_z\end{array}\right)u^m_{y,p,q}-\left(\frac{n_x n_z}{k^2\Delta z^2}+\frac{n_x^2-1}{ik\Delta z}\right)u^m_{y,p,q+1}+\left(\begin{array}{l}\frac{n_x n_y}{2k^2\Delta y^2}+\frac{n_x n_y}{2k^2\Delta z^2}\\ +\frac{n_x^2-1}{ik\Delta y}+n_x n_y+n_y\frac{Z_0}{Z}\end{array}\right)u^m_{z,p,q}-\frac{n_x n_y}{2k^2\Delta y^2}u^m_{z,p+2,q}-\frac{n_x n_y}{2k^2\Delta z^2}u^m_{z,p,q+2}+\frac{n_x n_z}{2k^2\Delta y^2}u^m_{y,p+2,q}+\frac{n_x n_z}{2k^2\Delta z^2}u^m_{y,p,q+2}=n_y\frac{Z_0}{Z}+n_x n_y \tag{10}$$

$$\left(\frac{n_y n_z}{ik\Delta y}-\frac{n_y^2-1}{ik\Delta z}-n_z\frac{Z_0}{Z}\right)u^m_{x,p,q}-\frac{n_y n_z}{ik\Delta y}u^m_{x,p+1,q}+\frac{n_y^2-1}{ik\Delta z}u^m_{x,p,q+1}+\left(\frac{n_y n_z}{2k^2\Delta y^2}+\frac{n_y n_z}{2k^2\Delta z^2}+\frac{n_x n_y}{ik\Delta z}+n_y n_z\right)u^m_{y,p,q}-\frac{n_y n_z}{k^2\Delta y^2}u^m_{y,p+1,q}-\left(\frac{n_y n_z}{k^2\Delta z^2}+\frac{n_x n_y}{ik\Delta z}\right)u^m_{y,p,q+1}+\frac{n_y n_z}{2k^2\Delta y^2}u^m_{y,p+2,q}-\left(\frac{n_y^2-1}{2k^2\Delta y^2}+\frac{n_y^2-1}{2k^2\Delta z^2}+\frac{n_x n_y}{ik\Delta y}-n_x\frac{Z_0}{Z}+n_y^2-1\right)u^m_{z,p,q}+\frac{n_y n_z}{2k^2\Delta z^2}u^m_{y,p,q+2}+\left(\frac{n_y^2-1}{k^2\Delta y^2}+\frac{n_x n_y}{ik\Delta y}\right)u^m_{z,p+1,q}-\frac{n_y^2-1}{2k^2\Delta y^2}u^m_{z,p+2,q}-\frac{n_y^2-1}{2k^2\Delta z^2}u^m_{z,p,q+2}+\frac{n_y^2-1}{k^2\Delta z^2}u^m_{z,p,q+1}=n_y^2-1-n_x\frac{Z_0}{Z} \tag{11}$$

$$\left(\frac{n_z^2-1}{ik\Delta y}-\frac{n_y n_z}{ik\Delta z}+n_y\frac{Z_0}{Z}\right)u^m_{x,p,q}-\frac{n_z^2-1}{ik\Delta y}u^m_{x,p+1,q}+\frac{n_y n_z}{ik\Delta z}u^m_{x,p,q+1}+\left(\frac{n_z^2-1}{2k^2\Delta y^2}+\frac{n_z^2-1}{2k^2\Delta z^2}+\frac{n_x n_z}{ik\Delta z}+n_z^2-1-n_x\frac{Z_0}{Z}\right)u^m_{y,p,q}-\frac{n_z^2-1}{k^2\Delta y^2}u^m_{y,p+1,q}-\left(\frac{n_z^2-1}{k^2\Delta z^2}+\frac{n_x n_z}{ik\Delta z}\right)u^m_{y,p,q+1}+\frac{n_z^2-1}{2k^2\Delta y^2}u^m_{y,p+2,q}-\left(\frac{n_y n_z}{2k^2\Delta y^2}+\frac{n_y n_z}{2k^2\Delta z^2}+\frac{n_x n_z}{ik\Delta y}+n_y n_z\right)u^m_{z,p,q}+\frac{n_y n_z}{k^2\Delta z^2}u^m_{z,p,q+1}+\left(\frac{n_y n_z}{k^2\Delta y^2}+\frac{n_x n_z}{ik\Delta y}\right)u^m_{z,p+1,q}+\frac{n_z^2-1}{2k^2\Delta z^2}u^m_{y,p,q+2}-\frac{n_y n_z}{2k^2\Delta y^2}u^m_{z,p+2,q}-\frac{n_y n_z}{2k^2\Delta z^2}u^m_{z,p,q+2}=n_y n_z \tag{12}$$

It can be seen from equation (3) that the computation is taken one by one in each transverse plane. Moreover, the inhomogeneous boundary conditions of equations (10-12) are introduced on the surface of PEC.

III. NUMERICAL EXAMPLES

In this part, all the numerical results are tested on the computer of Intel Xeon E7-4850 CPU with 8GB RAM. The plane wave with the incident angle of $\theta_{inc}=90^\circ \quad \phi_{inc}=0^\circ$ is used as the incidence source, and the whole simulation system are working at 300 MHz. It should be noted that the IBC-based combined field integral equation (IBC-CFIE) is set to be the rigorous solution for comparison.

At first, we consider a sphere with the radius of 5λ and the relative permittivity of $\varepsilon_r = 3.84 - j1.6$. In this numerical example, the mesh size is 0.05 *m.* Therefore, the calculation is split into 200 transverse planes to the paraxial direction. The full bistatic RCS result for the horizontal plane pattern of the proposed method is given and compared with that of Mie Series in Fig. 1. For the proposed method, the full bistatic RCS result is achieved by rotating the paraxial direction of PE. As shown in Fig. 1, it coincides well for these two methods.

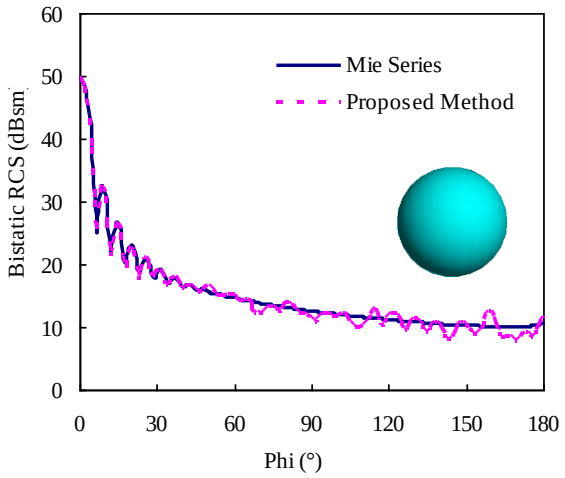

Fig. 1. Comparison of the RCS between the Mie Series and the proposed method for a sphere of the horizontal plane pattern.

Secondly, the EM scattering from a coated cone is considered with the coating thickness of $0.1m$ and the permittivity of $3.5-j1.5$. Its radius and height are $1m$ and $3m$, respectively. The mesh size is set to be $0.05\ m$ and the calculation is split into 60 transverse planes to the paraxial direction. The bistatic RCS of both the PEC and coated cones are compared in Fig. 2. It can be found that the bistatic RCS is decreased greatly at some angles for the coated cone when compared with the PEC cone with no coating. Therefore, the proposed method can be used as an efficient tool to design RCS reduction.

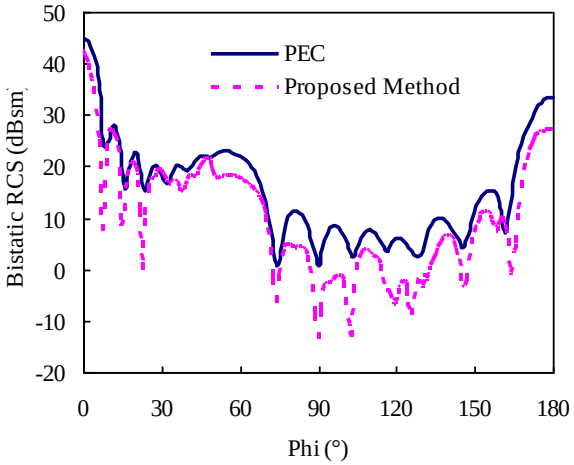

Fig. 2. Comparisons of the bistatic RCS between a coated cone and a PEC cone.

Thirdly, the EM scattering from a PEC missile coated with lossy medium is considered. Its coating thickness is $0.05m$ and the permittivity of the coating medium is $3-j$. As shown in Fig. 3, the size of this PEC missile model is given. The full bistatic RCS results of both the IBC-CFIE and the proposed method are shown and compared in Fig. 4. In this numerical example, there are seven rotating PE runs are applied. More specifically, the generalized minimal residual (GMRES) method is used as the solver of IBC-CFIE and the convergence precision is set to be $1e-3$. Moreover, the computational resources of these methods are also listed in Table 1. It can be concluded that both the memory requirement and the total CPU time of the proposed method can be reduced greatly when compared with the IBC-CFIE. Therefore, the proposed method can be used to fast analyze the electromagnetic scattering from electrically large coated targets with encouraging accuracy.

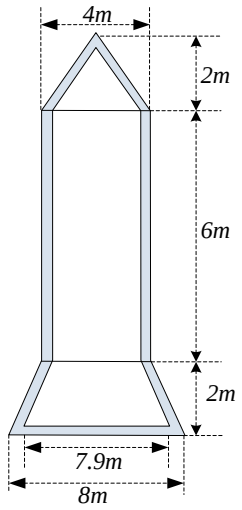

Fig. 3. Geometry structure of a PEC missile model.

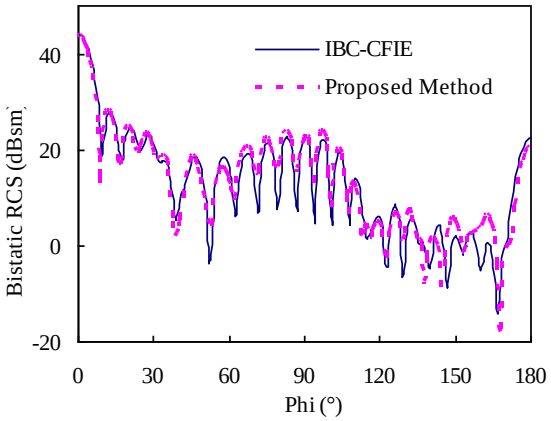

Fig. 4. Bistatic RCS of a coated missile model at the frequency of 300MHz.

Table 1: Comparisons of memory requirement and CPU time between the IBC-CFIE and the proposed method for the coated PEC missile at the frequency of 300 MHz

Method	Memory Requirement (MB)	CPU Time (s)
IBC-CFIE	904	5060
Proposed method	155	15

Finally, a coated PEC aircraft is modeled and its maximum size along x, y, and z directions are $12m$, $9m$, and $4.8m$, respectively. Its coating thickness is $0.01m$ and the permittivity of the coating medium is $1.5-j1.3$. Seven rotating PE runs are applied in this numerical example. The bistatic RCS is given in Fig. 5 and the computational resources of the coated PEC aircraft is also shown in Table 2.

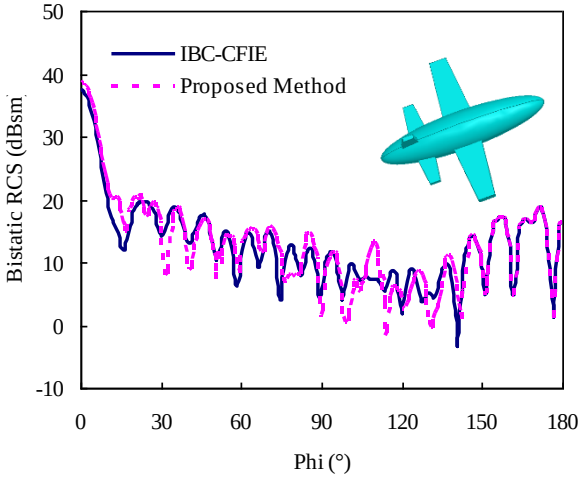

Fig. 5. Bistatic RCS of a coated aircraft model at the frequency of 300MHz.

Table 2: Comparisons of memory requirement and CPU time between the IBC-CFIE and the proposed method for the coated PEC aircraft at the frequency of 300 MHz

Method	Memory Requirement (MB)	CPU Time (s)
IBC-CFIE	823	1814
Proposed method	183	16

IV. CONCLUSION

An efficient solver based on PE is proposed to analyze the EM scattering from electrically large PEC which is coated with thin lossy medium. The Crank-Nicolson scheme is implemented for its accuracy and unconditional stability. In this way, the computations are taken plane by plane. More general boundary conditions are applied to the scattering targets. The first numerical example of a dielectric sphere is given to validate the accuracy of the proposed method. Furthermore, more complicated structures, such as coated missile and plane, are modeled to show the efficiency.

ACKNOWLEDGEMENT

This work was supported in part by Natural Science Foundation of 61701232, 61431006, Jiangsu Province Natural Science Foundation of BK20170854, the Young Elite Scientists Sponsorship Program by CAST of 2017QNRC001, the China Postdoctoral Science Foundation of 2017M620861, 2018T110127, the Fundamental Research Funds for the central Universities of No. 30917011317, and the State Key Laboratory of Millimeter Waves of K201805.

REFERENCES

[1] M. K. Karkkainen, "FDTD model of electrically thick frequency-dispersive coatings on metals and semiconductors based on surface impedance boundary conditions," *IEEE Trans. Antennas and Propagation*, vol. 53, no. 3, pp. 1174-1186, 2005.

[2] C. W. Penney, R. J. Luebbers, and J. W. Schuster, "Scattering from coated targets using a frequency-dependent, surface impedance boundary condition in FDTD," *IEEE Trans. Antennas and Propagation*, vol. 44, no. 4, pp. 434-443, 2002.

[3] J. H. Beggs, R. J. Luebbers, and K. S. Yee, "Finite-difference time-domain implementation of surface impedance boundary conditions," *IEEE Trans. Antennas and Propagation*, vol. 40, no. 1, pp. 49-56, 1992.

[4] J. Hu, L. Lei, and Z. P. Nie, "Fast solution of electromagnetic scattering from thin dielectric coated PEC by MLFMA and successive over-relaxation iterative technique," *IEEE Microwave & Wireless Components Letters*, vol. 19, no. 12, pp. 762-764, 2009.

[5] Z. P. Nie, "A highly efficient numerical solution for dielectric-coated PEC targets," *Waves in Random & Complex Media*, vol. 19, no. 1, pp. 65-79, 2009.

[6] S. F. Tao and R. S. Chen, "Electromagnetic scattering analysis of the conductor coated by multilayer thin materials," *IEEE Antennas and Wireless Propagation Letters*, vol. 12, pp. 1033-1036, 2013.

[7] B. H. Jung, T. K. Sarkar, and Y. S. Chung, "Solution of time domain PMCHW formulation for transient electromagnetic scattering from arbitrarily shaped 3-D dielectric objects," *Progress In Electromagnetics Research*, vol. 45, pp. 291-312, 2004.

[8] Z. He, D. Z. Ding, and R. S. Chen, "An efficient marching-on-in-degree solver of surface integral equation for multilayer thin medium-coated conductors," *IEEE Antennas Wireless Propag.*

Lett., vol. 15, pp. 1458-1461, 2016.

[9] R. Schmehl, B. M. Nebeker, and E. D. Hirleman, "Discrete-dipole approximation for scattering by features on surfaces by means of a two-dimensional fast Fourier transform technique," *Journal of the Optical Society of America A*, vol. 14, no. 11, pp. 3026-3036, 1997.

[10] K. Zhao, M. N. Vouvakis, and J. F. Lee, "The adaptive cross approximation algorithm for accelerated method of moments computations of EMC problems," *IEEE Trans. on Electromagnetic Compatibility*, vol. 47, no. 4, pp. 763-773, 2006.

[11] E. Bleszynski, M. Bleszynski, and T. Jaroszewicz, "AIM: Adaptive integral method for solving large-scale electromagnetic scattering and radiation problems," *Radio Science*, vol. 31, no. 5, pp. 1225-1251, 2016.

[12] Z. He, H. H. Zhang, and R. S. Chen, "Acceleration of the impedance matrix filling for marching-on-in-degree method by EDM," *Electromagnetics*, vol. 35, iss. 4, pp. 260-272, 2015.

[13] I. T. Chiang and W. C. Chew, "A coupled PEC-TDS surface integral equation approach for electromagnetic scattering and radiation from composite metallic and thin dielectric objects," *IEEE Trans. Antennas Propag*., vol. 54, no. 11, pp. 3511-3516, 2006.

[14] Z. He, D. Z. Ding, and R. S. Chen, "An efficient marching-on-in-degree solver of surface integral equation for multilayer thin medium-coated conductors," *IEEE Antennas Wireless Propag. Lett*., vol. 15, pp. 1458-1461, 2016.

[15] R. H. Hardin and F. D. Tappert, "Application of the split-step fourier method to the numerical solution of nonlinear and variable coefficient wave equations," *SIAM Rev*., vol. 15, pp. 423, 1973.

[16] A. E. Barrios, "A terrain parabolic equation model for propagation in the troposphere," *IEEE Trans. Antennas and Propagation*, vol. 42, no. 1, pp. 90-98, 1994.

[17] R. Martelly and R. Janaswamy, "Modeling radio transmission loss in curved, branched and rough-walled tunnels with the ADI-PE method," *IEEE Trans. Antennas and Propagation*, vol. 58, no. 6, pp. 2037-2045, 2010.

[18] Z. He and R. S. Chen, "Two way propagation modeling of expressway with vehicles by using the three-dimensional ADI-PE method," *IEEE Trans. Antennas and Propagation*, vol. 66, no. 4, pp. 2156-2160, 2018.

[19] A. A. Zaporozhets and M. F. Levy, "Bistatic RCS calculations with the vector parabolic equation method," *IEEE Trans. Antennas and Propagation*, vol. 47, no. 11, pp. 1688-1695, 1999.

[20] M. F. Levy, *Parabolic Equation Methods for Electromagnetic Wave Propagation*. London: The Institution of Electrical Engineers, 2000.

[21] Z. He and R. S. Chen, "A vector meshless parabolic equation method for three-dimensional electromagnetic scatterings," *IEEE Trans. Antennas and Propagation*, vol. 63, no. 6, pp. 2595-2603, 2015.

[22] Z. He, Z. H. Fan, D. Z. Ding, and R. S. Chen, "Efficient radar cross-section computation of electrically large targets with ADI-PE method," *Electronics Letters*, vol. 51, no. 4, pp. 360-362, 2015.

[23] Z. He, Z. H. Fan, D. Z. Ding, and R. S. Chen, "GPU-accelerated ADI-PE method for the analysis of EM scatterings," *Electronics Letters*, vol. 51, no. 21, pp. 1652-1654, 2015.

[24] Z. He and R. S. Chen, "A novel parallel parabolic equation method for electromagnetic scatterings," *IEEE Trans. Antennas and Propagation*, vol. 64, no. 11, pp. 4777-4784, 2016.

[25] A. A. Zaporozhets and M. F. Levy, "Bistatic RCS calculations with the vector parabolic equation method," *IEEE Trans. Antennas and Propagation*, vol. 47, no. 11, pp. 1688-1695, 1999.

[26] R. Martelly and R. Janaswamy, "An ADI-PE approach for modeling radio transmission loss in tunnels," *IEEE Trans. Antennas and Propagation*, vol. 57, pp. 1759-1770, 2009.

[27] Q. J. Zhang and W. Q. Wang, "A new alternating group explicit-implicit algorithm with high accuracy for dispersive equation," *Applied Mathematics and Mechanics*, vol. 29, no. 9, pp. 1221-1230, 2008.

[28] D. J. Evans and M. S. Sahimi, "The solution of nonlinear parabolic partial differential equations by the alternating group explicit (AGE) method," *Computer Methods in Applied Mechanics and Engineering*, vol. 84, no. 1, pp. 15-42, 2009.

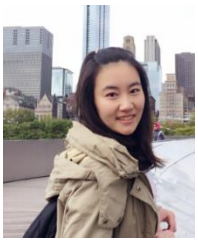

Zi He was born in Hebei, China. She received the B.Sc. and Ph.D. degrees in Electronic Information Engineering from the School of Electrical Engineering and Optical Technique, Nanjing University of Science and Technology, Nanjing, China, in 2011 and 2016, respectively. She has worked as a Visiting Scholar in the University of Illinois at Urbana and Champaign (UIUC) from September 2015 to September 2016. She works as a Postdoctor at the Science and Technology on Electromagnetic Scattering Laboratory, BIEF.

Since 2016, she has been an Assistant Professor with the Department of Communication Engineering, Nanjing University of Science and Technology. Her research interests include antenna, RF-integrated

circuits, and computational electromagnetics.

Hong-Cheng Yin was born in Jiangxi, China. He received the B.S. degree from Northwest Telecommunication Engineering Institute, Xi'an, China, in 1986, the M.S. degree from Beijing Institute of Environmental Features (BIEF), Beijing, China, in 1989, and the Ph.D. degree from Southeast University, Nanjing, China, in 1993, all in Electromagnetic Field and Microwave Technique. He is currently a Researcher at the Science and Technology on Electromagnetic Scattering Laboratory, BIEF. His research interests include numerical methods in electromagnetic fields, electromagnetic scattering and inverse scattering, radar target recognition. Yin is a Fellow of Chinese Institute of Electronics.

Ru-Shan Chen was born in Jiangsu, China. He received the B.Sc. and M.Sc. degrees from the Department of Radio Engineering, Southeast University, China, in 1987 and 1990, respectively, and the Ph.D. degree from the Department of Electronic Engineering, City University of Hong Kong, in 2001.

He joined the Department of Electrical Engineering, Nanjing University of Science and Technology (NJUST), China, where he became a Teaching Assistant in 1990 and a Lecturer in 1992. Since September 1996, he has been a Visiting Scholar with the Department of Electronic Engineering, City University of Hong Kong, first as Research Associate, then as a Senior Research Associate in July 1997, a Research Fellow in April 1998, and a Senior Research Fellow in 1999. From June to September 1999, he was also a Visiting Scholar at Montreal University, Canada. In September 1999, he was promoted to Full Professor and Associate Director of the Microwave and Communication Research Center in NJUST, and in 2007, he was appointed as the Head of the Department of Communication Engineering, NJUST. He was appointed as the Dean in the School of Communication and Information Engineering, Nanjing Post and Communications University in 2009. And in 2011 he was appointed as Vice Dean of the School of Electrical Engineering and Optical Technique, NJUST. Currently, he is a principal investigator of more than 10 national projects. His research interests mainly include computational electromagnetics, microwave integrated circuit and nonlinear theory, smart antenna in communications and radar engineering, microwave material and measurement, RF-integrated circuits, etc. He has authored or coauthored more than 260 papers, including over 180 papers in international journals.

Protection of Computer Enclosure against Coupled Electromagnetic Interference

Run Xiong [1], Wen Yang [2], Hai-Lin Chen [3], and Yan-Tao Duan [3]

[1] PLA Army Engineering University, Xuzhou, Jiangsu, China
xiongrun1983@ sina.com

[2] Army Research Institute of PLA, Kunming, Yunnan, China
76077381@qq.com

[3] PLA Army Engineering University, Nanjing, Jiangsu, China
hylinchen@126.com, yantaoduan@sina.com

Abstract ─ In this paper some suggested protection methods is proposed to improve the shielding effectiveness of computer enclosures. Slots and holes on the computer enclosure are divided into five types, and the coupled electromagnetic interference (EMI) into the enclosure is computed using the finite-difference time-domain (FDTD) method when each type slot exists. From comparison of both time domain electric field waveform and field distribution in the enclosure, vent array, joint laps, CD-ROM and display are found to be the main ways that the EMI penetrated into the enclosure. To improve the protection of the enclosure, waveguide window is used to replace vent array. Additionally, rivet number is increased, depth of the joint laps is increased and conductive gaskets are filled into the joint laps. From numerical analyses, it can be demonstrated that the suggested methods are efficient to improve shielding effectiveness of the computer enclosure. Some suggested methods are also proposed for the CD-ROM and display protection.

Index Terms ─ Electromagnetic interference (EMI), finite-difference time-domain (FDTD), shielding effectiveness (SE).

I. INTRODUCTION

With the development of the electronic technology, electronic equipment requires to work in a quiet electromagnetic environment. Electromagnetic shielding is frequently used to reduce electro-magnetic interference (EMI) of electronic equipment [1-2]. Shielding computer enclosure is an effective way to diminish the EMI [3-4]. However, in most applications, slots, holes, and even a window aperture have to be created on the walls of the computer enclosure for signal wiring, power supply, display, etc. These slots, unfortunately, provide electromagnetic energy coupling paths that allow outside electromagnetic waves to propagate into the enclosure; they thus degrade the shielding effectiveness (SE). Therefore, it is necessary to analyze SE of the shielding enclosures. EMI introduced into the enclosure by lines are as serious as that by coupling, however, only the EMI introduced by coupling are considered here.

The finite-difference time-domain (FDTD) method [5-11], which provides a simple and efficient way of solving Maxwell equations for a variety of problems, has been widely applied in solving many types of electromagnetic coupling problems. It is good at predicting the SE of a particular enclosure for it has numerous time-domain and frequency-domain information.

To simulate the EMI coupled into the computer enclosure, high power microwave (HPM) is used as the source. Total-field/scattered-field (TF/SF) boundary [5] is used to introduce the HPM. Convolution Perfectly Matched Layer (CPML) [12-13] absorbing boundary, which is good at solving late-time reflects, is used to truncate the computational domain. Considering that the EMI mainly penetrates into the enclosure through apertures rather than that through the walls, the perfect electric conducting plane is used to model the shield enclosure.

To find the main ways that EMI coupled into computer enclosure, the slots on computer enclosure are divided into five types and the coupled EMI into the enclosure is studied when each type slot exists. From comparison of both the electric field waveform and the field distribution in the enclosure, vent array, joint laps, CD-ROM and display are found to be the main ways that the EMI coupled into the computer enclosure.

To diminish coupled EMI into the enclosure, light transmitting and electromagnetic wave shielding composite materials can be used to produce the CD-ROM shell and display screen [10-11]. Waveguide

Submitted On: April 18, 2017
Accepted On: October 19, 2018

window is used to take place of vent array. Additionally, rivet number is increased, the depth of the joint lap is increased and conductive gaskets are filled into the joint laps. From numerical analyses, it can be seen that the suggested programs are efficient to improve SE of the computer enclosure. Only methods to reduce the coupled EMI through vent array and joint laps are studied here.

II. THE COMPUTATIOAL MODEL

To be simply, an industrial control computer enclosure is involved here, as shown in Fig. 1, where the slots on both front and back faces are also graphed. The enclosure is made up of bonding the metal sticks together, thus there are joint laps at the top of the four side surfaces.

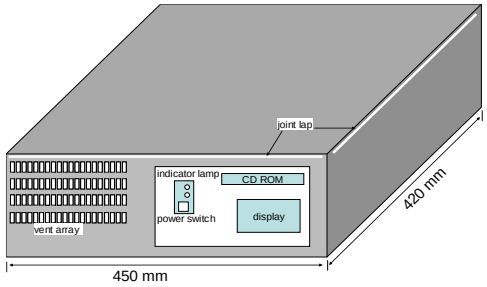

(a) Front face

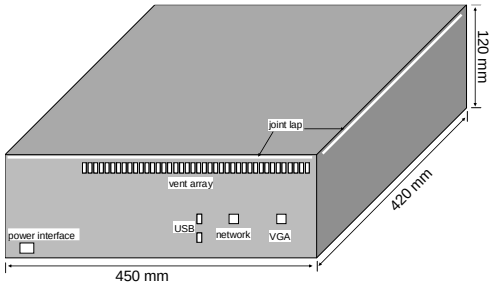

(b) Back face

Fig. 1. Various slots on computer enclosure.

HPM is used as the source here, whose waveform is graphed in Fig. 2. Here it is set,

$$E_0 = \begin{cases} 2.5\times10^5 \quad \text{V/m} & f \le 10\text{GHz} \\ 2.5\times10^6 / f(GHz)\text{V/m} & f > 10\text{GHz} \end{cases}. \quad (1)$$

It is set 50 ns<τ<10 μs, t_1=10 ns, and the repeat frequency is 1 kHz. The peak power of the HPM is:

$$P_{pk} = \begin{cases} 100\ GW & f \le 10GHz \\ 10^4 / f^2 GW & f > 10GHz \end{cases}. \quad (2)$$

The slots on the computer enclosure can be divided into five types, that is CD-ROM and display, vent array on the two faces, joint laps at the top of four enclosure side surfaces, power line and signal interfaces (containing slots for power line interface, USB, network, and VGA), the power switch and indicator light.

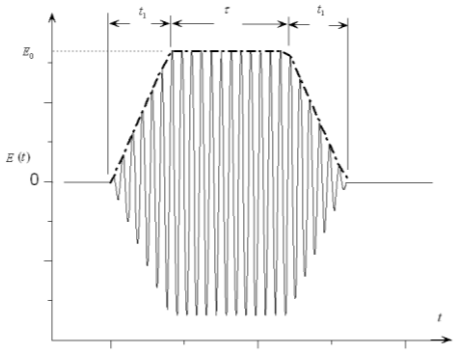

Fig. 2. Waveform of the HPM.

The SE used throughout the paper is given by:

$$SE = -20\log\left(\frac{\left|\bar{E}^{shield}\right|}{\left|\bar{E}^{inc}\right|}\right), \quad (3)$$

where, $\bar{E}^{shield}$ refers to the electric-field value when computer enclosure is placed, whereas $\bar{E}^{inc}$ refers to the electric-field value at the same location in the absence of the enclosure.

To evaluate the SE of the enclosure, all the three directional electromagnetic fields at the center of the enclosure is monitored first, and the waveform of the largest field direction is graphed. Additionally, the peak field value of the waveform is recorded and used to derive the total electric field component:

$$E_p(t) = 20\log\left[\sqrt{E_x(t)^2 + E_y(t)^2 + E_z(t)^2}\right] \text{ dBV/m} \quad (4)$$

To improve the protection of the enclosure, the coupled EMI into the enclosure is simulated when only one type of slot exists to find the main ways that the interface coupled into the computer enclosure. Then some suggested methods are proposed to limit the coupled EMI, and numerical simulation is occupied to verify the efficiency of these methods.

Cubic FDTD cells are used in this paper, and the cell size is Δ=0.5 mm in three directions. To satisfy the stability condition of the FDTD algorithm, the maximum time step is chose to be $\Delta t=\Delta/2c$, where c is the speed of light in the free space. The computational domain is truncated by 10-layers CPML absorbing boundary.

III. ANALYSES OF THE COUPLING WAYS

To find the main ways that EMI coupled in, the computational enclosure is illuminated by HPM when only one type of slot exists. The coupled electric field component into the enclosure in the three directions is monitored respectively, and time-domain waveform of the largest one is drew. Additionally, distribution of the largest total electric field component is also graphed. From analysis of the electric field component coupled into the enclosure when the five types of slots exist

lonely, and the main way that EMI coupled into the enclosure is identified.

A. Slots for CD-ROM and display

In this part the coupled EMI is studied when only the CD-ROM and display slots exist. The CD-ROM slot is 15 cm in length and 4 cm in width, and the slot dimension of the display is 17 cm×10 cm. The slot dimension of the CD-ROM and display is larger than the EMI wavelength, and these slots are modeled by standard FDTD grids. Both the CD-ROM and display slots are located on the front face of the enclosure. After FDTD simulation, both the electromagnetic field and the field distribution are monitored.

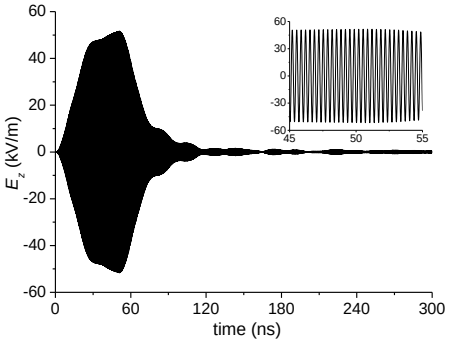

(a) Time-domain waveform

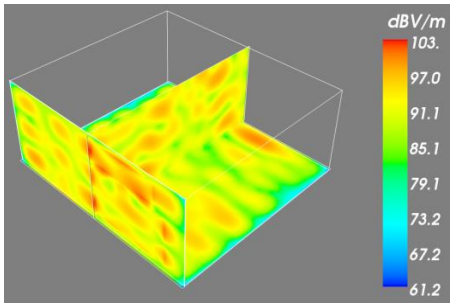

(b) Field distribution

Fig. 3. EMI coupled through CD-ROM and display.

The amplitude of the electric field component field E_x is 25.5 kV/m, and field component amplitude is 13.2 kV/m for E_y and 51.4 kV/m for E_z respectively. In Fig. 3 (a) is graphed the waveform of the electric field component E_z, and the waveform at the right up corner is the 10 ns waveform near the maximum amplitude. It can be seen that the electric field coupled into the enclosure is very large and decreased rapidly.

In Fig. 3 (b) is graphed the total electric field distribution in the enclosure. It can be seen that the electric field is larger than 61.2 dBV/m throughout the enclosure, and even reaches 103 dBV/m at some places, and the electric field is larger than 85 dBV/m at most places in the enclosure. Thus, it can be concluded that the enclosure can rarely shield HPM when CD-ROM and display exist on the enclosure.

B. Slots of vent array on the two faces

In this part the coupled EMI is studied when only the slots for vent array on the two faces exist. The vent array is composed of 4 lines of slots, and each line is composed of 20 thin-slots. The size of each slot is the same, with the dimension of 1.5 cm in height and 0.3 cm in width. The distance between left thin-slot and the right one is 0.3 cm, and the distance is 1.0 cm from the up thin-slot line to the down one. The dimension of the vent array is 12 cm×10 cm.

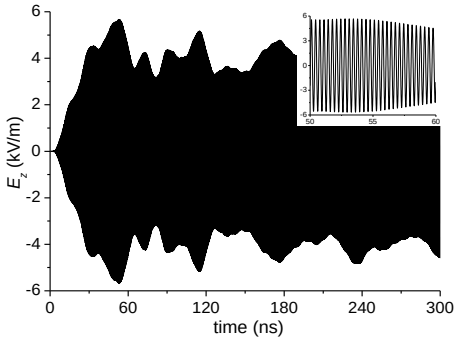

(a) Time-domain waveform

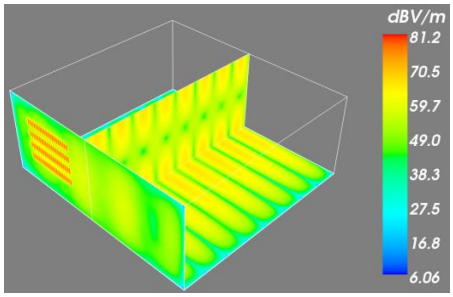

(b) Field distribution

Fig. 4. EMI coupled through vent array.

The dimension of the thin-slots of the vent array on the back face is the same as those on the front face. The vent array on the back face is in one line and consists of 40 thin-slots. The distance between the two thin-slots is 0.3 cm, and the dimension of the vent array is 24 cm× 1 cm. From FDTD simulation, both the time-domain electric field component and the field distribution are monitored, as graphed in Fig. 4.

The amplitude of the electric field component E_x is 1.3 kV/m, and field component amplitude is 2.2 kV/m for E_y and 5.7 kV/m for E_z respectively. In Fig. 4 (a) is graphed the waveform of E_z, and the waveform at the right up corner is the 10 ns waveform near the maximum amplitude. It can be seen that the electric field coupled into the enclosure is also large. It can also be seen that resonance occurs in the enclosure and the amplitude decreases very slowly.

In Fig. 4 (b) is graphed the total electric field distribution in the enclosure, and it is clear that the four lines of slots are conspicuous on the enclosure. It can also be seen that a resonance occurs in the enclosure and the coupled electric field is march lower compared with that when the CD-ROM and display exist. The amplitude of the electric field varies from 6.06 dBV/m to 81.2 dBV/m in the enclosure, and the amplitude is larger than 50 dBV/m at most areas. Thus, it can be concluded that the SE of the enclosure is limited when vent arrays exist on the two faces of the enclosure.

C. Slots of joint laps

In this part the coupled EMI is studied when only the slots for joint laps exist. The joint lap is located on the top of the enclosure, as shown in Fig. 5. The width of the joint laps is 0.5 mm, and the depth is 1.0 cm. The length of the joint laps is the same as the side perimeter of the enclosure. The joint lap on each side is divided into 3 parts by 2 rivets. After FDTD simulation, both the electromagnetic field and the field distribution are monitored, as graphed in Fig. 6.

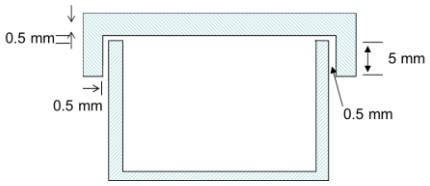

Fig. 5. The joint lap on the enclosure

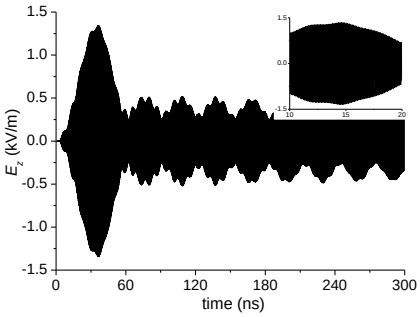

(a) Time-domain waveform

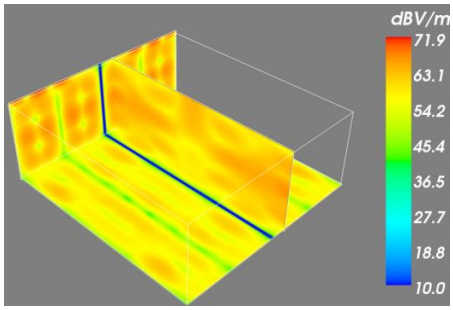

(b) Field distribution

Fig. 6. EMI coupled through joint laps.

The electric field component E_x is very low and even can be neglected, and the field component amplitude is 0.56 kV/m for E_y and 1.3 kV/m for E_x respectively. In Fig. 6 (a) is graphed the time-domain waveform of the electric field component E_z, and the waveform at the right up corner is the 10 ns waveform near the maximum amplitude. In Fig. 6 (b) is graphed the total electric field distribution in the enclosure. It can be seen that the amplitude of the electric field varies from 10.0 dBV/m to 71.9 dBV/m in the enclosure, and the amplitude is about 50 dBV/m at most areas.

D. Slots of power line and signal interfaces

In this part the coupled EMI is studied when only the slots for power Line and signal interfaces exist. The signal interfaces is composed of universal serial bus (USB), network and video graphics array (VGA). There are two slots of USB, one slot of network and VGA, and these slots are all located on the back face of the enclosure. The width of the USB slot is 1.5 cm, and the height is 0.6 cm. The network slot is 1.5 cm in width and 1.0 cm in height. The dimension of the VGA slot is 2.5 cm×2.0 cm.

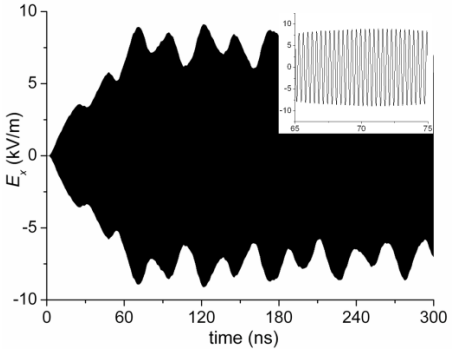

(a) Time-domain waveform

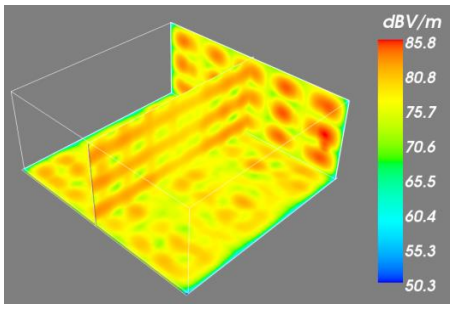

(b) Field distribution

Fig. 7. EMI coupled through slots of power line and signal interfaces.

The amplitude of the electric field component E_x is 9.0 kV/m, and field component amplitude is 1.3 kV/m for E_y and 5.5 kV/m for E_z respectively. In Fig. 7 (a) is graphed the time-domain waveform of the electric field component E_x. It can be seen that the coupled electric

field component E_x is much larger than other slots; resonance occurs in the enclosure and the amplitude decreases very slowly.

In Fig. 7 (b) is graphed the total electric field distribution in the enclosure. It can be seen that the coupled electric field in the enclosure is more uniformly distributed in the enclosure than other types of slots. The amplitude of the electric field varies from 50.3 dBV/m to 85.8 dBV/m in the enclosure, and the amplitude is larger than 80 dBV/m at most areas.

E. Slots for power switch and indicator lamp

In this part the coupled EMI is studied when only the slots for power switch and indicator lamp exist. The slot of the power switch is a square one with the width of 1 cm in each side. There are two indicators, one for power and another for hard disk. The slots of the two indicator lamp are all round holes, whose radius is 2 mm. Both the power switch and the two indictor lamp are located on the front face of the enclosure.

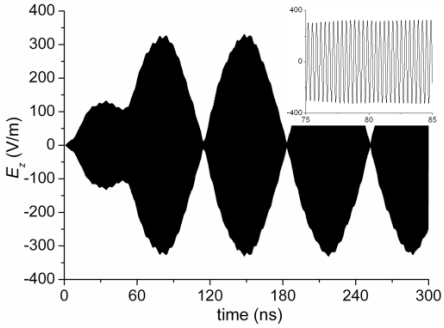

(a) Time-domain waveform

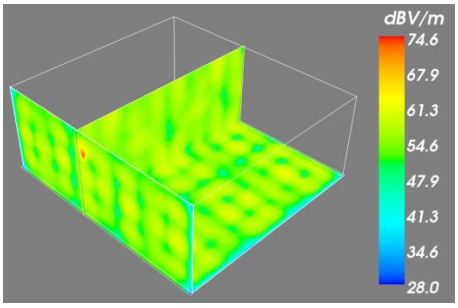

(b) Field distribution

Fig. 8. EMI coupled through slots of power switch and indicator lamp.

The coupled EMI is much lower than that when the other types of slots exist. The amplitude of the electric field component field E_x is 0.36 kV/m, and field component amplitude is 0.13 kV/m for E_y and 0.33 kV/m for E_z respectively. In Fig. 8 (a) is graphed the waveform of the electric field component E_x, and it is clear that resonance occurs. The total electric field distribution in the enclosure is graphed in Fig. 8 (b), and the location of the power switch is obvious. It can be seen from Fig. 8 (b) that the amplitude of the electric field varies from 28.0 dBV/m to 74.6 dBV/m in the enclosure, and the amplitude is larger than 60 dBV/m at most areas. It is worthy of noting that the electric field near the slots is much larger than the other areas, and the effect of this type slots on the SE is limited.

From the coupled EMI analyses when only one type slots exist above, some conclusions can be drawn:

(1) Joint laps, vent array, CD-ROM and the display are the main way that the EMI coupled into the enclosure.

(2) Resonance occurs when the EMI coupled into the enclosure, and the resonant frequency is not only depending on the enclosure size but also the size of the slots.

(3) The SE of the enclosure is limited when these types of slots exist, and the coupled electric field can even reach 103 dBV/m in the enclosure.

IV. PROTECTION METHODS

As demonstrated in the last part, vent array, joint laps, CD-ROM and the display are the main ways that EMI coupled into the enclosure. To diminish EMI coupled into the enclosure, light transmitting and electromagnetic wave shielding composite materials can be used to produce the CD-ROM shell and display screen [14-17]. Additionally, one can package CD-ROM into a metal box, or external drives may be used. Thus protection of CD-ROM and the display will not be discussed here.

In this part, we mainly focus on the programs to limit the EMI penetrated through vent array and joint laps. To limit the coupled EMI through the vent array, waveguide window is used to replace of the vent array. To limit the EMI coupled through the joint lap, rivet number is increased, the depth of the joint lap is increased and conductive gaskets are filled into the joint laps.

A. Protection of the vent array

Waveguide window, as graphed in Fig. 9, is an efficient way of letting air travel through while stopping electromagnetic wave propagating. The electromagnetic wave will vanish significantly when the wave frequency is lower than the stop frequency of the waveguide. To reduce the EMI under the frequency 40 GHz, a waveguide with sectional size 3 mm×3 mm and 15 mm in length is tested. The sectional area of the waveguide is the same as the area of the vent array on the two faces respectively.

Simulation is carried out again as the vent array is replaced by the waveguide window, and both the electric field waveform at the center and the field distribution in the enclosure are monitored.

Amplitude of the electric field component E_x is 7.8 V/m, and field component amplitude is 9.1 V/m for E_y and 23.0 V/m for E_z respectively. In Fig. 10 (a) is graphed the waveform of the electric field component E_z.

It is clear that the coupled EMI into the enclosure is greatly reduced when the vent array are replaced by the waveguide window.

The total electric field distribution in the enclosure is graphed in Fig. 10 (b), and location of the waveguide window is obvious. Compared with Fig. 4 (b), it is clear that the coupled EMI is greatly reduced. The amplitude of the electric field varies from 10.0 dBV/m to 66.3 dBV/m in the enclosure, and the amplitude is lower than 30 dBV/m at most areas. That means about a 20 dB decrease of SE is achieved. Thus it can be concluded that waveguide window is an efficient way to improve SE of the enclosure.

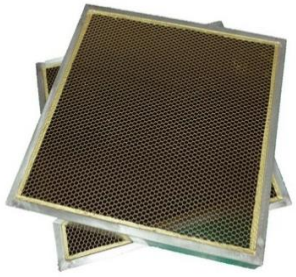

Fig. 9. Rectangular waveguide.

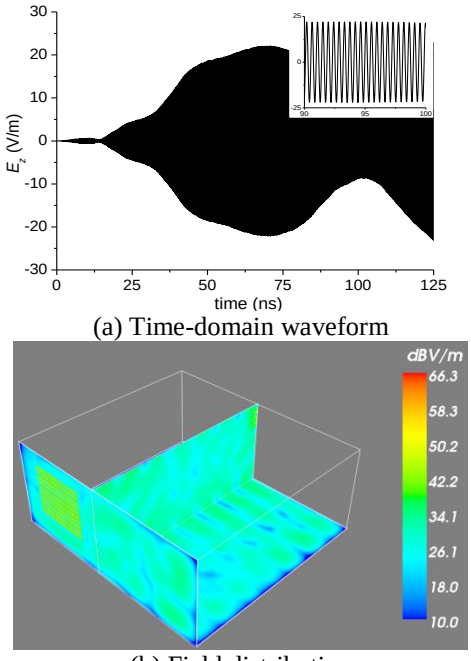

(a) Time-domain waveform

(b) Field distribution

Fig. 10. EMI coupled through waveguide window.

B. Protection of the joint laps

To protect the enclosure against EMI penetrated through joint laps, three methods are suggested. Firstly, the rivet number on one side of the enclosure is increased from 2 to 6, and then further to 13, as shown in Fig. 11. Secondly, the depth of the joint laps is increased from 5 mm to 10 mm when the rivet number is 6. Thirdly, conductive gaskets are filled into the joint laps, and the width is reduced from 5 mm to 3 mm when the rivet number is 6 and the lap depth is 10 mm, as shown in Fig. 11.

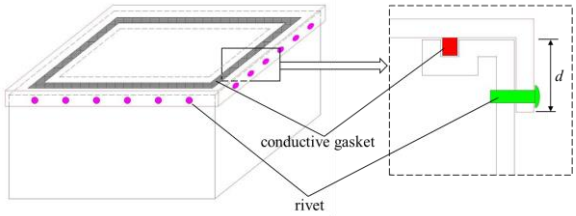

Fig. 11. Protection of joint laps.

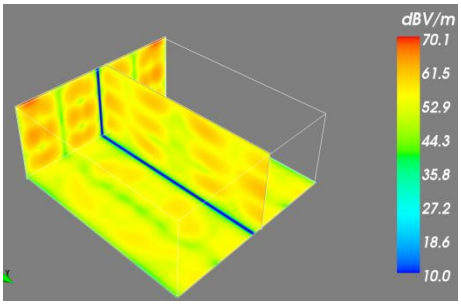

(a) 6 rivets

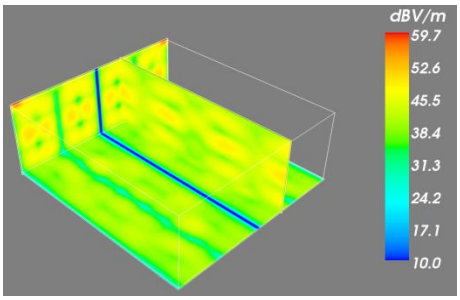

(b) 13 rivets

Fig. 12. Field distribution versus rivet number.

Firstly, the rivet number is increased from 2 to 6, which means the joint laps on each side is divided into 7 short joint laps. The width and depth of the joint laps are the same as that in the last part. It is worthy of noting that the rivets are equidistantly located, and the total length of the 7 short joint laps is the same as the long joint laps of the last section. In Fig. 12 (a) is graphed the field distribution in the enclosure when 6 rivet is used, and it can be seen that there is a 5-10 dB SE improvement compared with that in Fig. 6 (b). Additionally, the rivet number is further increased to 13, and the field distribution is presented in Fig. 12 (b). It is clear another 10 dB SE improvement is achieved when 13 rivets are used.

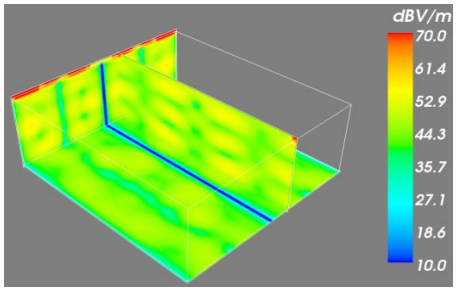

Fig. 13. Field distribution as the joint lap enlarged.

Secondly, the joint laps depth *d* is increased from 5 mm to 10 mm when 6 rivets are used, and the joint lap width is the same. The field distribution is presented in Fig. 13, and it can be seen that SE of the enclosure is improved 5-10 dB compared with that shown in Fig. 12 (a).

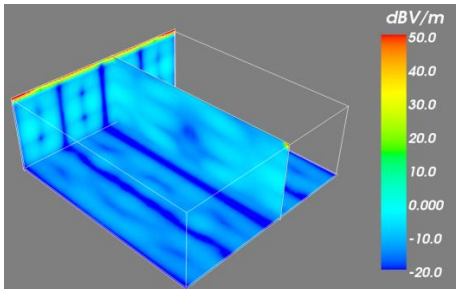

Fig. 14. Field distribution when joint laps is filled by conductive gaskets.

Thirdly, the joint laps are filled with conductive gaskets. Here the joint lap width is supposed to be reduced from 0.5 mm to 0.3 mm when conductive gaskets are filled, and the depth is 10 mm while 6 rivets are used. The field distribution is graphed in Fig. 14. It is clear that SE is greatly improved, and the coupled electric field is under 10 dBV/m at most areas except the areas adjacent to the joint laps.

From the analyses above, it can be concluded that increasing the rivet number, enlarging the joint laps depth, and filling conductive gaskets are all efficient ways to improve the SE of the enclosure.

V. CONCLUSIONS

In this paper, some suggested methods are studied to improve SE of the computer enclosure. Firstly, the slots on the enclosure are divided into five types and the coupled EMI into the enclosure is simulated when only one type slots exists. From comparison of both the electric field waveform and the field distribution in the enclosure, vent array, joint laps, CD-ROM and display are found to be the main ways that EMI coupled into the enclosure. Secondly, some suggested methods are presented to reduce the coupled EMI. Waveguide window can be used to replace of the vent array. To reduce the coupled EMI through the joint laps, rivet number and the depth of the joint laps can be increased, and conductive gaskets can be filled into the joint laps. From numerical analyses, it can be demonstrated that the proposed methods are efficient ways to improve the SE of the computer enclosure.

ACKNOWLEDGMENT

This work was supported in part by the School Foundation under Grant No. FD201506.

REFERENCES

[1] T. Cvetković, V. Milutinović, N. Dončov, and B. Milovanović, "Numerical investigation of monitoring antenna influence on shielding effectiveness characterization," *ACES Journal*, vol. 29, no. 11, pp. 837-846, 2014.

[2] M. R. Barzegaran and O. A. Mohammed, "Computational electromagnetics for the evaluation of EMC issues in multi-component energy systems," *ACES Journal*, vol. 29, no. 12, pp. 1077-1092, 2014.

[3] W. A. Radasky, C. E. Baum, and M. W. Wik, "Introduction to the special issue on high-power electromagnetics (HPEM) and intentional electromagnetic interference (IEMI)," *IEEE Trans Electromagnetic Comp*atibility, vol. 46, pp. 314-321, 2004.

[4] W. Abdelli, X. Mininger, L. Pichon, and H. Trabelsi, "Impact of composite materials on the shielding effectiveness of enclosures," *ACES Journal*, vol. 27, no. 4, pp. 369-374, 2012.

[5] A. Taflove and S. C. Hagness, *Computational Electrodynamics: The Finite-Difference Time-Domain Method*. 3rd ed., Artech House, 2005.

[6] A.Capozzoli, O. Kilic, C. Curcio, and A. Liseno, "The success of GPU computing in applied electromagnetics," *ACES Journal*, vol. 1, no. 4, pp. 113-116, 2016.

[7] M. F. Hadi, "Wide-angle absorbing boundary conditions for low and high-order FDTD algorithms," *ACES Journal*, vol. 24, no. 1, pp. 9-15, 2009.

[8] G. Liu, "Time-domain electromagnetic inversion technique for biological tissues by reconstructing distributions of Cole-Cole model parameters," *ACES Journal*, vol. 32, no. 1, pp. 8-14, 2017.

[9] A. V. Brovko, E. K. Murphy, and V. V. Yakovlev, "Waveguide microwave imaging: Solids volume fraction of particulate materials," *ACES Journal*, vol. 30, no. 11, pp. 1161-1167, 2015.

[10] R. Xiong, B. Chen, N.-H. Zhou, et al., "A new computational model for the FDTD analysis of

sub-structures on infinite plates," *ACES Journal*, vol. 28, no. 1, pp. 41-48, 2013.
[11] D. W. Sun and J. H. Yu, "Extending the 2-D contour path method to the 3-D," *ACES Journal*, vol. 10, pp. 655-657, 2011.
[12] J. P., Berenger, "A perfect matched layer for the absorption of electromagnetic waves," *Journal of Computational Physics*, vol. 114, pp. 110-117, 1996.
[13] J. A. Roden and S. D. Gedney, "Convolution PML (CPML): An efficient FDTD implementation of the CFS-PML for arbitrary media," *Microwave and Optical Technology Letters*, vol. 27, no. 5, pp. 334-339, Dec. 2000.
[14] K. Matumura, Y. Kagawa, and K. Baba, "Light transmitting electromagnetic wave shielding composite materials using electromagnetic wave polarizing effect," *Journal of Applied Physics*, vol. 101, no. 1, pp. 4270-4339, Dec. 2000.
[15] H. Shao, J. Guan, and Y. Wang, "Development of electromagnetic shielding composite materials," *Safety & EMC*, vol. 27, no. 1, pp. 334-339, 2008.
[16] M. S. Sarto, F. Sarto, M. C. Larciprete, et al., "Nanotechnology of transparent metals for radio frequency electromagnetic shielding," *IEEE Transactions on Electromagnetic Compatibility*, vol. 45, no. 4, pp. 586-594, 2003.
[17] W. M. Kim, D. Y. Ku, I.-K. Lee, et al., "The electromagnetic interference shielding effect of indium-zinc oxide/silver alloy multilayered thin films," *Thin Solid Films*, vol. 473, pp. 315-320, 2005.

Run Xiong was born in Sichuan Province, China, in 1983. He received the B.S., M.S. and Ph.D. degrees in Electric Systems and Automation from PLA University of Science and Technology, Nanjing, China, in 2005, 2010 and 2014 respectively. He is now with the National Key Laboratory on Electromagnetic Environment and Electro-optical Engineering, and his research interests include computational electromagnetics and EMC.

Wen Yang was born in Tongren, Guizhou, China, in 1982. He received B.S. degree in Electric Systems and its Automation from Nanjing Engineering Institute, China, in 2005. Currently, he is a Pioneer Engineer with the Army Research Institute of PLA, Kunming, Yunnan. His current research interest is computational electromagnetics and the electric system design.

Yan-Tao Duan was born in Hebei, China, in 1980. He received the B.S., M.S., and Ph.D. degrees in Electric Systems and Automation from the Nanjing Engineering Institute, Nanjing, China, in 2002, 2006, and 2010, respectively. He is currently a Lecturer with the National Key Laboratory on Electromagnetic Environmental Effects and Electro-optical Engineering, Army Engineering University of PLA, Nanjing, China. His research interests include computational electromagnetics, lightning, and EMP.

Effect of Aspect Ratio and Frequency of an Open-Ended, Coaxial Line on Admittance for Determination of Moisture in Tenera Oil Palm Fruit Using Finite Difference Method

E. M. Cheng [1,2], Z. Abbas [3], Mohamedfareq Abdulmalek [4], K. Y. You [5], K. Y. Lee [6], N. F. Mohd Nasir [1], M. S. Abdul Majid [1], and S. F. Khor [7]

[1] School of Mechatronic Engineering, University Malaysia Perlis (UniMAP)
Pauh Putra Campus, 02600 Arau, Perlis, Malaysia
emcheng@unimap.edu.my, nashrul@unimap.edu.my, shukry@unimap.edu.my

[2] Bioelectromagnetic Research Group (BioEM), University Malaysia Perlis (UniMAP)
Pauh Putra Campus, 02600 Arau, Perlis, Malaysia
emcheng@unimap.edu.my

[3] Physics Department, Faculty of Science, University Putra Malaysia, 43400 Serdang, Selangor, Malaysia
za@upm.edu.my

[4] Faculty of Engineering and Information Sciences, University of Wollongong in Dubai
Dubai Knowledge Village, Dubai, United Arab Emirates
mohamedfareqmalek@uowdubai.ac.ae

[5] School of Electrical Engineering, Faculty of Engineering, Universiti Teknologi Malaysia
Skudai, Johor 81310, Malaysia
kyyou@fke.utm.my

[6] Lee Kong Chian Faculty of Engineering & Science, Tunku Abdul Rahman University
Sungai Long Campus, Jalan Sungai Long, Sungai Long City, Cheras, 43000 Kajang, Selangor, Malaysia
kylee@utar.edu.my

[7] School of Electrical Systems Engineering, Univerisiti Malaysia Perlis (UniMAP)
Pauh Putra Campus, Arau, Perlis 02600, Malaysia
sfkhor@unimap.edu.my

Abstract ─ This paper intends to study the effect of variations of aspect ratio (the ratio of outer radius to inner radius of conductor) and frequency to the normalized admittance (normalized conductance and susceptance) of oil palm fruit with various moisture content (*MC*) on performance of RG405/U semi-rigid cable (open-ended coaxial line). Both finite difference method (FDM) and quasi-static model (admittance model) were used to compare response of normalised conductance and susceptance due to 30%, 40%, 60%, 70% and 80% of moisture content that explain all ripeness stage of oil palm fruit. Finite difference method is used to simulate complex admittance due to different *MC* in oil palm fruit in various ripeness. The FDM results were then compared with the quasi-static model through error analysis. The aspect ratio of 3.298 has smaller error of normalized conductance when frequency range <3 GHz.

Index Terms ─ Conductance, finite difference method, moisture content, normalized admittance, oil palm fruit, open-ended coaxial sensor, susceptance.

I. INTRODUCTION

Mathematical and computational modelling have been applied in electrical and electronic research since long before to study and simulate phenomena at a wide range of applications, from the basic circuit [1] to materials [2]. Many publications about computational electromagnetic modelling in various biological systems were observed [3]. The computational electrical and electromagnetic modelling are crucial in study on

Submitted On: October 6, 2017
Accepted On: October 19, 2018

heterogeneous model for biological matter due to its complication. Experimental methods are time consuming and incur high cost expenditure. Hence, computer simulation methods play an essential role in understanding electrical behavior in the biological system, including agricultural products. Maxwell's equations in differential form are the basis in computational electromagnetic modelling. Implementation of numerical modelling in agricultural issues is often to be conducted for engineering solution. Vagenas and Marinos-Kouris [4] implemented a finite element analysis on agricultural products to analyze diffusion of moisture during the drying process, e.g., Mung bean [5]. High voltage pulsed electric field was simulated for food preservation technology using the finite element method [6].

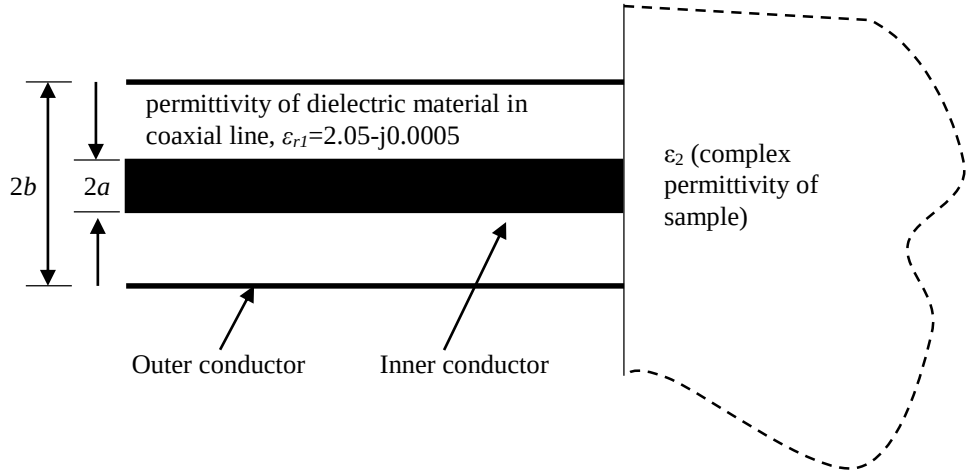

Fig. 1. An open-ended coaxial reflection sensor.

Many methods were proposed and developed to measure the quality and quality-related characteristics. They are primarily employ a non-invasive methods and sensing system to determine the quality of agricultural products. Electrical properties of agricultural products become a significant concerns among the public. Electrical properties are a mean for determining moisture, the maturity of agro products, etc. [7]. In addition, electrical property describes the feasibility of microwave heating to a material subject to microwave irradiation. It is crucial in the processing of food materials because the optimum electrical parameters need to be applied. The electrical study on a material could help to analyse electrical behaviour of materials due to exposure of electric field. The studies on electrical properties of agricultural products have led to the development of various electrical based instruments.

Oil palm industry is a primary economic activity in Malaysia. Malaysia is the second largest producer of palm oil in the world. In 2011, the palm oil sector contributes USD 16.8 billion to Malaysia's Gross National Income. As a result, many efforts were done to optimise harvest of oil palm fruit to achieve a high income generation. Over the last decade, many studies were conducted on oil palm fruit using electromagnetic methods. *MC* in oil palm fruit were investigated using low cost open-ended coaxial line [8-11]. This is due to the inverse relationship between water and oil content in oil palm fruit [12]. This relationship is used to study *MC* in oil palm fruit to determine ripeness of fruit [13] for maximum yield of palm oil. This work describes the electromagnetic behavior in oil palm fruit. It is highly important to simulate and model its behavior or response numerically for instrument development.

Many studies were conducted using a numerical method which; for example by using partial differential equations in determining the specification, dimension and requirements for optimum design of instrumentation and sensing system in oil palm harvesting. You *et al.* and Cheng *et al.* [14-16] implement numerical methods (finite element method and finite difference method) and quasi-static model on open-ended coaxial line to explore the interaction of microwave with oil palm fruit. Results that obtained can be used to determine the optimum harvesting time. However, the references [14-16] only studied a fixed aspect ratio, and meaningful comparison is hardly carried out. It is the motivation of this study to investigate an open ended coaxial line with different aspect ratio. The electromagnetic response of fruit on the coaxial line is crucial to analyse the performance of the sensing system in moisture inspection. To the best of our knowledge, there are no previous studies to model the aspect ratio of an open ended coaxial for determination of moisture in Tenera oil palm fruit. Currently, studies only use the commercially available open ended coaxial probe with fixed aspect ratio. Experimental work to study the effects of various aspect ratios are not available, as the design is limited to characteristic impedance at 50 Ω,

75 Ω and 93 Ω. The optimization is hardly carried out for determination of moisture in Tenera oil palm fruits. As a result, quasi-static model was compared with FDM method. Various aspect ratios have been studied to investigate the response of result with moisture in fruit. On the other hand, limited studies were conducted to model and study the effect of aspect ratio of an open ended coaxial for determination of moisture in Tenera oil palm fruit. Limited model can be found for comparison. Hence, comparison between FDM and AM helps to verify reliability of FDM in designing an open-coaxial sensor for optimised specification, since AM is well-known and it has been used extensively in investigation of open-ended coaxial probe. By investigating the optimised aspect ratio and frequency range through numerical study, an experimental work can be conducted to verify the finding. Next, the streamlined design can be implemented better in the oil palm industry.

An accurate and efficient method could facilitate the design of sensing system in agricultural product. It saves time and does not cause wastage of resources. As a result, it is paramount importance to compare FDM and AM on the effect of aspects ratios for the sake of determination of suitable aspect ratio for potential sensor development.

II. MATERIALS AND METHOD

A. Normalized admittance ($\tilde{Y}$)

An open-ended coaxial probe with radius *a* and *b* of inner and outer conductors, respectively is shown in Fig. 1. Figure 2 shows open-ended coaxial line in typical lumped-circuit model. However, the model varies according to the specification of coaxial line and frequency. $G(\varepsilon_{r2})$ represent conductance in circuit model where ε_{r2} is permittivity of sample, C_f is the fringing capacitance on the aperture of coaxial line, and $C(\varepsilon_{r2})$ is the capacitance of the sample with ε_{r2}. Both *C* and *G* are function of ε_{r1}. C_f, $C(\varepsilon_{r2})$ and $G(\varepsilon_{r2})$ vary based on the dimensions of the coaxial line, i.e., radius *a* and *b* as well as permittivity of the dielectric filling the line. C_0 in free space can be obtained as [17]:

$$C_0 = 2.38\varepsilon_0 (b - a). \quad (1)$$

The C_f and G_0 can be neglected at first approximation [18]. C_f can be obtained numerically [19] or measured merely both of capacitances [20]. On the other hand, it can be also determined approximately through quasi-static analysis [21-22]. The total capacitance, C_T ($=B_0/\omega$) and radiation conductance, G_0 in the air can also be defined in literature [23].

When the sensor is contacted with the sample, the permittivity of the sample, ε_{r2} changes the end capacitance and it gives the input admittance, Y_{in} as:

$$Y_{in} = G + jB, \quad (2)$$

where *G* and *B* are the real and imaginary parts of Y_{in}, namely conductance and susceptance, respectively.

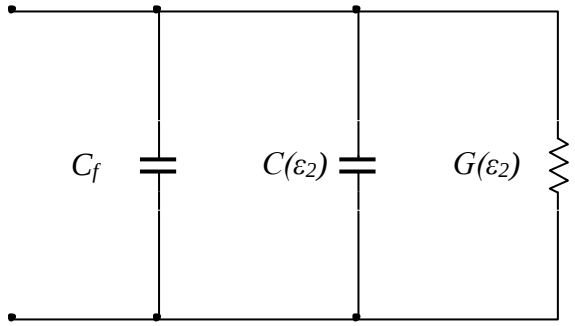

Fig. 2. Equivalent circuit for the open-ended coaxial sensor.

Admittance, Y_{in} is reciprocal of impedance, Z_{in} which can be determined through reciprocal of Z_{in}. In fact, Y_{in} is a measure of ability of a material to permit flow of electric current. On the other hand, *G* and *B* are defined as reciprocal of resistance, *R* and reactance, *X*, respectively. *G* (in Siemens) is ability to conduct frequency-independent electric current in a specific material. Meanwhile, *B* (in Siemens) is determined through reciprocal of *X*. Likewise, *B* play a similar role like *G* but it is subjected to frequency-dependent electric current. *R* is opposition of frequency-independent current due to chemical composition in a material.

In general, the input impedance can be expressed as:

$$Z_{in} = R + jX. \quad (3)$$

The input impedance model for lumped-circuit as shown in Fig. 2 can be expressed as:

$$Z_{in} = \frac{1}{j\omega C_f + j\omega C(\varepsilon_2) + G(\varepsilon_2)}. \quad (4)$$

In this work, input admittance of open-ended coaxial line, Y_{in} was studied due to the variation of *MC* and aspect ratio of the coaxial line using FDM. Results of FDM were compared with the admittance model for verification.

B. FDM for admittance

i) Calculation of admittance

Heavy calculation of simultaneous equations in the matrix is needed to implement FDM in admittance calculation. In this work, an iterative method was used to conduct calculation for electric potentials in scalar wave equation at every node to form a matrix [15-16]. The potential at a particular node is calculated based on potential values at adjacent nodes using Equation (5):

$$V_{m,n} = \frac{1}{4}\left(V_{m+1,n} + V_{m-1,n} + V_{m,n+1} + V_{m,n-1}\right), \quad (5)$$

where *m* and *n* are the row and column number,

respectively. Perfect electric conductor (PEC) and Perfect Matched Layer (PML) were used to define and restrict computational regions, respectively. The reflection occurs on the boundary between Polytetrafluoroethylene (PTFE) in the coaxial line and the sample. The electric flux density can be expressed in Equation (6) at the dielectric boundary:

$$D_{1n} = D_{2n}, \tag{6}$$

where D_{1n} and D_{2n} are the normal components of the electric flux density in region PTFE in coaxial line and the sample under test (oil palm fruit), respectively. According to Gauss' Law,

$$\oint D \cdot dl = \oint \varepsilon E \cdot dl = Q_{enc} = 0\,, \tag{7}$$

due to absence of free charge on the dielectric boundary. $E = -\nabla V$ is substituted in Equation (6) to be Equation (7):

$$0 = \oint \varepsilon \nabla V \cdot dl = \oint \varepsilon \frac{\partial V}{\partial n} \cdot dl\,, \tag{8}$$

where $\frac{\partial \mathrm{V}}{\partial \mathrm{n}}$ is the derivative of V normal to the contour l. Equation (7) on the boundary as shown in Fig. 1 can be expressed as:

$$V_0 = \frac{\varepsilon_1}{2(\varepsilon_1 + \varepsilon_2)} V_1 + \frac{\varepsilon_2}{2(\varepsilon_1 + \varepsilon_2)} V_3 + \frac{1}{4} V_2 + \frac{1}{4} V_4\,. \tag{9}$$

The potentials on boundary, V_{ring} were obtained through Equation (8) using finite difference method. The total potential, V_{area}, and the total charge, Q_{area}, on the aperture of the probe can be determined using Equations (10) and Equation (11), respectively [24]:

$$\mathrm{V_{area}} = \int_{\mathrm{a}}^{\mathrm{b}} \mathrm{V_{ring}}\, \mathrm{d}\rho\,, \tag{10}$$

$$\mathrm{Q_{area}} = \varepsilon \int_{\mathrm{a}}^{\mathrm{b}} \int_{0}^{2\pi} \frac{\mathrm{V_{ring}}}{\rho}\, \rho \mathrm{d}\phi\, \mathrm{d}\rho\,, \tag{11}$$

where ρ is the radius at aperture of the coaxial probe, and ϕ is the azimuthal angle on aperture. The normalized and characteristic admittance are given in Equations (12) and (13):

$$\frac{Y}{Y_0} = \tilde{Y} = \frac{j\omega C_T}{Y_0}\,, \tag{12}$$

$$Y_0 = \frac{2\pi}{\sqrt{\frac{\mu_0}{\varepsilon_1}} \cdot ln\left(\frac{b}{a}\right)}\,, \tag{13}$$

where μ_0 is the free space of permeability, since PTFE is a non-magnetic material.

ii) Truncation of infinite computation region

In FDM computation, the extent of the sample to be simulated is only part of the actual sample because the fringing field of the open-ended coaxial sensor could only be reached around 2mm depths. The actual dimension of the sample (oil palm fruit) is much greater than 1 cm. Therefore, the PML condition must be applied to reduce the mesh size. A PML is an artificial absorbing layer for a computational electromagnetic solution. It commonly used to restrict computational regions in numerical method to simulate problems with open boundaries. For practical reasons, the infinite space is usually truncated due to the limitation of computing machine used. PML is helpful to avoid the undesired reflection in computation [25]. Thus, the computation solution is achievable. To produce a reflectionless boundary, computation/truncated region (region 1/ region 2) interface for the normally impinging wave should theoretically abide by:

$$\Gamma = \frac{\eta_1 - \eta_2}{\eta_1 + \eta_2} = 0, \tag{14}$$

and

$$\eta = \sqrt{\frac{\mu(1 + \sigma / j\omega\mu)}{\varepsilon(1 + \sigma / j\omega\varepsilon)}}\,. \tag{15}$$

It can be achieved by equating $\varepsilon_1 = \varepsilon_2$ and $\mu_1 = \mu_2$ where ε_1, ε_2, μ_1, μ_2, k_1, k_2, η_1 and η_2 are the permittivity of region 1, permittivity of region 2, permeability of region 1, permeability of region 2, wave number of field at region 2, intrinsic impedance of media in region 1 and intrinsic impedance of media in region 2, respectively. The voltage at truncated nodes, V_2 was solved using:

$$V_2 = V_1 e^{-jk_2 x - \sigma \eta_2 x}\,, \tag{16}$$

where V_1 is the voltage of the node at boundary of computation region.

iii) Numerical modeling error

The modeling errors are due to several assumptions made in arriving at the mathematical model. To simplify the computation work, a nonlinear system may be represented by a multiple linear PDE unit. For instance, the truncation error and round-off error are common numerical error.

The truncation error was advent due to the elimination of terms in infinite series. High-order terms in the Taylor series expansion were neglected in derivation finite difference schemes and causes truncation error. Finer meshes can reduce the truncation errors by reducing the mesh size [26]. Besides, truncation errors can be reduced using a large number of terms as well in the series expansion of derivatives. In other words, higher-order approximations should be implemented in computation.

Round-off errors restrict precision when used for computation. The size limitation of registers in the arithmetic unit of the computer causes round-off errors. Using double-precision arithmetic can help to minimise round-off errors. If all operations implemented using integer arithmetic, the round-off errors can be avoided.

C. AM (Quasi-static model)

The work by [27] described the homogeneous case, in which an air-filled coaxial line is radiated into the free space. At the same time, the aperture admittance has been formulated as Equation (17):

$$\tilde{Y} = \frac{jk_2}{k_1 \ln(b/a)} \times \int_0^{\infty} \frac{d\zeta}{\zeta(\zeta^2 - k_2^2)^{1/2}} \left| J_0(\zeta a) - J_0(\zeta b) \right|^2 \quad , \quad (17)$$

where k_1 and k_2 are wave number at internal media and external media, respectively. ζ is a parametric equation which was defined in [27].

The open-ended coaxial probe began to be applied as a sensor in biological sensing during the early 1980s. The literatures [28]-[31] formulated the electrical property such as aperture admittance or impedance in capacitance terms. The open-ended coaxial sensor can be implemented up to 1 GHz using [31]:

$$\tilde{Y} = \frac{j\omega(\varepsilon_r C_0 + C_f) + G(\varepsilon_r)^{2.5}}{Y_0} . \quad (18)$$

Since excitation of the coaxial probe is a TEM mode, neither the electric field nor magnetic field oscillates along the direction of propagation. Equation (17) express dominate wave (TEM) at the coaxial aperture probe. In other words, AM depict reflection occur at aperture of the probe.

It was extended to oil palm fruit moisture sensing recently [11]. The assumption which the sample under test can be represented more accurate with the presence of conductive element was made by Brady and Stuchly [32-33]. The capacitance formulation became inapplicable at higher operating frequency because the actual theoretical value is not satisfied with capacitance formulation at a higher frequency, especially for lossy materials with one single value of capacitance, C_T [34]. Misra [22] simplified the model in approximated series expansion. The aperture admittance which is presented in rational function model as expressed in Equation (19) was used to determine the complex permittivity of materials, ε_r.

$$\tilde{Y} = \frac{\sum_{n=1}^{4} \sum_{p=1}^{8} \alpha_{np} (\sqrt{\varepsilon_r})^p (j\omega a)^n}{1 + \sum_{m=1}^{4} \sum_{q=0}^{8} \beta_{mq} (\sqrt{\varepsilon_r})^q (j\omega a)^m} , \quad (19)$$

where α_{np} and β_{mq} are the coefficients of the Equation (19). These two coefficients are determined by the size and the type of coaxial sensor. This model was developed in the early 1990s [35-37].

The normalized admittance, $\tilde{Y}$ has real and imaginary parts, namely normalized conductance, G/Y_0 and susceptance B/Y_0, in which can be written as [38-39]:

$$\tilde{Y} = \frac{G}{Y_0} + j\frac{B}{Y_0} , \quad (20)$$

where

$$\frac{G(0)}{Y_0} = \frac{\sqrt{\varepsilon_r}}{\ln\left(b/a\right)\sqrt{\varepsilon_c}} \int_0^{2\pi} \frac{1}{\sin\theta} \times \left[J_o\left(k_o\sqrt{\varepsilon} b \sin\theta\right) - J_o\left(k_o\sqrt{\varepsilon} a \sin\theta\right) \right]^2 d\theta \quad , \quad (21)$$

$$\frac{B(0)}{Y_0} = \frac{\sqrt{\varepsilon_r}}{\pi \ln\left(b/a\right)\sqrt{\varepsilon_c}} \times \int_0^{\pi} \begin{bmatrix} 2\,Si\left(k_o\sqrt{\varepsilon\left(a^2 + b^2 - 2ab\cos\theta\right)}\right) \\ -Si\left(2k_o\sqrt{\varepsilon_r}\, a \sin\left(\frac{\theta}{2}\right)\right) \\ -Si\left(2k_o\sqrt{\varepsilon_r}\, b \sin\left(\frac{\theta}{2}\right)\right) \end{bmatrix} d\theta \quad , \quad (22)$$

where ε_c is the dielectric constant of the material that fills the coaxial line and ε_r is the dielectric constant in the sample, k_o is the free space propagation constant, J_o is the zero-order Bessel function, and *Si* is the sine integral. Equations (21) and (22) can be approximated by the first terms of the Taylor series expansion [39].

III. RESULTS AND DISCUSSION

From Fig. 3 to Fig. 7, it can be observed that the theoretical normalized conductance and susceptance varies with frequency, aspect ratio (*b/a*) and moisture content (*MC*) in oil palm fruit. There are five *MC* values reported in this section, namely 30%, 40%, 60%, 70% and 80% that depict all the ripeness stage of oil palm fruit. 30% and 40% *MC* represent the minimum amount of water content in oil palm fruit or maximum accumulation of oil content (ripe stage). The 60% *MC* is located in the transition region where the *MC* decreases drastically. Meanwhile, 70% and 80% *MC* indicates the maximum amount of *MC* in oil palm fruit or minimum accumulation of oil content (immature stage). On the other hand, the aspect ratio, *b/a* which were studied in this work are 1.57, 2, 3.298, 4 and 5, respectively.

The normalized conductance, G/Y_0 increases with frequency. This can be explained by the conductance, $G = \frac{\sigma}{\varepsilon} \cdot C$ where $\frac{\sigma}{\varepsilon}$ increases with frequency [15]. Hence, *G* and G/Y_0 increases with frequency as shown in Fig. 3 to Fig. 7. However, the G/Y_0 increases with *MC* as well for all *b/a*. It is because dielectric constant and loss factor of oil palm fruit increases with *MC* [15]. In all aspect ratios, G/Y_0 at high *MC* is higher than low *MC*. It

might be due to the increment of conductivity as *MC* increase. The presence of high *MC* faciltate the activities of ionic substance in fruit, e.g., fatty acids, since water is good ionic solvent. The formation of ionic subtstance in fruit due to water heighthened conductivity of fruit. On the other hand, it can be observed that the discrepancy of G/Y_0 between FDM and AM increase progressively when frequency increases. It might be due to the assumption made by AM where the sample has infinite extent. This assumption is inapplicable in this work as the coverage of electric field from the aperture of the coaxial line is limited within 2 mm of thickness [40]. Nevertheless, PML was applied to define the extent of coverage of field in fruit using FDM. Same percentage of *MC* at infinite and finite extent exhibit different effect to wave propagation. At high frequencies, the applied field has poorer ability to penetrate into fruit. Moreover, high frequencies of applied field in infinite extent of fruit is invalid as the coverage of fringing field from the coaxial line is merely 2 mm. It does not consistent with assumption made by AM where the propagation medium is considered infinite in size. However, FDM defined the computed region within 2 mm thickness. The assumption above of AM lead to inaccurate computation. It does not confirm to the limitation of open-ended coaxial line. Hence, it was believed that FDM is more paractical to be used to simulate behaviour of electrical admittance.

It can be noticed that low *b/a* exhibit low level of G/Y_0 for all level of *MC*. It can be deduced through Equation (13). High *b/a* lead to low Y_0 and in turn, it causes high G/Y_0. It can be seen through variation of G/Y_0 where the variation for $b/a = 5$ is the widest compared with other lower *b/a*, i.e., 1.57, 2, 3.298 and 4. The aspect ratio, $b/a = 3.298$ presents considerably smaller error compared with b/a = 1.57, 2, and 4 when frequency < 3GHz. This aspect ratio indicates the smallest average error, i.e. 0.03 Siemen. Commercial RG405/U coaxial cable has $b/a = 3.298$. It indicates RG405/U coaxial cable is appropriate for application in moisture sensing for frequency < 3GHz [15-16]. For frequency > 3 GHz, the smallest average error is shown by the smallest *b/a* (=1.57) coaxial line, i.e., 0.30 Siemen. It suggests that lower *b/a* lead to a better agreement between FDM and AM in term of G/Y_0 for frequency > 3GHz. The average error of low *b/a* for frequency range > 3GHz is significantly lower than high *b/a*. It can be seen through drastic increment of G/Y_0 from AM when *b/a* increases. The increment of *b/a* also indicates that the capacitance between the inner and outer conductor as well as fringing capacitance decrease. Subsequently, it causes an increment of *G*. AM does not take fringing effect into account. As a result, AM is discrepant from FDM, especially at high frequencies. In addition, increment of *b/a* lead to the decrement of capacitive effect in coaxial line. Subsequently, inductive effect becomes significant in coaxial line. The inductive effect could charge the ionic substance inductively and cause the vigorous activity of ionic substance in fruit. It enhances *G* due to increment of conductivity. AM is more sensitive to *b/a* than FDM. It might be due to the aforementioned assumption. The assumption presumes homogeneous structure of the infinite region in the sample. The resistance of sample on the flow of electric current due to the movement of ionic substance in fruit is degraded. It could clarify that higher *MC* lead to a severe discrepancy between AM and FDM.

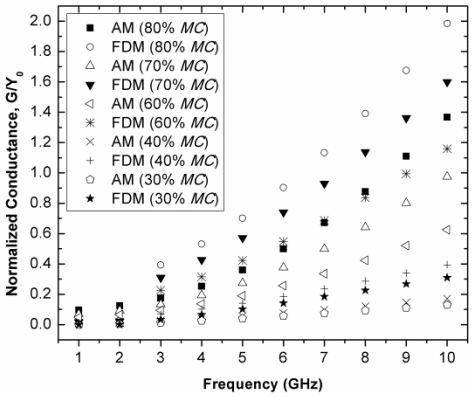

Fig. 3. The variation of G/Y_0 which $b/a = 1.57$ over frequency using FDM and AM.

Likewise, the normalized susceptance, B/Y_0 increases with frequency. The lumped-circuit in the coaxial sensor is equivalent to a *RLC* circuit. Therefore, susceptance, *B* vary with resistance, capacitance and inductance. Generally, it can be seen that increment of frequency causes capacitive reactance, X_c decreases and hence yield to the increment of B/Y_0. However, B/Y_0 from AM decreases when frequency > 7 GHz for $b/a > 3.298$. When $b/a > 3.298$, the capacitance decline due to the increment of distance between inner and outer conductor of the coaxial line. The assumption of AM increases the effect of G/Y_0 when *b/a* increases. When $b/a > 3.298$, it turns coaxial line to be inductive. Hence, the increment of frequency leads to decrement of B/Y_0. The decrement is even drastic when *MC* is high. This is due to the presence of a substantial ionic substance which can increase the conductivity of fruit. These ionic substances act as charge carrier to conduct current between inner and outer conductor. It was justified through higher *b/a*, i.e., 4 and 5 (Fig. 11 and Fig. 12) where these *b/a* values exhibit the greatest error range, especially $b/a = 5$ where its error is up to 35 Siemens. Meanwhile, the errors of B/Y_0 between FDM and AM that presented in Fig. 8 to Fig. 12 increases with frequency. It is similar to G/Y_0. For $b/a \leq 2$ (Fig. 8 to Fig. 9), the error range that presented is similar which is within 1.8 Siemens. However, the error range that shown by $b/a = 3.298$ (Fig. 10) is less than 1 Siemen. FDM exhibit consistent

trendline as B/Y_0 of all *MC* increases. Specification of finite computation region within 2 mm range sustain the domination of capacitive effect in coaxial line. It might be due to consistency between coverage of open-ended coaxial line and the finite computation region in FDM. Consideration of the fringing effect in FDM also play a vital role. Also, the increment of *MC* results in the increase of B/Y_0. Substantial *MC* enhance the effect of capacitive as *MC* has high dielectric constant. It is due to the the high polar moment tht presented in water molecule, H_2O.

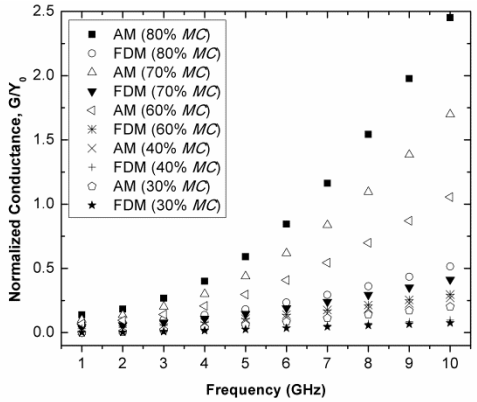

Fig. 4. The variation of G/Y_0 which b/a=2 over frequency using FDM and AM.

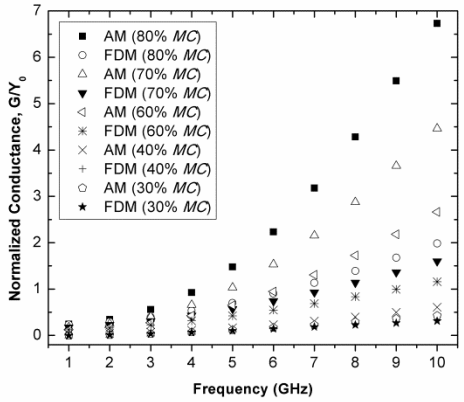

Fig. 5. The variation of G/Y_0 which b/a = 3.298 over frequency using FDM and AM.

It can be noticed that B/Y_0 of FDM has better agreement with AM when frequency ≤ 2 GHz. It can be seen through the lowest error that presents between AM and FDM as shown from Fig. 8 to Fig. 12. However, the frequency that < 2 GHz is highly sensitive with the presence of an ionic substance in fruit. It may lead to the discrepancy between computation and real case because the moisture is the paramount importance, instead of presented ionic substance in fruit. Ionic conductivity, σ has significant effect in 1 GHz, since dielectric properties in agriculture are primarily dependent on water activity and ionic conductivity, σ of fluids contained in their cellular structure [41-42]. This implies that variation of $\tilde{Y}$ can be due to polar moment of water molecule and ionic conductivity of fluids as well.

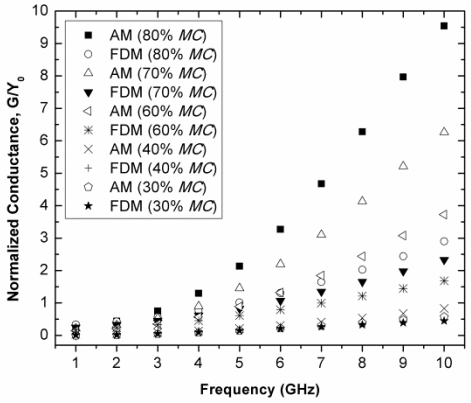

Fig. 6. The variation of G/Y_0 which b/a = 4 over frequency using FDM and AM.

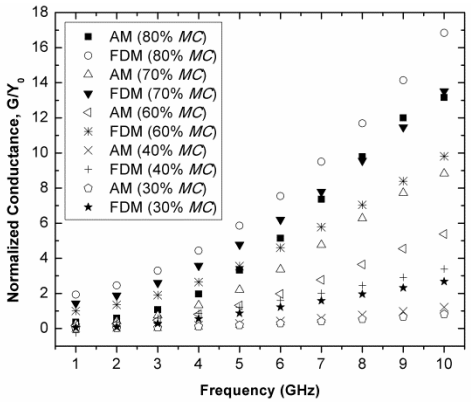

Fig. 7. The variation of G/Y_0 which b/a = 5 over frequency using FDM and AM.

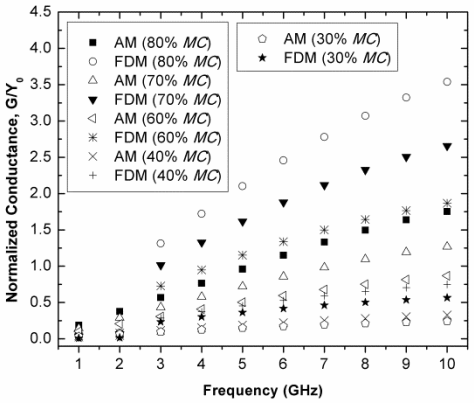

Fig. 8. The variation of B/Y_0 which b/a = 1.57 over frequency using FDM and AM.

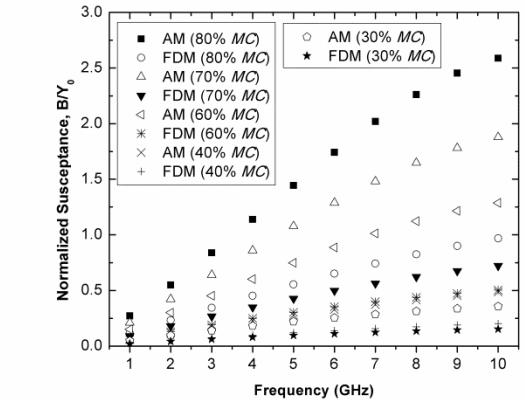

Fig. 9. The variation of B/Y_0 which b/a = 2 over frequency using FDM and AM.

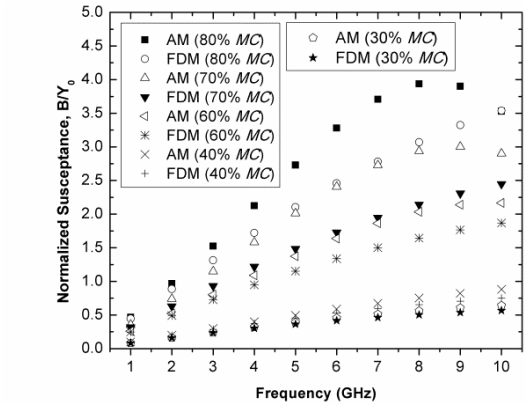

Fig. 10. The variation of B/Y_0 which b/a = 3.298 over frequency using FDM and AM.

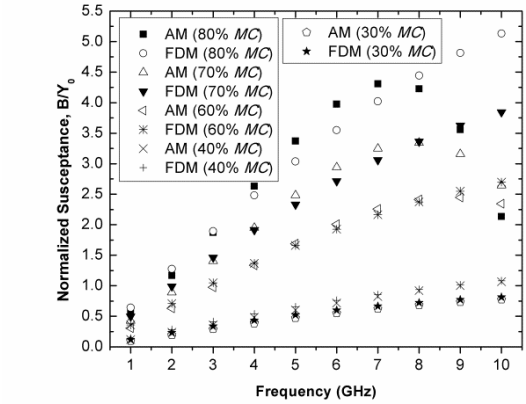

Fig. 11. The variation of B/Y_0 which b/a = 4 over frequency using FDM and AM.

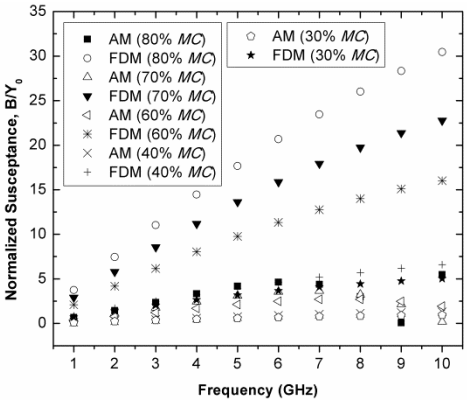

Fig. 12. The variation of B/Y_0 which b/a = 5 over frequency using FDM and AM.

IV. CONCLUSIONS

In this work, the admittance was simulated using FDM and AM on an aperture of open-ended coaxial line. The comparison was conducted between FDM and AM. It can be observed that finite difference method shows better agreement with AM in term of G/Y_0. G/Y_0 of FDM and AM increases with frequency and *MC* for all *b/a*. The error of G/Y_0 between FDM and AM increase with frequency. The assumed infinite computation region by AM is the main cause to these error. Ratio b/a = 3.298 exhibit the least error of G/Y_0 when frequency < 3GHz. When b/a > 3.298, coaxial line turn to be inductive. It becomes major reason to the increment of error. Generally, B/Y_0 increases with frequency *MC* and *b/a*. However, AM exhibit anomaly behavior where B/Y_0 decreases when b/a > 3.298 due to the transition from capacitive to inductive. Suffice to say, FDM and AM have the best agreement in terms of G/Y_0 and B/Y_0 at b/a = 3.298 when frequency ≤ 2 GHz. It implies that aspect ratio of b/a = 3.298 is suggested to be used for study.

REFERENCES

[1] Z. Song, F. Duval, D. Su, and A. Louis, "Stable partial inductance calculation for partial element equivalent circuit modeling," *ACES J.*, vol. 25, no. 9, pp. 738-748, 2010.

[2] C. Filippo, M. Agostino, and M. Giuliano, "An overview of equivalent circuit modeling techniques of frequency selective surfaces and metasurfaces," *ACES J.*, vol. 29, no. 12, pp. 960-976, 2014.

[3] C. Salvatore, B. Emanuela, and M. Andrea, "A microwave imaging approach based on amplitude-

only data for the reconstruction of the electromagnetic field induced in biological phantoms," *ACES J.*, vol. 16, no. 2, pp. 79-89, 2001.

[4] J. A. Tuszynski, P. Winter, D. White, C.-Y. Tseng, K. K. Sahu, F. Gentile, I. Spasevska, S. I. Omar, N. Nayebi, C. D. M. Churchill, M. Klobukowski, and R. M. A. El-Magd, "Mathematical and computational modeling in biology at multiple scales," *Theor. Biol Med. Model.*, vol. 11, no. 52, pp. 1-42, 2014.

[5] G. K. Vagenas and D. Marinos-Kouris, "Finite element simulation of drying of agricultural products with volumetric changes," *Appl. Math. Modelling*, vol. 15, no. 9, pp. 475-482, 1991.

[6] Z. Huang, H. Zhu, and S. Wang, "Finite element modeling and analysis of radio frequency heating rate in mung beans," *Trans. ASABE*, vol. 58, no. 1, pp. 149-160, 2015.

[7] B. Qin, Q. Zhang, G. V. Barbosa-Cánovas, B. G. Swanson, and P. D. Pedrow, "Pulsed electric field treatment chamber design for liquid food Pasteurization using a finite element method," *Trans. ASAE*, vol. 38, no. 2 pp. 557-565, 1995.

[8] S. O. Nelson, "Electrical properties of agricultural products (a critical review)," *Trans. ASAE*, vol. 16, no. 2, pp. 384-400, 1973.

[9] K. Y. You, A. Zulkifly, L. L. You, K. Y. Lee, and E. M. Cheng, "Palm oil moisture monitoring based on dielectric properties at microwave frequencies," *Int. J. Microw. Opt. Tech.*, vol. 9, no. 4, pp. 294-302, 2014.

[10] A. Zulkifly, K. Y. You, A. S. Halim, H. Jumiah, S. Elias, K. Kaida, and Z. Azmi, "Fast and simple technique for determination of moisture content in oil palm fruits," *Jpn. J. Appl. Phys.*, vol. 44, no. 7A**,** pp. 5272-5274, 2005.

[11] A. Zulkifly, K. Y. You, A. S. Halim, K. Kaida, H. Jumiah, and S. Elias, "Complex permittivity and moisture measurements of oil palm fruits using an open-ended coaxial sensor," *IEEE Sens. J.*, vol. 5, no. 6, pp. 1281-1287, 2005.

[12] K. Y. Lee, A. Zulkifly, M. D. Nur Sharizan, and K. Y. You, "Portable microwave instrumentation system for determination of moisture content in oil palm fruits," *Jpn. J. Appl. Phys.*, vol. 48, no. 12R, 120219, 2009.

[13] C. W. S. Hartley, *The Oil Palm*. Longman, London, 1988.

[14] A .Ariffin, S. R. Mat, M. Banjari, and O. W. E. Wan, "Morphological changes of the cellular component of the developing palm fruit (Tenera: Elaeis Guineesis)," *Palm Oil Research Institute of Malaysia Bulletin*, no. 21, pp. 30-34, 1990.

[15] K. Y. You and A. Zulkifly, *Open-Ended Coaxial Sensor Handbook: Formulations, Microwave Measurements and Applications*. Saarbrücken, Germany: LAP Lambert Academic Publishing, 2010.

[16] E. M. Cheng, A. Zulkifly, A. M. MohamedFareq, K. Y. Lee, K. Y. You, S. F. Khor, H. Jumiah, and Z. Hishamuddin, "Finite difference analysis of an open-ended, coaxial sensor made of semi-rigid coaxial cable for determination of moisture in Tenera oil palm fruit," *ACES J.*, vol. 31, no. 10, pp. 1181-1192, 2016.

[17] E. M. Cheng, A. Zulkifly, A. R. S. Hasliza, K. Y. Lee, K. Y. You, H. Jumiah, Z. Hishamuddin, and S. F. Khor, "Analysis on monopole antenna for moisture determination in oil palm fruit using finite difference method," *J. Electr. Eng. Technol.*, vol. 11, no. 6, pp. 1754-1762, 2016.

[18] S. Khandige and D. Misra, "Characterization of the layered dielectrics using an open-ended coaxial line sensor," In *Proceeding of Conference on Precision Electromagnetic Measurements Digest*, pp. 65-66, 27th June-1st July, 1994.

[19] M. A. Stuchly and S. S. Stuchly, "Coaxial line reflection methods for measuring dielectric properties of biological substances at radio and microwave frequencies-A review," *IEEE Trans. Instrum. Meas.*, vol. 29, no. 3, pp. 176-183, 1980.

[20] G. B. Gajda and S. S. Stuchly, "Numerical analysis of open-ended coaxial lines," *IEEE Trans. & Microwave Theory Tech.*, vol. MTT-31, no. 5, pp. 380-384, 1983.

[21] M. A. Stuchly, T. W. Athley, G. M. Samaras, and G. E. Taylor, "Measurement of radio frequency permittivity of biological tissue with an open-ended coaxial line: Part II-Experimental results," *IEEE Trans. & Microwave Theory Tech.*, vol. 30, no. 1, pp. 87-92, 1982.

[22] D. Misra, "A quasi-static analysis of open-ended coaxial lines," *IEEE Trans. & Microwave Theory Tech.*, vol. MTT-35, no. 10, pp. 925-928, 1987.

[23] J. M. Anderson, G. B. Gajda, and S. S. Stuchly, "Analysis of an open-ended coaxial line sensor in layer dielectric," *IEEE Trans. Instrum. Meas.*, vol. IM-35, no. 1, pp.13-18, 1986.

[24] M. A. Stuchly, M. M. Brady, S. S. Stuchly, and G. Gadja, "Equivalent circuit of an open-ended coaxial line in a lossy dielectric," *IEEE Trans. Instrum. Meas*., vol. IM-31, no. 2, pp. 116-119, 1982.

[25] A. Taflove, *Computational Electrodynamics: The Finite Difference Time Domain Method*. Boston, MA: Artech House, 1995.

[26] Z. Pei-bai, *Numerical Analysis of Electromagnetic Fields*. New York: Springer-Verlag Berlin Heidelberg, pp. 88-92, 1993.

[27] H. Levine and C. H. Papas, "Theory of the circular diffraction antenna," *J. Appl. Phys.* 22(1): 29-43, 1951.

[28] E. C. Burdette, F. L. Clain, and J. Seals, "In vivo

probe measurement technique for determining dielectric properties at VHF through microwave frequencies," *IEEE Trans. & Microwave Theory Tech*., vol. MTT-28, no. 4, pp. 414-427, 1980.

[29] H. Bussey, "Dielectric measurement in a shielded open circuit coaxial line," *IEEE Trans. Instrum. Meas.*, 29:120-124, 1980.

[30] M. A. Stuchly and S. S. Stuchly, "Coaxial line reflection methods for measuring dielectric properties of biological substances at radio and microwave frequencies-A review," *IEEE Trans. Instrum. Meas.*, 30:228-229, 1980.

[31] T. W. Athey, M. A. Stuchly, and S. S. Stuchly, "Measurement of radio-frequency permittivity of biological tissues with an open-ended coaxial line-Part I," *IEEE Trans. & Microwave Theory Tech*., 30(1), pp. 82-86, 1982.

[32] M. M. Brady, S. A. Symons, and S. S. Stuchly, "Dielectric behavior of selected animal tissue *in vitro* at frequencies from 2 to 4 GHz," *IEEE Trans. Biomedical Eng*. 28: 305-307, 1981.

[33] M. A. Stuchly, M. M. Brady, S. S. Stuchly, and G. Gadja, "Equivalent circuit of an open-ended coaxial line in a lossy material," *IEEE Trans. Instrum. Meas*., 31:116-119, 1982.

[34] D. Misra, M. Chabbra, B. R. Epstein, M. Mirotznik, and K. R. Foster, "Noninvasive electrical characterization of materials at microwave frequencies using an open-ended coaxial line: Test of an improved calibration technique," *IEEE Trans. Microwave Theory Tech*., 38:8-14, 1990.

[35] S. S. Stuchly, C. L. Sibbald, and J. M. Anderson, "A new aperture admittance model for open-ended waveguides," *IEEE Trans. & Microwave Theory Tech.*, vol. 42, pp. 192-198, 1994.

[36] J. M. Anderson, C. L. Sibbald, S. S. Stuchly, and K. Caputa, "Advances in dielectric measurements using an open-ended coaxial line sensor," *CCECE/ CCGEI*, pp. 916-919, 1993.

[37] J. M. Anderson, G. B. Gajda, and S. S. Stuchly, "Dielectric measurements using a rational function model," *IEEE Trans. & Microwave Theory Tech.*, vol. 42, pp. 199-204, 1994.

[38] K. Y. You, Z. Abbas, and K. Khalid, "Application of microwave moisture sensor for determination of oil palm fruit ripeness," *Meas. Sci. Review*, vol. 10, no. 1, pp. 7-14, 2010.

[39] N. Marcuvtiz, *Waveguide Handbook.* Boston, MA: Boston Tech. Pub., 1964.

[40] C. L. Pournaropoulos and D. Misra, "A study on the coaxial aperture electromagnetic sensor and its application in material characterization," *IEEE Trans. Instrum. Meas.*, vol. 43, no. 2, pp. 111-115, 1994.

[41] M. Kent and A. C. Jason, *Water Relations of Foods*. New York: Academic Press, 1975.

[42] R. E. Mudgett, S. A. Goldblith, D. I. C. Wang, and W. B. Westphal, "Prediction of dielectric properties in solid food of high moisture content at ultrahigh and microwave frequencies," *J. Food. and Preservation*, vol. 1, no. 2, pp. 119-151, 1977.

Ee Meng Cheng was born in 1980. He obtained his B.Sc (Honours)-Instrumentation Science in Universiti Putra Malaysia in 2004. He pursued his M.Sc. in Wave Propagation at the Institute for Mathematical Research on 2005 in Universiti Putra Malaysia and his Ph.D in Microwave at the Faculty of Science in 2007 in Universiti Putra Malaysia. Recently, he is a Senior Lecturer in School of Mechatronic Engineering, Universiti Malaysia Perlis. On the other hand, he is also Chartered Engineer from Institution of Engineering and Technology as well as Engineering Council, United Kingdom. His main personnel research interest is in the computational electromagnetic modeling, microwave dielectric spectroscopy, wave propagation in RF & microwave and microwave sensors development for food and agricultural applications.

Zulkifly Abbas was born in Alor Setar, Malaysia, in 1962. He received the B.Sc. degree with honors in Physics from the University of Malaya, Kuala Lumpur, in 1986, the M.Sc. degree in Microwave Instrumentation from the Universiti Putra Malaysia (UPM), Serdang, in 1994, and the Ph.D. degree in Electronic and Electrical Engineering from the University of Leeds, Leeds, U.K., in 2000. He is currently an Associate Professor with the Department of Physics, UPM, where he has been a faculty member since 1987. His main personnel research interest is in the theory, simulation, and instrumentation of electromagnetic wave propagation at microwave frequencies focusing on the development of microwave sensors for agricultural applications.

Mohd Fareq bin Abdul Malek obtained his B.Eng (Honours)-Electronic and Communication Engineering in The University of Birmingham, United Kingdom in 1994. He pursued his M.Sc. (Eng) in Microelectronic Systems and Telecommunications at The University of Liverpool, United Kingdom in 2003 and Ph.D. in

Electrical Engineering (Radio Frequency and Microwave) in 2005 at The University of Liverpool, United Kingdom. Currently, he is Associate Professor in Faculty of Engineering and Information Sciences, University of Wollongong in Dubai. His main personnel research interest is in electron maser, antenna design, embedded computing and microwave absorber development.

Kok Yeow You was born in 1977. He obtained his B.Sc. Physics (Honours) degree in Universiti Kebangsaan Malaysia in 2001. He pursued his M.Sc. in Microwave at the Faculty of Science in 2003 and his Ph.D. in Wave Propagation at the Institute for Mathematical Research in 2006 in Universiti Putra Malaysia. Recently, he is a Senior Lecturer at Radio Communication Engineering Department, Universiti Teknologi Malaysia. His main personnel research interest is in the theory, simulation, and instrumentation of electromagnetic wave propagation at microwave frequencies focusing on the development of microwave sensors for agricultural applications.

Kim Yee Lee was born in Muar, Johor, Malaysia. He received his B.Sc. Physics, M.Sc. Microwaves, and Ph.D. Microwaves all from the Universiti Putra Malaysia in year 2002, 2004, and 2008 respectively. In December 2007, He joined Universiti Tunku Abdul Rahman as a Lecturer in Department of Electronics and Electrical Engineering. His areas of research include microwave measurement technique, microwave circuit and instrumentation, control and automation, material properties measurement, and instrumentation calibration.

Nashrul Fazli Mohd Nasir received his Bachelor Degree in Biomedical Engineering from Universiti Malaya and later pursued his M.Sc. in Biomedical Engineering at Keele University (UK). He later received his Ph.D. in Electrical Engineering and Computer Engineering from Royal Melbourne Institution of Technology (RMIT) University, Australia. His research interests are in Biomaterials, Biosensors and Material Characterization in Biomedical Engineering. Currently, he is the Deputy Dean of Students Affair and Alumni for the School of Mechatronic Engineering, Universiti Malaysia Perlis.

Mohd Shukry Abdul Majid has more than 15 years of experience in teaching, research, and industries. He received his B.Eng. in Mechanical Engineering from University Manchester Institute of Science and Technology (UMIST) in 2001. Straight after, he worked as a Research and Development (R&D) Engineer at a semiconductor industry before joining Universiti Malaysia Perlis (UniMAP) as a Lecturer. He completed his M.Sc. in Mechanical Systems Engineering from the University of Liverpool in 2004 and his Ph.D. in Composite Engineering from Newcastle University, UK in 2011. Currently, he is serving Universiti Malaysia Perlis as an Associate Professor at School of Mechatronic Engineering. His current research interests lie in the strength of material's area with emphasis on the composite piping, looking at the performance of composite structures, NDE's of composites and natural fibre/green composites, hybrid reinforced/filled polymer composites, fire retardant, lignocellulosic reinforced/filled polymer and biodegradable composites. On the other hand, he received his professional engineer qualification (Ir.) from Board of Engineer Malaysia (BEM) in Mac 2016 and has been a Chartered Engineer (CEng) from the Engineering Council, United Kingdom since 2014.

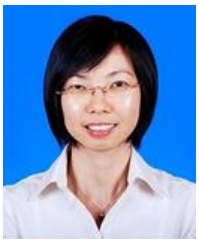

Shing Fhan Khor was born in 1982. She obtained her B.Sc. with Edu. (Honours)-Physics in Universiti Putra Malaysia in 2007. She pursued her Ph.D. in Materials Science at the Faculty of Science in 2011 in Universiti Putra Malaysia. Recently, she is a Senior Lecturer at School of Electrical Systems Engineering, Universiti Malaysia Perlis (UniMAP). Her main personnel research interest is in the glass science and focusing on dielectric, optical, mechanical and thermal properties.

Modeling and Experiment on Active Magnetic Bearing as Force Actuators to Detect Inner Race Fault of Rolling Element Bearing

Yuanping Xu, Jin Zhou, and Chaowu Jin

College of Mechanical and Electrical Engineering
Nanjing University of Aeronautics and Astronautics, Nanjing, 210016, China
ypxu@nuaa.edu.cn, zhj@nuaa.edu.cn, jinchaowu@nuaa.edu.cn

Abstract ─ As one of the important components in the rotating machinery, the condition of rolling element bearing has a great impact on the system performance. Therefore, the fault detection for the rolling element bearing is important and many methods have been proposed. Following our previous work on the outer race defect diagnosis, in this paper, the active magnetic bearing (AMB) is employed as an exciter to apply electromagnetic force to detect the inner race defects. The theoretical model of a nonlinear bearing-pedestal system model with the inner race defect under the electromagnetic force is developed and investigated. The simulation and experimental results show that the characteristic signal of inner race defect is amplified under the electromagnetic force through the AMBs, which is helpful for improving the diagnosis accuracy.

Index Terms ─ Active magnetic bearings, fault detection, inner race, rolling element bearings.

I. INTRODUCTION

For the rotating machinery, the health condition of rolling element bearing has a great impact on the performances. Therefore, fault detection for the rolling element bearing is very important and many methods have been proposed, which can be classified as vibration measurement, acoustic measurement, temperature measurement and wear analysis [1]. Vibration measurement has been the most widely used method in the health monitoring application.

A lot of methods have been proposed to model the vibration response of a bearing. McFadden and Smith [2,3] proposed a theoretical defected rolling element bearing model. Wang and Harrap [4] presented the envelope autocorrelation analysis for diagnosing multiple element defects of rolling element bearings. Tandon and Choudhury [5] investigated the dynamic response of the rings due to localized defects under axial load. Sunnersjo [6] proposed a two degrees of freedom (DOF) bearing dynamic model and applied Hertz contact theory to calculate the deflection. Feng [7] developed a four DOF bearing-pedestal model, which include two DOF pedestal model. Tadina [8] developed an improved bearing model and investigated the vibrations of a rolling element bearing during run-up.

AMBs are commonly used as bearings to support rotor, but they also can be used for fault detection as exciters [9]. Humphris [10] utilized AMBs as both levitation and perturbation to monitor and diagnose the shaft condition. Zhu et al. [11] modeled a crack rotor levitated by AMBs and found that crack would have big effects on the whole system. Mani et al. [12,14] and Quinn et al. [13] applied excitation from the AMB to a cracked rotor bearing system and used multiple scale method to diagnose the rotor crack. Similarly, Sawicki [15] applied harmonic balance method based on sinusoidal excitation generated from AMBs for rotor crack detection. Chasalevris [16] investigated the response of a simple elastic rotor supported by two fluid-film bearings, while one of the bearings was worn under the AMB transient excitation.

Although AMBs have been used for the fault detection, few studies are reported on rolling element bearings. In our previous work [17], the AMB is employed as an exciter to detect the outer race defects and we found that the outer race fault signals amplified significantly under AMBs force. Following our previous work on the outer race defect, this paper investigates dynamic response of inner race defect under electromagnetic force excitation.

The remainder of the paper is organized as follows. Section 2 describes the model of rolling element bearing system with inner race defect under AMB force. The simulation and experimental results are presented in Section 3 and Section 4, respectively. Conclusions are drawn in Section 5.

II. ROLLING ELEMENT BEARING MODELING

A. Contact force

Figure 1 shows the bearing schematic, where N is number of rolling elements; d_b is the element diameter; D is the pitch diameter; r_0 is the radial clearance; α

Submitted On: May 22, 2018
Accepted On: October 4, 2018

is and the contact angle. The bearing is modeled with two orthogonal DOF and the outer race is fixed in the pedestal. The slippage of rolling elements, the mass and the inertia of the rolling elements are ignored. The displacement of the shaft can be divided into x and y directions and the contact deformation for the ith rolling element δ_i is given by:

$$\delta_i = x\cos\theta_i + y\sin\theta_i - r_0. \tag{1}$$

The angle of the rolling element θ_i shown in Fig. 1 is given as:

$$\theta_i = \omega_c t + \frac{2\pi}{N}(i-1), \tag{2}$$

$$\omega_c = \frac{\omega_s r}{(R+r)}, \tag{3}$$

where ω_s is the shaft speed; ω_c is the cage speed; r and R in Fig. 1 are the inner and outer race radius.

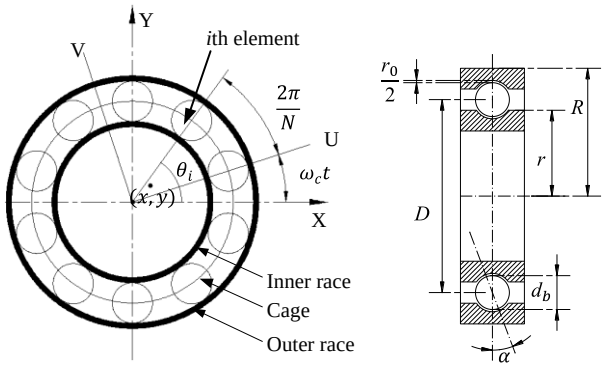

Fig. 1. Schematic of a rolling element bearing.

According to the Hertz theory, the non-linear contact force F is given by [1,18-19]:

$$F = K_b\delta^n, \tag{4}$$

where δ is the contact deformation; K_b is the nonlinear contact stiffness depending on the bearing geometry and the elasticity of material [18], for the rolling element bearing considered in this paper, the computed value is 2.14×10^9 N/m$^{1.5}$; the exponent $n = 1.5$ is for ball bearings. Due to the fact that compression Hertz forces occurs only for positive values of δ, therefore the γ_i is employed to represents the contact state:

$$\gamma_i = \begin{cases} 1 & \text{if } \delta_i > 0 \\ 0 & \text{if } \delta_i \le 0 \end{cases}. \tag{5}$$

The contact force is the sum of each of the rolling elements and the total force along the x and y axes can be obtained as:

$$F_{bx} = \sum_{i=1}^{N}\gamma_i K_b\delta_i^{1.5}\cos\theta_i, \tag{6}$$

$$F_{by} = \sum_{i=1}^{N}\gamma_i K_b\delta_i^{1.5}\sin\theta_i. \tag{7}$$

The damping of rolling element bearing can be estimated using Kramer method [20] as:

$$c_s = (0.25-2.5)\times10^{-11}K_l, \tag{8}$$

where K_l is the linearized stiffness of the rolling element bearing.

B. Inner race defect modeling

The inner race defect is modeled as a slight dent and the geometrical interpretation of the faults is shown in Fig. 2.

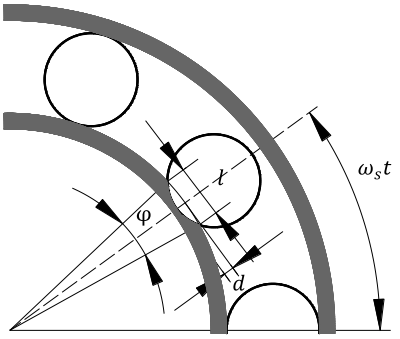

Fig. 2. Defect on inner race.

The length of the dent is l and the following relationship can be established from Fig. 2:

$$d = r_b - \sqrt{r_b^2 - (l/2)^2}, \tag{9}$$

$$\varphi = 2\sin^{-1}(l/2r), \tag{10}$$

where r_b is the ball radius; φ is the central angle of the inner defect; d is the max increment of the radial clearance.

When the rolling element moves into the defected area, the radial clearance will increase rapidly, which causes a decline of the contact force and results vibration. The varying clearance Δd caused by the defect is modeled as a half sinusoidal wave [17]. The relation between the varying clearance and angular position is give as follows:

$$\Delta d(\theta_i) = \begin{cases} d\sin\left[\pi\dfrac{\bmod(\theta_i,2\pi)-\left(\omega_s t-\dfrac{\varphi}{2}\right)}{\varphi}\right], & \bmod\left(\omega_s t-\dfrac{\varphi}{2},2\pi\right) < \bmod(\theta_i,2\pi) < \bmod\left(\omega_s t+\dfrac{\varphi}{2},2\pi\right) \\ 0, & \text{otherwise} \end{cases}. \tag{11}$$

The notation $\mathrm{mod}(\theta_i,2\pi)$ in Eq. (11) denotes the modulo operation. From Eq. (9), the $\Delta d(\theta_i)$ value range is 0 to 3×10^{-3} mm considering l as 0.2 mm.

Therefore, when the rolling element is not located in the defected region, the actual radial clearance r_a is:

$$r_a = r_0. \tag{12}$$

When the rolling element is located in the defected region, the actual radial clearance r_a is:

$$r_a = r_0 + \Delta d. \tag{13}$$

Therefore, the contact forces can be calculated as follows:

$$F_{bx} = \sum_{i=1}^{N} \gamma_i K_b \left(x\cos\theta_i + y\sin\theta_i - r_a\right)^{1.5} \cos\theta_i, \tag{14}$$

$$F_{by} = \sum_{i=1}^{N} \gamma_i K_b \left(x\cos\theta_i + y\sin\theta_i - r_a\right)^{1.5} \sin\theta_i. \tag{15}$$

B. Bearing-pedestal modeling

The model of Feng et al. [7] is adopted to study the dynamics of rolling element bearings, which is shown in Fig. 3. The model has four DOF, including two DOF of inner race (x_s, y_s) and two DOF of pedestal (x_p, y_p).

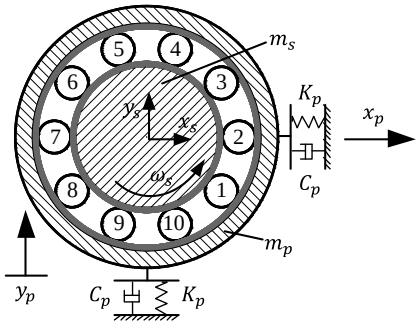

Fig. 3. Four-DOF bearing-pedestal model.

Followed by the above analysis, the whole contact forces of the model considering inner race and pedestal can be calculated as follows:

$$F_{bx} = \sum_{i=1}^{N} \gamma_i K_b \left[\left(x_s - x_p\right)\cos\theta_i + \left(y_s - y_p\right)\sin\theta_i - r_a\right]^{1.5} \cos\theta_i, \tag{16}$$

$$F_{by} = \sum_{i=1}^{N} \gamma_i K_b \left[\left(x_s - x_p\right)\cos\theta_i + \left(y_s - y_p\right)\sin\theta_i - r_a\right]^{1.5} \sin\theta_i. \tag{17}$$

Considering the nonlinear contact force, the equations of motion of bearing-pedestal system can be written as follows:

$$m_s\ddot{x}_s + c_s\dot{x}_s + F_{bx} = F_u\cos\omega_s t + F_{MX}, \tag{18}$$

$$m_s\ddot{y}_s + c_s\dot{y}_s + F_{by} = F_u\sin\omega_s t - m_s g + F_{MY}, \tag{19}$$

$$m_p\ddot{x}_p + c_p\dot{x}_p + K_p x_p - F_{bx} = 0, \tag{20}$$

$$m_p\ddot{y}_p + c_p\dot{y}_p + K_p y_p - F_{by} = -m_p g, \tag{21}$$

where m_s is the mass of the shaft and the inner race; c_s is the bearing damping; m_p is the mass of the pedestal; K_p and c_p are the stiffness and damping of the pedestal. F_{MX} and F_{MY} is the electromagnetic force applied to the system in the x and y direction, respectively, which are presented later. F_u is the unbalance force.

C. AMB force modeling

Ignoring the hysteresis loss and eddy current effect, the electromagnetic force provided by AMBs can be calculated by [21]:

$$F_{AMB} = \frac{1}{4}\mu_0 n_a^2 A\frac{i^2}{s^2}\cos\beta, \tag{22}$$

where μ_0 is the permeability in the vacuum; n_a is the number of coil windings; A is the area of the pole face; i is the bias current value; s is the nominal air gap and β is the angle between forces and magnetic poles. Table 1 lists the AMB parameters. Figure 4 shows the schematic of the AMB structure adopted in this paper, which the bottom two poles are activated.

Table 1: AMB parameters

Air Gap (AMB clearance) s	0.28 mm
Polar face area A	2.0×10^{-4}m^2
Windings of a coil n_a	240
Half angle between two poles β	22.5 degree

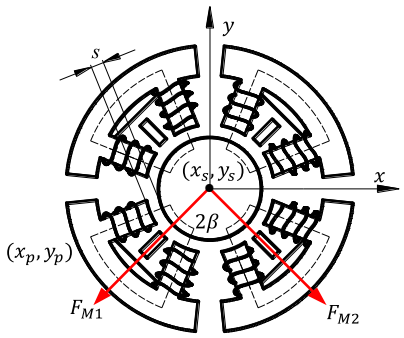

Fig. 4. The schematic of the AMB structure.

When the rolling element is located at the defected region, the rotor and the pedestal will vibrate and the nominal air gap s between the rotor and AMBs will change simultaneously since the AMBs are fixed on the stator together with the pedestal. Therefore, the electromagnetic force of each AMB can be written as:

$$F_{M1} = \frac{\mu_0 n_a^2 A i^2\cos\beta}{4\left[s + \left(y_s - y_p\right)\cos 2\beta + \left(x_s - x_p\right)\sin 2\beta\right]^2}, \tag{23}$$

$$F_{M2} = \frac{\mu_0 n_a^2 A i^2\cos\beta}{4\left[s + \left(y_s - y_p\right)\cos 2\beta + \left(x_p - x_s\right)\sin 2\beta\right]^2}. \tag{24}$$

Therefore, the total electromagnetic force along the x and y directions is:

$$F_{MX} = -\left(F_{M1}\sin 2\beta - F_{M2}\sin 2\beta\right), \quad (25)$$

$$F_{MY} = -\left(F_{M1}\cos 2\beta + F_{M2}\cos 2\beta\right). \quad (26)$$

III.SIMULATION RESULTS

A. Model parameters

The nonlinear differential Eq. (18-21) is evaluated numerically using the fourth-order Runge-Kutta algorithm and the transient response is obtained. The parameters adopted in simulation are shown in Table 2.

Table 2: Model parameters

1. Parameters of 61901 Rolling Element Bearings	
Outer race radius R	10.59 mm
Inner race radius r	7.41 mm
Number of ball N	10
Contact stiffness K_b	2.14×10^9 N/m$^{3/2}$
Ball diameter d_b	3.18 mm
Pitch diameter D	18 mm
Contact angle α	0°
Radial clearance r_0	3 μm
B_N	4.1
2. Other Inputs	
Mass of shaft/inner race m_s	1.2 kg
Bearing contact damping c_s	200 N · s/m
Mass of pedestal m_p	2 kg
Pedestal stiffness K_p	1.5×10^7 N/m
Damping in pedestal c_p	3000 N · s/m
Bias current i	1 A

The vertical acceleration responses for the pedestal with an inner racer faulty bearing are calculated respectively considering the electromagnetic force is applied or not. The frequency spectrum of the vibration signal is obtained using envelope method rather than the Fast Fourier Transform Algorithm (FFT) directly because in most cases, these defect frequencies cannot be detected in the frequency spectrum of a raw vibration signal due to the dominant high frequencies caused by the resonant components.

B. Inner race defect under electromagnetic force

For a rolling element bearing, the inner race defect frequency is given by [1]:

$$f_{BPFI} = \frac{1}{2} f_s \left(1 + \frac{d_b}{D}\cos\alpha\right) N, \quad (27)$$

where f_s is the shaft rotating speed in Hz.

The defect on the inner race will rotate along the shaft haft rotating speed and will go through the loading zone every cycle. Thus the peaks at BPFI (Ball Pass Frequency Inner), the combination of the BPFI with inner ring (shaft frequency) will be found in the frequency domain. Figures 5 (a) and (b) show the simulated vertical pedestal acceleration in time domain due to inner race defect with and without electromagnetic force. It is clear that the vibration amplitudes aggravate obviously under the electromagnetic force. The envelope spectrum (Hilbert transform) for the time domain in Fig. 5 (c) shows a frequency peak at 30 Hz, which is the rotating frequency. The theoretical inner race defect frequency BPFI calculated by Eq. (27) is 176.5 Hz which equals to the simulation value, indicating the model is accurate. It can be seen from the Fig. 5 (c) that for a small defect, the amplitude of defect characteristic frequency BPFI and the combination of the BPFI with inner ring rotating frequency are small in the frequency spectrum. However, there is clear increase for these peaks under the electromagnetic force. This may be attributed to the electromagnetic force property, which changes periodically due to the periodically changing of the air gap. In other words, when the rolling elements locate at the defected area, the rotor will vibrate, causing a varying air gap and leading to the same periodically varying electromagnetic force. Because the electromagnetic force varying frequency equals to the inner race defect characteristic frequency f_{BPFI}, the f_{BPFI} characteristic signal will be amplified clearly.

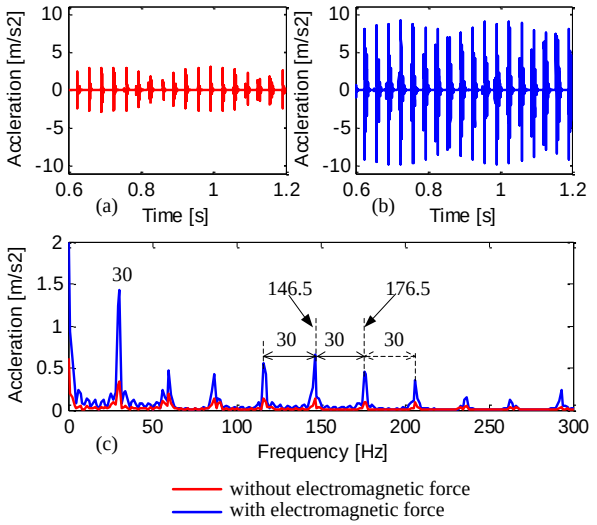

Fig. 5. Simulated pedestal vertical vibration with bearing inner race defect, $l = 0.2$mm, at 1800 rpm (30 Hz): (a) bearing without electromagnetic force, (b) bearing with electromagnetic force, and (c) frequency spectrum of the envelope between 0.6 and 1.2s.

IV. EXPERIMENTAL INVESTIGATION

The experimental test rig for this study is a rotor AMB system designed and built as a research platform at Nanjing University of Aeronautics and Astronautics, as shown in Fig. 6. The rotor was supported by two radial and two thrust AMBs. However, for this study, the

system is rearranged that the rotor is supported by rolling element bearings rather than AMBs and the AMBs are employed as the non-contact exciters to apply online electromagnetic force during the operation. One acceleration sensor is installed on the pedestal vertically to record the acceleration vibration data.

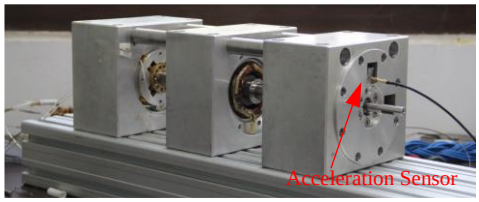

Fig. 6. The test rig.

Fig. 7. The damage process using electric discharge machine.

Figure 7 shows inner race damage process using electric discharge machine. The width of this damage is around 0.2 mm.

The experiment is performed at 1800 rpm (30 Hz) under radial AMB force with 1A bias current. Figure 8 shows the experimental results. Figures 8 (a) and 8 (b) are the time domain acceleration signal with and without AMBs, respectively. Corresponding envelope frequency spectrum (Hilbert transform) comparisons for the faulty inner race bearing are shown in Fig. 8 (c) and Fig. 8 (d). It can be seen that for an incipient defect, when electromagnetic force is not applied, the vibration amplitudes in the time domain, the peaks of f_{BPFI} and the combination of the BPFI with inner ring in frequency spectrum are small. However, there is clear increase in peaks at peaks of f_{BPFI} and the combination of the BPFI with inner ring under electromagnetic force. The experimental peak frequency of f_{BPFI} is 177.7 Hz, which almost coincides with the simulation results (176.5 Hz) and the theoretical calculation from Eq. (27). Both experimental and simulation results show an increase in the acceleration response as a result of the defect in the inner race.

V. CONCLUSION

The health condition of rolling element bearing has a great impact on the rotating machinery performances. In this paper, the dynamics of an inner race fault rolling element bearing with AMBs as force actuators is studied. We investigate a nonlinear bearing pedestal model with the inner race defect under the electromagnetic force and obtain the numerical simulation results. The results show that under the electromagnetic force generated from AMBs, the peaks of f_{BPFI} and the combination of the BPFI with inner ring in frequency spectrum for the inner race are amplified clearly, which is helpful for improving the diagnosis accuracy. In order to verify our theoretical calculation, an experiment is performed, which validate theoretical results.

Since the single defect model with AMBs excitation is validated, we think this model may also be available for multiple defects. In the future, the multiple defects condition and sensitivity of this method will be investigated.

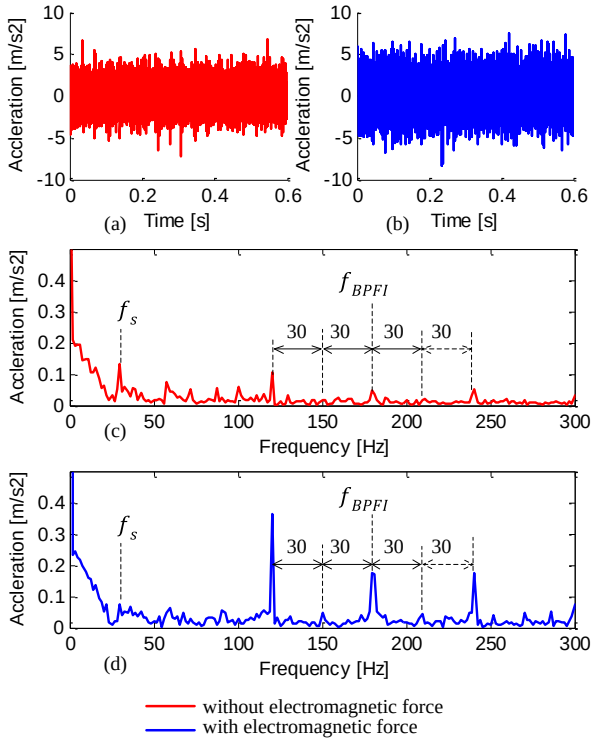

Fig. 8. Experimental pedestal vertical vibration with bearing inner race defect, $l = 0.2\mathrm{mm}$, at 1800 rpm (30 Hz): (a) bearing without electromagnetic force, (b) bearing with electromagnetic force, (c) the envelope frequency spectrum for a, and (d) the envelope frequency spectrum for b.

ACKNOWLEDGMENT

This work is supported by Open Project Program of Jiangsu Key Laboratory of Large Engineering Equipment Detection and Control (JSKLEDC201502).

REFERENCES

[1] M. S. Patil, J. Mathew, P. K. Rajendrakumar, and S. Desai, "A theoretical model to predict the effect of localized defect on vibrations associated with ball bearing," *International J. Mechanical Sciences*, vol. 52, no. 9, pp. 1193-1201, 2010.

[2] P. D. McFadden and J. D. Smith, "Model for the vibration produced by a single point defect in a rolling element bearing," *J. Sound and Vibration*, vol. 96, no. 1, pp. 69-82, 1984.

[3] P. D. McFadden and J. D. Smith, "The vibration produced by multiple point defects in a rolling element bearing," *J. Sound and Vibration*, vol. 98, no. 2, pp. 263-273, 1985.

[4] W. Y. Wang and M. J. Harrap, "Condition monitoring of ball bearings using an envelope autocorrelation technique," *Machine Vibration*, vol. 5, no. 1, pp. 34-44, 1996.

[5] N. Tandon and A. Choudhury, "An analytical model for the prediction of the vibration response of rolling element bearings due to a localized defect," *J. Sound and Vibration*, vol. 205, no. 3, pp. 275-292, 1997.

[6] C. S. Sunnersjö, "Varying compliance vibrations of rolling bearings," *J. Sound and Vibration*, vol. 58, no. 3, pp. 363-373, 1978.

[7] N. S. Feng, E. J. Hahn, and R. B. Randall, "Using transient analysis software to simulate vibration signals due to rolling element bearing defects," *The 3rd Australian Congress on Applied Mechanics*, Sydney, pp. 689-694. 2002.

[8] M. Tadina and M. Boltežar, "Improved model of a ball bearing for the simulation of vibration signals due to faults during run-up," *J. Sound and Vibration*, vol. 330, no. 17, pp. 4287-4301, 2011.

[9] J. T. Marshall, M. Kasarda, and J. Imlach, "A multipoint measurement technique for the enhancement of force measurement with active magnetic bearings," *J. Engineering for Gas Turbines and Ppower*, vol. 125, no. 1, pp. 90-94, 2003.

[10] R. R. Humphris, "A device for generating diagnostic information for rotating machinery using magnetic bearings," *The MAG Conference & Exhibition for Magnetic Bearings, Magnetic Drives and Dry Gas Seals*, 1992.

[11] C. Zhu, D. A. Robb, and D. J. Ewins, "The dynamics of a cracked rotor with an active magnetic bearing," *J. Sound and Vibration*, vol. 265, no. 3, pp. 469-487, 2003.

[12] G. Mani, D. D Quinn, M. Kasarda, D. J. Inman, and R. G. Kirk, "Health monitoring of rotating machinery through external forcing," *Proceedings of ISCORMA-3*, Cleveland, USA, pp. 19-23, 2005.

[13] D. D Quinn, G. Mani, M. Kasarda, T. Bash, D. J. Inman, and R. G. Kirk, "Damage detection of a rotating cracked shaft using an active magnetic bearing as a force actuator—Analysis and experimental verification," *IEEE/ASME Trans. Mechatronics*, vol. 10, no. 6, pp. 640-647, 2005.

[14] G. Mani, D. D Quinn, and M. Kasarda, "Active health monitoring in a rotating cracked shaft using active magnetic bearings as force actuators," *J Sound and Vibration*, vol. 294, no. 3, pp. 454-465, 2006.

[15] J. T. Sawicki, M. I. Friswell, Z. Kulesza, A. Wroblewsk, and J. D. Lekki. "Detecting cracked rotors using auxiliary harmonic excitation," *J. Sound and Vibration*, vol. 330, no. 7, pp. 1365-1381, 2011.

[16] A. Chasalevris, F. Dohnal, and I. Chatzisavvas, "Experimental detection of additional harmonics due to wear in journal bearings using excitation from a magnetic bearing," *Tribology International*, vol. 71, pp. 158-167, 2014.

[17] Y. Xu, L. Di, J. Zhou, C. Jin, and Q. Guo, "Active magnetic bearings used as exciters for rolling element bearing outer race defect diagnosis," *ISA Transactions*, vol. 61, pp. 221-228, 2016.

[18] J. Sopanen and A. Mikkola, "Dynamic model of a deep-groove ball bearing including localized and distributed defects, Part 1: Theory," *Proceedings of the Institution of Mechanical Engineers, Part K: J. Multi-body Dynamics*, vol. 217, no. 3, pp. 201-211, 2003.

[19] N. Sawalhi and R. B. Randall, "Simulating gear and bearing interactions in the presence of faults: Part I. The combined gear bearing dynamic model and the simulation of localised bearing faults," *Mechanical Systems and Signal Processing*, vol. 22, no. 8, pp. 1924-1951, 2008.

[20] E. Kramer. *Dynamics of Rotors and Foundations*. Berlin: Springer-Verlag, 1993.

[21] G. Schweitzer and E. H. Maslen, *Magnetic Bearings*. Springer, Berlin, Germany, 2009.

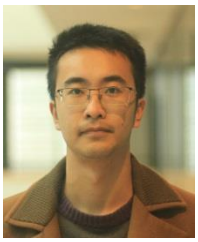

Yuanping Xu received his Ph.D. degree in Mechanical Engineering from Nanjing University of Aeronautics and Astronautics (NUAA) in 2018. From 2016 to 2017, he was a Guest Ph.D. Student in Ecole Polytechnique Federale Lausanne (EPFL), Switzerland. He is currently a Lecturer in the College of Mechanical and Electrical Engineering, NUAA. His research focuses on magnetic levitation.

Jin Zhou received her Ph.D. degree in Mechanical Engineering from China University of Mining and Technology (CUMT) in 2001. From 2012 to 2013, she was a visiting scholar in the Rotating Machinery and Control Laboratory (ROMAC) of the University of Virginia. She is currently a Full Professor in the College of Mechanical and Electrical Engineering, NUAA. Her research focuses on magnetic bearings and vibration control. She was the member of Program Committee of the 14th International Symposium on Magnetic Bearings (2014) and the Program Chair of the 16th International Symposium on Magnetic Bearings, 2018.

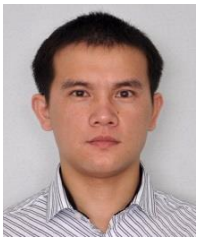

Chaowu Jin obtained the B.S., M.S., and Ph.D. degree in Mechanical Engineering from NUAA from 2002 to 2011. He is currently an Associate Professor in the College of Mechanical and Electrical Engineering, NUAA. His research focuses on magnetic bearings.

Calculating Electromagnetic Force Created by Static Suspension Device Used in Permanent Magnet Electrodynamic Suspension Vehicle

Wenlong Zhang [1], Kunlun Zhang [1], Yin Chen [2], and Xijun Liu [3]

[1] Key Laboratory of Magnetic Suspension Technology and Maglev Vehicle Ministry of Education
Southwest Jiaotong University, Chengdu, 610031, China
zhangwenlong2010@outlook.com, zhangkunlun@263.net

[2] Electric Design and Research Institute
China Railway Eryuan Engineering Group Co., Ltd., Chengdu, 610031, China
chenyin_swjtu@126.com

[3]Aviation Engineering Institute
Civil Aviation Flight University of China, Guanghan, 618307, China
edwiin85617@163.com

Abstract ─ In response to the shortcomings of existing devices, a novel electrodynamic suspension (EDS) device—based on a semicircular track and cylindrical permanent magnet (PM) Halbach array—is presented in this paper. It enables a vehicle to statically levitate above a semicircular track. In order to calculate the electromagnetic force created by this novel device, we first create a 2-D equivalent linear model of the cylindrical PM Halbach array, build differential equations (based on the linear model) for the magnetic vector potentials, and produce the expression of the electromagnetic force per unit length by solving the equation system. Next, by integrating the electromagnetic force per unit length with the arc direction of the inner semicircular track, the vertical electromagnetic force created by the novel device can be determined. Analytic expression results, and those of a finite element analysis (FEA) model built by Maxwell are compared, and show the average relative error to be 3.02%. The novel device is rational, and the analytic expression is accurate.

Index Terms ─ Analytical calculation, cylindrical PM Halbach array, EDS, electromagnetic force, static levitation.

I. INTRODUCTION

The translational motion of a PM above a conductive plate simultaneously creates an electrodynamic levitation force. Because EDS systems are simple, reliable, and stable, they have become a popular research topic in the Maglev field. Magplane is the most common example of this system [1,2]. At low speeds, drag force dominates and results in a small levitation force insufficient for vehicle suspension [3-5]. In order to overcome the deficiencies of existing devices, various topologies—using coils or conductive plates—have been proposed to minimize drag force and maximize levitation force. Lawrence Livermore National Laboratory proposed an Inductrack suspension system [6], in which a coil was placed below a PM array. Kratz and Chen studied a null-current EDS system [7,8] with a double PM Halbach array and conductive plate. Musolino numerically studied a null-flux system with PMs, a cylindrical conductive sheet, and null-flux coil [9]. These topologies all share the characteristic of reduced drag force, but the vehicle cannot be suspended in stationary and low-speed states. Bird studied an electrodynamic wheel [10,11] able to suspended a vehicle at any speed state. However, structural constraints of the PM wheel and track result in a limited levitation force that is only applicable to small devices. A novel electrodynamic suspension device is proposed in this paper. The device, shown in Fig. 1, is able to produce a large electromagnetic force at any vehicle state. Meanwhile, calculating electromagnetic force created by this device.

Numerical computation results are usually accurate [12-14], but fail to reflect the inherent relationships among different parameters. Alternatively, analytical calculations herein consist of a 2-D and 3-D model, Chen studied a null-flux topology using the 3-D model [15], while Cho derived the 2-D force equations for a single Halbach PM array moving above a conductive plate [4]. The advantage of the latter is also useful for 2-D modeling because it enables the magnetic field and force to be neatly formulated with respect to the conducting boundary [16].

The objective of this paper is to analytically derive

Submitted On: April 28, 2016
Accepted On: October 19, 2018

the general 2-D force that can be immediately used to compute the force due to eddy currents that is rotating above a semicircular track.

II. PROPOSED SYSTEM

The proposed configuration employs the same PM arrangement on each of the two guide-ways, as shown in Fig. 1. The 3-D and 2-D schematic of this cylindrical EDS system are shown in Fig. 2 and Fig. 3.

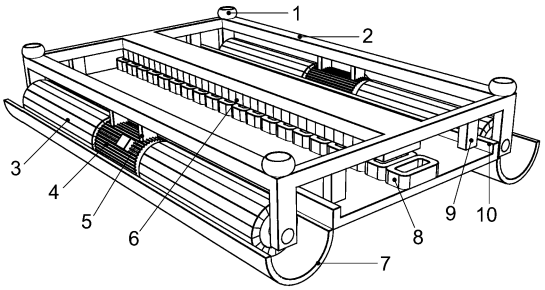

Fig. 1. Configuration of the cylindrical EDS device. 1: air spring, 2: chassis assembly, 3: PM Halbach rotor, 4: rotating motor with double extensions, 5: fixed module for motor, 6: propulsion magnets, 7: semicircular track, 8: LSM windings, 9: supporting block for location, and 10: limit baffle plate.

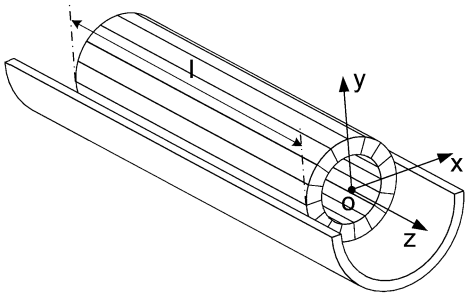

Fig. 2. 3-D schematic of the cylindrical EDS system.

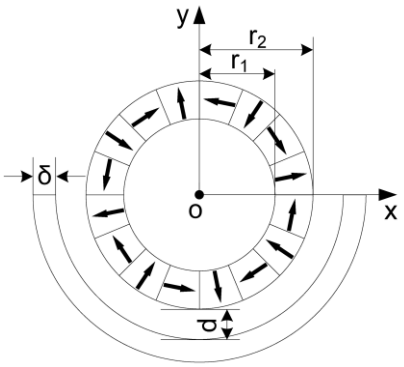

Fig. 3. 2-D schematic of the cylindrical EDS system.

In a maglev frame, four cylindrical PM modules are in pairs and symmetrically arranged in the track along the left and right sides. On each side, two modules are installed on the output shafts of the rotating motor with double extensions. While the maglev vehicle operates in the static state, the geometric center of the output shaft, cylindrical PM module, and semicircular guide groove are coincided in a side. The two rotating motors, which are fixed on both sides of the suspension frame and rotate in opposite directions at the same speed, drive the PM Halbach rotors. Relative movement between the PM rotors and the guide rail creates an eddy current in the rail, thereby generating the electromagnetic force. The resultant force is shown as only the vertical levitation force when there is no lateral movement. Otherwise, it includes the lateral guiding force.

III. EQUIVALENT MODEL

In Fig. 4, the unit arc length sheet, by means of symbol Δs, obtains the electromagnetic force F_0 of the PM rotor. The *x* and *y* components of this force are the guiding force F_{x0} and levitation force F_{y0}, respectively. By integrating the electromagnetic force, F_0, with the arc direction of the semicircular track, the vertical levitation force created by the cylindrical PM array can be determined. Where F_0 is the vertical electromagnetic force in the equivalent linear model as shown in Fig. 5. Without regard to lateral movement, the resultant force F_{x0} is zero as a consequence. We only discuss the approximate analytical expression of the vertical electromagnetic force in this paper.

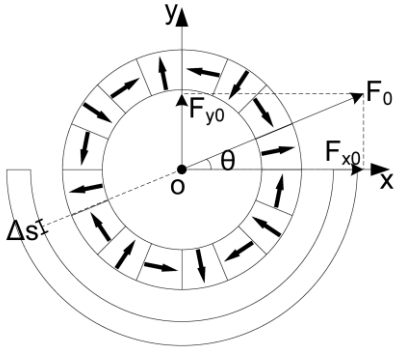

Fig. 4. 2-D cylindrical EDS model and its forces.

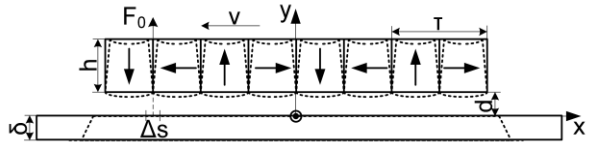

Fig. 5. The 2-D equivalent model.

IV. GOVERNING EQUATIONS

The 2-D equivalent linear model for the analytical solution is shown in Fig. 6. The axial length of the semicircular track is assumed to be sufficient, while the track itself is assumed to have constant conductivity, be nonmagnetic, and simply connected.

A. Conductive region, Ω_{II}

The surface density of an eddy current induced in a conductive plate by a moving source can be expressed as:

$$\boldsymbol{J} = \sigma \boldsymbol{E}, \tag{1}$$

$$\boldsymbol{E} = \boldsymbol{v} \times \boldsymbol{B}, \tag{2}$$

where $\boldsymbol{J}$ = surface density of the eddy current, σ = conductivity, $\boldsymbol{E}$ = electric field intensity, $\boldsymbol{v}$ = velocity vector, and $\boldsymbol{B}$ = magnetic flux density. Additionally, it is represented by the scalar equation:

$$J = -\sigma v B_y^s. \tag{3}$$

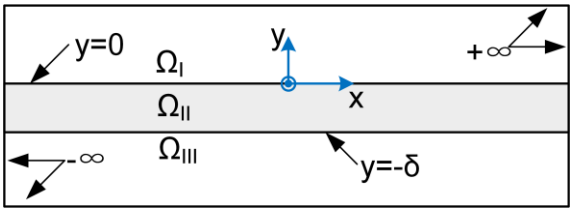

Fig. 6. Illustrating the conductive and nonconductive regions and boundaries.

Based on Ampère's circuital law and fundamental equation,

$$\nabla \times \boldsymbol{H} = \boldsymbol{J} + (\sigma + j\omega\varepsilon)\boldsymbol{E}, \tag{4}$$

$$\boldsymbol{B} = \nabla \times \boldsymbol{A}, \tag{5}$$

$$-\nabla\varphi = \boldsymbol{E} + j\omega\boldsymbol{A}, \tag{6}$$

$$\boldsymbol{B} = \mu_0 \boldsymbol{H}, \tag{7}$$

where $\boldsymbol{H}$ = magnetic field strength, ω = source frequency, ε = permittivity of the conductive plate, $\boldsymbol{A}$ = magnetic vector potential, φ = electric potential, and μ_0 = permeability of the conductive plate. Substituting (5), (6), and (7) into (4) and rearranging leads to:

$$\nabla^2 \boldsymbol{A} + k^2 \boldsymbol{A} = -\mu \boldsymbol{J} + \nabla\left(\nabla \cdot \boldsymbol{A} - \frac{k^2}{j\omega}\varphi\right), \tag{8}$$

and

$$k^2 = -j\omega\mu(\sigma + j\omega\varepsilon), \tag{9}$$

where k is a propagation function, using the Lorenz gauge,

$$\nabla \cdot \boldsymbol{A} - \frac{k^2}{j\omega}\varphi = 0. \tag{10}$$

The magnetic vector potential equation is:

$$\nabla^2 \boldsymbol{A} + k^2 \boldsymbol{A} = -\mu \boldsymbol{J}, \tag{11}$$

and in the 2-D model—as the magnetic vector potential, $\boldsymbol{A}$, only has a z component—is:

$$\nabla^2 A_z^{II} + k^2 A_z^{II} = -\mu J, \text{ in } \Omega_{II}. \tag{12}$$

B. Nonconductive regions, Ω_I, Ω_{III}

Because $\boldsymbol{J}$=0 in the nonconductive regions Ω_I and Ω_{III}, (11) simplifies to:

$$\nabla^2 A_z^{I} + k^2 A_z^{I} = 0, \text{ in } \Omega_I, \tag{13}$$

$$\nabla^2 A_z^{III} + k^2 A_z^{III} = 0, \text{ in } \Omega_{III}. \tag{14}$$

C. Boundary conditions

The conducting boundary conditions for the tangential field on the conductive plate surfaces are:

$$H_x^{I} - H_x^{II} = 0, \text{ at } y = 0, \tag{15}$$

$$H_x^{II} - H_x^{III} = 0, \text{ at } y = -\delta. \tag{16}$$

Based on the relationship between magnetic field strength and magnetic vector potential,

$$H_x = -\frac{1}{\mu}\frac{\partial A_z}{\partial y}. \tag{17}$$

Using (17) in (15) and (16) may lead to:

$$-\frac{\partial A_z^{I}}{\partial y} - \left(-\frac{\partial A_z^{II}}{\partial y}\right) = 0, \text{ at } y = 0, \tag{18}$$

and

$$-\frac{\partial A_z^{II}}{\partial y} - \left(-\frac{\partial A_z^{III}}{\partial y}\right) = 0, \text{ at } y = -\delta. \tag{19}$$

The inner boundary conditions of the joint face on the conductive plate surfaces are:

$$A_z^{I} = A_z^{II}, \text{ at } y = 0, \tag{20}$$

and

$$A_z^{II} = A_z^{III}, \text{ at } y = -\delta. \tag{21}$$

Additionally, the outer non-conducting boundary conditions are:

$$\lim_{y \to +\infty} A_z^{I} = 0, \tag{22}$$

and

$$\lim_{y \to -\infty} A_z^{III} = 0. \tag{23}$$

D. Source field

In the 2-D equivalent linear model, space magnetic field due to a PM Halbach array can be expressed as [17,18]:

$$B_x^s = B_0 e^{-p(-y+d)} e^{j(px-\pi/2)}, \tag{24}$$

and

$$B_y^s = B_0 e^{-p(-y+d)} e^{jpx}, \tag{25}$$

where

$$B_0 = [B_r(1 - e^{-ph})\sin\frac{\pi}{m}] / (\frac{\pi}{m}), \tag{26}$$

and B_x^s = magnetic flux density of the source field x-component, B_y^s = magnetic flux density of the source field y-component, B_r = magnet remanence, m is the

number of magnets in one pole-pair, and $p = \pi / \tau$ (where τ = pole pitch).

V. GENERAL SOLUTION

Applying the separation of variables principal to (11)-(13), the solution within each region is [8, 18]:

$$A_z^{\mathrm{I}} = (C_1 e^{-R_1 y} + C_2 e^{R_1 y}) e^{jpx}, \tag{27}$$

$$A_z^{\mathrm{II}} = [C_3 e^{-R_2 y} + C_4 e^{R_2 y} + \phi(y)] e^{jpx}, \tag{28}$$

$$A_z^{\mathrm{III}} = (C_5 e^{-R_3 y} + C_6 e^{R_3 y}) e^{jpx}, \tag{29}$$

where $R_i = \sqrt{p^2 - k_i^2}$, $\phi(y) = \dfrac{\mu_0 \sigma v B_0 e^{-p(-y+d)}}{k_2^2}$.

C_1-C_6 are unknowns that must be determined by means of boundary conditions (18)-(23). Therefore, the reflected field due to the induced current in the conducting plate may be expressed as:

$$B_x^r = -\frac{\partial A_z^{\mathrm{II}}}{\partial y}, \tag{30}$$

and

$$B_y^r = -\frac{\partial A_z^{\mathrm{II}}}{\partial x}. \tag{31}$$

When the translational motion of a PM is above the conductive plate, the total field is:

$$B_x = B_x^s + B_x^r, \tag{32}$$

$$B_y = B_y^s + B_y^r, \tag{33}$$

and the surface density of the eddy current is:

$$J_e = -\sigma v B_y. \tag{34}$$

VI. FORCE EQUATIONS

A. Electromagnetic force of an equivalent linear model

The vertical electromagnetic forces per unit width and length evaluated along the top of the plate surface is:

$$F_0 = -\frac{1}{2} \mathrm{Re} \int_{-\delta}^{0} J_e B_x^* dy, \tag{35}$$

where B_x^* is the complex conjugate of the magnetic field x-component.

B. Electromagnetic force of a 2-D cylindrical model

In order to calculate the electromagnetic force of the 2-D cylindrical model, it did this integral by along the arc direction in inboard semicircular track shown in Fig. 4. When $\Delta s \to 0$, $ds = R \cdot d\theta$, where R = the inside radius of the semicircular track. The levitation force of the Halbach rotor can be expressed as:

$$\begin{aligned} F_y &= \int_0^{\pi R} F_0 \sin\theta ds = \int_0^{\pi} F_0 R \sin\theta d\theta \\ &= -\frac{1}{2} \mathrm{Re} \int_0^{\pi} \int_{-\delta}^{0} J_e B_x^* R \sin\theta dy d\theta \end{aligned}. \tag{36}$$

VII. MODEL VALIDATION

The 2-D equivalent linear modeling approach was validated by creating an equivalent radial electromagnetic force for a PM Halbach rotor using a finite element analysis (FEA) model.

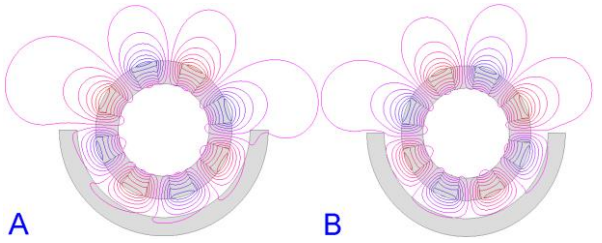

Fig. 7. PM Halbach rotor magnetic field transient simulation contour—plot at 360 rpm (shown in A) and 1620 rpm (shown in B).

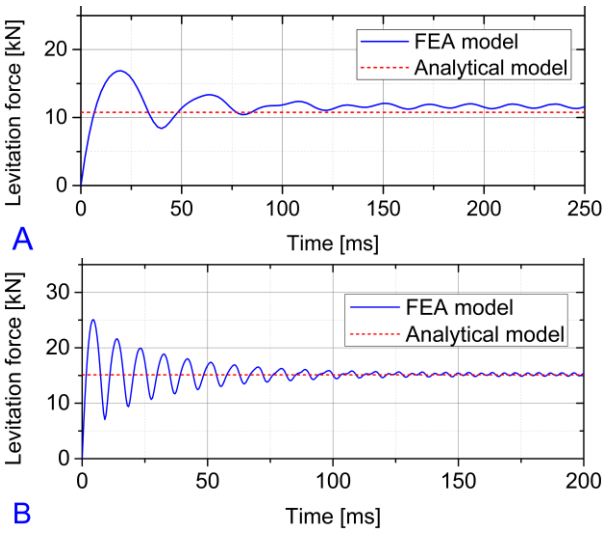

Fig. 8. 2-D transient results for the four pole-pair Halbach rotor at 360 rpm (shown in A) and 1620 rpm (shown in B).

Figure 7 shows the Halbach rotor magnetic field transient vector potential contour—plot at one timestep. Figure 8 shows the levitation force for rotating speeds of 360 rpm and 1620 rpm. The simulation parameters are shown in Table 1.

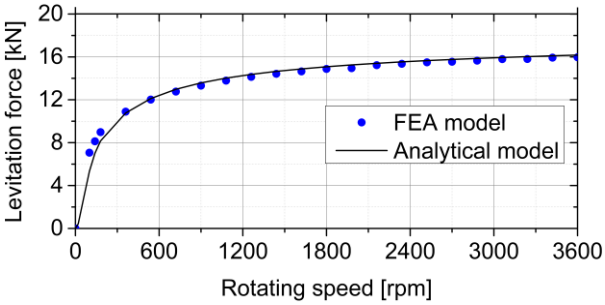

Fig. 9. The levitation force at different rotating speeds.

Figure 9 compares the analytic expression results with those of the finite element method built by Maxwell business software. They describe different rotational speeds with the parameters shown in Table 1. Figure 10 shows that the average relative error is 3.02%.

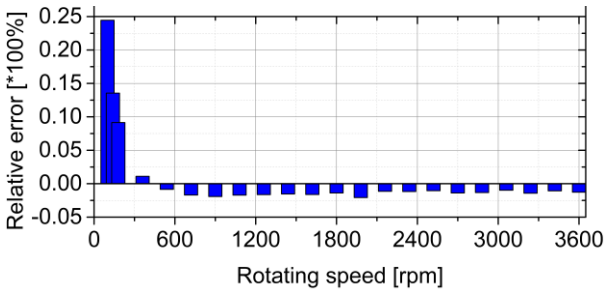

Fig. 10. Levitation force relative error as a function of rotating speed.

Table 1: Simulation parameters

Description		Value
Magnet	Number of pole-pairs, p	4
	Remanence, B_r	1.18 T
	Relative permeability, μ_r	1.067
	Outer radius, r_2	150 mm
	Inner radius, r_1	100 mm
	The axial length of a single magnet, l	1000 mm
Track	Conductivity, σ	3.8×10^7 S/m
	Outer radius, r_4	230 mm
	Inner radius, r_3	190 mm
	The thickness of track, δ	40 mm
	The length of a track, l_t	1000 mm
Air Gap	The vertical air gap between rotor and track, d	40 mm

VIII. DISCUSSION

From Fig. 9, the levitation force increases gradually and tends to saturation at 0-3600 rpm. Additionally, the nonmagnetic metal track can be used as an anti-magnet to concentrate magnetic field lines at higher rotor rotation speeds, as shown in Fig. 7.

The vertical magnetic force enables the vehicle to statically levitate above the semicircular track. Hence, the levitation force is analyzed for the different vertical air gap occurring at w = 720 rpm, 1620 rpm, and 3060 rpm. The vertical levitation stiffness was investigated in the same run. The steady vertical motion was interrupted every millimeter when the vertical air gap was between 20 and 50 millimeters. The result of such levitation force is shown in Fig. 11. The slope of the points on the levitation force curve gives the magnitude of the vertical stiffness. We plot the obtained stiffness coefficient as a function of the vertical air gap to show how the stiffness increases rapidly as the gap is reduced, as shown in Fig. 12.

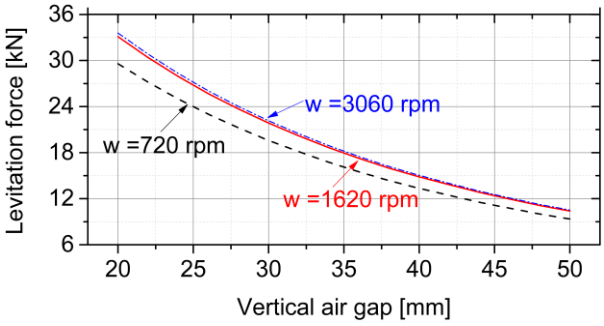

Fig. 11. The electromagnetic force and vertical air gap, when w =720 rpm, 1620 rpm, and 3060 rpm.

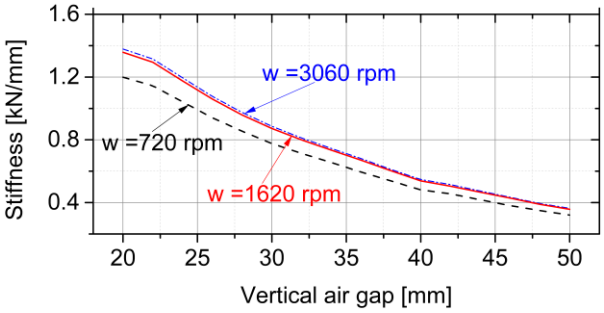

Fig. 12. Stiffness coefficient and vertical air gap when w =720 rpm, 1620 rpm, and 3060 rpm.

Using the structure parameters shown in Table 1 of the cylindrical PM electrodynamic suspension vehicle, a single cylindrical PM module can create a levitation force of 15000N at a rotating speed of 1620 rpm—calculated by the analytic and FEA method.

However, there is some limitation in our model. Unlike other electrodynamic systems that use the conductor plate and Halbach PMs, in this model, the magnetic field on the semicircular guide groove has a periodicity change, thus causing periodic, small-range fluctuations to the levitation force.

IX. CONCLUSION

A cylindrical PM EDS device that enables a vehicle to statically levitate above a semicircular track has been presented. A 2-D equivalent analytic calculation method has been deduced through second order vector potential and integral analysis. The method models the forces created when a Halbach rotor is rotating and moving above a semicircular, nonmagnetic metal guideway. The analytic model was validated by the finite element method.

ACKNOWLEDGMENT

This article was supported by the Key Laboratory Project of the Ministry of Education (No. 2682013ZT18). The authors would like to thank the Ansys Corporations for the use of their finite element analysis software, Maxwell.

REFERENCES

[1] J. Fang, A. Radovinsky, and D. B. Montgomery, "Dynamic modeling and control of the magplane vehicle," *Proceedings of The 18th International Conference on Magnetically Levitated Systems and Linear Drives*, Maglev'2004, China, Oct. 2004.

[2] D. B. Montgomery, "Overview of the 2004 magplane design," *Proceedings of The 18th International Conference on Magnetically Levitated Systems and Linear Drives*, Maglev'2004, China, Oct. 2004.

[3] H. Hieronymus, J. Miericke, F. Pawlitschek, and M. Rudel, "Experimental study of magnetic forces on normal and null flux coil arrangements in the inductive levitation system," *Applied Physics*, vol. 3, no. 9, pp. 359-366, 1974.

[4] H. Cho, H. Han, J. Bang, H. Sung, and B. Kim, "Characteristic analysis of electrodynamic suspension device with permanent magnet Halbach array," *J. Appl. Phys.*, vol. 105, 2009.

[5] H. Cho, D. K. Bae, H. Sung, and J. Lee, "Experimental study on the electrodynamic suspension system with HTSC and PM Halbach array magnets," *IEEE Trans. Appl. Superconduct.*, vol. 18, no. 2, pp. 808-811, 2008.

[6] R. F. Post and D. D. Dyutov, "The Inductrack: A simpler approach to magnetic levitation," *IEEE Trans. Appl. Superconduct.*, vol. 10, no. 1, pp. 901-904, 2000.

[7] R. Kratz and R. F. Post, "A-current electrodynamic levitation system," *IEEE Trans. Appl. Superconduct.*, vol. 12, no. 1, pp. 930-932, 2002.

[8] Y. Chen and K. Zhang, "Electromagnetic force calculation of conductor plate double Halbach permanent magnet electrodynamic suspension," *ACES Journal*, vol. 29, no. 11, pp. 916-922, 2014.

[9] A. Musolino, M. Raugi, R. Rizzo, and E. Tripodi, "Stabilization of a permanent-magnet Maglev system via null-flux coils," *IEEE Trans. on Plasma Sci.*, vol. 43, no. 5, pp. 1242-1247, 2015.

[10] J. Z. Bird and T. A. Lipo, "Modeling the 3-D rotational and translational motion of a Halbach rotor above a split-sheet guideway," *IEEE Trans. Magn.*, vol. 45, no. 9, pp. 3233-3242, 2009.

[11] J. Z. Bird and T. A. Lipo, "Calculating the forces created by an electrodynamic wheel using a 2-D steady-state finite-element method," *IEEE Trans. Magn.*, vol. 44, no. 3, pp. 365-372, 2008.

[12] P. Zheng, B. Yu, H. Yan, Y. Sui, J. Bai, and P. Wang, "Electromagnetic analysis of a novel cylindrical transverse-flux permanent-magnet linear machine," *ACES Journal*, vol. 28, no. 9, pp. 878-890, 2013.

[13] H. Rezaei and S. V. Zadeh, "Modelling and analysis of permanent electrodynamic suspension systems," *Prog. Electromagn. Res. M*, vol. 36, pp. 77-84, 2014.

[14] A. N. Khodabakhsh, S. V. Zadeh, and A. H. Isfahani, "Finite element analysis and experimental implementation of the cylindrical permanent magnet electrodynamic suspension system," *Electromagnetics*, vol. 29, no. 7, pp. 563-574, 2009.

[15] Y. Chen, W. Zhang, J. Z. Bird, S. Paul, and K. Zhang, "A 3-D analytic-based model of a null-flux Halbach array electrodynamic suspension device," *IEEE Trans. Magn.*, vol. 51, no. 11, article# 8300405, 2015.

[16] N. Paudel and J. Z. Bird, "General 2-D steady-state force and power equations for a traveling time-varying magnetic source above a conductive plate," *IEEE Trans. Magn.*, vol. 48, no. 1, pp. 95-100, 2011.

[17] J. F. Hoburg, "Modeling maglev passenger compartment static magnetic field from linear halbach permanent magnet arrays," *IEEE Trans. Magn.*, vol. 40, no. 1, pp. 59-64, 2004.

[18] Y. Chen, "Characteristic Analysis of Low Speed Electrodynamic Suspension," *Ph.D. Dissertation*, Department of Electrical Engineering, Southwest Jiaotong University, Chengdu, China, 2015.